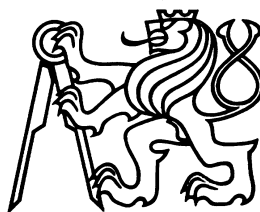


**CZECH TECHNICAL UNIVERSITY IN
PRAGUE**

**FACULTY OF NUCLEAR SCIENCE AND
PHYSICAL ENGINEERING**

Department of Physics



**Jet Reconstruction in Au+Au
Collisions at RHIC**

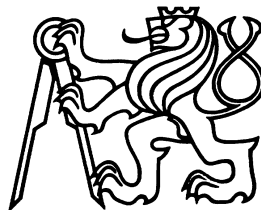
DOCTORAL THESIS

Author: **Ing. Jan Rusňák**
Supervisor: **RNDr. Jana Bielčíková, Ph.D.**

ČESKÉ VYSOKÉ UČENÍ TECHNICKÉ V
PRAZE

FAKULTA JADERNÁ A FYZIKÁLNĚ
INŽENÝRSKÁ

Katedra fyziky



Rekonstrukce jetů ve srážkách
 $Au+Au$ na urychlovači RHIC

DISERTAČNÍ PRÁCE

Vypracoval: Ing. Jan Rusňák
Vedoucí práce: RNDr. Jana Bielčíková, Ph.D.

Bibliographic Entry

| | |
|-----------------------|---|
| Author | Ing. Jan Rusňák, Czech Technical University in Prague, Faculty of Nuclear Sciences and Physical Engineering, Department of physics |
| Title of Dissertation | Jet Reconstruction in Au+Au Collisions at RHIC |
| Degree Programme | Application of natural sciences (D4CS) |
| Field of Study | Nuclear engineering (3901V016) |
| Supervisor | RNDr. Jana Bielčíková Ph.D, Nuclear Physics Institute, CAS, Department of Nuclear Spectroscopy |
| Academic year | 2016/17 |
| Number of Pages | 161 |
| Keywords | jety, srážky těžkých iontů, STAR, RHIC, dekonvoluce |

Bibliografický záznam

| | |
|------------------|--|
| Autor | Ing. Jan Rusňák, České vysoké učení technické v Praze, Fakulta jaderná a fyzikálně inženýrská, Katedra fyziky |
| Název práce | Rekonstrukce jetů ve srážkách Au+Au na urychlovači RHIC |
| Studijní program | Aplikace přírodních věd (D4CS) |
| Studijní obor | Jaderné inženýrství (3901V016) |
| Školitel | RNDr. Jana Bielčíková Ph.D, Ústav jaderné fyziky AVČR, v.v.i., Oddělení jaderné spektroskopie |
| Akademický rok | 2016/17 |
| Počet stran | 161 |
| Klíčová slova | jetý, srážky těžkých iontů, STAR, RHIC, dekonvoluce |

Abstract

Jet interaction with the medium provides sensitive observables to study properties of the hot and dense nuclear matter created in heavy-ion collisions. However, due to the large and fluctuating background, full jet reconstruction in heavy-ion collisions is an extremely challenging task.

We present a novel measurement of the inclusive spectra of reconstructed jets in central Au+Au collisions at $\sqrt{s_{\text{NN}}} = 200$ GeV by the STAR Collaboration at RHIC. Jets are reconstructed using charged tracks from the time projection chamber.

We utilize an experimental technique in which jet reconstruction is stable against the emission of an additional soft hadron, even in the high-multiplicity environment. In this technique the large combinatorial background is suppressed by a threshold cut on the leading hadron of each jet candidate. This cut, however, is not safe against collinear splitting of hard partons and thus is systematically explored. The jet spectra are fully corrected for background fluctuations and detector effects utilizing Bayesian and SVD unfolding techniques.

Suppression of jet yield is measured by comparison to p+p collisions. The broadening of jet structure due to jet quenching is explored by comparing measurements with different resolution parameters (R) in Au+Au and p+p collisions.

KEYWORDS: jets, heavy-ion collisions, STAR, RHIC, unfolding

Abstrakt

Interakce jetů s okolním prostředím představuje jednu z hlavních sond pro studium vlastností husté a horké jaderné hmoty vzniklé v jádro-jaderných srážkách. Avšak díky značnému a vysoce proměnlivému pozadí je úplná rekonstrukce jetů nanejvýš obtížným úkolem.

V této práci představujeme nové měření inkluzivního spektra rekonstruovaných jetů v centrálních srážkách Au+Au při těžiškové energii na nukleonový pár $\sqrt{s_{NN}} = 200$ GeV detekovaných experimentem STAR na urychlovači RHIC. Jety jsou zrekonstruované z drah nabitých částic detekovaných v časové projekční komoře.

Používáme experimentální techniku rekonstrukce jetů, která je stabilní vůči emisí nízkoenergetických hadronů dokonce i v prostředí s vysokou četností částic. Silné kombinatorické pozadí je potlačeno kritériem na hybnost vedoucího hadronu v každém jetu. S touto podmínkou však rekonstrukční algoritmus přestává být stabilní vůči kolineárnímu rozdělení partonů. Tento efekt je proto systematicky studován. Jetová spektra jsou korigována vůči fluktuujícímu pozadí a detektorovým efektům pomocí dekonvolučních metod.

Potlačení produkce jetů je určeno srovnáním s výsledky z p+p srážek. Rozšíření jetů v důsledku zhašení jetů je zkoumáno srovnáním výsledků pro různé jetové poloměry R ve srážkách Au+Au a p+p.

KLÍČOVÁ SLOVA: jety, srážky těžkých iontů, STAR, RHIC, dekonvoluce

Prohlášení

Prohlašuji, že jsem svou disertační práci napsal samostatně a výhradně s použitím citovaných pramenů.

Nemám závažný důvod proti použití tohoto školního díla ve smyslu § 60 Zákona č. 121/2000 Sb., o právech souvisejících s právem autorským a o změně některých zákonů (autorský zákon).

V Rynholci dne 25. 9. 2017

Ing. Jan Rusňák

Acknowledgments

No words can express my gratitude towards my supervisor Dr. Jan Bielčíková, who provided me with full support throughout my graduate research. She gave me hundreds of precious advices and introduced me to many great physicists and most of all, she has never lost patience. She is also the only person who carefully read this manuscript several times.

I am also thankful to Dr. Peter Jacobs from the Lawrence Berkeley National Laboratory who is an architect of this particular jet analysis. Each time I got to a dead end he brought me back.

Last but not least, I would like to thank to my wife and my kids who had to give up their time with me to this never ending work. I hope I will now have time to pay it back.

Contents

| | |
|---|-----------|
| Acknowledgements | i |
| 1 Standard Model | 4 |
| 1.1 Elementary Particles | 4 |
| 1.2 Strong Interaction | 8 |
| 1.2.1 Color Charge | 8 |
| 1.2.2 Running Coupling Constant | 9 |
| 1.2.3 Asymptotic Freedom | 10 |
| 1.2.4 Confinement | 10 |
| 2 Heavy-Ion Collisions | 12 |
| 2.1 Quark Gluon Plasma | 12 |
| 2.1.1 Space-time Evolution of Heavy-Ion Collision | 13 |
| 2.2 Probes of the QCD Medium | 16 |
| 2.2.1 Direct Photons | 16 |
| 2.2.2 Heavy Quarks | 17 |
| 2.2.3 Jets | 19 |
| 3 Jets | 20 |
| 3.1 Jet Evolution | 20 |
| 3.1.1 Initial Conditions | 21 |
| 3.1.2 Hard Scattering | 22 |
| 3.1.3 Fragmentation and Hadronization | 22 |
| 3.2 Jets in Heavy Ion Collisions | 25 |
| 3.2.1 Cold Nuclear Matter and nPDF | 26 |
| 3.2.2 Hot Nuclear Matter | 26 |
| 3.2.3 Jet Quenching | 27 |
| 3.2.4 Inclusive Jet Cross Section | 32 |
| 3.2.5 Leading Hadron Bias | 32 |
| 3.3 Jet Reconstruction Algorithms | 34 |
| 3.3.1 Cone Algorithms | 35 |
| 3.3.2 Clustering Algorithms | 36 |
| 3.3.3 Jet Reconstruction in Heavy Ion Collisions | 39 |

| | | |
|----------|---|------------|
| 3.4 | Recent Jet Measurements at RHIC and the LHC | 40 |
| 3.4.1 | Jets in p+p Collisions | 40 |
| 3.4.2 | Cold Nuclear Matter Effects on Jet Production | 45 |
| 3.4.3 | Jet Quenching Measurements | 49 |
| 4 | RHIC and STAR | 61 |
| 4.1 | RHIC | 61 |
| 4.1.1 | The Accelerator Complex | 62 |
| 4.2 | STAR Experiment | 63 |
| 4.2.1 | TPC | 67 |
| 4.2.2 | HFT | 69 |
| 5 | Service Work Related to HFT | 72 |
| 5.1 | PXL Survey and Alignment | 72 |
| 5.2 | Λ_c Reconstruction with HFT | 75 |
| 6 | Jet Analysis in Au+Au Data | 79 |
| 6.1 | Dataset | 79 |
| 6.1.1 | Tracking efficiency | 81 |
| 6.1.2 | Momentum resolution | 85 |
| 6.2 | Jet Reconstruction | 89 |
| 6.3 | Correction for Underlying Event Background | 89 |
| 6.3.1 | p_T^{lead} cut | 91 |
| 6.3.2 | δp_T | 94 |
| 6.4 | Correction for Instrumental Effects | 97 |
| 6.4.1 | Instrumental Response | 97 |
| 6.4.2 | Jet Reconstruction Efficiency | 98 |
| 6.4.3 | Jet Energy Resolution | 98 |
| 6.5 | Unfolding | 102 |
| 6.5.1 | Bayesian Unfolding | 103 |
| 6.5.2 | Singular Value Decomposition (SVD) Unfolding | 104 |
| 6.5.3 | Prior Distribution | 104 |
| 6.5.4 | Optimal Value of Regularization Parameter | 105 |
| 6.5.5 | Response Matrix Construction | 107 |
| 6.6 | Systematic Uncertainties | 115 |
| 6.6.1 | Shape Uncertainties | 115 |
| 6.6.2 | Correlated Uncertainties | 116 |
| 6.6.3 | Jet Energy Scale Uncertainty | 118 |
| 6.7 | Bin-shift Correction | 118 |
| 7 | Parametrized Model | 120 |
| 7.1 | Comparison to STAR Data | 121 |
| 7.2 | Parametrized Model Closure Test | 124 |

| | | |
|-----------|--|------------|
| 8 | p+p Reference for R_{AA} | 126 |
| 8.1 | Inclusive Jet Spectrum from PYTHIA | 126 |
| 8.2 | Run12 p+p Analysis | 127 |
| 9 | Results and Discussion | 132 |
| 9.1 | Corrected Charged Jet Spectra | 132 |
| 9.2 | Spectra Ratios - different p_T^{lead} cuts | 134 |
| 9.3 | Spectra Ratios - different R | 135 |
| 9.4 | R_{CP} | 137 |
| 9.5 | R_{AA} | 139 |
| 9.6 | Comparison to Theoretical Models and Other Experiments | 143 |
| 10 | Summary | 147 |
| | Appendices | 149 |
| A | STAR Data Production Chain | 150 |
| B | Bad Run List | 151 |
| C | List of Acronyms | 152 |
| | Bibliography | 154 |
| | Published Papers | 162 |

Chapter 1

Standard Model

1.1 Elementary Particles

Standard Model of particle physics (SM) is a theoretical framework which describes physical properties of particles and their interactions. It recognizes several elementary particles: 12 fermions - building blocks of matter and 5 bosons - force mediators.

However, history knows many objects which were considered to be elementary particles before. Already in the 5th century B.C., Democritus continued in the legacy of his teacher Leucippus and further developed a hypothesis, that the entire matter is formed from small, further indivisible (“uncuttable”=“atomos” in Greek), solid objects of different sizes and shapes, moving continuously in random directions and interacting mechanically. This was however a pure philosophical theory with no experimental foundations. It was not before the 19th century when a further step was made. John Dalton showed that the ratios of masses of elements which form a compound in a chemical reaction are always ratios of small numbers. This brought him to the formulation of his atomic theory. His theory stated five key points:

1. Elements are made of extremely small particles called atoms.
2. Atoms of a given element are identical in size, mass, and other properties; atoms of different elements differ in size, mass, and other properties.
3. Atoms cannot be subdivided, created, or destroyed.
4. Atoms of different elements in simple whole-number ratios form chemical compounds.
5. In chemical reactions, atoms are combined, separated, or rearranged.

The fact that even the atom has its internal structure was brought to the light in 1897 when J. J. Thomson discovered the electron in cathode rays. His pudding model of atom [1], where electrons were evenly distributed inside a massive and positively charged medium, was quickly disproved by Ernest Rutherford and his students - Hans Geiger and Ernest

Marsden - who found during their experiments with irradiation of a thin gold foil with alpha particles [2, 3, 4] that most of the atomic mass and positive charge is concentrated in a small volume inside the center of the atom [5]. A few years later Rutherford bombarded nitrogen gas with alpha particles and observed that hydrogen nuclei were produced during the reaction [6] - from this observation he concluded that the hydrogen nucleus is a single particle which is a basic building block of more complex nuclei, like that of nitrogen. He named this particle proton. A few years later, in 1932, James Chadwick observed that beryllium bombarded by alpha particles emits neutral particles capable of kicking out hydrogen nuclei from some materials [7]. Due to the absence of an electric charge, the new particle was called neutron.

A rapid development of the particle accelerator experiments after the World War II was followed by discoveries of numerous new hadrons, quickly filling the imaginary particle ZOO. It became evident that these hadrons cannot present the elementary particles and both theorists and experimentalists started to look for some simpler constituents. In 1964, two scientists - Murray Gell-Mann and George Zweig - independently formulated a theory which introduced three new hypothetical particles with a fractional charge from which the known hadrons are composed. In the Gell-Mann's paper [8] they are called "quarks", whereas Zweig suggested the term "aces" [9]. It was the name "quark" which was finally adopted by the scientific community. The corresponding quantum number which distinguishes different quark types was called flavor. As noted, three flavors were required by the contemporary theory. These were later called u (up), d (down) and s (strange).

With the development of the electro-weak theory a need of more quarks became apparent, namely the Glashow–Iliopoulos–Maiani mechanism of suppressing the flavor-changing neutral currents published in 1970 [10] required the existence of the fourth quark. The discovery of the J/ψ meson in 1974 was one of those happy accidents (which are in physics and mathematics so common) when some breaking discovery is made on two distant places independently and almost in the same time. The experiment at the Brookhaven National Laboratory (BNL) in Upton, New York, measured the invariant mass of electron - positron pairs produced in the collisions of protons with the nuclei of the beryllium fixed target. This measurement revealed a sharp resonance at $3.1 \text{ GeV}/c^2$. The team named the newly discovered meson "J". The paper describing the observation was submitted to the Physical Review Letters on November 12, 1974 [11]. However only one day later, November 13, another paper was submitted to the same journal [12]. A team from the Stanford Linear Accelerator Center (SLAC) in California observed a similar resonance in the invariant mass spectrum of electron - positron pairs produced in the electron - positron annihilation at the SLAC electron - positron storage ring SPEAR. The team at SLAC named the particle ψ meson. In order to satisfy both teams, the J/ψ was chosen as the official name of the new meson. However more interesting than its discovery was the inner structure of this meson. Its decays revealed that it is a bound state of a new, heavier quark (and its anti-quark) - the charm quark - as predicted by Glashow.

For a long time, physicists considered the charge conjugation parity symmetry (CP-symmetry) to be one of the basic symmetries of our universe. It states that interchanging a particle with its antiparticle (charge conjugation symmetry) and inverting its spatial coor-

dinates (parity symmetry) should not change the physical processes in any way. However in 1964 a violation of the CP-symmetry was observed in the decays of neutral kaons [13].

In order to describe the effect of CP-violation within the framework of the theory of weak interaction, Makoto Kobayashi and Toshihide Maskawa hypothesized a model with 6 quark fields instead of 4 [14]¹. Although they admitted introducing new quark fields is not the only way how to solve the problem, the discovery of Υ meson at Fermilab by the E288 experiment four years later in 1977 [15], proved the correctness of their idea. It was quickly discovered that the Υ meson is a bound state of a previously unknown, even heavier quark and its anti-quark, which was given name “beauty”, “bottom” or just “b” quark.

The last member of the quark family - the top quark (or t -quark) was inaccessible in the 70’s with the energies achieved at contemporary accelerators due to its very large mass. Only with the launch of the Tevatron collider at Fermilab physicists got the opportunity to produce the top quark in laboratory conditions. In 1995 two Tevatron experiments - CDF and D0 - announced the discovery of the top quark with the 5σ significance of the signal [16, 17].

Nowadays there are six quark flavors known. These 6 flavors are divided into 3 generations (or families). The first generation consists of the u and d quark, the s and c quarks form the second generation and the b and t the last one. There is a strong theoretical and experimental evidence against the existence of a fourth or higher generation of fermions [18, 19].

Since Democritos the family of the elementary particles evolved significantly. Their latest “family photo” is on Fig. 1.1. Together with the 3 generations of quarks there are also 3 generations of leptons presented. That is the conventional part of the family whose members possess half-integer spin values and obey Fermi-Dirac statistics. The second half of the family are nonconformists, integer spin particles obeying Bose-Einstein statistics: 4 gauge bosons with spin 1 and the youngest child, Higgs boson with spin 0.

Despite the perpetual effort (both intellectual and physical) of the mankind, our knowledge even about the most simple building blocks of matter is still incomplete and further evolving. The question is, whether it is even possible to gain such a level of knowledge which would completely fill the gaps in our understanding of the Universe. Most of the physicists just leave this question to philosophers and continue in their never ending pursuit.

¹The paper was published in 1973, even before the observation of the charm quark!

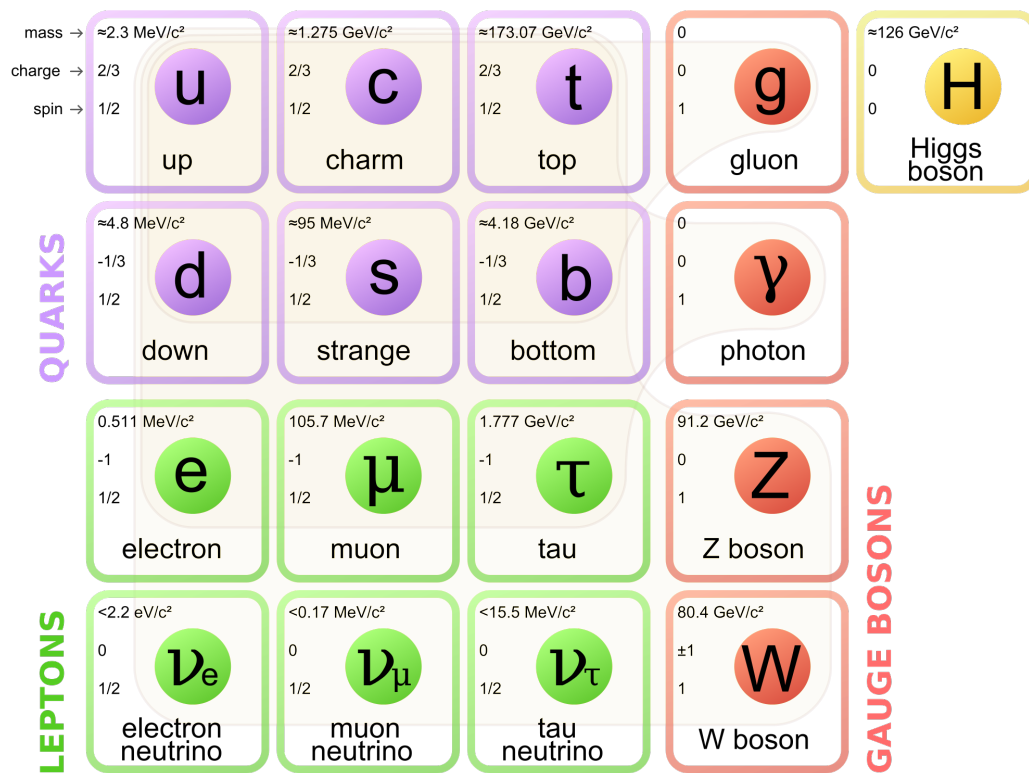


Figure 1.1: Elementary particles and their properties. Figure adopted from [20].

1.2 Strong Interaction

Contemporary physics recognizes four elementary interactions - electromagnetic, weak, strong and gravitational. Gravitational force is by far the weakest of them, however its omnipresence (every massive particle is an elementary source of the gravity), the absence of a repulsive gravitational force and its unlimited range make it the main governing force of the Universe. Hypothetical mediator of the gravitational force - graviton - is still waiting for its discovery.

Electromagnetic and weak interactions are mediated by spin-1 bosons and theoretically described within the framework of the Electro-Weak theory. Similarly to gravitational force, range of the electromagnetic force is unlimited, since it is mediated by massless photons. On the other hand weak interaction is mediated by massive W^\pm and Z bosons. These bosons are short-living with lifetime $< 10^{-24}$ s, thus limiting the effective range of the interaction to distances of 10^{-17} m.

The strong interaction derives its name from its relative strength in comparison with the other elementary forces. It has a coupling constant of ≈ 1 , much larger than electromagnetic coupling constant ($\approx 10^{-2}$) and weak coupling constant ($\approx 10^{-6}$). It is its extraordinary strength which binds protons and neutrons together into stable nuclei despite the electromagnetic repulsion between protons. The strong force interaction between protons and neutrons arises from much smaller scale, from the interaction between quarks and gluons - fundamental carriers of the strong charge.

1.2.1 Color Charge

The quarks possess a quantum number called ‘color’, which can acquire 3 different values denoted for example 1, 2, 3 or red, green, blue. The requirement of three colors comes e.g. from the fact that we observe 3 quark states with $J = 3/2$ as baryon Δ^{++} ($u^\uparrow u^\uparrow u^\uparrow$) which should otherwise not exist due to the Pauli exclusion principle. The weak interaction changes the quark flavor, however the strong processes are flavor-conserving and flavor-independent. On the other hand the weak interaction is independent from the quark color. Therefore it is natural to identify the color quantum number as the charge of the strong interaction.

Quantum Chromodynamics (QCD) is a non-Abelian gauge field theory which describes the strong interactions of quarks and gluons.

The QCD Lagrangian is given as

$$L = \sum_q \bar{\psi}_{q,a} (i\gamma^\mu \partial_\mu \delta_{ab} - g_s \gamma^\mu t_{ab}^C A_\mu^C - m_q \delta_{ab}) \psi_{q,b} - \frac{1}{4} F_{\mu\nu}^A F_{A\mu\nu}, \quad (1.1)$$

where ψ are quark-field spinors, q is a quark flavor, m_q quark mass, γ^μ are the Dirac γ matrices, and a is a color index, which runs from 1 to $N_q = 3$. The A_μ^C are gluon fields with C running from 1 to $N_g = 8$. The t_{ab}^C are 3x3 matrices and correspond to 8 generators of the $SU(3)$ group. The field tensor $F_{\mu\nu}^A$ is defined as

$$F_{\mu\nu}^A = \partial_\mu A_\nu^A - \partial_\nu A_\mu^A - g_s f_{ABC} A_\mu^B A_\nu^C, \quad (1.2)$$

where the f_{ABC} are the structure constants of the $SU(3)$ group.

1.2.2 Running Coupling Constant

Similarly to Quantum-Electro-Dynamics (QED), the QCD coupling can be renormalized in order to avoid the ultra-violet divergences arising from quantum loops.

In the case of the QED the coupling constant α is no more a constant²⁾, but a function of the energy scale Q^2 at which the process of interest is being explored, corresponding to the transferred momentum q^2 in the interaction as $Q^2 \equiv -q^2$ ³⁾. The reason is the screening of the charge by a cloud of virtual electron-positron pairs. This cloud gets polarized by the charge it surrounds, making it effectively weaker. The larger the distance, the stronger the screening effect is.

The scale dependency of the coupling can be reformulated in terms of the β function

$$Q \frac{d\alpha}{dQ} \equiv \alpha\beta(\alpha) \tag{1.3}$$

$$\beta(\alpha) = \beta_0 \frac{\alpha}{\pi} + \beta_1 \left(\frac{\alpha}{\pi} \right)^2 + \dots$$

The terms β_0, β_1, \dots correspond to diagrams with 1 loop, 2 loops, etc. The first term equals to

$$\beta_0 = 2/3. \tag{1.4}$$

Restricting to the case of 1 loop diagrams ($\beta(\alpha) \simeq \beta_0 \frac{\alpha}{\pi}$), $\alpha(Q^2)$ becomes

$$\alpha(Q^2) = \frac{\alpha(Q_0^2)}{1 - \frac{\beta_0 \alpha(Q_0^2)}{2\pi} \ln\left(\frac{Q^2}{Q_0^2}\right)}, \tag{1.5}$$

with Q_0 being an arbitrary energy scale at which one knows the value of $\alpha(Q_0^2)$ from measurements.

However the situation changes significantly in the QCD case. The coupling constant α_s can be analogically renormalized, however due to the gluon self interaction, additional terms arise in the calculation and for the first term of the β function one gets

$$\beta_0^{\text{QCD}} = \frac{2N_f - 11N_C}{6}, \tag{1.6}$$

where $N_C = 3$ is number of colors. This leads to the following form of the strong coupling scale dependency

²Despite this fact, we will continue to call the quantity $\alpha(Q^2)$ a coupling “constant“.

³In this perspective, the fine structure constant $\alpha = 1/137$ is corresponding to a very low scale of electron mass $\alpha(Q^2 = -m_e^2)$

$$\alpha_s(Q^2) = \frac{12\pi}{(33 - 2N_f) \ln(\frac{Q^2}{\Lambda_{\text{QCD}}^2})}, \quad (1.7)$$

where we have introduced an arbitrary scale $Q_0 \equiv \Lambda_{\text{QCD}} \approx 220$ MeV typical for QCD. Since most of the QCD problems are hard or impossible to solve directly, a perturbation theory is often used. The perturbation theory is however valid only in a region where $\alpha_s \ll 1$, which corresponds to the energies $Q \gg \Lambda_{\text{QCD}}$. Λ_{QCD} therefore represents an infrared cutoff for the perturbation theory.

In analogy to QED, quark color charge is also effectively weakened by the virtual quark-antiquark pairs. On the other hand, virtual gluons around the quark strengthen the quark's color charge. This is called anti-screening. The anti-screening is responsible for the appearance of the negative term in Eq. 1.6.

1.2.3 Asymptotic Freedom

The presence of a negative term in Eq. 1.6 results in a very specific behavior of the strong coupling constant with respect to the coupling constant of QED. Even if one would evaluate α_s with six quark flavors $N_f = 6$, the value of β_0 is negative and therefore the α_s will become arbitrary small for sufficiently high energy scales (or equivalently, at small distances)

$$Q^2 \rightarrow \infty \Rightarrow \alpha_s \rightarrow 0. \quad (1.8)$$

This behavior is called asymptotic freedom, since it allows quarks and gluons to act as free particles at very small distances.

1.2.4 Confinement

On the other hand, at larger distances (or equivalently in the low energy regime), the strength of the coupling rises above all limits. This would suggest a possibility of a quark confinement at larger distances, however at this point the perturbation theory is no longer valid.

There are ongoing efforts among the theoretical physicists to derive the correct form of the quark-(anti)quark potential either from the pure QCD or its combination with other theory [21].

Nevertheless quarks are never observed as free particles, rather they are always bound into colorless objects and a valid theory should account for that fact. Therefore, within the framework of the "string model" [22, 23], the quark-quark potential is assumed to have the form prescribed by the following empirical formula

$$V_{strong}(r) = -\frac{4}{3} \cdot \frac{\alpha_s}{r} + kr. \quad (1.9)$$

The first term of Eq. 1.9 is a Coulomb-like potential, dominating at small distances. At larger distances the strength of the potential is governed by the second term (since $\alpha_s \sim r$). A high energy "string" is created between two quarks, energy density is rising with the distance between quarks increasing, until reaching some critical distance r_c , where the energy density between the quarks is high enough to create a new quark - anti-quark pair. These new quarks are immediately interacting with the original quarks, effectively reducing the strong potential and once again forming colorless objects.

Chapter 2

Heavy-Ion Collisions

In order to test the QCD predictions, especially the regime of asymptotic freedom, one needs to probe the nucleons at very high Q^2 . Deep inelastic scattering of electrons on protons is an example of such a probe. Even though this is a very clean probe used to measure the parton distribution functions it is insensitive to the gluon content of the nucleon, since the electron interacts only via weak and electric charge while gluons poses only color charge. Hadron collisions are thus the only way how to explore the gluon content of nucleons. Moreover, much higher Q^2 are achievable for nucleon-nucleon collisions than for electron-nucleon collisions. However, for the study of matter in the state of deconfinement, higher baryonic and energy densities are necessary. In 1980 Edward Shuryak suggested that such conditions could be achieved by colliding heavy ions [24]. Pioneering steps in performing heavy-ion collisions were made at the Alternating Gradient Synchrotron (AGS) at Brookhaven National Laboratory (BNL) and at the Super Proton Synchrotron (SPS) at CERN. However a real breakthrough came in year 2000 with the commission of the world's first dedicated heavy-ion collider, the Relativistic Heavy Ion Collider (RHIC) at BNL, NY, USA. This magnificent machine will be further discussed in Chapter 4.1.

2.1 Quark Gluon Plasma

It was Rolf Hagedorn, who in the framework of his Bootstrap Model (BSM) [25] concluded, that there is a temperature value, called Hagedorn temperature T_H , at which the hadron gas undergoes a phase transition. After reaching T_H , the temperature of the system remains constant and the energy added to the system is spent on production of new particles. This idea was in contradiction to Fermi-Pomeranchuk-Landau model [26, 27, 28] of hadronic matter, where the growth of the temperature was unlimited. However the BSM was successful in describing observed exponential growth of the hadron mass spectra and hence attained a lot of attention. At the end of 70's, Rolf Hagedorn with his colleagues reformulated the BSM, treating the hadron states as bags of quarks and gluons, instead of being point-like massive particles. The Hagedorn temperature T_H , in the context of QCD called "critical temperature" T_C , was then understood as the boundary of the transition

from hadron gas to quark gluon plasma [29]. Both smooth crossover and a sharp phase transition are possible within this model.

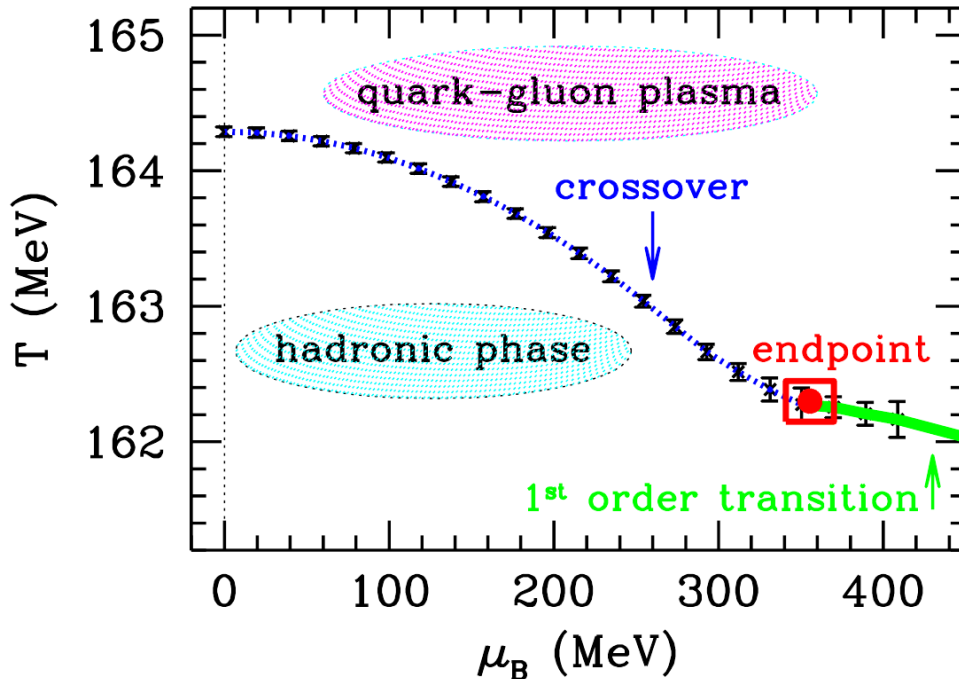


Figure 2.1: Lattice QCD calculation of the critical curve of the phase transition between hadron gas and quark gluon plasma [30].

The latest numerical calculations of the lattice QCD put the value of the transition (at zero baryon chemical potential) to $T_C = 154 \pm 9$ MeV [31], however this value generally changes between 150 and 170 MeV depending on the treatment of quark properties in the calculation [32]. The calculations also show, that there is a critical value of the baryon chemical potential, below which the transition is a smooth crossover, while above this value the system undergoes a first order phase transition [30]. One can then speak about a critical T - μ curve as seen on Fig. 2.1 with a critical point separating the phase transition region from the crossover.

Determining the exact position of the critical point is one of the main goals of the RHIC Beam Energy Scan (BES) program, which started the first phase of data-taking in 2010 and finished it in 2014. Preparations are being made for its second phase, which is planned for 2018-2019 and should lead to an order of magnitude larger statistics [34]. A schematic coverage of the BES program in the QCD phase diagram is illustrated in Fig. 2.2.

2.1.1 Space-time Evolution of Heavy-Ion Collision

When the system undergoes the phase transition (or the crossover), color degrees of freedom emerge. This leads to a rapid rise of the entropy density, which is manifested in the increase

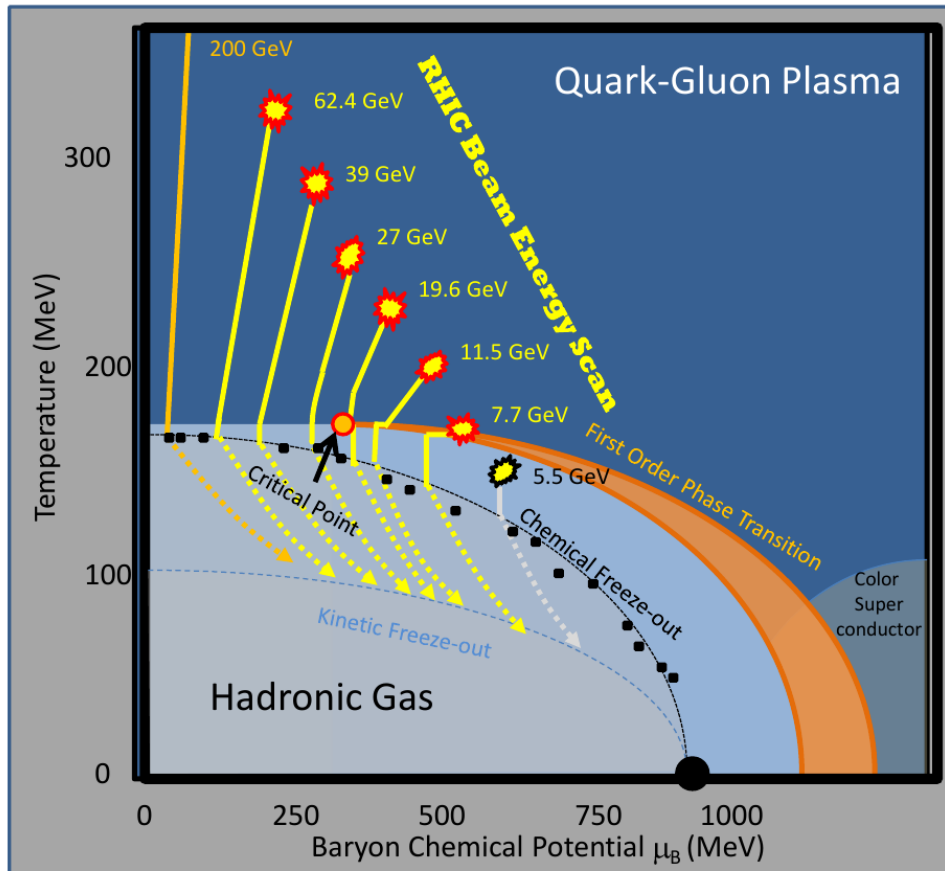


Figure 2.2: Coverage of the RHIC BES program in the QCD phase diagram. Yellow trajectories represent schematics of the collision evolution at different energies of the BES program. The red circle symbolizes the critical point. Note, that yellow lines and the red circle are for illustrative purpose only. Figure taken from [33].

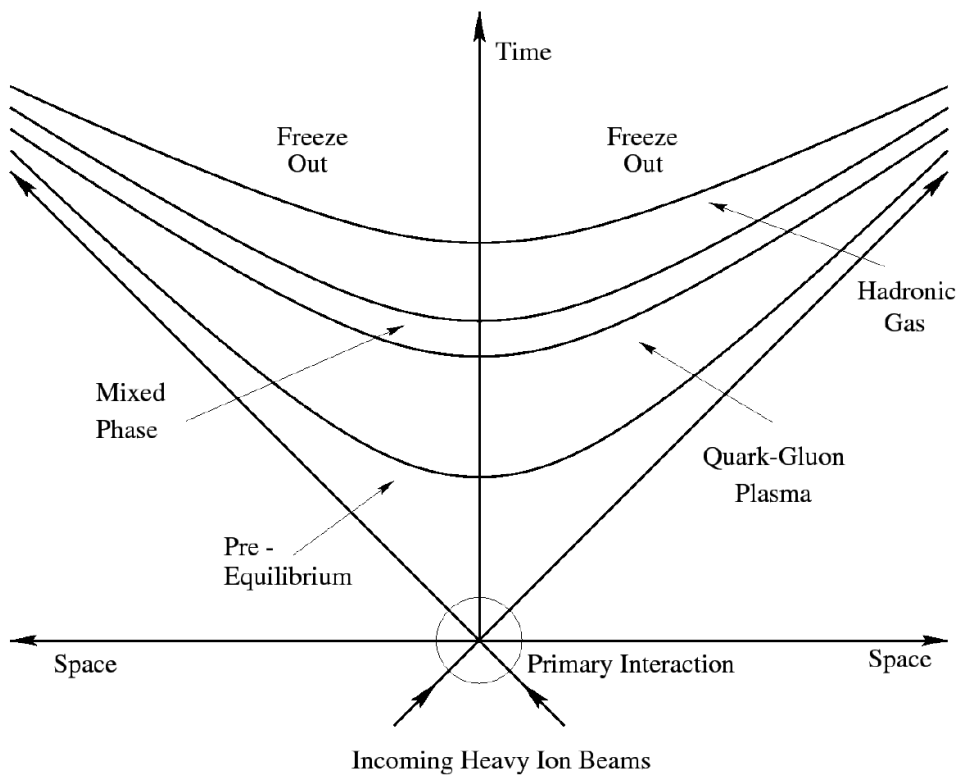


Figure 2.3: Space-time evolution of the heavy-ion collision, assuming formation of the quark gluon plasma.

of the pressure and temperature of the system (temperature of the quark gluon plasma is no more limited by the critical temperature and can rise above this value), followed by the system expansion. Expansion of the “fireball” cools down the system according to $T = T_0 \cdot \left(\frac{\tau_0}{\tau}\right)^{1/3}$ [35], where T_0 is the initial temperature at time τ_0 , when the QGP reaches the thermal equilibrium. At time τ_p the system reaches the critical temperature T_C and the phase transition to the hadron gas begins. This process is called hadronization. At time $\tau_h \approx 10 \cdot \tau_p$ the hadronization is completed and all quarks are confined within hadrons. This is called chemical freeze-out.

The newly created hadrons can interact and exhibit collective motion. The fireball expansion continues until the probability of hadron interactions drops close to zero so the elastic collisions between the hadrons which would change their momenta do not occur anymore. The system has just reached the kinetic freeze-out.

Fig. 2.3 schematically shows the space-time evolution of the matter created after a heavy-ion collision, going through the QGP formation, hadronization, chemical freeze-out and finally the kinetic freeze-out.

2.2 Probes of the QCD Medium

In the case of heavy-ion collisions, the quark gluon plasma can be formed only for very limited time period and only in a small volume. Therefore it cannot be studied directly, but several indirect probes have been suggested to detect the QGP and explore its properties.

2.2.1 Direct Photons

In the deconfined state, a quark can annihilate with a corresponding anti-quark and produce a photon in the following reactions:

$$q + \bar{q} \rightarrow \gamma + g \tag{2.1}$$

$$q + \bar{q} \rightarrow \gamma + \gamma. \tag{2.2}$$

However the second process is suppressed with respect to the first one by the order of $\frac{\alpha}{\alpha_s} \approx 0.02$.

A gluon can also produce a photon, via the Compton process:

$$g + q \rightarrow \gamma + q \tag{2.3}$$

$$g + \bar{q} \rightarrow \gamma + \bar{q}. \tag{2.4}$$

The emitted photons interact with the surrounding medium only electromagnetically, thus having a mean free path large enough to escape the collision region. The momentum and the production rate of the created photons depends on the momentum of quarks and

gluons coming to the reactions. However their momentum distributions are driven by the thermodynamics of the medium. Therefore the photons carry the information about the state of the quark gluon plasma at the moment of their production.

Unfortunately, there are many competing sources of the photons which need to be subtracted. These include reactions of hadrons, mainly pions:

$$\pi^+ + \pi^- \rightarrow \gamma + \rho^0 \quad (2.5)$$

$$\pi^\pm + \pi^0 \rightarrow \gamma + \rho^\pm \quad (2.6)$$

and also decays of neutral mesons, mainly:

$$\pi^0 \rightarrow \gamma + \gamma. \quad (2.7)$$

In the initial phase of the heavy-ion collision the constituent partons of the colliding nuclei can also interact via quark - antiquark annihilation and gluon - quark inelastic scattering, thus producing photons by the same mechanisms as in the QGP, but carrying no information about the medium.

It was shown, that the shape of the photon spectrum at a given temperature is similar for both the QGP and the hadron gas [36]. Distinguishing the QGP from the hadron gas would not be possible in such a case. However, the temperature of the QGP can reach much higher values, since the temperature of the hadron gas is limited by the Hagedorn temperature.

2.2.2 Heavy Quarks

By heavy quarks one usually means c , b and t -quarks. As light quarks are considered u and d -quarks. Depending on the point of view, the s -quark is sometimes considered as light, sometimes as heavy. We will focus our discussion on the c and b -quarks in this section.

Mass of the heavy quarks is generated dominantly by coupling to the Higgs field, while mass of the light quarks is generated dominantly through the Yukawa coupling to the QCD vacuum and only a small fraction by coupling to the Higgs field (see Fig. 2.4). Therefore, in case of restoration of the chiral symmetry, the light quarks would loose much of their mass and become even lighter, while the heavy quarks would retain basically all of their mass. This means heavy quarks remain heavy even in the presence of the QGP.

Heavy quarks are produced at the initial phase of the nucleus - nucleus collision in hard parton scattering in gluon fusion and $q\bar{q}$ annihilation:

$$g + g \rightarrow Q + \bar{Q} \quad (2.8)$$

$$q + \bar{q} \rightarrow Q + \bar{Q}, \quad (2.9)$$

where q , \bar{q} are light (anti)quarks in the incoming nuclei, while Q and \bar{Q} are produced heavy (anti)quarks. In order to create a quark anti-quark pair with a mass m_Q , the minimal momentum transfer is $Q = 2m_Q$. The corresponding reaction timescale is $\tau = 1/\sqrt{Q^2} \simeq$

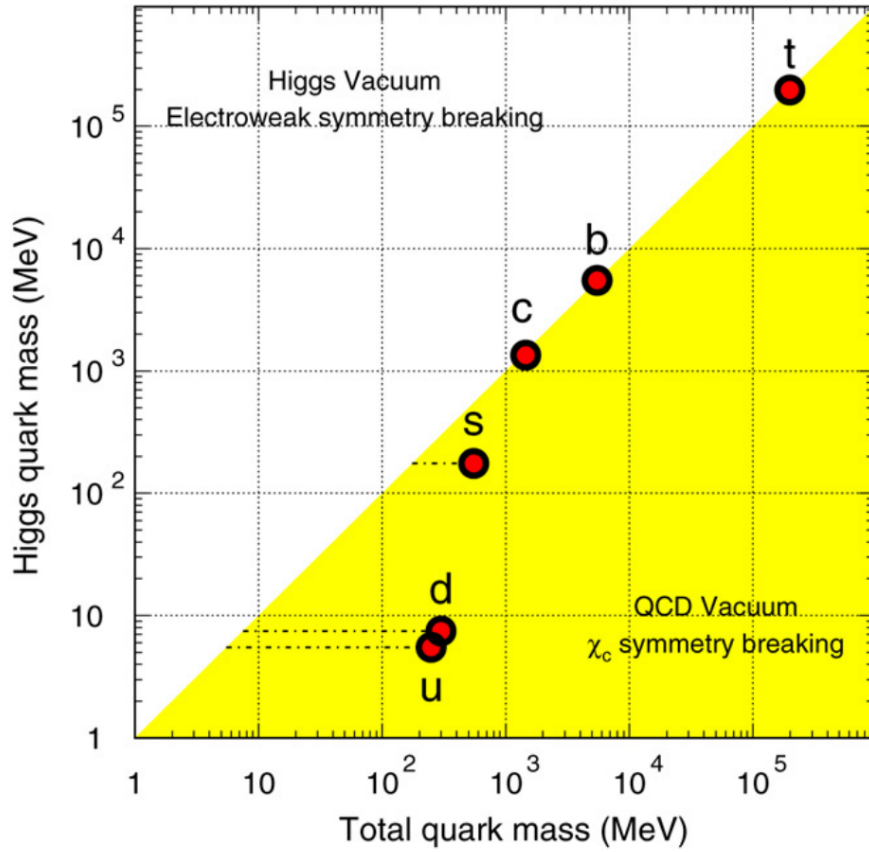


Figure 2.4: Quark masses in the QCD vacuum and the Higgs vacuum. In the case of the chiral symmetry breaking, light quarks generate their mass dominantly through the Yukawa coupling to the QCD vacuum, while the heavy quarks generate their mass by coupling to the Higgs field. Taken from [37].

$1/2m_Q$, which corresponds to $\tau \approx 0.1$ fm/ c for charm quarks and $\tau \approx 0.02$ fm/ c for bottom quarks. These are much smaller values than the time of the QGP duration and therefore the heavy quarks have enough time to interact with the medium.

2.2.3 Jets

In the early stages of heavy-ion collisions, hard (high Q^2) scattering processes produce back-to-back pairs of partons with high transverse momentum p_T . These recoiled partons fragment by radiating gluon brehmsstrahlung into small angles around the original trajectory. These gluons then produce $q\bar{q}$ pairs or radiate another gluon. When the distance between created quarks increases to ~ 1 fm, the energy flux tube between the quarks is so high, that it is sufficient to generate new $q\bar{q}$ pairs which then combine together with the rest of free quarks into color charge neutral mesons and baryons. This process results in creation of a collimated cluster of hadrons traveling in the direction of the original parton and reflecting the physical properties of the original parton (four-momentum, spin).

Due to the fact that jets originate in hard processes (with α_s being small), perturbation theory is applicable for calculation of their cross section. The pQCD calculations describe measurements of jet production in elementary collisions (p+p, e+e) with high accuracy [38].

Jets are produced in early stage of the collision, allowing them to interact with the surrounding medium. A parton (and its brehmsstrahlung gluons) traversing through the hot, dense, strongly interacting quark gluon plasma will undergo multiple collisions with the surrounding color charged quarks and gluons and will lose a portion of its energy during each collision. This would result in softening and broadening of the final jet. Suppression of high momentum jets in heavy-ion collisions (with respect to the elementary p+p collisions) was therefore suggested as one of the possible indications of the presence of the quark gluon plasma [39].

We will discuss formation, evolution and reconstruction of jets more thoroughly in the Chapter 3.

Chapter 3

Jets

We saw in the Chapter 1 that the color charged objects - quarks and gluons, even though considered as elementary particles, cannot be observed individually due to the property of color confinement. A high energy nucleon-nucleon collisions can result in high momentum transfers q between colliding partons (i.e. both the real and virtual quarks and gluons forming the original nucleon). Such scattered partons will have a high transverse momentum and high virtuality $\sim Q$ (where Q is the energy scale of the process). They will reduce their virtuality by emitting gluons into small angles and producing quark - anti-quark pairs. After reaching the value of $Q \approx 1$ GeV the cascade stops and all free quarks form colorless hadrons. Retaining the total momentum of the initial hadron, the whole cascade moves as a narrow spray of baryons and mesons until eventually reaching the detector and being measured. The final spray of particles is called a *jet*. To be more specific, one can distinguish jet at the detector level, particle level or at the parton level. The theory of QCD can calculate in the perturbative regime the initial hard scattering cross section and parton splitting. Therefore it deals with the jet at the parton level. On the other hand the experimental physicists measure jets at the detector level. The particle level and its connection to both the parton and detector level remains a domain of Monte-Carlo simulations.

3.1 Jet Evolution

Jet evolution can be divided into several logical steps, corresponding to the different jet levels mentioned in the introduction of this chapter. This also simplifies the calculation of the inclusive jet cross section since the QCD factorization theorem [40] states that this cross section can be calculated (as will be shown latter in Eq. 3.16) as a convolution of 3 independent functions:

- parton distribution function
- hard scattering cross section
- fragmentation function

Each of these functions relates to a different stage of the evolution of the jet and will be discussed in a more detail on the following lines.

3.1.1 Initial Conditions

Colliding nucleons can be seen as composite objects consisting of 3 real quarks and a large number of virtual quarks and gluons. Each of these objects - partons - carries a part of the nucleon's momentum. Probability of finding a parton a within a nucleon A with fraction of total momentum $x_a = p_a/p_A$ is given by a parton distribution function (PDF) $f_{a/A}(x_a, Q^2)$. The shape of this probability distribution is obtained from deep inelastic scattering (DIS) experiments where a lepton is collided with a nucleon. Such measurements were extensively carried out for example at the HERA facility [41]. Fig. 3.1 shows the combined results of two HERA's experiments - ZEUS and H1.

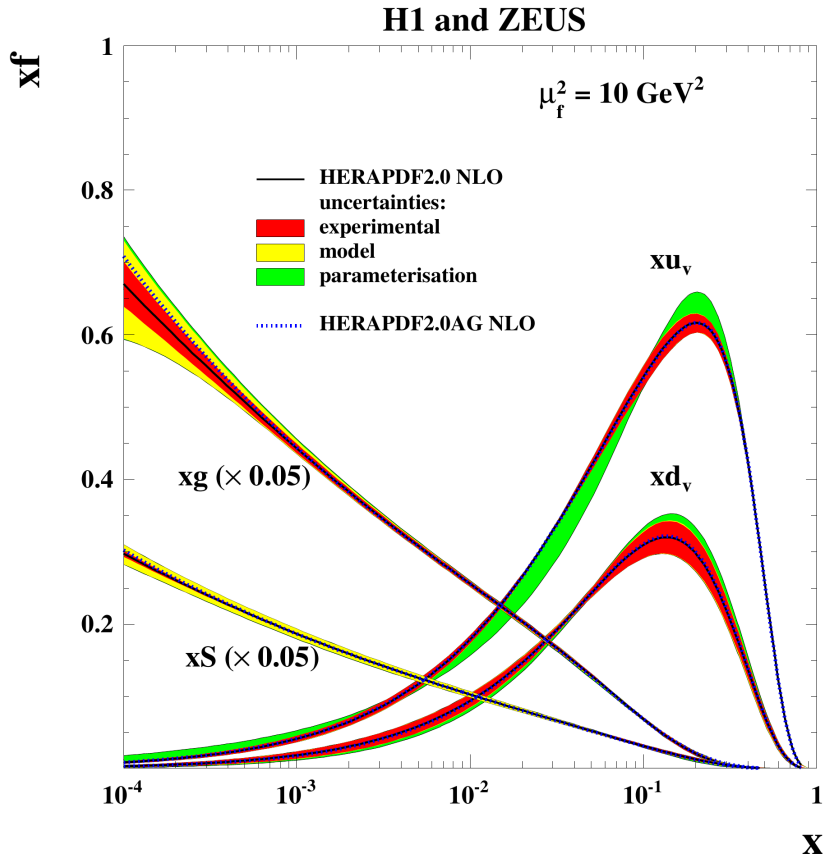


Figure 3.1: The parton distribution functions xu_v , xd_v , $xS = 2x(\bar{U} + \bar{D})$ and xg combined from the ZEUS and H1 experiments calculated at $\mu_F^2 = 10 \text{ GeV}^2$. The gluon and sea distributions are scaled down by a factor of 20. Figure taken from [42].

Since the probability of radiating a gluon by a quark or of gluon creating a quark -

anti-quark pair strongly depends on transferred momentum, the PDFs are functions of Q^2 . They are often evaluated at the energy scale $Q^2 = \mu_F^2$, where μ_F is so called factorization scale - energy scale below which the pQCD is no more applicable. Above this value the dependence on Q^2 is calculable within the framework of pQCD, using the DGLAP evolution equation [43, 44, 45]

$$Q^2 \frac{\partial f_a(x, Q^2)}{\partial Q^2} = \sum_b \int_x^1 \frac{dz}{z} \frac{\alpha_s}{2\pi} P_{ab}(z) f_b\left(\frac{x}{z}, Q^2\right), \quad (3.1)$$

where $P_{ab}(z)$ is a splitting function - the probability of parton b splitting into parton a with a momentum fraction z of the initial parton b . By combining measurements from several experiments and by calculating the PDFs at different values of Q^2 whole sets of PDFs are obtained. These sets can be then used e.g. by MC generators. Interpolation between discrete values of PDFs is provided via the LHAPDF library which contains a large number of different PDF sets [46].

3.1.2 Hard Scattering

By hard scattering one means a parton scattering with high transferred momentum. Therefore such a process is easily calculable in pQCD. The cross section of such process can be calculated as

$$\frac{d\hat{\sigma}}{dt} \Big|_{a+b \rightarrow c+d} = \frac{1}{16\pi\hat{s}^2} |\mathcal{M}|^2, \quad (3.2)$$

where all the variables are in the center of mass (CMS) frame, thus denoted with a “hat”, t and s are Mandelstam variables [48], \mathcal{M} is the scattering amplitude of the specific process. At RHIC energies the most dominant interactions are qg and qq as can be seen on Fig. 3.2.

3.1.3 Fragmentation and Hadronization

The scattered parton is accelerated during time period of the order of $1/E \ll 1$ fm and radiates gluon bremsstrahlung. The gluons are preferably radiated into small angles (Θ) following the relation [49]

$$\frac{dN}{d\Theta^2} \sim \frac{1}{\Theta^2}. \quad (3.3)$$

The emitted gluons can further split into two gluons or create a $q\bar{q}$ pair. The probabilities of such splittings can be described by the aforementioned splitting functions, encountered in Eq. 3.1. The splitting functions can be calculated in pQCD. In the leading order the functions are flavor independent and have the following dependence on the momentum fraction x [50]

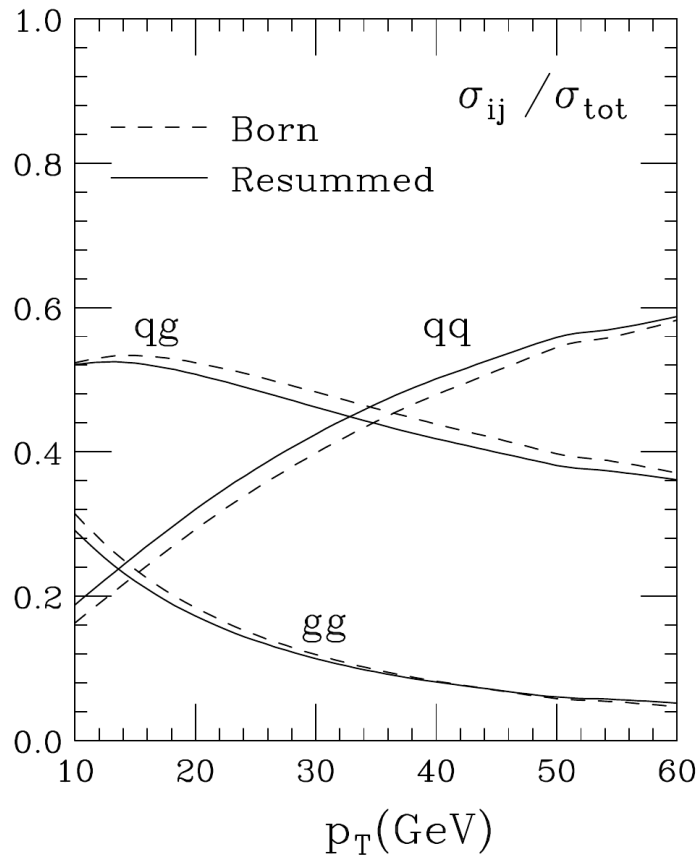


Figure 3.2: Calculation of inclusive jet cross section contributions for different initial parton configurations for p+p collisions at \sqrt{s} 200 GeV. The calculation is done at leading order (dashed) and next to leading logarithm (full). Figure taken from [47].

$$\begin{aligned}
P_{qq}(x) &= P_{\bar{q}\bar{q}}(x) = \frac{4}{3} \left[\frac{1+x^2}{1-x} \right]_+, \\
P_{qG}(x) &= P_{\bar{q}G}(x) = \frac{1}{2} [x^2 + (1-x)^2], \\
P_{Gq}(x) &= P_{G\bar{q}}(x) = \frac{4}{3} \left[\frac{1+(1-x)^2}{x} \right], \\
P_{GG}(x) &= 6 \left\{ \left[\frac{x}{1-x} \right]_+ + \frac{1-x}{x} + x(1-x) + \left(\frac{33-2n_f}{36} - 1 \right) \delta(1-x) \right\},
\end{aligned} \tag{3.4}$$

where n_f is the number of quark flavors and the notation $[F(x)]_+$ defines a distribution such that for any sufficiently regular test function $f(x)$ it holds

$$\int_0^1 dx f(x) [F(x)]_+ = \int_0^1 dx (f(x) - f(1)) F(x). \tag{3.5}$$

Additional relations come from the momentum conservation law. A quark splits into a quark and a gluon with momentum fractions x and $(1-x)$, therefore $P_{qq}(x) = P_{Gq}(1-x)$, similarly gluon splits into two gluons or quark - anti-quark pair, hence $P_{qG}(x) = P_{qG}(1-x)$ and $P_{GG}(x) = P_{GG}(1-x)$. The splitting functions have a pole in $x \rightarrow 0$ or $x \rightarrow 1$, therefore the parton dominantly transfers almost all or almost none of its momentum and two new partons continue parallel in the direction of the original parton.

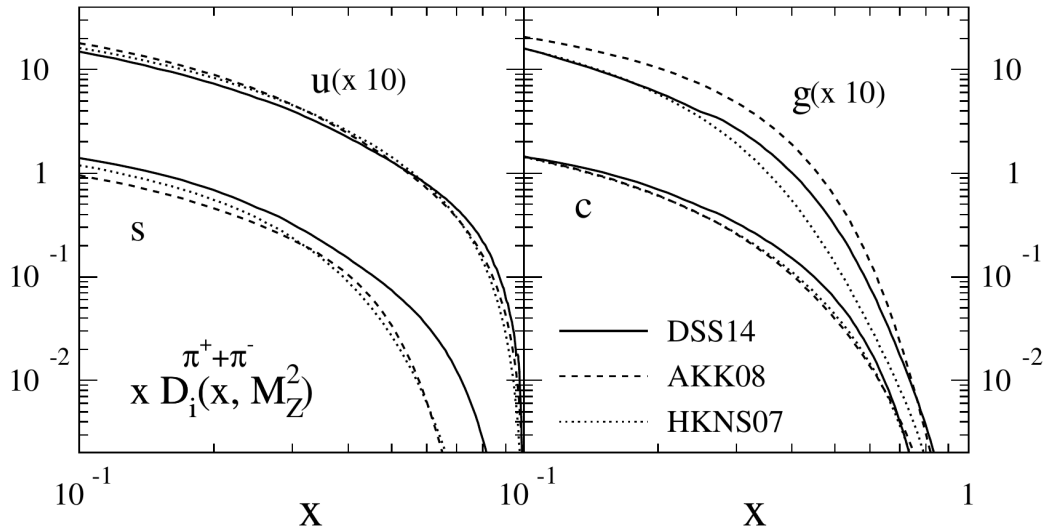


Figure 3.3: The NLO parton fragmentation functions of gluon, u , s and c quark evaluated at $Q^2 = M_Z^2$ GeV². Figure taken from [51].

The second mechanism of production of quarks and anti-quarks is triggered when the distance between scattered quarks becomes sufficiently large (~ 1 fm). Then the quark-

quark potential (Eq. 1.9) becomes so high that the energy density between the quarks is sufficient to create a new $q\bar{q}$ pair.

With further evolution of the cascade the distance between partons rises and the momentum transfers drop to values of the order of Λ_{QCD} and the partons hadronize into observable particles. Unfortunately non-perturbative effects cannot be neglected at such a low energy scale and the pQCD calculations break down. The theoretical description of the hadronization process is therefore treated only via theoretical models. The Monte Carlo simulators usually treat the parton splitting and hadronization together as a single process.

For the final state it is useful to introduce an analogue of the initial state parton distribution functions, parton fragmentation function (FF) $D_i^h(x, Q^2)$ as a probability that a parton i fragments into a hadron h with the momentum fraction x . In case of light quarks and gluons the functions are usually parametrized at some initial energy scale μ_0^2 as [51]

$$D_i^h(x, \mu_0^2) = Nx^\alpha(1-x)^\beta(1+\gamma(1-x)^\delta). \quad (3.6)$$

The normalization constant N and parameters $\alpha, \beta, \gamma, \delta$ depend on the energy scale and also on the type of the hadron and parton. Their values are obtained from global fits to the data from e^+e^- , $e + \text{hadron}$ and $\text{hadron} + \text{hadron}$ collisions. Values of $D_i^h(x, Q^2)$ at different energy scales Q^2 can be obtained from the evolution equation

$$\frac{\partial}{\partial \ln Q^2} D_i^h(x, Q^2) = \sum_j \int_x^1 \frac{dz}{z} P_{ji}(z, \alpha_s(Q^2)) D_j^h\left(\frac{x}{z}, Q^2\right). \quad (3.7)$$

Recent measurements of the parton fragmentation functions are shown on Fig. 3.3. When comparing the gluon and u quark FF, it can be seen that hadrons coming from a u quark will generally have a higher momentum and will be less abundant than those in the case of a gluon.

3.2 Jets in Heavy Ion Collisions

As already mentioned, jets are a promising probe of the QCD medium created in heavy ion collisions, for several reasons. The hard scattering occurs on a time scale much smaller than is the duration of the deconfined phase, hence the initial jet production is not affected by the final state effects of the medium. This also implies that the hard scattered parton (i.e. parton level jet) has enough time to interact with the surrounding medium. Effects as medium induced gluon radiation are expected to appear and to alter the parton momentum (and overall jet fragmentation) significantly. Due to a high virtuality of the scattered partons the jet production cross section is calculable perturbatively in the p+p collisions. This cross section can be then scaled to the A+A (nucleus - nucleus) collisions, assuming the initial state effects are known and under control.

3.2.1 Cold Nuclear Matter and nPDF

The initial state effects are explored by measurements in asymmetric collision systems such as p+A or d+A where the energy density is insufficient to produce the hot QGP medium and only a cold nuclear (confined) medium is present. Historically the first observation of the cold nuclear matter (CNM) effect was the measurement of an excess of high p_T hadrons in p+Be, p+Ti, and p+W collisions with respect to the p+p collisions at Fermilab [52], later referred to as the *Cronin effect*. Additional CNM effects are *shadowing* and *anti-shadowing*. In a nucleus the low- x partons (i. e. partons with low momentum fraction) are more likely to interact with partons from the neighboring nucleons and eventually recombine, forming a higher- x parton. As a result, there is a deficit of low- x partons (shadowing) and an excess of high- x partons (anti-shadowing) in the nucleus [53]. Actually there are even more CNM effects and not all of them are theoretically explained. However they can be taken into account by modifying the parton distribution function for nuclei. Such modified PDFs are called *nuclear parton distribution functions* (nPDF) and are obtained from experimental data.

3.2.2 Hot Nuclear Matter

Since the agreement of the pQCD calculations with the measured cross sections in p+p collisions is remarkable (see e.g. results in Section 3.4.1), any difference between the scaled cross section for A+A collisions and the measured value has to come from the final state effects of the hot medium¹.

In order to quantify the size of the effects caused by the medium one defines nuclear modification factor R_{AA} . It quantifies the change of spectra due to the hot nuclear effects by comparing A+A jet yield (or cross section) with appropriately scaled p+p yield (cross section). It is defined as

$$R_{AA} = \frac{\frac{d^2 N_{AA}}{N_{events} dp_{T,jet} d\eta}}{\langle N_{bin} \rangle \cdot \frac{d^2 N_{pp}}{N_{events} dp_{T,jet} d\eta}} \quad (3.8)$$

or equivalently for the cross section

$$R_{AA} = \frac{\frac{d^2 \sigma_{AA}}{dp_{T,jet} d\eta}}{\langle N_{bin} \rangle \cdot \frac{d^2 \sigma_{pp}}{dp_{T,jet} d\eta}}, \quad (3.9)$$

or for the combination of the yield and the cross section

$$R_{AA} = \frac{\frac{1}{N_{events}} \cdot \frac{d^2 N_{AA}}{dp_{T,jet} d\eta}}{T_{AA} \cdot \frac{d^2 \sigma_{pp}}{dp_{T,jet} d\eta}}, \quad (3.10)$$

¹More precisely it has to come from the final state effects of both the hot (deconfined) and cold (confined) medium.

where $\langle N_{bin} \rangle$ is the mean number of binary collisions in the A+A collisions determined from the Glauber Monte Carlo model [54, 55]. The nuclear overlap function T_{AA} is defined as the mean number of binary collisions divided by the p+p inelastic cross-section:

$$T_{AA} = \frac{\langle N_{bin} \rangle}{\sigma_{pp}^{inelastic}}. \quad (3.11)$$

3.2.3 Jet Quenching

Partons traversing through the QGP can suffer many elastic scatterings with quarks and gluons of the plasma and as a result lose their energy. This collisional energy loss mechanism was first suggested by Bjorken [39] and its size was estimated to be $dE/dx \sim \alpha_s^2 \sqrt{\epsilon}$. Here ϵ is the energy density of the QGP. For a reasonable value of the QGP temperature $T = 250$ MeV the collisional energy loss for a light quark propagating in a hot medium amounts to 0.2 - 0.3 GeV/fm [56].

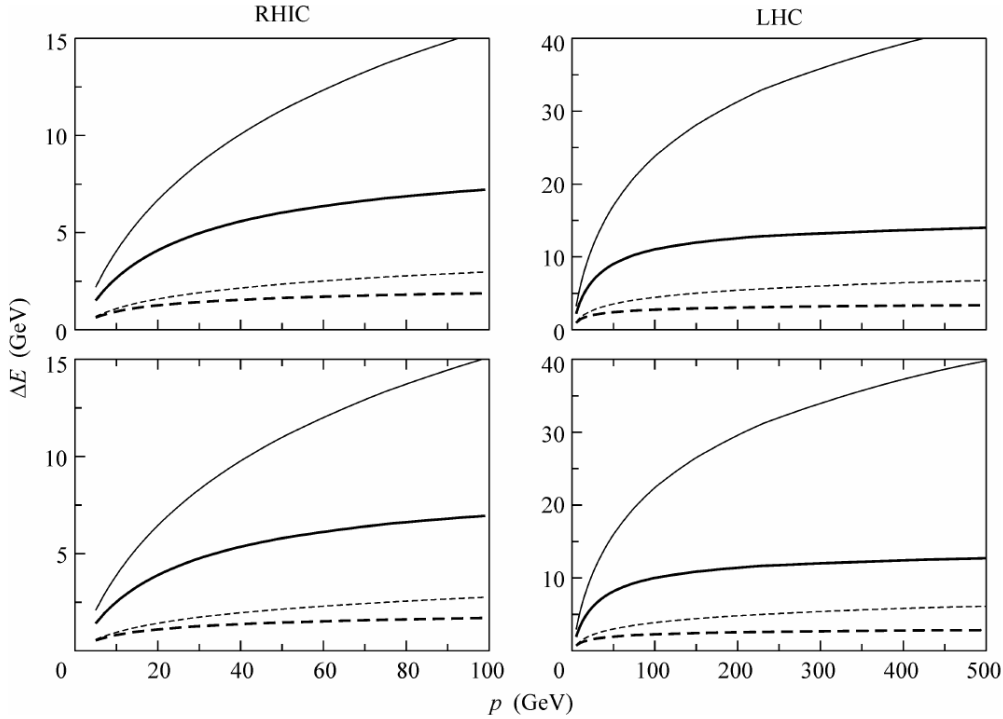


Figure 3.4: Light quark radiative (solid line) and collisional (dashed line) energy loss for RHIC (left) at $\sqrt{s_{NN}} = 200$ GeV and LHC (right) at $\sqrt{s_{NN}} = 5.5$ TeV conditions for $L = 5$ fm. The thick curves correspond to the running α_s and thin curves to $\alpha_s = 0.5$. The upper panels show the results for the T-independent Debye mass $\mu_D \approx 0.57$ GeV, and the lower panels for the T-dependent Debye mass from the lattice calculations. Figure adopted from [57].

The second source of the parton energy loss in dense matter is the gluon bremsstrahlung, an effect analogical to the QED bremsstrahlung. The radiated gluons can also suffer multiple scatterings due to the interactions with the medium, traversing a mean free path λ until they eventually decohere.

Calculations show that the radiative energy loss dominates over the collisional energy loss significantly [57]. Fig. 3.4 shows size of the collisional and radiation energy loss at both RHIC and LHC energies. In both cases, the radiative energy loss dominates.

In the limit of high initial parton energy the average radiative energy loss $\langle \Delta E \rangle$ depends on the medium size L and the transport coefficient \hat{q} as [58, 59, 60, 61]

$$\langle \Delta E \rangle \propto \alpha_s L^2 \hat{q}. \quad (3.12)$$

The quadratic dependence on L^2 marks a difference between the QCD and QED bremsstrahlung (QED radiative energy loss being only $\propto L$). The transport coefficient \hat{q} encodes both the thermodynamical (temperature, energy density, ...) and transport (viscosity, conductivity,...) properties of the medium and is defined as the average medium-induced transverse momentum squared $\langle q_T^2 \rangle$ transferred to the projectile per mean free path λ ,

$$\hat{q} \equiv \frac{\langle q_T^2 \rangle}{\lambda}. \quad (3.13)$$

By comparing the transport coefficients of the cold and hot nuclear matter [59, 62]

$$\frac{\hat{q}_{hot}}{\hat{q}_{cold}} \simeq 20 \quad (3.14)$$

and taking into account the relation in Eq. 3.12, it is apparent that the partons will lose their energy in the hot medium much more significantly.

Jet fragmentation function is therefore strongly modified in the presence of the QGP and consequently a modified jet is produced. This is a phenomenon known as *jet quenching*. The jet quenching manifests itself in several observable effects:

- suppression of high- p_T particle and jet yields [39, 63],
- di-jet transverse momentum imbalance [64, 65],
- modified internal structure of the final jets (softer hadron spectra, larger multiplicity, increased angular broadening, ...) [66, 67, 68].

Suppression of high- p_T particle and jet yields with respect to the yield in p+p collisions scaled by the average number of binary collisions would result in R_{AA} values smaller than one. However two different processes can lead to values of $R_{AA} < 1$.

First, complete jet absorption with a given probability $P_{abs}(p_T) > 0$ would result in $R_{AA} < 1$ (this corresponds to the case when the A+A spectrum on Fig. 3.5 moves down).

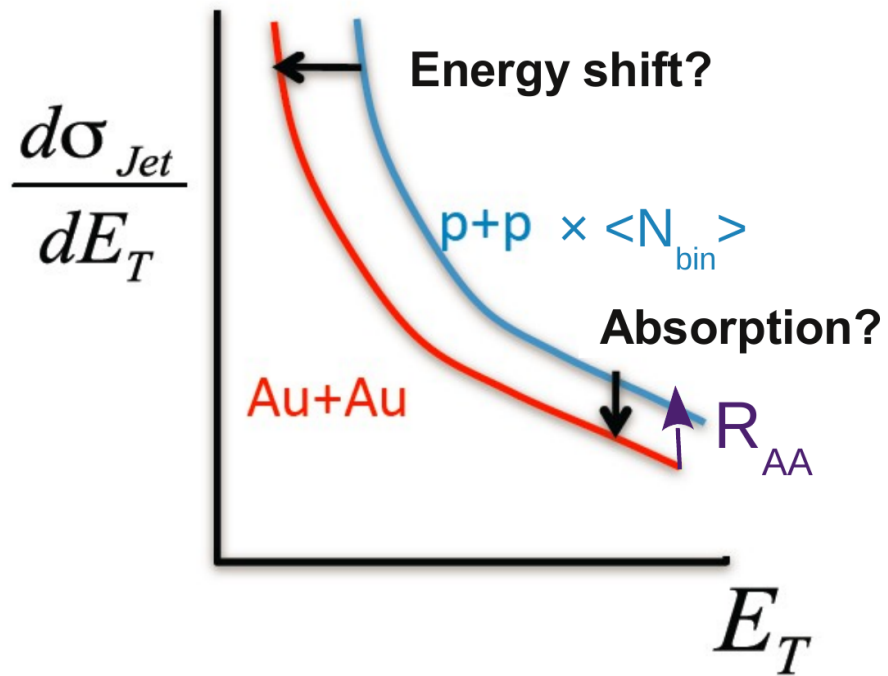


Figure 3.5: A schematic plot of a hypothetical jet cross section in p+p and A+A collisions and possible sources of the spectrum modification.

Second, if most of the jets lose part of their momentum the whole A+A spectrum on Fig. 3.5 would move to the left. Due to the shape of the spectrum, this would also result in $R_{AA} < 1$.

Although the way how the R_{AA} is calculated infers the first explanation, the second one is equally valid and any R_{AA} results should be interpreted in this way. From the theoretical point of view, the difference is in the amount of the average energy loss in the medium. For sufficiently high values the jet can be completely absorbed, for smaller values it will only lose a part of its energy. In order to determine which of these mechanisms is more relevant one has to look at more differential quantities than R_{AA} alone.

Di-jet transverse momentum imbalance - If there is no gluon radiation, two back-to-back jets are formed as a result of the hard scattering. Due to an initial nonzero transverse momentum distribution k_T of quarks inside the colliding hadrons, the resulting jets are not perfectly back-to-back, but form an angle slightly varying from π [69]. When fragmenting in vacuum, the transverse momentum of both jets should be equal (modulo the k_T smearing). The situation changes in the presence of the QGP. If the hard scattering does not happen exactly in the center of the QGP fireball, but further away from the center or even at the edge of the region where the QGP is formed, then each of these two jets travels (at parton level) a different distance in the medium.

In the most extreme case the first jet escapes the medium immediately and the second one travels through the whole volume of the QGP fireball. In such cases the more affected jet could become significantly softer (and broader) than its unmodified counterpart. This is the motivation to measure the quantity A_J , di-jet asymmetry defined as

$$A_J = \frac{p_{T,1} - p_{T,2}}{p_{T,1} + p_{T,2}}, \quad (3.15)$$

where $p_{T,1}$ and $p_{T,2}$ are transverse momenta of the first (trigger) and second (away-side) jet. In case of no modification the di-jet asymmetry would be close to zero. The second extreme - a value of $A_J \simeq 1$ - would indicate a complete absorption of the away side jet.

Modified internal structure of the jets - A parton moving through the color charged medium would radiate bremsstrahlung gluons, which will later hadronize, producing a large number of softer hadrons. Also the jet fragments can undergo multiple elastic collisions with the quarks and gluons of the QGP medium. Therefore the final jet products can be radiated into larger angles than in the case of the vacuum fragmentation.

Jet quenching and the QCD critical point

Fig. 3.6 shows the calculated dependence of the transport coefficient on the energy density for different systems. Apparently the jet quenching can be used to distinguish between cold matter and hot QGP medium, since $\hat{q}_{hot} \gg \hat{q}_{cold}$, in agreement with Eq. 3.14. On the other hand, Fig. 3.6 gives no support for conclusion that the phase transition in the

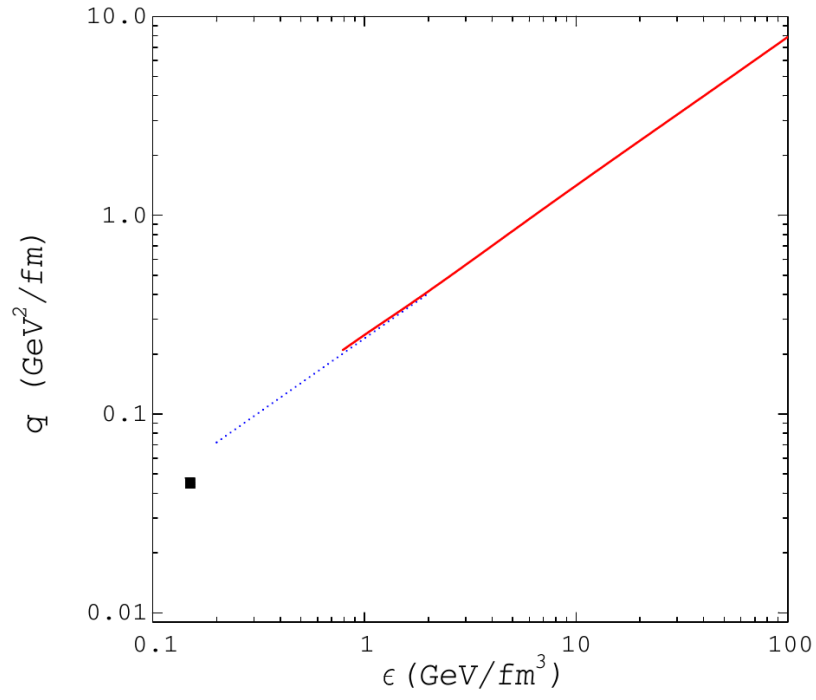


Figure 3.6: Transport coefficient \hat{q} as a function of energy density for different media: cold matter (black point), massless hot pion gas (dotted line) and (ideal) QGP (solid curve). Figure adopted from Ref. [70].

region with the energy density $\epsilon \approx 1 \text{ GeV}/\text{fm}^3$ can be easily detected by measuring the jet quenching [70].

3.2.4 Inclusive Jet Cross Section

By connecting the steps outlined in Sec. 3.1 the QCD factorization theorem [40] enables us to calculate the inclusive cross section for the production of a high- p_T hadron in the nuclear reaction of $A+B \rightarrow h+X$ as a convolution of the parton distribution functions $f_{a/A}$ with the parton-parton differential cross section $\frac{d\hat{\sigma}_{ab \rightarrow cd}}{d\hat{t}}$ and with the parton fragmentation functions $D_{h/c}$. In the leading order of the pQCD the calculation gives [71]

$$\begin{aligned}
E_h \frac{d^3\sigma_{AB \rightarrow hX}}{d^3p} &= K_{\text{NLO}} \sum_{abcd} \int_0^1 dz_c \int_{x_a \text{ min}}^1 \int_{x_b \text{ min}}^1 dx_a dx_b \\
&\times f_{a/A}(x_a, Q_a^2) f_{b/B}(x_b, Q_b^2) \\
&\times \frac{\hat{s}}{\pi z_c^2} \frac{d\hat{\sigma}_{ab \rightarrow cd}}{d\hat{t}} \delta(\hat{s} + \hat{u} + \hat{t}) D_{h/c}(z_c, Q_c^2) .
\end{aligned} \tag{3.16}$$

Here K_{NLO} is a phenomenological factor accounting for NLO corrections, x_a, x_b are the momentum fractions of the interacting partons, $z_c = p_h/p_c$ is the momentum fraction of the measured hadron h . This equation however over-predicts hadron production at p_T below $4 \text{ GeV}/c$. This can be partly corrected by introducing generalized parton distribution functions

$$\tilde{f}_a(x, k_T, Q^2) \approx f_a(x, Q^2) g(k_T), \quad g(k_T) = \frac{e^{-k_T^2/\langle k_T^2 \rangle}}{\pi \langle k_T^2 \rangle}, \tag{3.17}$$

reflecting a small intrinsic k_T -smearing of the scattered partons due to the initial state soft radiation. The mean value $\langle k_T^2 \rangle$ needs to be determined from data.

3.2.5 Leading Hadron Bias

As discussed in Section 3.2.3, the scattered parton propagating through the nucleus can suffer additional scatterings which result in gluon bremsstrahlung and energy loss of the leading parton. This effect can be taken into account by using modified parton fragmentation function $\tilde{D}_{h/c}(z, Q^2)$ [72]

$$\tilde{D}_{h/c}(z, Q^2) \equiv D_{h/c}(z, Q^2) + \Delta D_{h/c}(z, Q^2) . \tag{3.18}$$

By comparing modified and unmodified parton FFs, as on Fig. 3.7, it can be seen that in the case of heavy nuclei the fragmentation function shifts from high momentum fractions to lower ones. Jets modified by the QCD medium will thus contain more and softer components and this modification affects the leading hadron of the jet as well.

Effect of a bias imposed on a jet population e.g. by requiring a minimal value of the momentum of the leading hadron can therefore be significantly different in p+p collisions with respect to A+A collisions.

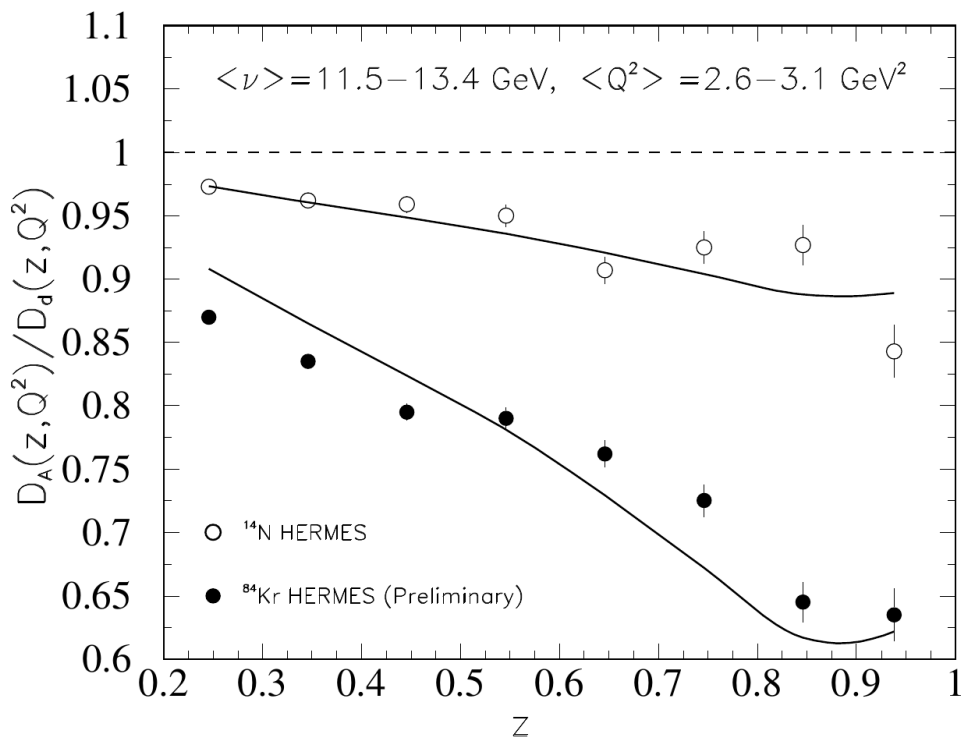


Figure 3.7: Measured and predicted values of the ratio of medium-modified parton fragmentation function over unmodified function. Measurements done by the HERMES Collaboration. Figure taken from [72].

3.3 Jet Reconstruction Algorithms

From the experimental point of view, jets are simply defined as the output of the jet reconstruction algorithm. A good algorithm should fulfill the following conditions:

- Order independence
- Infrared and collinear safety
- Easy usage
- Detector independence
- Highly efficiency combined with short computing time

Order independence - the algorithm should produce the same results at the parton level (when applied on theoretical calculations), hadron level (when applied on MC simulations) and at the detector level (when applied on experimental data).

Infrared safety - the algorithm should be insensitive to any soft radiation in the event. This means that any radiated soft gluons (and products of their hadronization) will not affect the shape or even the number of reconstructed jets.

Collinear safety - the algorithm should be insensitive to any collinear radiation in the event as well as to any splitting of particles caused by the detectors. Let us assume we have a particle which deposits its energy in two neighboring calorimetric towers. Such a particle could be reconstructed as two collinear particles. If the algorithm fails in this case to generate the same jets as it would generate in the case of properly reconstructed particle, it is collinear unsafe.

Easy usage - one has to be able to use the algorithm on experimental data.

Detector independence - the algorithm should be independent on the detector properties as much as possible.

High efficiency and short computing time - no significant jet should be missed and left unreconstructed while demands on the computer resources should be minimized. Computing time which evolves like $\mathcal{O}(N^x)$ with $x \leq 3$ is probably the upper boundary for any practical use.

Nowadays, there are two basic classes of the jet reconstruction algorithms which (at least partially) fulfill the requirements - cone algorithms and clustering algorithms.

3.3.1 Cone Algorithms

As the name suggests, cone algorithms make a virtual cone around the highest- p_T particles²⁾ (these starting particles are called **seeds**) and all particles inside the cone are proclaimed as the jet particles. A simple cone algorithm can look as follows:

- 1) Find all particles with energy above a user-specified threshold and make around them a circle of (user-specified) radius $R = \sqrt{(\Delta\phi)^2 + (\Delta\eta)^2}$ in the $\eta - \phi$ space, where η is the pseudorapidity and ϕ is the azimuthal angle.
- 2) Calculate total energy and total momentum as the sum of energy and momenta of all the particles inside the circles.
- 3) Particles within the circles now form a proto-jet. Declare the non-intersecting proto-jets as final jets. If some jets do intersect, declare only the most energetic one as the final jet.

The above mentioned algorithm is very simple and fast (like $\mathcal{O}(N)$, where N is the number of particles), unfortunately it is not collinear safe³⁾. For a practical use, additional improvements are therefore needed.

Also it is important that the center of the cone is aligned with the jet's momentum vector. If it is not the case, we have to set the center of the cone to the position of the momentum vector. Then we recalculate the momentum and see if it is now aligned with the center of the cone. If not, we have to repeat this step until they are aligned. This iteration process is called "stabilization".

Among the cone algorithms there is only one which is both infrared and collinear safe, the SIScone algorithm [73].

SIScone algorithm

A Seedless Infrared-Safe Cone algorithm or just "SIScone" algorithm represents a state of the art cone algorithm that is not only IR-safe but also collinear-safe. The basic steps of the jet reconstruction are:

- 1) Put the set of current particles equal to the set of all particles in the event.
- 2) Find all stable cones of a radius R for the current set of particles.
- 3) For each stable cone, create a proto-jet from the current particles contained in the cone, and add it to the list of proto-jets.
- 4) Remove all particles that are in stable cones from the list of current particles.

²⁾Depending on the level at which we are using the algorithm, as the "particles" one treats partons (parton level), hadrons (hadron level), tracks or calorimetric towers or both (detector level), depending on the particular experiment.

³⁾It is the p_T threshold for seeds what affects the collinear safeness.

- 5) Repeat steps (2) - (4) until no new stable cones are found.
- 6) Run a split–merge procedure on the full list of proto-jets.

The key step in avoiding the IR and collinear instability is the second one. As mentioned earlier, seeds are the source of the collinear instability. A seedless approach is therefore needed. The SIScone algorithm solves this by trying to identify all distinct cones (cones having a different particle content), and testing the stability of each one. For each and every enclosure, one can always move the corresponding cone without changing its contents into a position where two particles (points) lie on its boundary. If one considers each circle whose boundary is defined by a pair of points in the set, and considers all permutations of the edge points being contained or not in the enclosure, then one will have identified all distinct circular enclosures.

Speed of the SIScone algorithm is $\mathcal{O}(Nn \ln n)$, where N is the number of particles and n is the typical number of particles in a circle of radius R .

3.3.2 Clustering Algorithms

Clustering algorithms start by selecting a starting particle and then sequentially add other particles that are close enough (e.g. close in the $\eta - \phi$ space) to the arising jet. Contrary to the cone algorithms, the formed jets have no fixed shape. This method better reflects the way the real jets are formed.

k_T algorithm [74]

- 1) For set of particles with index j , transverse momentum p_{Tj} , position ϕ_j, η_j , calculate “beam distance” $d_j = p_{Tj}^2$.
- 2) For each pair of particles i and j calculate “distance” $d_{ij} = \min(p_{Ti}^2, p_{Tj}^2) \frac{(\Delta\phi)^2 + (\Delta\eta)^2}{R^2}$, with a user-defined resolution parameter R .
- 3) Find $d_{min} = \min(d_{ij}, d_j)$.
- 4) If $d_j = d_{min}$ add object j to the list of final jets, else if $d_{ij} = d_{min}$ merge objects j and i together.

Anti- k_T algorithm [75]

The k_T algorithm starts the clustering from the soft particles and is thus sensitive to the presence of a soft background. The anti- k_T algorithm overcomes this inconvenience and starts the clustering from the hard particles. Change is in the steps (1) and (2):

- 1) ...calculate $d_j = p_{Tj}^{-2}$.
- 2) ...calculate $d_{ij} = \min(p_{Ti}^{-2}, p_{Tj}^{-2}) \frac{(\Delta\phi)^2 + (\Delta\eta)^2}{R^2}$

Both algorithms are quite slow, $\mathcal{O}(N^3)$. Since they are collinear and IR safe, high computing demands represent the only disadvantage. However, there is an implementation of these algorithms in the FastJet software [76], which reaches speed of $\mathcal{O}(N \ln N) - \mathcal{O}(N^2)$. One of the latest versions - FastJet 3.4 - is used in this analysis.

k_T vs. anti- k_T

There is a major difference between these two algorithms in the way they respond to a soft background. Suppose we reconstruct jets in a hard event (without background) and denote such a set of jets J_i . Then we add soft background and run those algorithms again. The new set of jets J'_i will be different. Not only the energy of the jets will be higher by the soft energy, but also the shapes of the jets will be changed - content of particles from the hard event will not be the same in the original jets J_i compared to the new jet sets J'_i . This is called “back reaction”. The effect of back reaction is highly suppressed for the anti- k_T in comparison to the k_T algorithm [75]. The background-sensitivity of the k_T algorithm also results in another feature: the shape of the final jets reconstructed by the k_T is more or less irregular, whereas the anti- k_T jets are regular, resembling cone jets.

Because of their properties, in our analysis the anti- k_T algorithm is used for the primary jet reconstruction, whereas the k_T algorithm is used to reconstruct jets which are used to determine background energy density.

Resolution parameter R

Properties of the reconstructed jets depend also on the parameter R for the cone algorithms as well as for the clustering algorithms. Jets with a larger R will recover more energy of the original parton, on the other hand the larger jet is more sensitive to the presence of background. In our analysis values of $R = 0.2, 0.3$ and 0.4 are used.

Recombination scheme

Merging of protojets in step (4) is done via one of the following recombination schemes:

- E scheme - 4-momentum of particles/protojets is summed. Energy value has to be assigned to each track.
- p_T, p_T^2 scheme
- E_T, E_T^2 scheme

The energy scheme is a default choice for most of the algorithms and it is also used in this analysis. For the other schemes the first step is to make the initial momenta massless (rescaling the energy to be equal to the 3-momentum for the p_T and p_T^2 schemes, rescaling to the 3-momentum to be equal to the energy in the E_T and E_T^2 schemes). Then for all 4 schemes the recombination p_r of p_i and p_j is a massless 4-vector satisfying

$$\begin{aligned}
p_{T,r} &= p_{T,i} + p_{T,j} \\
\phi_r &= (w_i \phi_i + w_j \phi_j) / (w_i + w_j) \\
y_r &= (w_i y_i + w_j y_j) / (w_i + w_j),
\end{aligned}
\tag{3.19}$$

where the weight $w_i = p_{T,i}$ for p_T and E_T schemes and $w_i = p_{T,i}^2$ for p_T^2 , E_T^2 schemes.

Jet areas

Jet area can be defined and calculated in various ways, the FastJet framework offers three alternative definitions of the jet area [77]:

- Active area - Many soft “ghost” particles are added to the event and the reconstruction procedure is performed once more. Soft ghosts do not affect the content of original hard particles in reconstructed jets, since the FastJet clustering algorithms are IR safe. The jet area is then proportional to the number of ghosts contained in the jet. Next to the original hard jets there are also many soft, “ghost” jets found.
- Passive area - One soft ghost is added to the event. One looks for a jet which contains the ghost. This is repeated many times and the jet area is proportional to the probability of finding the ghost in the jet.
- Voronoi area - Voronoi diagrams [78] are constructed for the event and the jet area is calculated as the sum of Voronoi areas of jet’s constituent particles.

The passive area method is used in this analysis.

After calculating the jet areas A_j one calculates pedestal energy distribution in the event as median jet p_T divided by corresponding jet area

$$\rho = \text{med}\left(\frac{p_T^j}{A_j}\right)
\tag{3.20}$$

using all jets in the event (by using the median the hard jets are effectively excluded and only the soft jets are used for the noise distribution calculation). As already mentioned, for the purpose of the ρ calculation the k_T jets are used. Jet p_T is then corrected on average for the soft background contamination as:

$$p_T^{corr} = p_T - A\rho.
\tag{3.21}$$

Jet types

If jets are reconstructed only from charged tracks (recorded e.g. with a time projection chamber) it is common to call such objects *charged jets*. On the other hand, if also neutral energy would be included (by utilizing information from a calorimeter), one would be speaking about *full jets*.

3.3.3 Jet Reconstruction in Heavy Ion Collisions

In heavy-ion collision high multiplicity environment, the hard jets are produced together with a large amount of soft particles forming so called underlying event (UE). This large background is strongly fluctuating both jet-by-jet and event-by-event. Distinguishing between the jet particles and background particles is impossible not only technically, but even in principle, due to laws of quantum-mechanics. Therefore any jet properties have to be studied on ensemble-averaged basis.

Until recently, most of the jet analyzes in heavy-ion collisions were restricted only to study of two particle correlations in order to minimize problems with the UE. Analyzes which performed full jet reconstruction used jet population which was highly biased by requirement of sufficiently high p_T of the jet constituents. Unfortunately, neither of these approaches is suitable for jet quenching study. Therefore we seek a method of full jet reconstruction which would be collinear safe, with a low infrared cutoff and unbiased as much as possible towards softly fragmenting jets.

3.4 Recent Jet Measurements at RHIC and the LHC

3.4.1 Jets in p+p Collisions

Both the LHC and RHIC experiments measured inclusive jet cross sections in p+p collisions over their whole kinematic range.

Measurement of the differential inclusive jet cross section in polarized p+p collisions at $\sqrt{s} = 200$ GeV by the STAR Collaboration [79] is shown on Fig. 3.8. Jet reconstruction was performed using a midpoint cone jet reconstruction algorithm with a cone size of $R = 0.4$. Bottom panel shows the comparison of data with an NLO pQCD calculation [80]. The measured cross section agrees with the theory within the systematic uncertainties, which are however large ($\sim 50\%$).

Fig. 3.9 presents both the measured jet cross section in p+p collisions and jet yields in d+Au collisions at $\sqrt{s} = 200$ GeV [81] measured by the PHENIX Collaboration. Jets were reconstructed using the anti- k_T algorithm and $R = 0.3$. The p+p cross section agrees well with the pQCD NLO calculation [82] within the experimental uncertainties.

ALICE measurements of the full jet cross section in p+p collisions at $\sqrt{s} = 2.76$ TeV [83] are plotted on Fig. 3.10. Jets were reconstructed using anti- k_T algorithm with $R = 0.2$ and 0.4 . The measured data were compared to an NLO pQCD calculation [84]. As can be seen on the ratio plots in the bottom panels of the Fig. 3.10 a better agreement between the NLO calculation and the data is achieved when a hadronic correction to the ATLAS data [85] is included. The ALICE Collaboration also conducted a measurement of charged jet cross section at a higher collisional energy of $\sqrt{s} = 7$ TeV [86]. Comparison of data to MC generators presented on Fig. 3.11 shows that some of the tunes of the generators describe the p+p data well while the other tunes can differ more than 100%.

Measurement of the jet cross section in p+p collisions at the collision energy of $\sqrt{s} = 7$ TeV at the LHC was also carried out by the ATLAS Collaboration [87]. Kinematical reach of this measurement is much higher than that of ALICE as can be seen on Fig. 3.12. The data were also compared to the NLO pQCD calculation with nonperturbative corrections [88]. The NLO calculation was performed with three different PDF sets. Ratios of the NLO calculations to data are plotted at the bottom of Fig. 3.12. One can see that within the uncertainties of the measurement, there is a good agreement between the theoretical prediction and the measured data, especially for the MSTW 2008 and NNPDF 2.1 PDF sets.

In summary, all presented results demonstrate a good agreement between the measurements and the theoretical pQCD calculations. From this one can conclude that the jet production in the elementary collisions is well understood within the QCD.

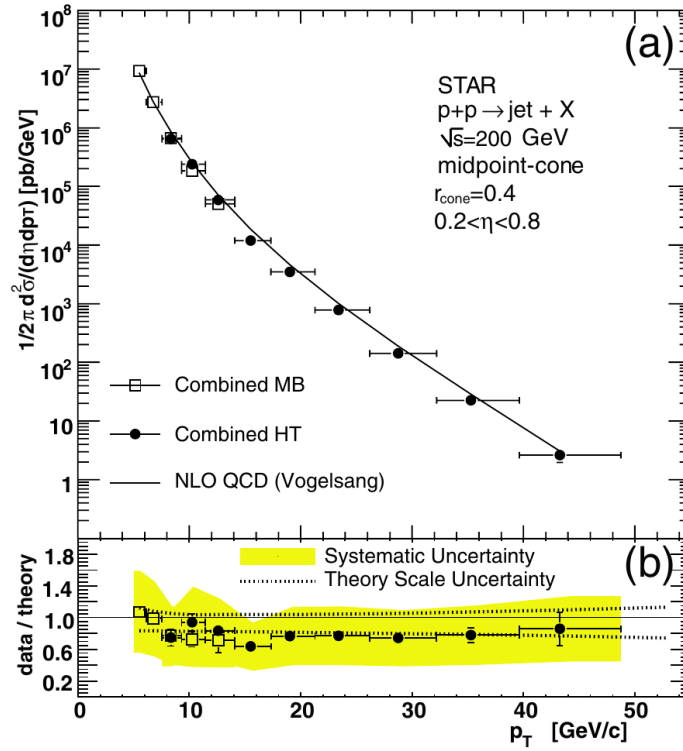


Figure 3.8: Inclusive full jet cross section in p+p collisions at $\sqrt{s} = 200$ GeV measured by STAR (a) and comparison with NLO pQCD calculation (b). Published in Ref. [79].

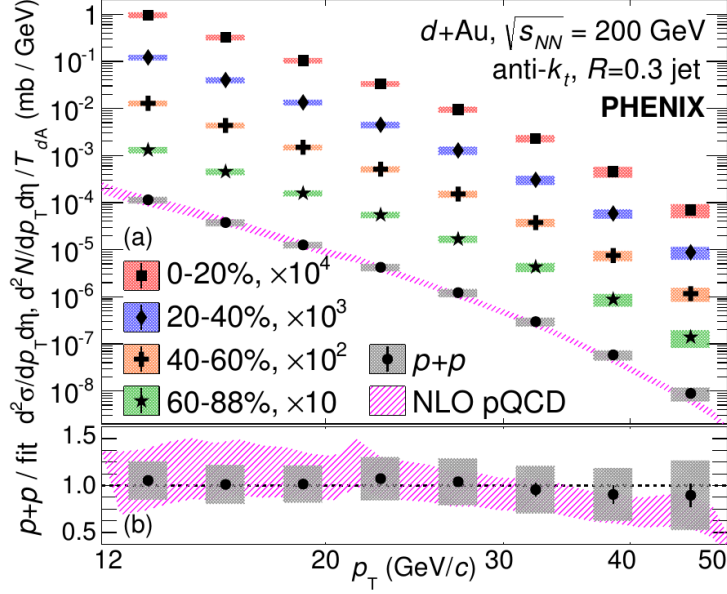


Figure 3.9: Inclusive full jet cross section in p+Au and d+Au collisions at $\sqrt{s} = 200$ GeV measured by the PHENIX Collaboration and comparison of p+p data with NLO pQCD calculation. Published in Ref. [81].

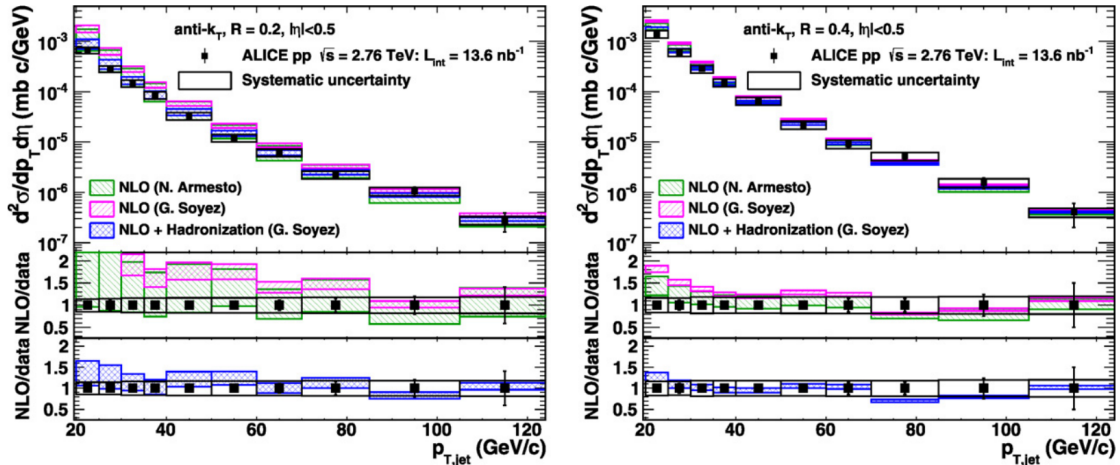


Figure 3.10: Inclusive full jet cross section in p+p collisions at $\sqrt{s} = 2.76$ TeV measured by ALICE compared with NLO pQCD calculations (top). The ratio of NLO pQCD calculations to data (bottom). Published in Ref. [83].

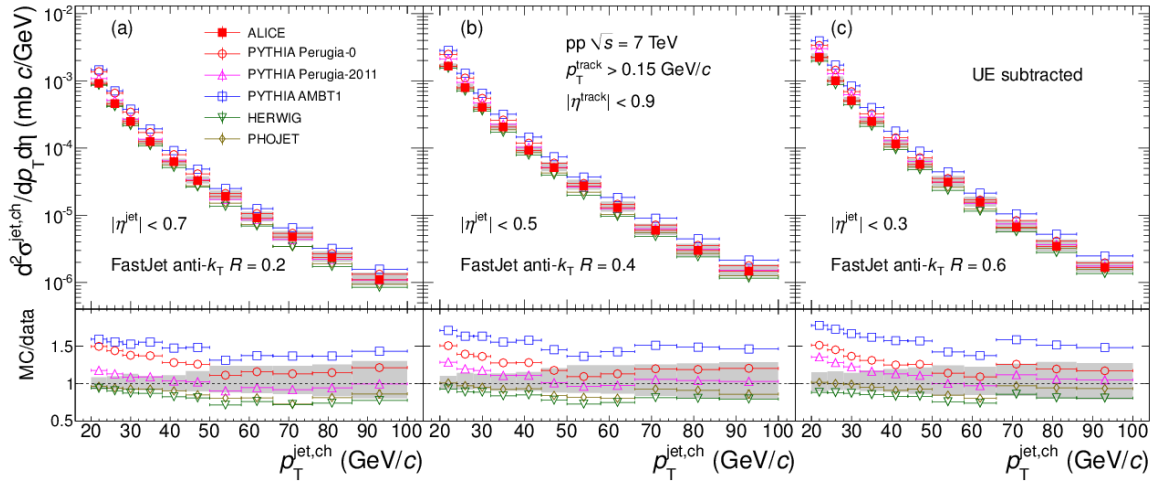


Figure 3.11: Top: Inclusive full jet cross section in p+p collisions at $\sqrt{s} = 7.0$ TeV measured by the ALICE Collaboration compared to several MC generators: PYTHIA tune AMBT1, PYTHIA tune Perugia-0, PYTHIA tune Perugia-2011, HERWIG, and PHOJET. Bottom: Ratio MC/data. The results are shown as a function of R (left to right). Published in Ref. [86].

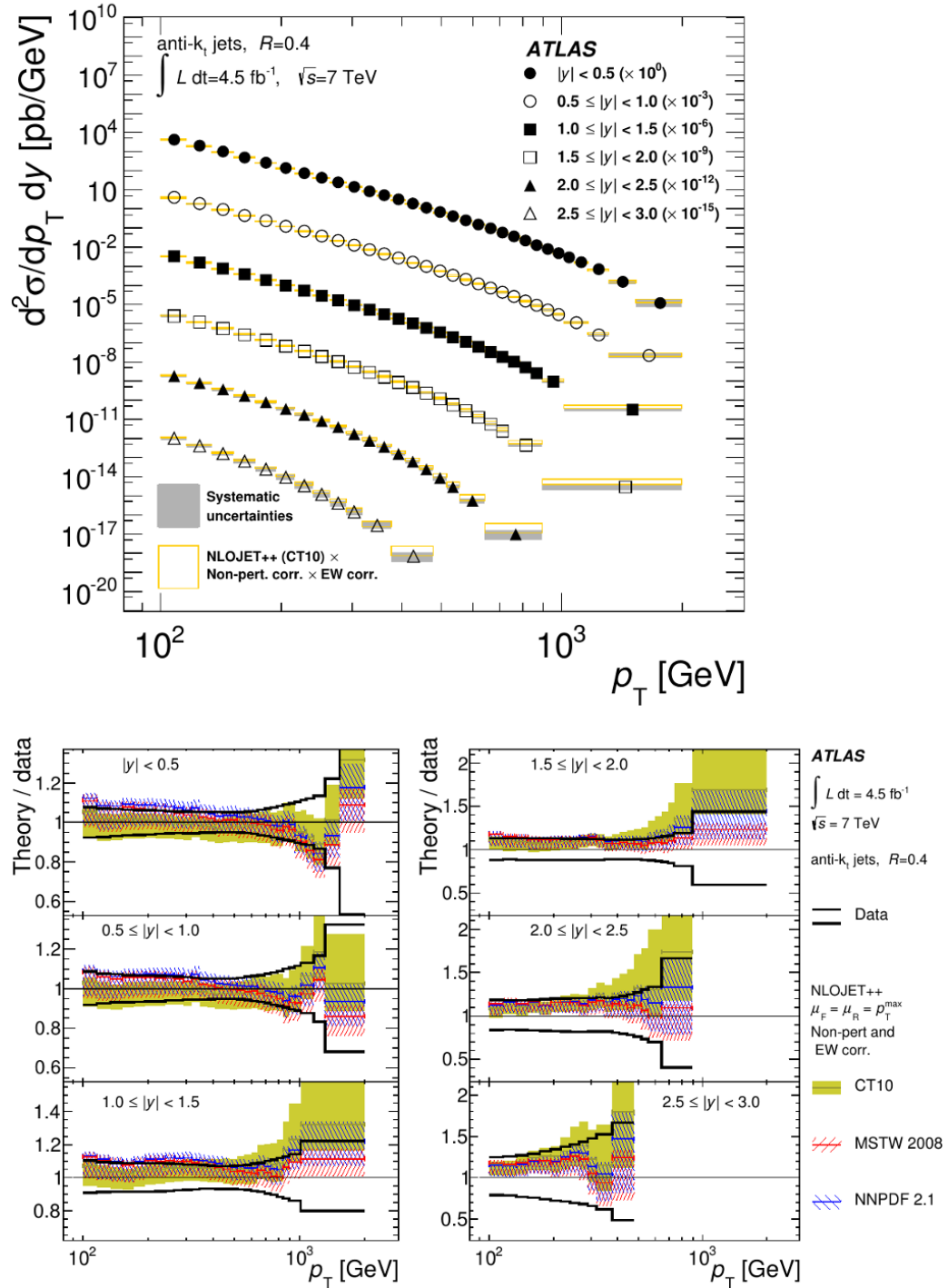


Figure 3.12: Top: Inclusive full jet cross section in p+p collisions at $\sqrt{s} = 2.76$ TeV measured by ATLAS for various rapidity intervals (see legend). The jets were reconstructed for $R = 0.4$. Bottom: Ratio of NLO pQCD calculations over data. Three different PDF sets were used for the theoretical calculations: CT10, MSTW 2008 and NNPDF 2.1. Published in Ref. [87].

3.4.2 Cold Nuclear Matter Effects on Jet Production

When comparing inclusive jet cross section in p+Pb or d+Au collisions with p+p collisions there is no sign of any suppression or enhancement of the jet production in this more complex system (see e.g. the PHENIX measurement on Fig. 3.13 or results from ALICE, Fig. 3.14).

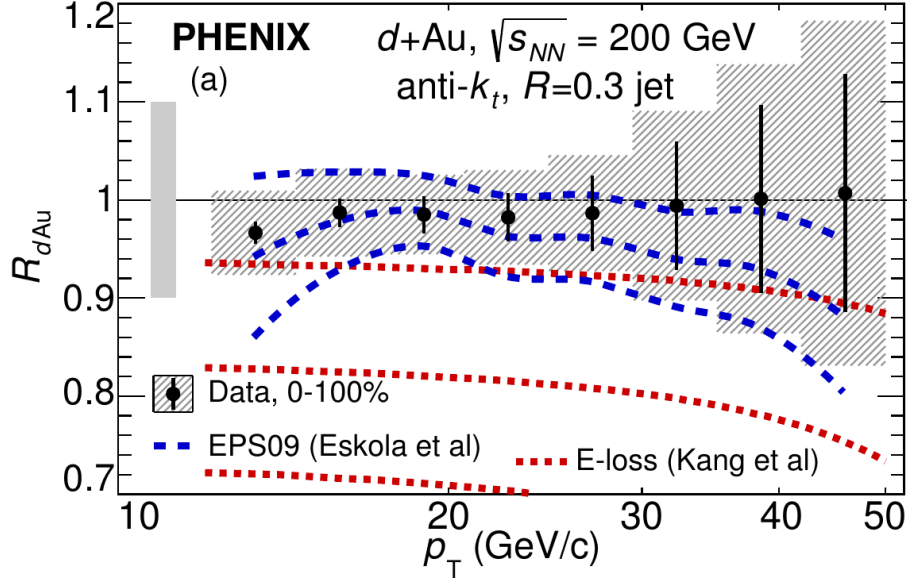


Figure 3.13: Multiplicity integrated R_{dAu} measured by the PHENIX Collaboration and its comparison with the theoretical calculation incorporating nPDFs. Published in Ref. [81].

However the situation changes when one starts to look at the nuclear modification factor in different multiplicity classes. Recent PHENIX measurements (see Fig. 3.15) clearly showed a significant suppression (enhancement) in the most central (most peripheral) d+Au collisions. The size of the suppression/enhancement increases with the jet momentum. The same observation was made by ATLAS at the LHC collision energy of 5 TeV [90] as can be seen on Fig. 3.16, which shows a similar trend, most profound in the mid-rapidity region.

Interestingly the magnitude of the effect in the central and peripheral collisions is the same, just with an opposite sign, therefore it cancels out in the centrality integrated measurement. Explanation of this observation is a subject of ongoing discussion. Kinematic bias on centrality selection [92] could explain the suppression in the central collisions, however it completely fails in describing the enhancement in the peripheral collisions. Since the R_{pPb} in the ATLAS results scales with proton- x , a scenario in which the modifications arise from a novel feature of the proton wavefunction at large x has been suggested [93, 94]. In any case the presence of such correlations would challenge the use of factorization theorem for describing the hard scattering processes in collisions involving nuclei.

On the other hand, the most recent measurements of the multiplicity dependent nuclear

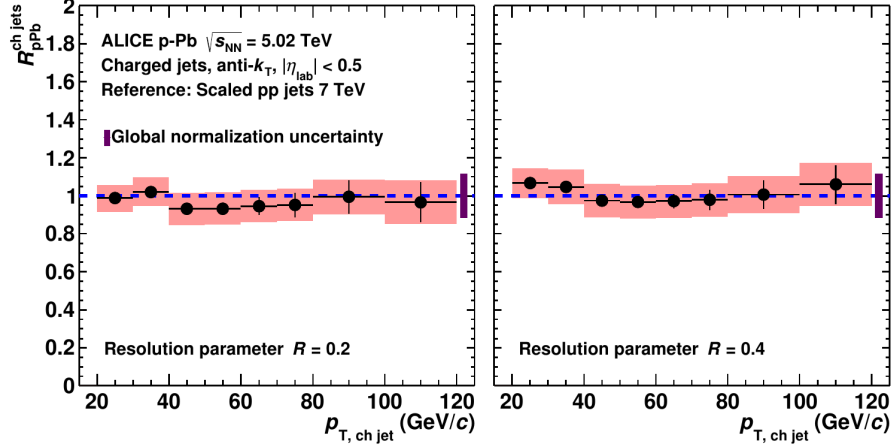


Figure 3.14: ALICE measurements of the nuclear modification factor R_{pPb} of charged jets for $R = 0.2$ (left) and $R = 0.4$ (right). Published in Ref. [89].

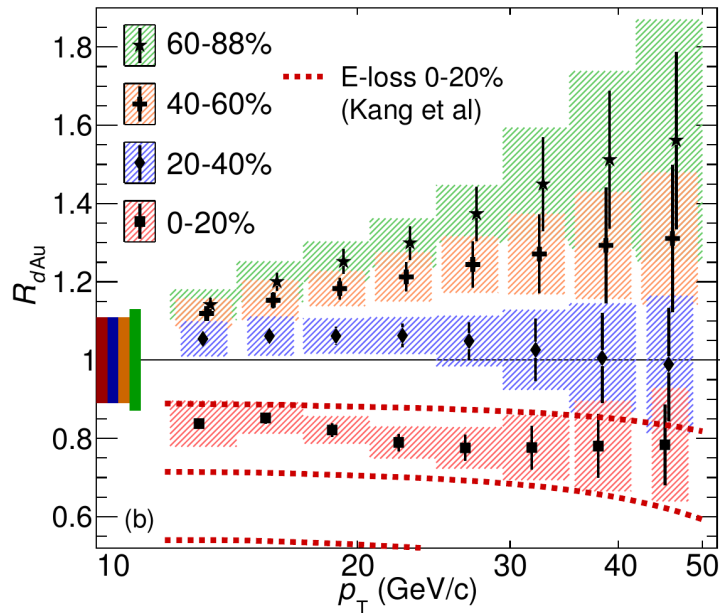


Figure 3.15: Full jet R_{dAu} measured by the PHENIX Collaboration in several multiplicity classes. Published in Ref. [81].

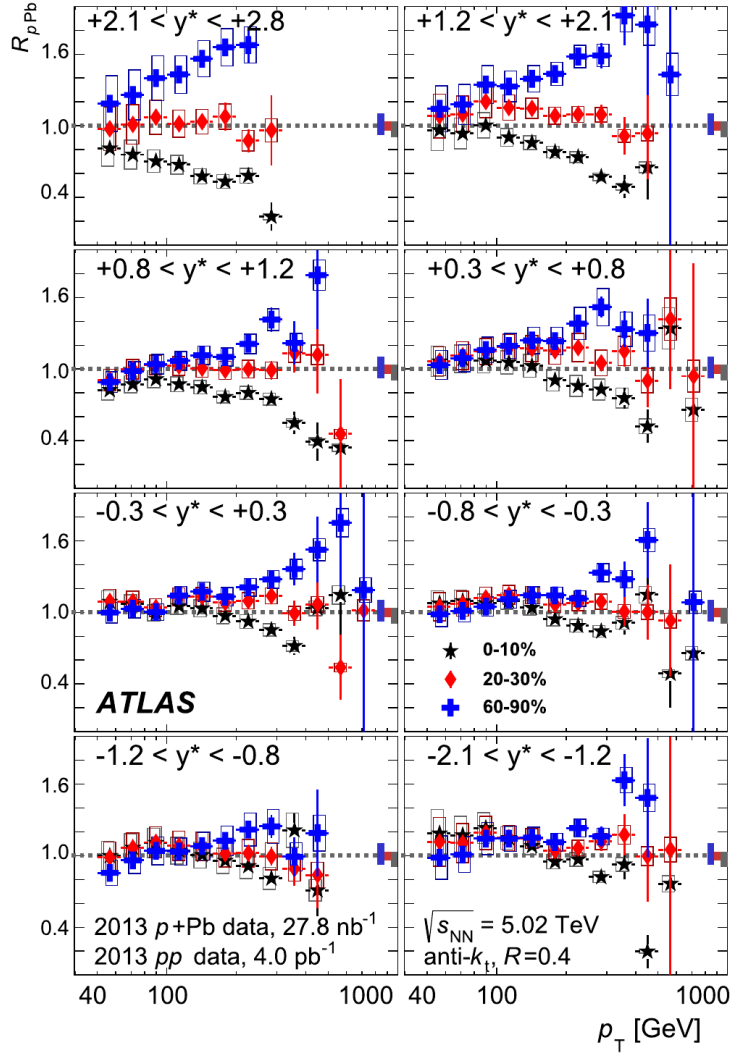


Figure 3.16: R_{pPb} values for $R = 0.4$ jets in p+Pb collisions at $\sqrt{s_{NN}} = 5.02$ TeV in central (stars), mid-central (diamonds) and peripheral (crosses) events measured at the ATLAS experiment. Each panel shows the jet R_{pPb} in a different rapidity range. Published in Ref. [90].

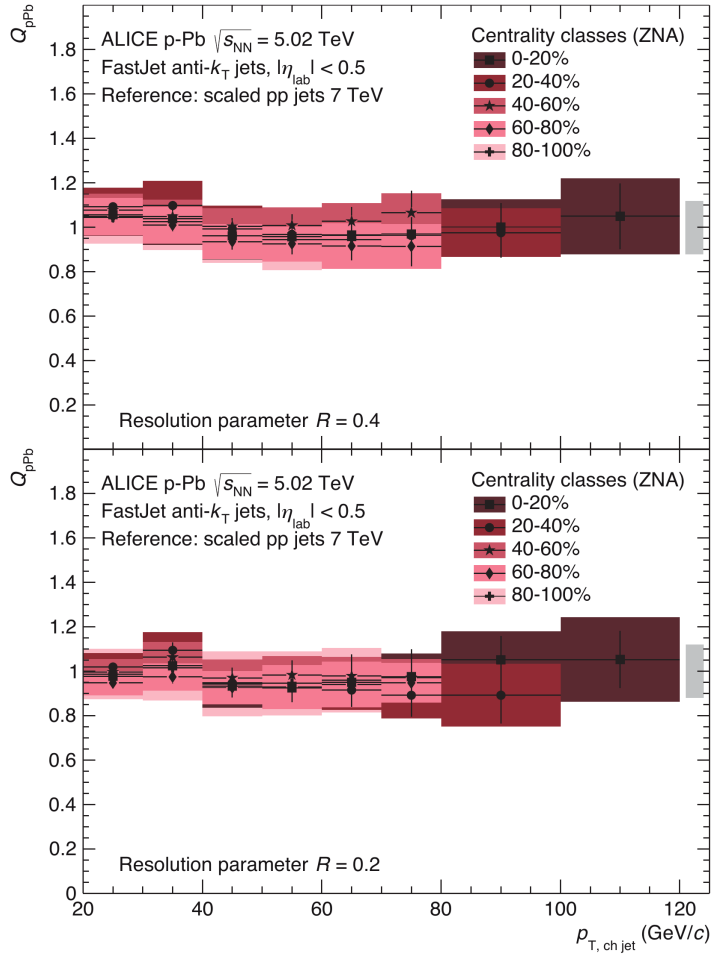


Figure 3.17: Charged jet Q_{pPb} measured by the ALICE Collaboration in several multiplicity classes for $R = 0.4$ (top) and 0.2 (bottom). Published in Ref. [91].

modification factor Q_{pPb} ⁴⁾ by the ALICE collaboration shown on Fig. 3.17 does not confirm the results of PHENIX and ATLAS since no multiplicity dependence was observed [91].

3.4.3 Jet Quenching Measurements

Suppression of the jet production in central heavy-ion collisions is one of the key signatures of the QGP, as discussed in Section 3.2.3. Nuclear modification factor R_{AA} (Eq. 3.9) of the jet cross section is thus a key observable for heavy ion jet measurements.

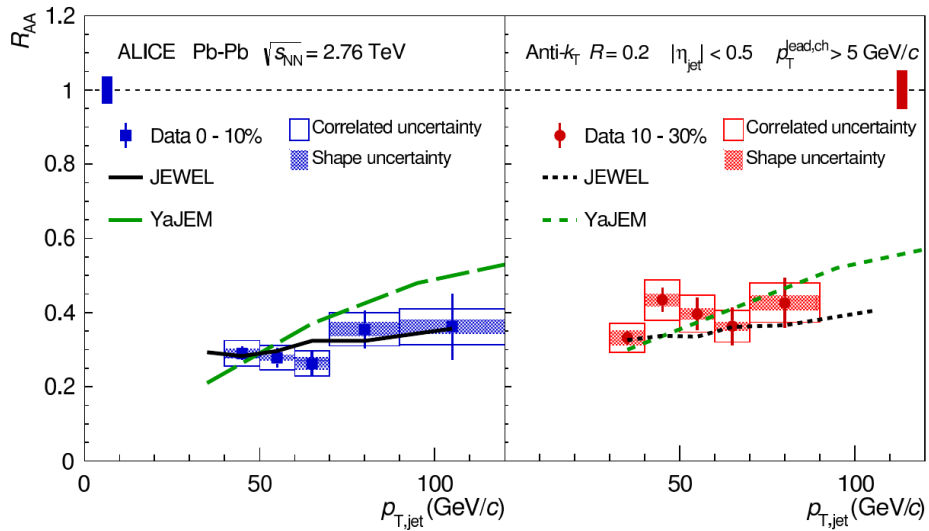


Figure 3.18: R_{AA} for $R = 0.2$ jets with the leading track requirement of 5 GeV/c in 0–10% (left) and 10–30% (right) most central Pb+Pb collisions measured by the ALICE experiment compared to calculations from YaJEM [95] and JEWEL [96] models. Published in Ref. [97].

The ALICE Collaboration has published R_{AA} of fully reconstructed full jets (charged tracks + neutral energy) with a cut on leading charged hadron momentum $p_{\text{T}}^{\text{lead}} > 5$ GeV/c [97]. This result is shown on Fig. 3.18. In the most central Pb+Pb collisions the R_{AA} slowly rises from ~ 0.3 at 40 GeV/c to ~ 0.4 at 100 GeV/c. In the semi-central collisions the R_{AA} is more consistent with a constant trend. In both cases the results are well described by the JEWEL model [96]. Also the YaJEM model [95] describes the data reasonably well, but overestimates the R_{AA} at high p_{T} in the most central collisions. Both models simulate the parton shower in the medium in a non-analytical way, using modified Monte Carlo generators for parton showers in vacuum. While JEWEL focuses mainly on collisional energy loss mechanism and radiative energy loss treats only in a schematic way, YAJEM on the other hand focuses primarily on the treatment of the radiative energy loss [98].

⁴The ALICE collaboration uses Q_{pPb} for denoting the multiplicity dependent R_{pPb} .

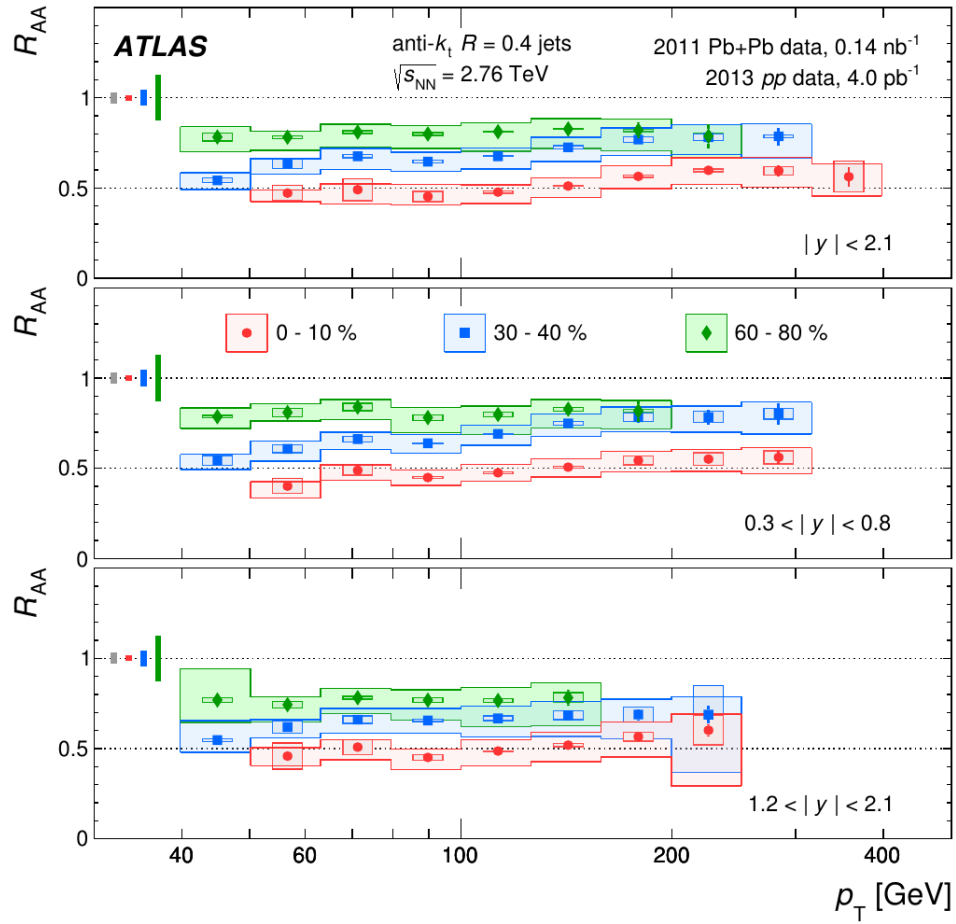


Figure 3.19: Full jet R_{AA} measured by the ATLAS collaboration at $\sqrt{s_{NN}} = 2.76$ TeV as a function of p_T in different centrality bins with each panel showing a different range in rapidity. Published in Ref. [99].

The ATLAS Collaboration, utilizing its great calorimetric capabilities, measured the nuclear modification factor of the full jets, as shown on Fig. 3.19. Within the momentum range accessible with the ATLAS detector and in the rapidity region $1.2 < |y| < 2.1$ there is no sign of a p_T dependence of the R_{AA} suppression, reaching value of $R_{AA} \approx 0.5$ for the most central Pb+Pb collisions [99]. In the mid-rapidity region, there is only a slight increase of the R_{AA} with increasing momentum for the central and semi-central Pb+Pb collisions.

The weak increase of the R_{AA} and its magnitude in the central collisions are described quantitatively by theoretical calculations with $\mathcal{O}(\alpha^3)$ accuracy [100].

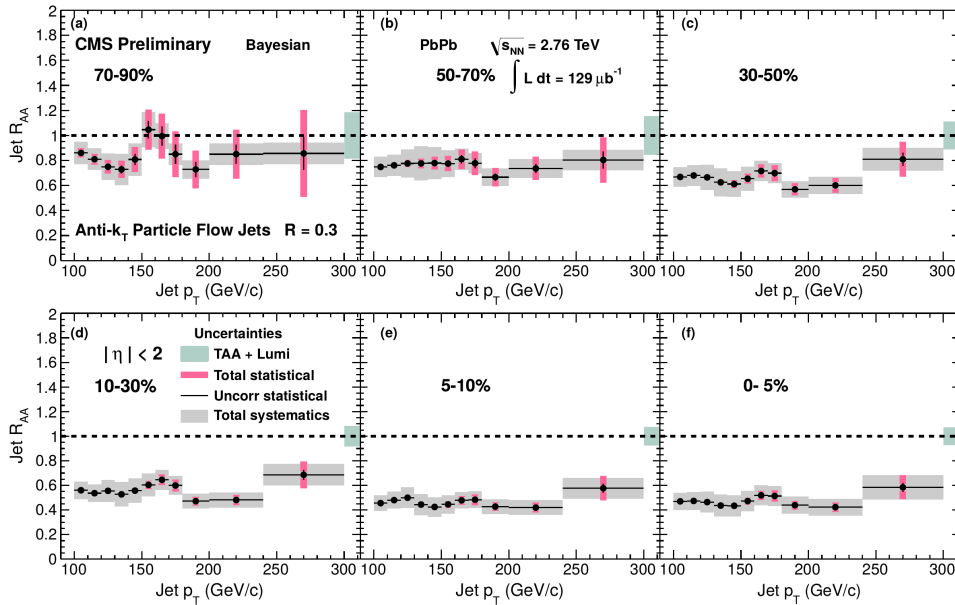


Figure 3.20: Full jet R_{AA} measured by the CMS collaboration at $\sqrt{s_{NN}} = 2.76$ TeV as a function of p_T with each panel showing a different centrality class. Jets were reconstructed with $R = 0.3$. Published in Ref. [101].

The R_{AA} measurement done by the CMS collaboration [101] and presented on Fig. 3.20 is in a good agreement with the ATLAS results.

Hadron+Jet Measurements

The trade-off between the suppression of the combinatoric background and the imposition of a bias on the jet constituents seems to be inevitable in the heavy-ion collisions. But not necessarily. The hadron+jet measurements represent a clever way how to overcome this difficulty. First, a high momentum hadron triggers the event selection. This reliably picks up an event resulting from a hard collision. The jets are reconstructed only in the region opposite to the trigger direction. No jet constituent cuts have to be applied on these recoil jets, because the background is estimated by selecting a low momentum trigger. The

recoil jet spectrum obtained with the low momentum trigger is then subtracted from the spectrum obtained with the high momentum trigger. The remaining jets are assumed to present a signal (which still needs to be corrected for the background fluctuations and the detector effects).

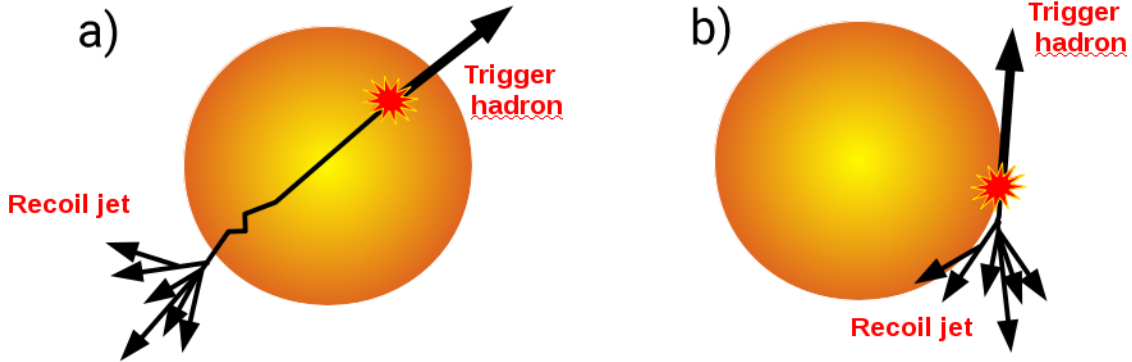


Figure 3.21: Two possible extreme biases of the recoil jet selection caused by the hadron trigger: a) maximal path length b) minimal path length.

The remaining problem is what is the dominant nature of the bias caused by the hadron trigger. There are two extreme scenarios illustrated on Fig. 3.21. Either the recoil jet population can be biased towards the jets with longer in-medium path lengths or the jet population can be biased towards tangential jets which do not traverse through the medium at all.

A pioneering hadron+jet measurement was conducted by the ALICE Collaboration [102]. Fig. 3.22 shows the recoil jet spectra in Pb+Pb collisions at $\sqrt{s_{NN}} = 2.76$ TeV for two different momentum ranges of the hadron trigger. One can clearly see that the left hand side (LHS) part of the spectra is practically identical for both triggers whereas on the right hand side (RHS) the spectrum corresponding to the high momentum trigger is dominant. Since the LHS contains mainly the combinatoric background it is no surprise that this part of the spectrum does not depend on the trigger momentum.

Fig. 3.23 shows I_{AA} of recoil jets, which is defined as ratio of the recoil jet yield normalized per trigger in central Pb+Pb collisions with respect to p+p collisions scaled by the mean number of binary collisions. The measured value of $I_{AA} \sim 0.6$ does not significantly depend neither on the jet size R nor the jet momentum.

The STAR Collaboration has also made a novel hadron+jet measurement in Au+Au collisions recently. The procedure is similar to what was done by ALICE, but with one significant difference. Instead of subtracting the recoil jet spectra for two different trigger ranges in order to remove the background, the background was estimated by creating a large set of mixed events [103]. The signal spectrum was then obtained by subtracting the jet yield in mixed events from the yield in events with a high p_T trigger.

Fig. 3.24 shows the corrected recoil jet yields normalized per trigger together with the

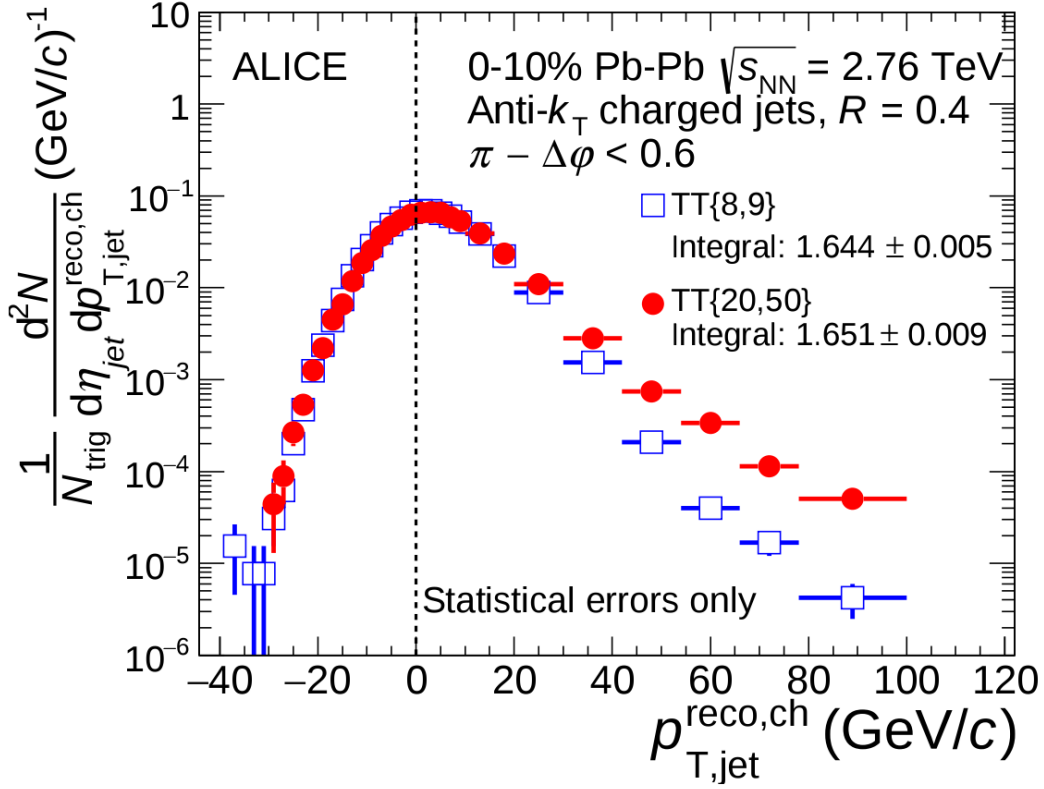


Figure 3.22: Recoil jet spectra in Pb+Pb collisions at $\sqrt{s_{NN}} = 2.76$ TeV for two different momentum ranges of the hadron trigger, 8-9 GeV/c (blue) and 20-50 GeV/c (red). Published in [102].

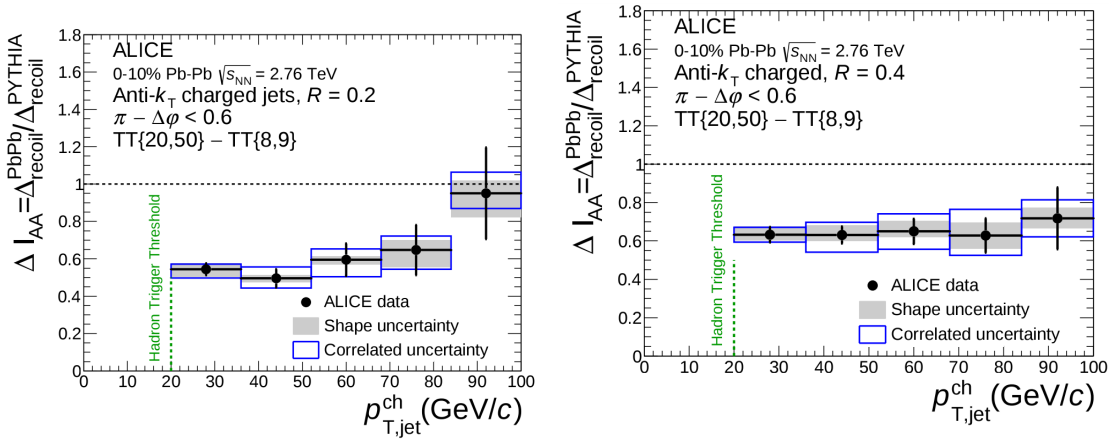


Figure 3.23: I_{AA} of recoil jets for the jet resolution parameter $R = 0.2$ (left) and $R = 0.4$ (right) measured by the ALICE Collaboration [102].

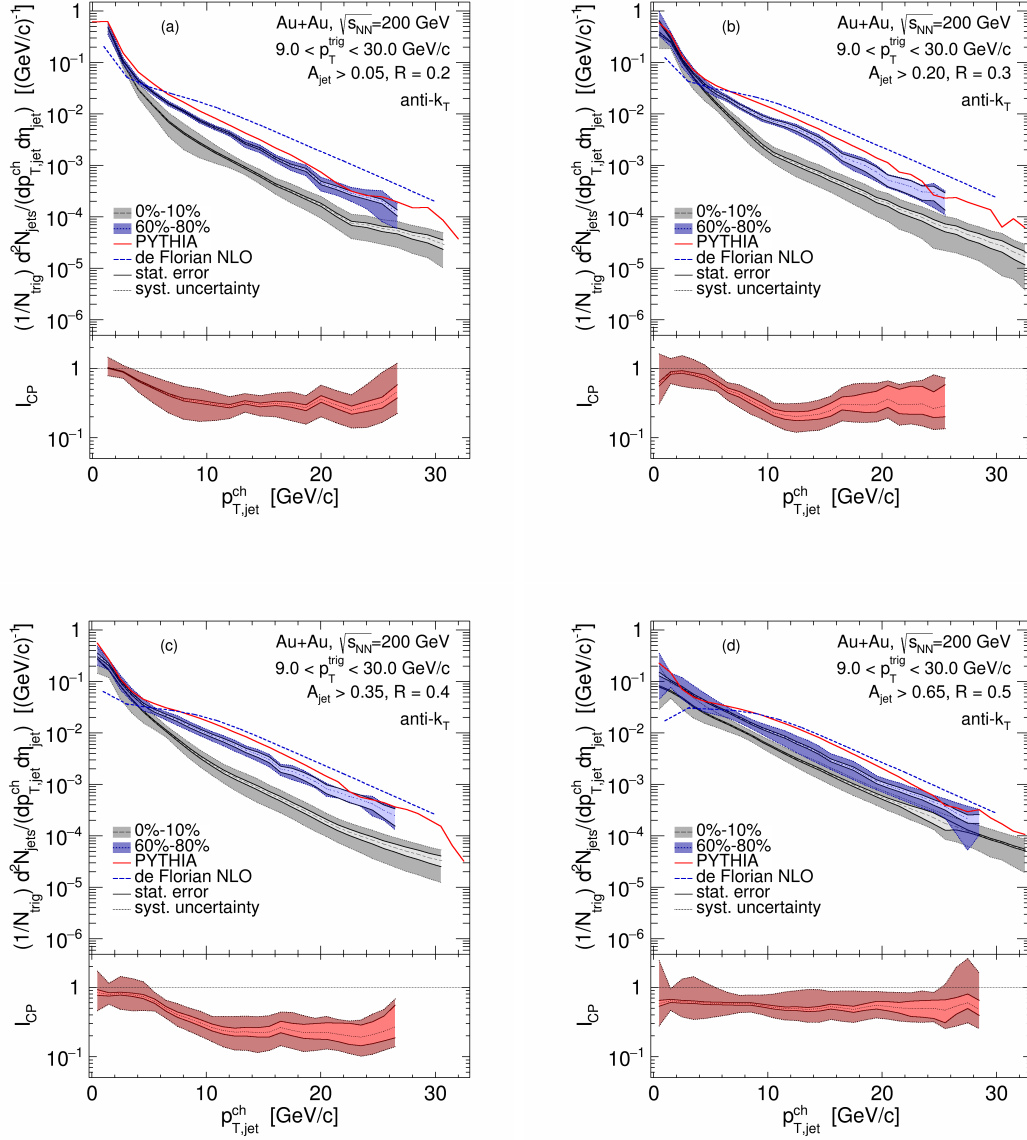


Figure 3.24: Fully corrected recoil charged jet yield per trigger (upper panels) and I_{CP} (bottom panels) in Au+Au collisions at $\sqrt{s_{NN}} = 200$ GeV for the jet resolution parameters $R = 0.2 - 0.5$ measured by the STAR Collaboration [103].

I_{CP} - ratio of the recoil jet yield in central Au+Au collisions with respect to peripheral collisions normalized by the mean number of binary collisions. Up to $R = 0.4$ the I_{CP} remains constant, but for the largest jets with $R = 0.5$ the I_{CP} is significantly closer to unity. This would suggest that for the jets with $R = 0.5$ the recoil jet energy is largely recovered.

Di-jet Imbalance

Modification of the jet structure due to the medium induced gluon radiation is a much stronger effect than higher order gluon radiation which can happen also in p+p collisions and this makes the R_{AA} so interesting quantity. However the size of the effect is dependent on the distance the jet has traveled in the medium. By triggering on the most energetic jet in the event one biases the selection towards the least modified jets. There is a high probability that the second (away-side) jet has interacted with the medium and has been thus significantly modified. Jet asymmetry A_J (Eq. 3.15) should be therefore sensitive to the modification of the jets due to the presence of the QGP.

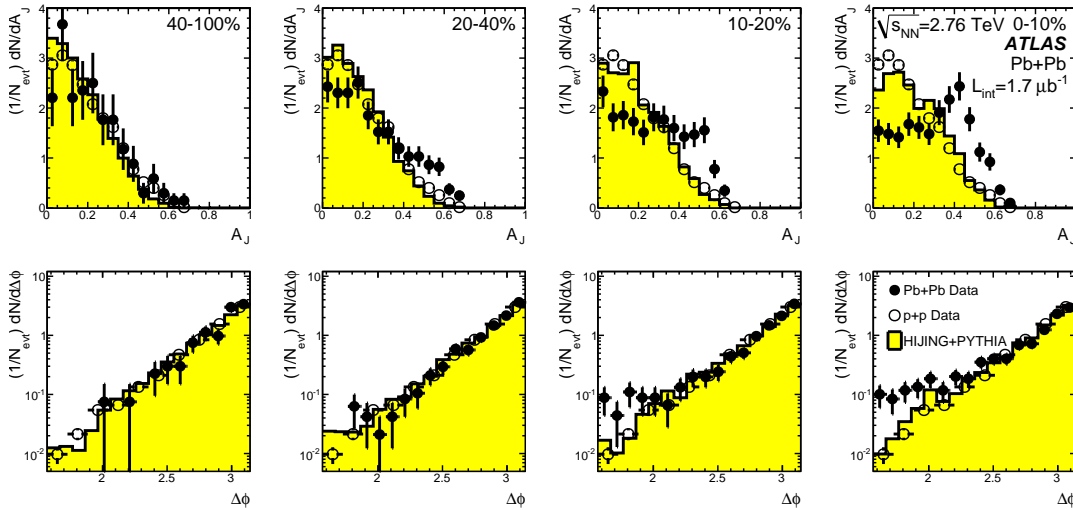


Figure 3.25: Top: Di-jet asymmetry distributions for data (points) and unquenched HIJING with superimposed PYTHIA di-jets (solid yellow histograms), as a function of collision centrality (left to right from peripheral to central events). Proton-proton data from $\sqrt{s_{NN}} = 7$ TeV, analyzed with the same jet selection, is shown as open circles. Bottom: Distribution of $\Delta\phi$, the azimuthal angle between the two jets, for data and HIJING+PYTHIA, also as a function of centrality. Published in Ref. [104].

Both the ATLAS and CMS Collaborations measured the di-jet asymmetry in Pb+Pb collisions [104, 105]. The ATLAS results are compared to di-jets generated with PYTHIA Monte Carlo (MC) and embedded into heavy ion background simulated with HIJING MC generator. The HIJING events were generated without jet quenching. The CMS Collaboration compares its measurement to di-jets generated with PYTHIA MC embedded

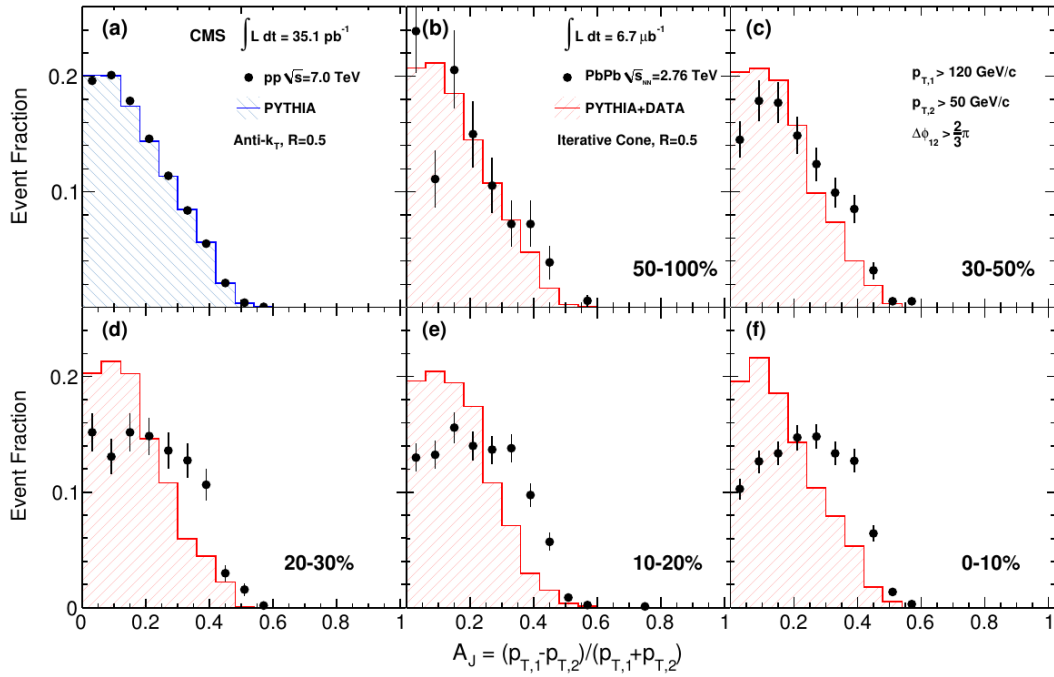


Figure 3.26: Di-jet asymmetry A_J for 7 TeV p+p collisions (a) and 2.76 TeV Pb+Pb collisions in several centrality bins: (b) 50–100%, (c) 30–50%, (d) 20–30%, (e) 10–20% and (f) 0–10%. Data are shown as black points, while the histograms show (a) PYTHIA events and (b)-(f) PYTHIA events embedded into Pb+Pb data. Published in Ref. [105].

into real Pb+Pb events. In both cases the measured asymmetry in Pb+Pb collisions is significantly higher than what is obtained from the embedded PYTHIA events. This suggests the source of the asymmetry is the parton energy loss in the QGP. These results are shown on Fig. 3.25 and 3.26.

Another CMS measurement presented on Fig. 3.27 shows the dependence of the away-side jet missing momentum, which is calculated for each event as

$$\not{p}_T^{\parallel} = \sum_i -p_{T,\text{track}}^i \cos(\phi_{\text{track}}^i - \phi_{\text{leading jet}}), \quad (3.22)$$

on the di-jet asymmetry A_J . The same analysis as for real data was performed also on PYTHIA di-jets embedded into heavy ion events generated by the HYDJET MC event generator. In both cases the missing momentum \not{p}_T^{\parallel} from the away side jet is recovered by including soft particles down to momentum of 0.5 GeV/ c even for events with a high di-jet asymmetry. Moreover Fig. 3.28 shows that the missing momentum would not be fully recovered when one would limit the calculation only to tracks inside the jet cone even with a large radius of $R = 0.8$. This would suggest that the parton shower is significantly broadened and softened by the interaction with the medium.

The procedure of the A_J measurement in Au+Au collisions at STAR [106] is different than what was performed by the ATLAS and CMS Collaborations. It proceeds in the following way:

1. Jets are reconstructed only from tracks with $p_T > 2$ GeV/ c .
2. For the same set of events jets are reconstructed from tracks with $p_T > 0.2$ GeV/ c .
3. Event-by-event, jets obtained in the second step are geometrically matched to those reconstructed in the first step.
4. A_J of matched di-jets is calculated.

The same analysis is also performed for high-tower triggered p+p events embedded into minimum bias Au+Au events. Such a sample contains jets not modified by the medium and is used as a reference.

By comparing Au+Au A_J distributions (full symbols) to those obtained for the p+p + Au+Au events (open symbols) shown on Fig. 3.29, one can see that for the jet radius of $R = 0.2$ the Au+Au distribution differs significantly from the distribution measured in embedded p+p events for both types of jets ($p_T^{\text{track}} > 2.0$ GeV/ c and $p_T^{\text{track}} > 0.2$ GeV/ c). However in the case of the radius of $R = 0.4$ the situation changes. Highly biased jets ($p_T^{\text{track}} > 2.0$ GeV/ c) still exhibit a different shape of the A_J distribution for Au+Au and embedded p+p events, but the distributions become nearly identical once the track momentum cut is lowered to $p_T^{\text{track}} > 0.2$ GeV/ c .

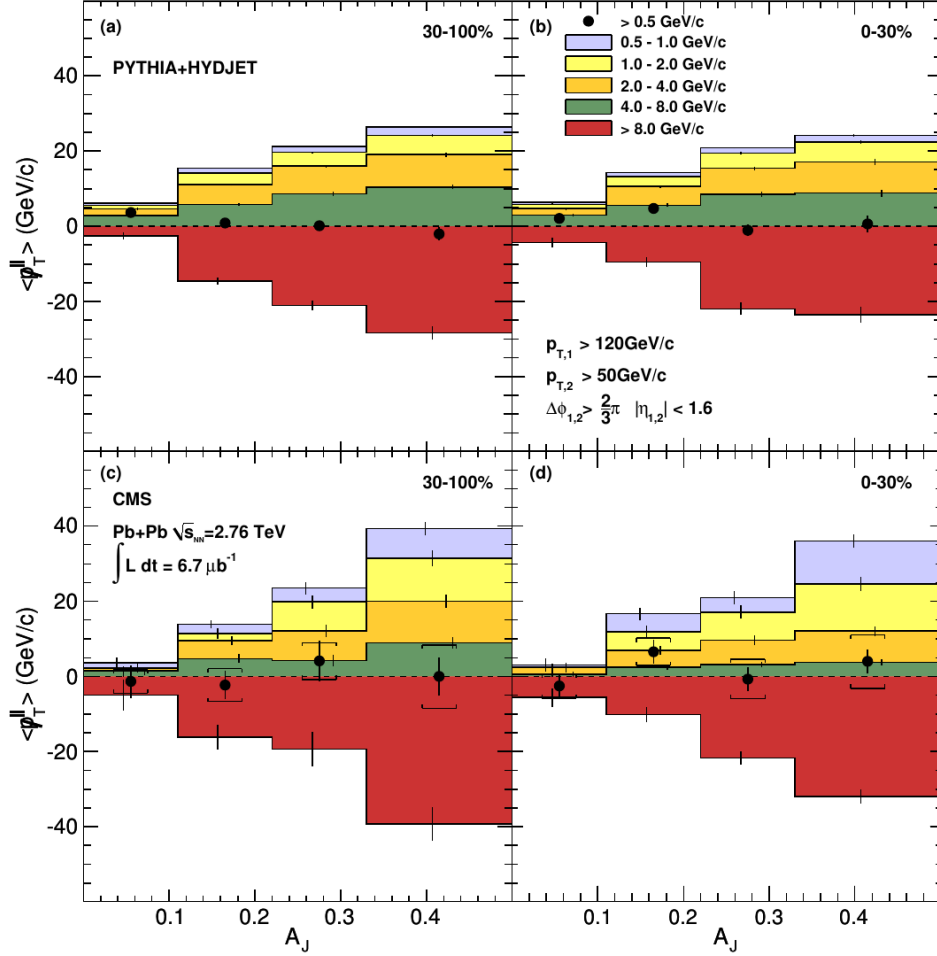


Figure 3.27: Average missing transverse momentum, $\langle p_T^{\parallel} \rangle$, for tracks with $p_T > 0.5 \text{ GeV}/c$, projected onto the leading jet axis (solid circles). The $\langle p_T^{\parallel} \rangle$ values are shown as a function of di-jet asymmetry A_J for 30–100% centrality (left) and 0–30% centrality (right). Colored bands show the contribution to the $\langle p_T^{\parallel} \rangle$ for five ranges of track p_T . The top and bottom rows show results for PYTHIA + HYDJET and Pb+Pb data respectively. Published in Ref. [105].

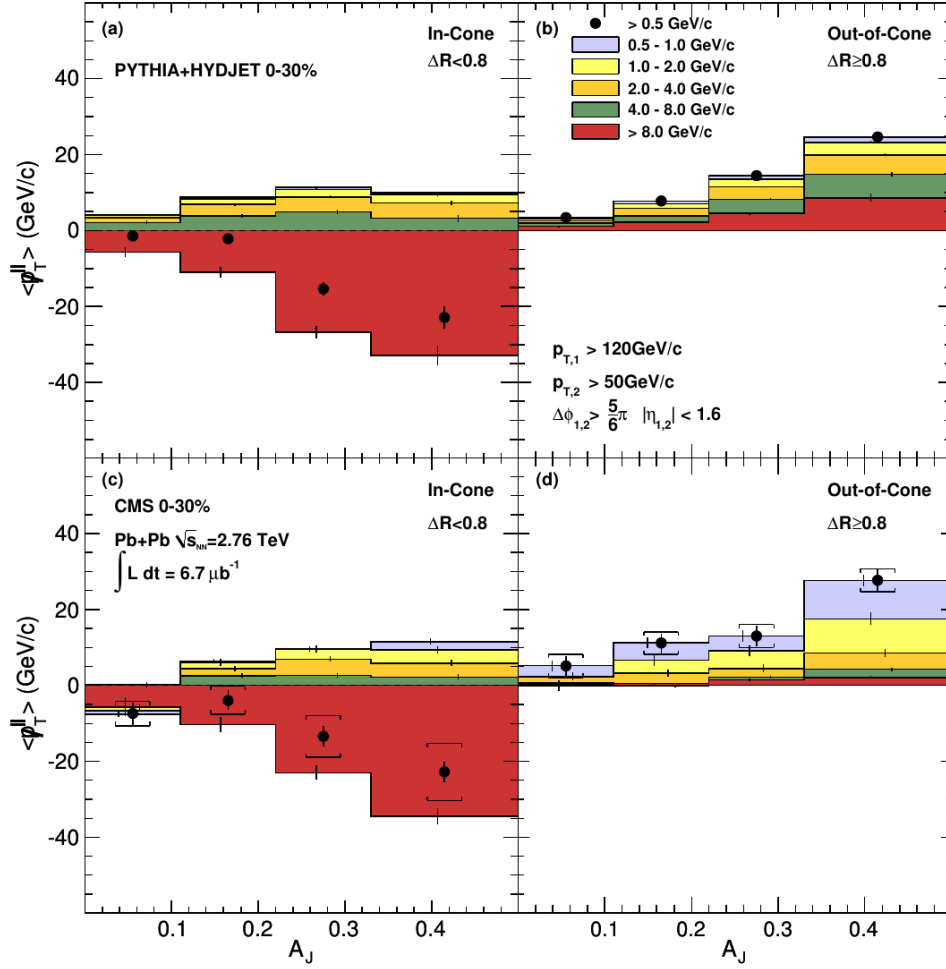


Figure 3.28: Average missing transverse momentum, $\langle p_T^\parallel \rangle$, for tracks with $p_T > 0.5$ GeV/c, projected onto the leading jet axis (solid circles). The $\langle p_T^\parallel \rangle$ values are shown as a function of di-jet asymmetry A_J for 0–30% centrality, inside ($\Delta R < 0.8$) one of the leading or subleading jet cones (left) and outside ($\Delta R > 0.8$) the leading and subleading jet cones (right). Published in Ref. [105].

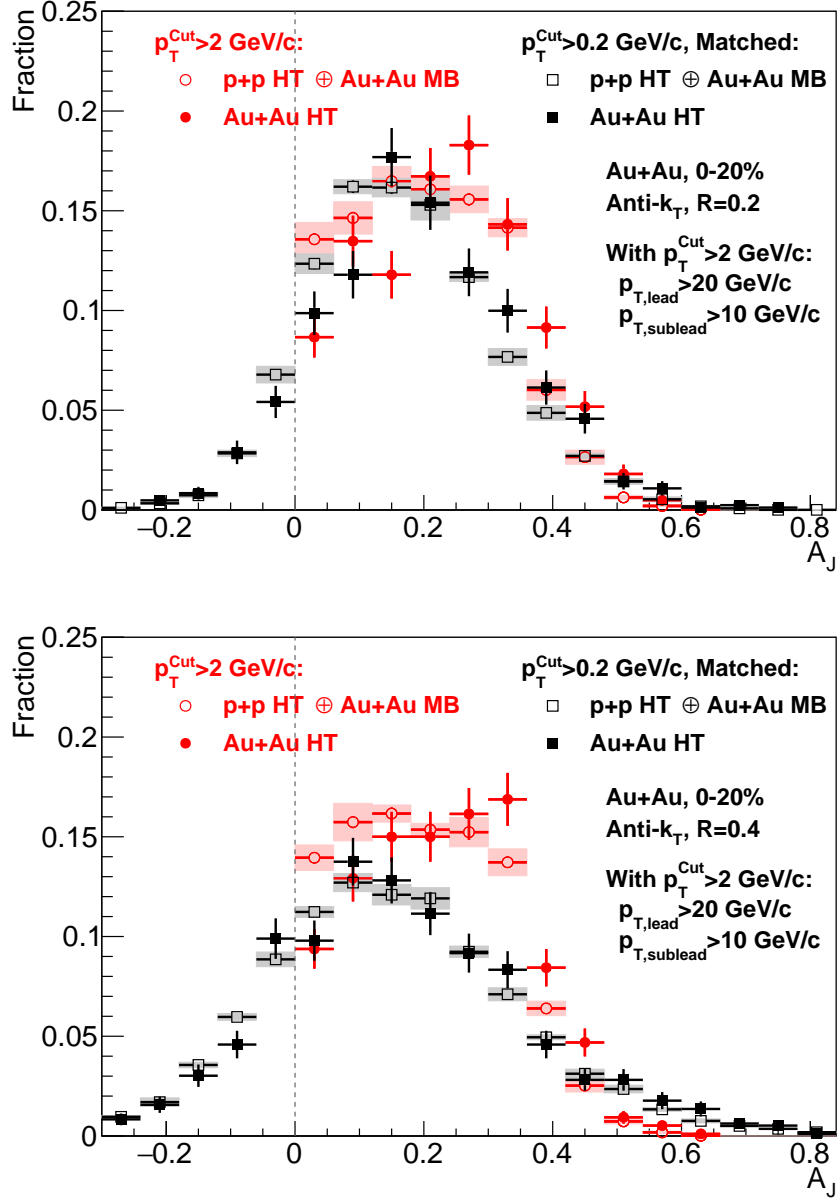


Figure 3.29: Normalized A_J distributions for Au+Au high tower (HT) data (filled symbols) and p+p HT data embedded into Au+Au MB background (open symbols) measured by STAR. The red data points are for jets found using only constituents with $p_T^{\text{Cut}} > 2 \text{ GeV}/c$ and the black ones for matched jets found using constituents with $p_T^{\text{Cut}} > 0.2 \text{ GeV}/c$. Top: $R = 0.2$. Bottom: $R = 0.4$. Published in [106].

Chapter 4

RHIC and STAR

4.1 RHIC

The Relativistic Heavy Ion Collider (RHIC) is currently the only operational dedicated heavy-ion collider in the world. Even though there is also a heavy-ion program running at the Large Hadron Collider (LHC), the p+p collisions are the main area of interest at the LHC. In the following text we will concentrate exclusively on RHIC.

The RHIC facility is situated in the Brookhaven National Laboratory at Long Island, New York, USA. It was commissioned in 2000 and it continues to work flawlessly to the present day. RHIC is composed of two separated rings which are 3834 m long in circumference with six intersecting sections - interaction points. At these intersecting sectors the four RHIC main experiments were placed. These were BRAHMS, PHOBOS, PHENIX and STAR.

The PHOBOS and BRAHMS experiments completed their operation in 2005 and 2006 respectively. The PHENIX experiment finished the data collecting in 2016 and the collaboration is now preparing for a transition to sPHENIX, a successor of PHENIX. It will consist of a hadronic and an electro-magnetic calorimeter and precise tracking detectors (silicon strip detector, pixel detector, time projection chamber) with a full coverage in azimuth, making it a great tool for the jet and Υ measurements [107].

STAR is currently the only remaining operational experiment, continually undergoing new upgrades and improvements so it can even after almost two decades of operation collect data which satisfy the ever-changing needs of the physical community.

Due to the separation of the rings and the wide versatility of the whole acceleration complex, the RHIC collider can operate with a large variety of collision systems and at different collision energies. The most common collision systems are Au+Au, p+p, d+Au, p+Au. But also additional systems are collided, such as Cu+Cu, U+U, p+Al, Cu+Au.

Au+Au collisions represent a unique tool for hot nuclear matter studies, while asymmetric systems such as d+Au or p+Au should explore the domain of the cold nuclear matter effects. Together with the heavy-ion program, there also runs a very important and unique program of colliding polarized protons, making RHIC an indispensable machine for

the spin physics.

4.1.1 The Accelerator Complex

There are two main acceleration scenarios possible at the RHIC facility: acceleration of protons or acceleration of heavy-ions.

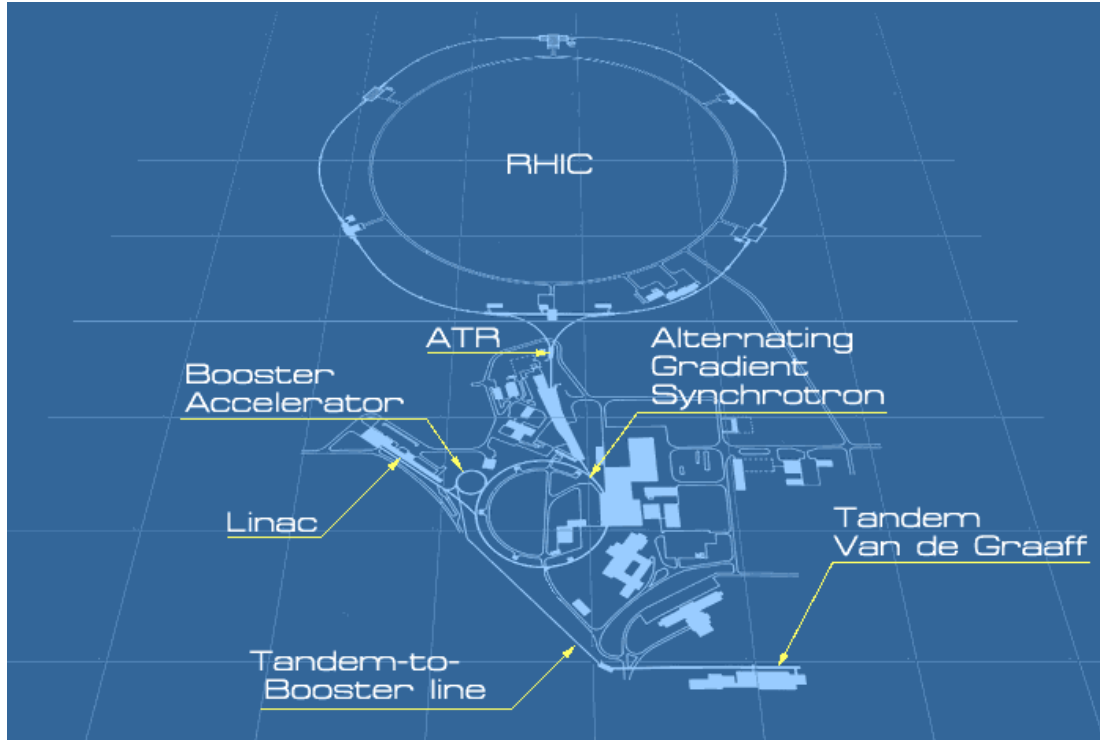


Figure 4.1: Scheme of the RHIC complex.

In case of the heavy-ion scenario, the chain starts with a pulsed sputter ion source [108], which produces a beam of negative ions with a charge $Q_T = -1e$. These ions are extracted and transferred to the Tandem Van de Graaff accelerator [109]. In the first half of the Tandem they are accelerated to the potential of 14MV, then they pass the stripping foil, lose electrons and with a positive charge of Q_T ($Q_T = +12e$ for gold nuclei) are accelerated in the second half of the Tandem back to the ground potential, acquiring additional energy of $14 \cdot Q_T$ MeV. There is also a second Tandem Van de Graaff available, which can provide an additional beam of different nuclei for asymmetric collisions (e.g. Cu+Au). After leaving the Van de Graaff accelerator the beam passes through a next stripping foil which increases the charge of the gold nuclei to $Q_T = +32e$. By the transfer line the beam is transported to the Booster synchrotron. After several injections, the beams are captured into six bunches which are accelerated to 95 MeV per nucleon (MeV/ u). At the exit of the Booster all but two electrons are stripped from the ions by another stripping foil. Four cycles of Booster are used to fill the Alternating Gradient Synchrotron (AGS) and these

24 bunches are debunched and rebunched into 4 final bunches, which are then accelerated up to 8.86 GeV/ u . At the exit from the AGS the last two electrons are stripped off and the bunches are transferred by the AGS to RHIC (AtR) beamline into the RHIC storage rings.

The second scenario is the acceleration of the polarized protons. Protons produced by a polarized proton source [110] are accelerated by a 200 MeV Linac and brought to the Booster. From the Booster the proton bunches continue in the same way as heavy-ions do.

Once in RHIC, the beams are accelerated to the final energy and then pass to the storage cycles. During the storage cycles the bunches are being held together in the longitudinal direction using RF cavities operating at 197 MHz [109].

Bending and focusing of the beam is accomplished by using superconducting magnets. 396 dipole magnets provide the bending, whereas 492 quadrupole magnets provide the focusing of the beam. In addition several hundreds of smaller correcting magnets are also used. The magnets are cooled to a temperature lower than 4.5 K by circulation of supercritical helium. It takes one week to cool down the whole accelerator from the room temperature to the operational temperature [109].

4.2 STAR Experiment

STAR is an acronym for the Solenoidal Tracker At RHIC. Its main purpose is to explore the properties of the QGP and to measure several QGP signature observables simultaneously. STAR is therefore designed to measure properties of hadrons over the full azimuth and at mid-rapidity. Information obtained from several subdetectors is combined in order to perform particle identification, momentum and energy measurement.

STAR is a complementary experiment to PHENIX and vice versa. PHENIX is composed mainly from fast and sensitive calorimeters, which however (mainly due to the enormous price) cover only a part of the azimuth. The STAR data taking rate is smaller than that of PHENIX, therefore STAR is able to record only a fraction of events with respect to its counterpart. On the other hand STAR can provide a more complete picture of the nuclear collision events due to the larger variety of available subdetectors. Some of these detectors can be seen on Fig. 4.3. Six of them have a barrel-shape and provide a full azimuthal coverage:

- Heavy Flavor Tracker (HFT) (2014-2016)
- Time Projection Chamber (TPC)
- Barrel Electro-Magnetic Calorimeter (BEMC)
- Barrel Shower-Max Detector (BSMD)
- Barrel Time Of Flight (BTOF)
- Muon Telescope Detector (MTD) (since 2014)

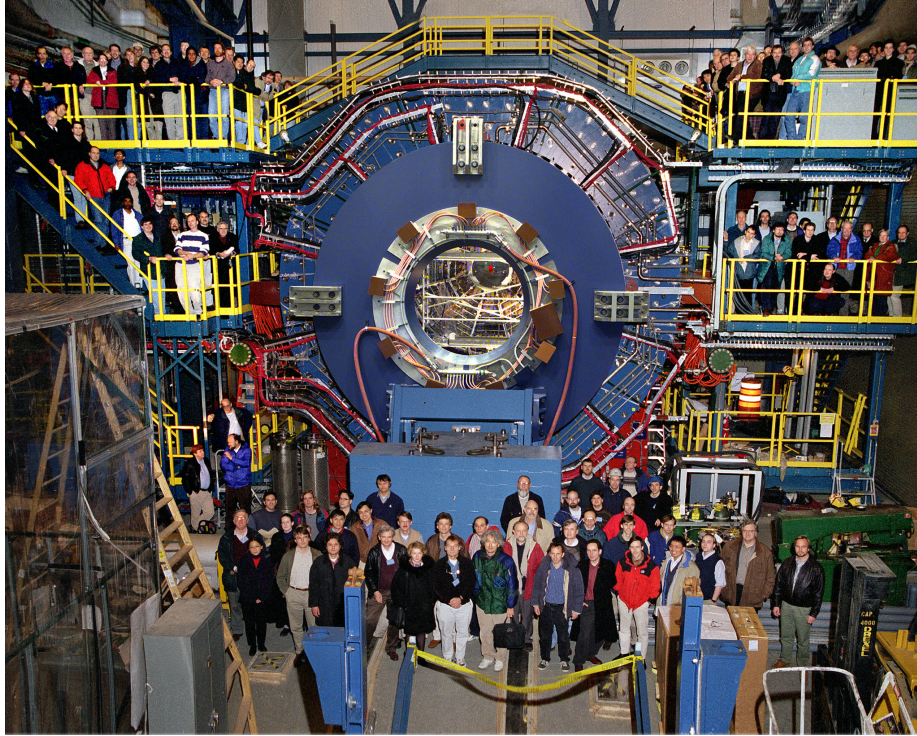


Figure 4.2: Members of the STAR Collaboration standing before the STAR detector.

There are also two forward rapidity detectors:

- Endcap Electro-Magnetic Calorimeter (EEMC)
- Forward GEM Tracker (FGT)

Even with the Data Acquisition (DAQ) upgrade, which STAR underwent in 2010 and which increased the record rate from 100 to 1000 Hz, it is not possible to record all the events. Therefore interesting events are preselected by fast trigger detectors. Besides the BEMC and TOF which are used for triggering there are also additional coincidental paired detectors:

- Vertex Position Detector (VPD)
- Beam-Beam Counter (BBC)
- Zero Degree Calorimeter (ZDC)

Bellow we describe in more detail some of the STAR subdetectors.

TPC: The heart of the STAR detector is formed by the Time Projection Chamber (TPC). This large cylindrical gas detector is able to reconstruct up to several thousand tracks of charged particles created in heavy-ion collisions. The TPC is also capable of particle

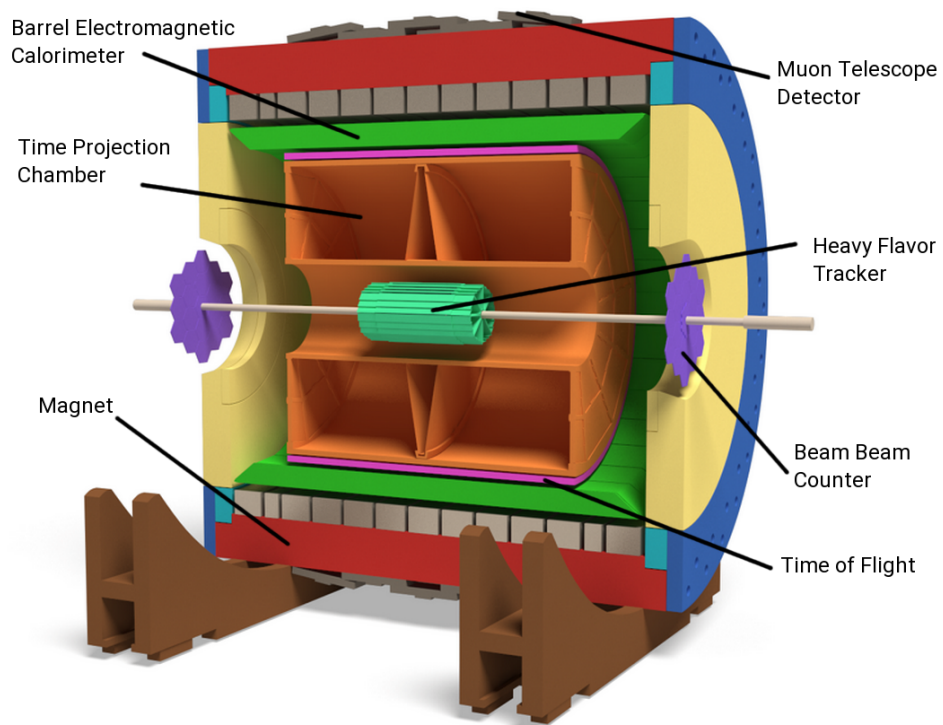


Figure 4.3: A 3D model of the STAR detector and its main subdetectors. NB: Heavy Flavor Tracker and Muon Telescope Detector were not installed in 2011. Figure adopted from [111].

identification (PID) based on ionization loss dE/dx measurement. Since the TPC is the main detector used in our analysis, it will be described in a more detail later.

VPD+BTOF: In order to improve the PID capabilities, the STAR detector was equipped with the Time of Flight (TOF) system in 2009. It consists of two subdetectors - Vertex Position Detector (VPD) and Barrel TOF (BTOF).

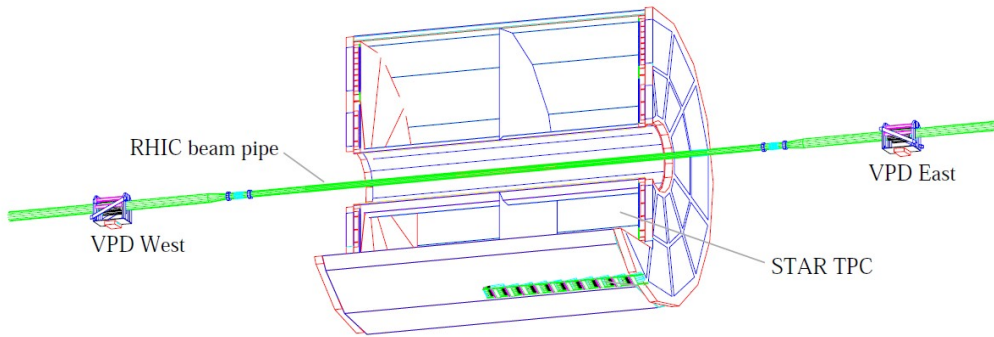


Figure 4.4: The STAR TPC and VPD detectors.

The VPD is placed around the beam pipe in a distance of $z = \pm 5.7$ m and it measures start time of the flight of a particle, whereas the stop time is measured by the Barrel TOF (BTOF), mounted around the TPC. The BTOF uses a Multi-gap Resistive Plate Chamber (MRPC) technology.

BEMC: The TPC and BTOF are surrounded by the Barrel ElectroMagnetic Calorimeter (BEMC), which is a fast lead-scintillator calorimeter designed to collect energy of neutral particles and also to distinguish between electrons and hadrons. It is divided into 120 segments in azimuthal angle and 40 segments in pseudorapidity. This makes 4800 calorimetric towers in total, each tower having its individual readout. Resolution (effective size of the towers) of the BEMC is 0.05×0.05 ($\Delta\phi \times \Delta\eta$). The main goal of the BEMC is to measure and trigger on the transverse energy deposition, mainly from e^+ , e^- and photons. Calorimetric triggers are called high-tower triggers.

Due to their speed both the BEMC and TOF are also used as a trigger of high-energetic events.

Magnet: The outermost part of the STAR detector is a massive solenoidal room-temperature magnet producing a magnetic field of 0.5 T. The magnetic field bends the trajectories of the charged particles and allows a momentum measurement.

HFT: In years 2014-16 the STAR capability of precise vertex measurements was enabled by addition of a new Heavy Flavor Tracker (HFT), a 4-layer silicon detector placed between the TPC and the beam pipe.

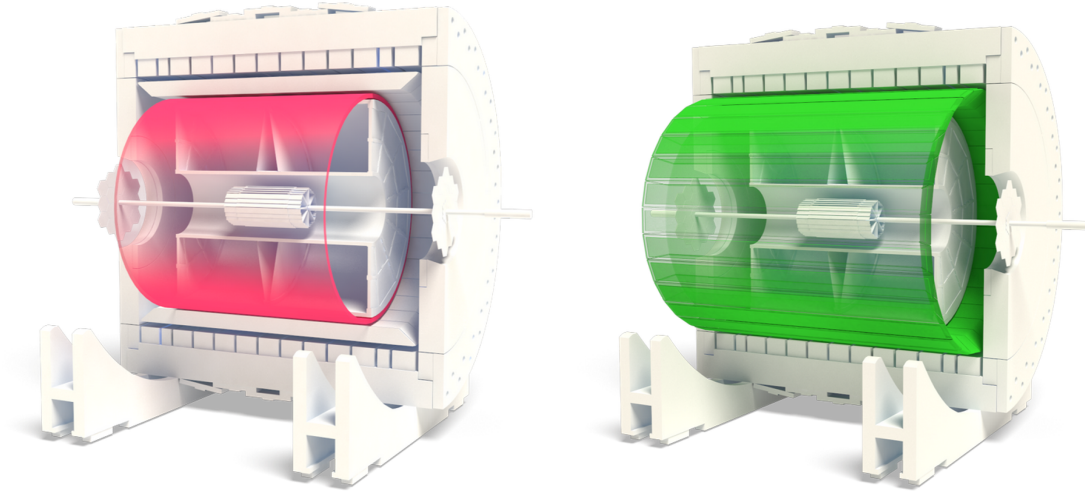


Figure 4.5: Position of the BTOF (left) and BEMC (right) inside the STAR detector. Figure adopted from [111].

The HFT, TPC, TOF and BEMC have full acceptance in azimuth and pseudorapidity acceptance of $|\eta| < 1.0$.

4.2.1 TPC

The TPC is a 4.2 meter long barrel detector with an outer radius of 2.0 m, filled with gaseous argon (90%) and methane (10%) pressurized slightly above the atmospheric pressure. The detector is divided into two sections by a thin high-voltage carbon coated membrane. The membrane is kept at the voltage of -28 kV, while the end-caps at both ends of the TPC are kept at 0 V. This forms a uniform electric field of approx. 135 V/cm in the longitudinal direction.

A charged particle which goes through the TPC ionizes the gas along its trajectory. Electrons created during the ionization start to drift along the electric field direction towards the end-cap. The end-caps contain $2 \times 70,000$ pads with anode multi-wire proportional chambers (MWPC) in which the electron signal is amplified and recorded. The grid formed by the MWPC wires allows determination of two coordinates (x,y) of each track segment. The z (longitudinal) coordinate is determined from the drift time of the electrons, since their drift speed is known (and calibrated every few hours). All together we obtain the necessary information for a 3-dimensional track reconstruction of each charged particle coming through the TPC.

The STAR TPC also provides dE/dx measurements by measuring the energy of created electrons along the path of the charged particle. Its acceptance for tracking and dE/dx measurement is $|\eta| < 1.0$ at full efficiency, and extends up to $|\eta| < 1.8$ with reduced efficiency and resolution. The spacial resolution is $460 \mu\text{m}$ in x, y and $700 \mu\text{m}$ in z .

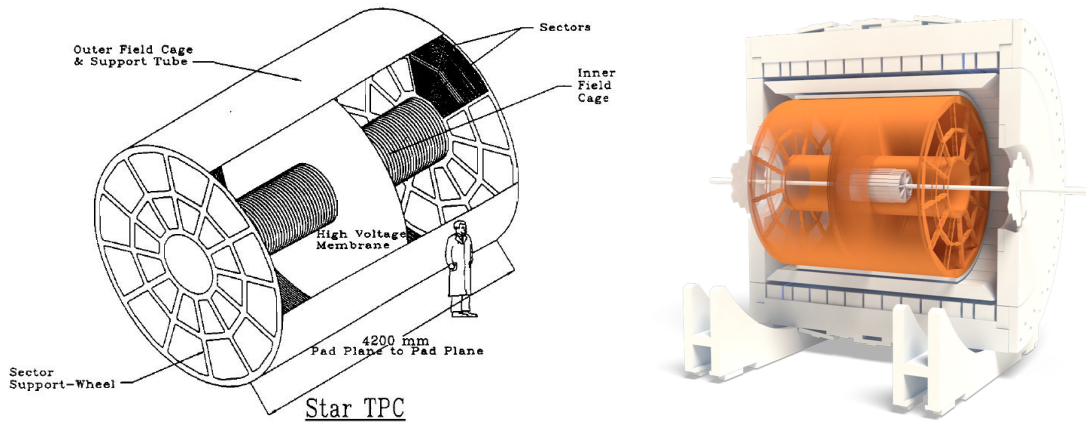


Figure 4.6: Left: Schematic picture of the STAR Time Projection Chamber. Left: Highlighted position of the TPC inside STAR. Figure adopted from [111].

Pile-up

A disadvantage of the TPC detector is its relative slowness - the drift time from the membrane to the end-cap is $\sim 40 \mu\text{s}$. Once the bunch crossing time is comparable or smaller than the TPC drift speed, it can happen that several events together will be recorded during one read-out. This is called pile-up and it is an issue especially in p+p collisions where the bunch crossing rates are much higher than in Au+Au collisions. The relatively small interaction rate in Au+Au collisions allows to use a special class of pile-up protected triggers. In such a case the event is recorded only if there is no other event $40 \mu\text{s}$ before or after this event. However, no such trigger class is implementable in p+p collisions, where one usually has to remove the pile-up tracks track-by-track, based on some selection criteria. These criteria usually are:

- small distance of closest approach (DCA) of the track to the primary vertex,
- a match in a fast detector (BEMC, TOF),
- small distance between the primary vertex position reconstructed from the TPC and from the VPD (event-by-event).

Tracking

The track reconstruction software uses the Kalman filter iterative procedure to create the track from the TPC hits. The process starts with hits in the outermost layers, where the track density is lowest and thus the signal is clearest. A helix is fitted to the collection of a few first hits and is extrapolated to the lower layers. A hit nearby the helix is added to the collection and a new fit is calculated. If the χ^2 value of the fit is sufficiently low, the hit is kept, otherwise it is rejected. If more than one hit in the given layer satisfies the χ^2 criterion, the one which results in the lowest χ^2 value is accepted. The procedure continues

until the innermost layer is reached. The resulting helix is called a global track. Once the position of the primary vertex (PV) is calculated, all global tracks with the DCA to the PV less than 3 cm are refitted with the addition of the PV to the list of the fit points. These new helices are then called primary tracks.

4.2.2 HFT

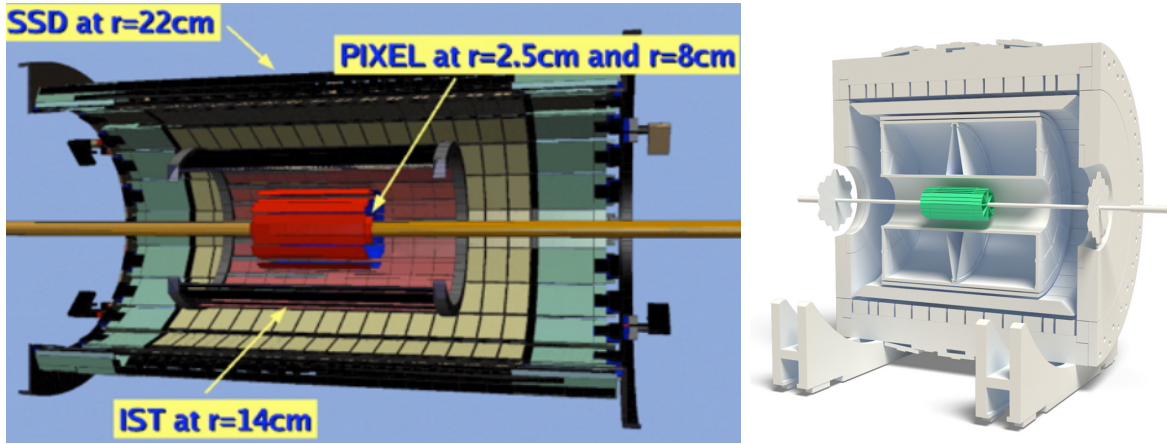


Figure 4.7: Left: Heavy Flavor Tracker for STAR. Right: Position of the HFT inside STAR. Figure adopted from [111].

STAR TPC vertex resolution is of the order of units of mm and it is insufficient for reconstruction of decay-vertices of shortly living resonances containing heavy quarks. Heavy quarks represent a very important probe of the QGP medium and therefore reconstruction and measurement of mesons and baryons containing heavy (namely charm) quark was a task of most importance at RHIC. This was a motivation for the design of the STAR's Heavy Flavor Tracker (HFT).

The Heavy Flavor Tracker consists of 3 separate subdetectors, each utilizing different technology.

- Silicon Strip Detector (SSD) - SSD utilizes doublesided silicon strip detectors providing excellent resolution in $R-\phi$ direction of $\sigma_{R-\phi} = 20 \mu\text{m}$, but very moderate resolution alongside the beam axis z , $\sigma_z = 740 \mu\text{m}$. The SSD is an existing detector with upgraded readout electronics in order to match the STAR's DAQ II data recording capabilities. Its radius is 22 cm and the length is 106 cm.
- Intermediate Silicon Tracker (IST) - IST consists of single-sided double-metal silicon pad sensors with $600 \mu\text{m} \times 6 \text{mm}$ pitch. Its resolution is $\sigma_{R-\phi} = 170 \mu\text{m}$ and $\sigma_z = 1800 \mu\text{m}$. Purpose of the ITS is to connect the tracks from the SSD down to the Pixel Detector and therefore such resolution is sufficient. The ITS is placed at the radius of 14 cm.

- Pixel Detector (PXL) - The most important part of the HFT are the two layers of the Pixel Detector, at the radius of 8.2 and 2.9 cm. Based on novel MAPS technology, the PXL is capable of an excellent resolution of $\sigma = 7.8 \mu\text{m}$.

Pixel Detector

Since the author was involved in the testing of the PXL the detector will be described in a more detail here. The PXL represents a state of the art micro vertexing detector. It utilizes novel technology of Monolithic Active Pixel Sensors (MAPS), used in a high energy physics experiment for a very first time.

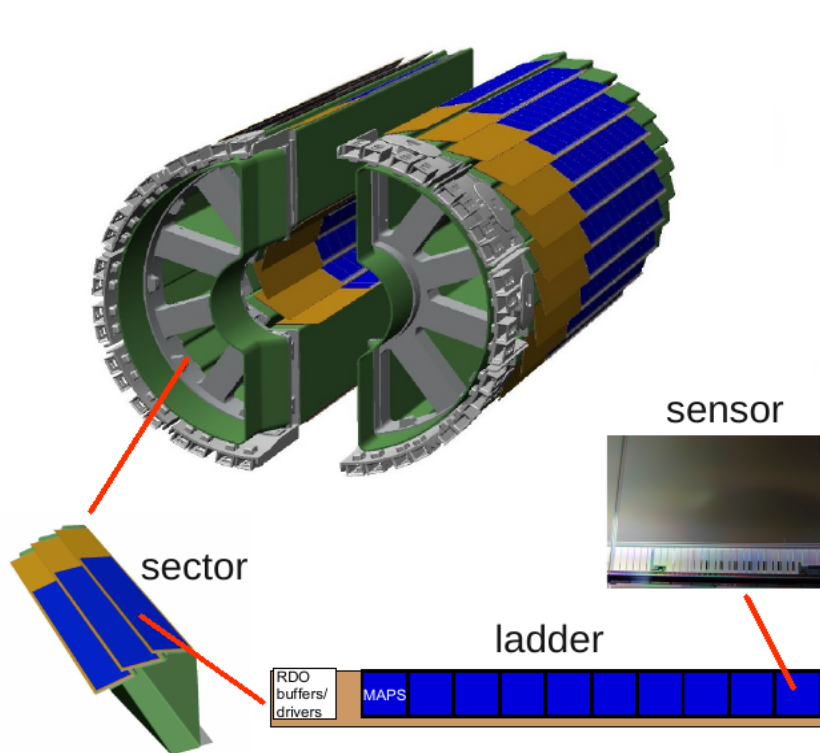


Figure 4.8: The STAR's PXL detector, its sector, ladder and sensor. Figures adopted from [112].

It is divided into 10 sectors, each sector contains 3 ladders in the outer layer and 1 ladder in the inner layer. Each ladder contains ten sensors. One sensor contains approximately 890 000 pixels with a $20.7 \mu\text{m}$ pitch. Next to the pixels, which represent the active area of the detector, the sensor contains also approx. 3 mm wide strip of readout electronics.

The sensor is based on commercial CMOS technology, allowing its relatively cheap production using industrial standards. A cross-section of a MAPS pixel is shown on Fig. 4.9. Electric signal is created mainly in a $15 \mu\text{m}$ thick p-epi layer, small contribution comes also from p++ layer.

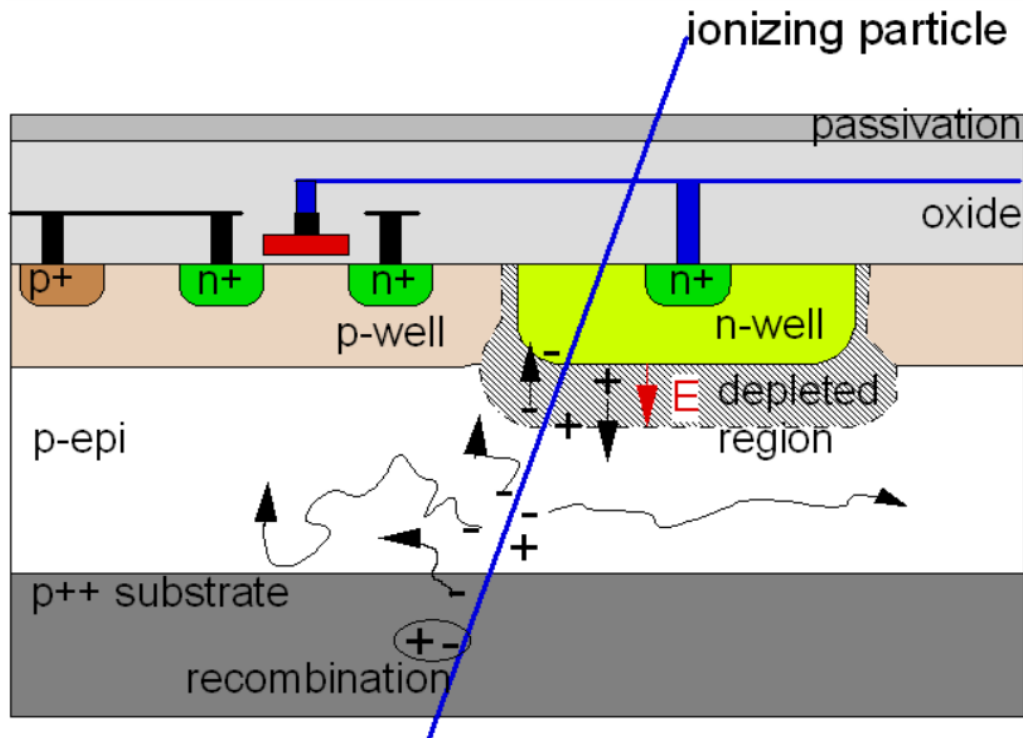


Figure 4.9: Cross-section of a MAPS pixel.

In order to provide an extraordinary pointing resolution to the primary vertex of the order of a few microns, several conditions have to be satisfied:

- reduction of Multiple Coulomb Scattering (MPS),
- close position to the collision point.

In order to minimize the MPS, the sensor is thinned down to only $50 \mu\text{m}$. The second condition was satisfied by placing the inner layer of the PXL detector just around the beam pipe. Although the sensors are relatively radiation hard, it is expected that the extremely high charged track densities at such a close distance to the collision point will lead to significant damage of the detectors after one or two years of running. Therefore the whole detector is designed for rapid replacement. The whole procedure of replacing the PXL detector should not take more than 12 hours. Two sets of the PXL detectors and 40 spare ladders were made to replace damaged detector units when needed.

Chapter 5

Service Work Related to HFT

5.1 PXL Survey and Alignment

In order to achieve the designed micrometer resolution of the PXL detector, one needs to know the exact position of each pixel. However, this is both technically impossible and computationally demanding, because one would need an enormous database to store the required information for each pixel separately. Therefore one has to reduce the measurement to a limited number of pixels per sensor and the position of the rest is then calculated by a proper interpolation method.

In our measurement, we used optical scanning machine with resolution $\sigma_{x,y} \simeq 1 \mu\text{m}$ and $\sigma_z \simeq 1 \mu\text{m}$, where the z-axis is perpendicular to the sensor's surface. The device was also equipped with a low-pressure feather probe to survey parts of the ladders covered with the overlaying neighboring ladders, achieving comparable resolution as the optical scanner. Each sector was mounted on a rotary head with high rotation angle resolution and surveyed with the optical scanner and feather probe. Author's task was to find an optimal way of the sector's survey and to program the survey machine so the whole process could be fully automated.

In order to simplify the survey several coordinate systems had to be established, as shown on Fig. 5.1. The sensor coordinate system was determined by finding 2 features at the surface of sensor with known x, y position. A third point with a given x, y position was then measured in order to fix the coordinate system in the z direction (perpendicular to the sensor surface). The sector coordinate system was determined by measuring position of 3 tooling balls at the edges of the sector. The PXL-half coordinate system is given by the position of 3 kinematic mounts on its support construction. Once installed, the whole PXL detector was aligned with the STAR coordinate system by matching tracks to other layers of the HFT and to the TPC and TOF detectors.

A complete survey of the sector took more than 16 hours, it was therefore necessary to choose the coordinate system features in a such way the survey machine can find them reliably, otherwise the machine would have to be supervised during the whole measurement. That would be unpractical and costly. It was also necessary to avoid often switching

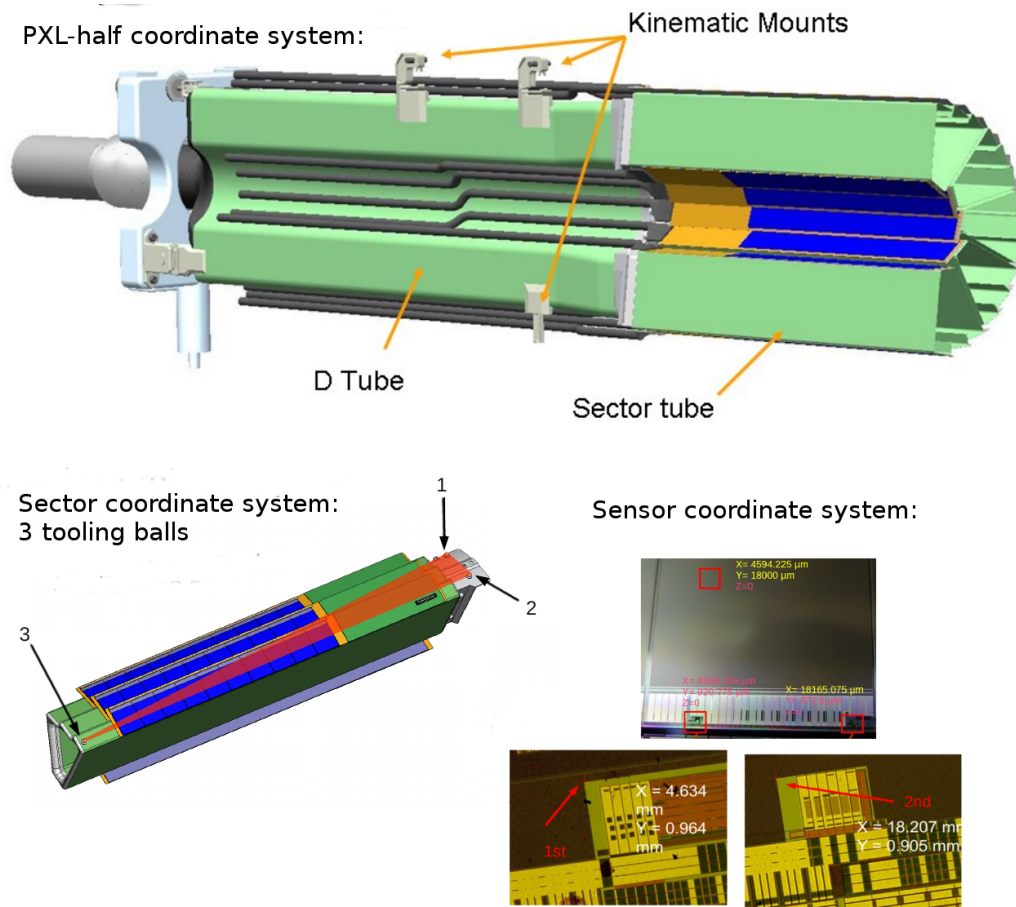


Figure 5.1: Different local coordinate systems used on the HFT. Author's archive and [112].

between the optical probe and the feather probe, since it was a time consuming operation. Last but not least a careful attention had to be paid to the path the probe was traveling between the measurements, otherwise the PXL sector as well as the probe could be easily damaged or destroyed.

Interpolation Technique

For each sensor, only 40×40 points were measured. Precise position of each pixel within the sector coordinate system is then calculated using thin-plate spline (TPS) fit. The thin-plate spline fit uses a 2D spline to match all the measured points exactly (or with a given flexibility) and simultaneously minimizes the so-called binding energy given by

$$E[f(x, y)] = \iint_{R^2} \left(\frac{\partial^2 f}{\partial x^2} + 2 \frac{\partial^2 f}{\partial x \partial y} + \frac{\partial^2 f}{\partial y^2} \right) dx dy. \quad (5.1)$$

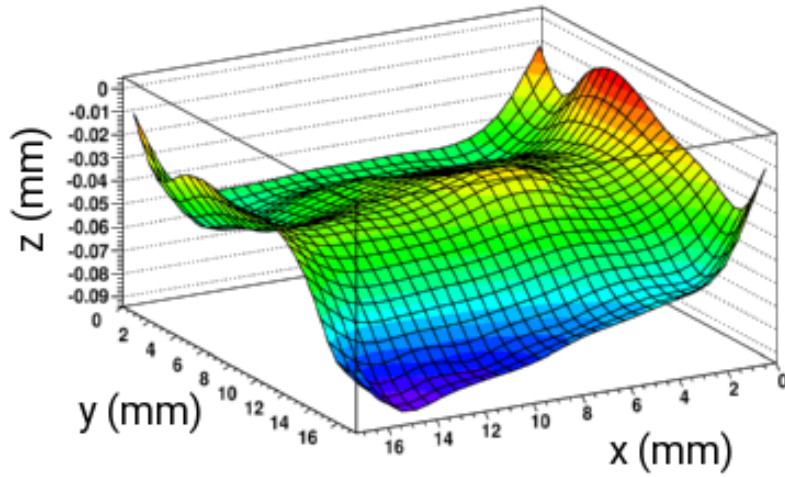


Figure 5.2: The TPS fit of a surveyed sensor.

Once all the HFT sectors were surveyed the measured points on the surface of each sensor were fitted by the thin-plate spline. The fit parameters together with the relative coordinates of the sensor, sector (obtained from the survey) and the HFT half (obtained from the track alignment) were recorded into a MySQL database. Each time a pixel sensor records a hit, the corresponding TPS fit is loaded from the database and z position of the pixel is evaluated. The pixel position in the local sensor coordinates is then transformed to the STAR global coordinate system. This information is then saved and used by the tracking software.

5.2 Λ_c Reconstruction with HFT

In central Au+Au collisions at RHIC, a baryon to meson enhancement has been observed in the intermediate p_T region ($2 < p_T < 6$ GeV/ c) [113] relative to p+p collisions. This could be explained by a hadronization mechanism involving collective multi-parton coalescence rather than independent vacuum fragmentation [114]. The same hadronization mechanism is also expected to be present in the charmed sector. Since the mass of the Λ_c baryon is not much different from that of D^0 meson, the ratio Λ_c/D^0 is expected to be enhanced. This enhancement is also considered as one of the signatures of quark gluon plasma.

The decay length of Λ_c is very short, $c\tau_{\Lambda_c} \simeq 60$ μm . This makes secondary vertex reconstruction of Λ_c a very difficult task even with the HFT capabilities.

In order to optimize the procedure of the Λ_c reconstruction, we prepared simulated data sets of Au+Au events containing a fixed number of Λ_c per event. First, the Λ_c baryon simulated by PYTHIA was let to decay into the decay channel of interest, namely K^- , π^+ , p . The triplets of the decay products were embedded into Au+Au events simulated by the HIJING event generator. The whole events were then propagated through the STAR detector simulated by the Geant 4 software.

In this simulation, the Λ_c have been reconstructed through their hadronic decays by pairing tracks identified as K^- , π^+ , p and calculating the invariant mass. The reconstruction code implements Kalman filter procedure [115] to find the secondary vertex.

Kalman Filter

Kalman filter (KF) is an iterative procedure for estimating true values of unknown variables based on inaccurate measurements varying over time and suffering from statistical noise and other effects. In our case, KF is first used to calculate a helical track of daughter particles from the measured points in the TPC, starting from the points at the outer layer of the TPC. Using this information, decay point of the mother particle (secondary vertex, SV) is calculated. Daughter tracks are then transported to the position of the SV and properties of the mother particle are recalculated. Once the position of the SV is estimated, a new parameter - decay length - is added to the estimation process. Daughter particles are then transported again to the new estimate of the SV. The whole process is repeated until the change of the SV position is sufficiently small.

Analysis

In order to reduce large combinatorial background in the Λ_c reconstruction, several topological cuts had to be used. We have optimized the following cuts (cf. Fig. 5.3):

- gDCA (DCA of the daughter particle to the PV),
- DCA_{V0} (DCA of the daughter particle to the SV),
- decay length,

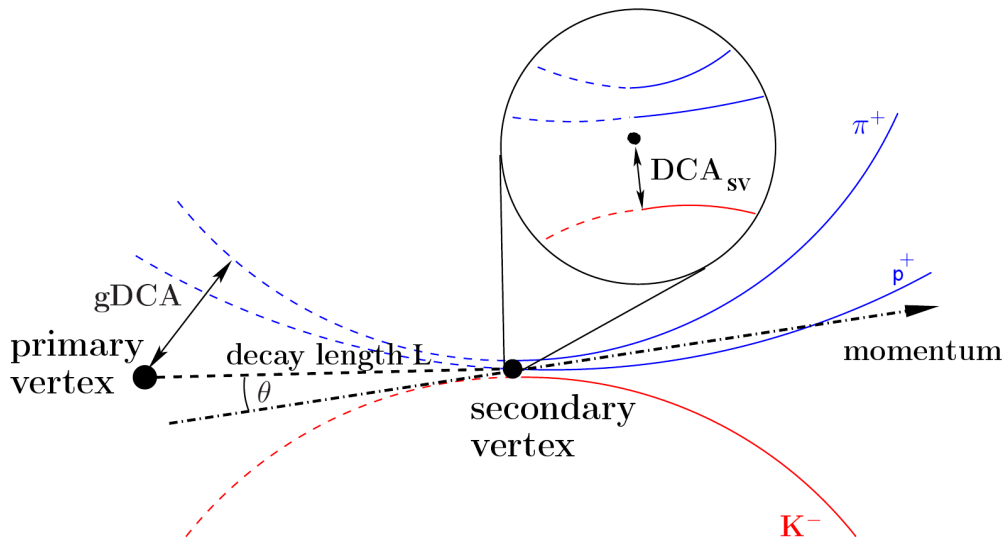


Figure 5.3: A schematic decay of Λ_c into pion, proton and kaon.

- decay length/decay length uncertainty,
- track significance ($\text{gDCA}/\sigma_{\text{gDCA}}$).

The simulated data set consisted of 20k + 20k events of HIJING central Au+Au collisions at $\sqrt{s_{NN}} = 200$ GeV with 1 or $18\Lambda_c$ per event with included pileup hits in the PIXEL detector expected for the RHIC-II luminosity period during which the HFT was operational. Additional 10k events without any Λ_c were used for the background estimation. As already mentioned, only the $\Lambda_c \rightarrow p\pi^+K^-$ decay channel was used. Thus its branching ratio was enhanced from 5 to 100%.

Results

Reconstructed invariant mass spectra were fitted by a Gaussian combined with the second order polynomial fit. Fig. 5.4 shows an example of these results for the central Au+Au collisions in Λ_c momentum range $4 < p_T < 5$ GeV/c. The signal significance σ is calculated as

$$\sigma = \frac{s}{\sqrt{b+s}}, \quad (5.2)$$

where s stands for the “signal” and is calculated as the integral of the Gaussian peak between 2.25 and 2.32 GeV/c² and the background b is calculated as the integral of the polynomial function in the same region. The significance uncertainty was estimated by repeating the calculation with the fit parameters shifted within the fit uncertainties. The obtained significance was then corrected for the expected number of events, expected content of Λ_c per event and correct branching ratio of the $\Lambda_c \rightarrow p\pi^+K^-$ decay channel.

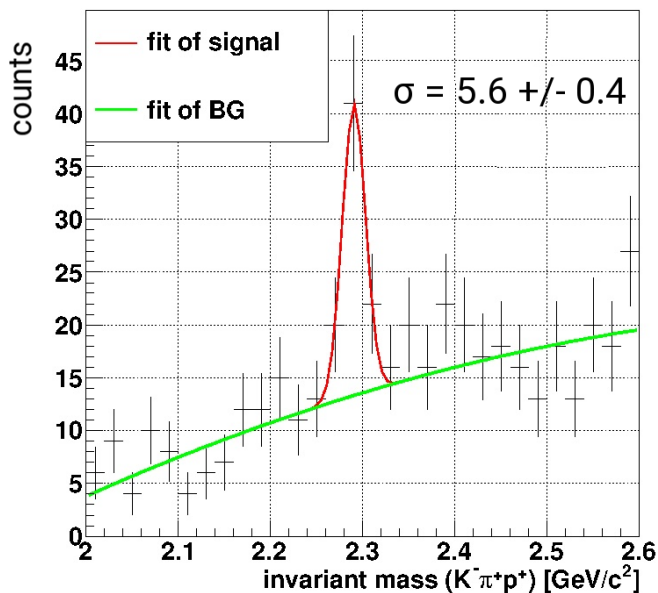


Figure 5.4: Invariant mass of reconstructed Λ_c in the momentum range $4 < p_T < 5$ GeV/ c in simulated environment of central Au+Au collisions.

Tab. 5.1 shows the corrected signal significance for several p_T bins and different collision centralities. For comparison, Tab. 5.2 shows the results obtained without the use of the Kalman filter [116, 117].

It is clear that the Kalman filter technique can increase the reach of the Λ_c reconstruction into lower p_T regions which are of a great interest for the baryon/meson ratio studies.

| $p_T^{\Lambda_c}$ [GeV/ c] | 1.5-2.0 | 2-3 | 3-4 | 4-5 |
|----------------------------------|---------------|---------------|----------------|----------------|
| central Au+Au collisions (CC) | 2.0 ± 0.8 | 3.1 ± 0.6 | 4.4 ± 0.6 | 5.6 ± 0.4 |
| enhanced production in CC | 4.8 ± 0.7 | 8.5 ± 1.2 | 13.6 ± 1.8 | 10.2 ± 1.6 |
| peripheral Au+Au collisions (PC) | 3.9 ± 0.9 | 6.3 ± 1.0 | 9.2 ± 2.0 | 10.2 ± 1.6 |

Table 5.1: The maximal obtained significance of the Λ_c invariant mass peak using the Kalman Filter.

| $p_T^{\Lambda_c}$ [GeV/c] | 1.5-2.0 | 2-3 | 3-4 | 4-5 |
|----------------------------------|---------|-----|------|------|
| central Au+Au collisions (CC) | - | 2.7 | 4.6 | 5.5 |
| enhanced production in CC | - | 6.6 | 11.6 | 10.1 |
| peripheral Au+Au collisions (PC) | - | 4.3 | 6.6 | 8.3 |

Table 5.2: The maximal obtained significance of the Λ_c invariant mass peak without the Kalman Filter. Obtaining a clear signal in the lowest p_T bin was not possible. Results from [116, 117].

Chapter 6

Jet Analysis in Au+Au Data

6.1 Dataset

For our data analysis, we use high quality RHIC Run11 data from Au+Au collisions at $\sqrt{s_{NN}} = 200$ GeV. We restrict ourselves to 0-10% most central and 60-80% peripheral Au+Au collisions from minimum bias (MB) trigger. The centrality class is determined based on the correspondence between measured charged track multiplicity and corresponding collision centrality derived from the Glauber model Monte Carlo simulation [54, 55]. Fig. 6.1 shows a comparison of the STAR charged track multiplicity distribution in central Au+Au collisions at $\sqrt{s_{NN}} = 200$ GeV and Glauber model calculation. The discrepancy between the STAR data and the Glauber model in the peripheral region is caused by the lower efficiency of the MB trigger at low multiplicities.

In order to avoid the pile-up events, we are using data from pile-up protected minimum bias triggers “vpd-zdc-mb-protected” (Trigger ID: 350003, 350013, 350023, 350033, 350043).

Event selection

Only events with the position of the reconstructed primary vertex (PV) close to the middle of the TPC were selected by imposing the following conditions:

- $|z_{\text{vertex}}| < 30$ cm
- $\sqrt{x_{\text{vertex}}^2 + y_{\text{vertex}}^2} < 2$ cm

The STAR data recording chain is described in Appendix A. The individual data taking sessions are called “runs”. For each run the mean values of charged particle multiplicity measured by the TPC in $\eta < 0.5$ ($\langle \text{refMult} \rangle$) and PV z -position ($\langle z_{\text{vertex}} \rangle$) were calculated.

Runs and run days (i.e. a group of runs taken during one day) which satisfied at least one of the following conditions were removed from the analysis:

- $|\mu_{\text{day}} - \mu_{\text{year}}| > \sigma_{\text{year}},$

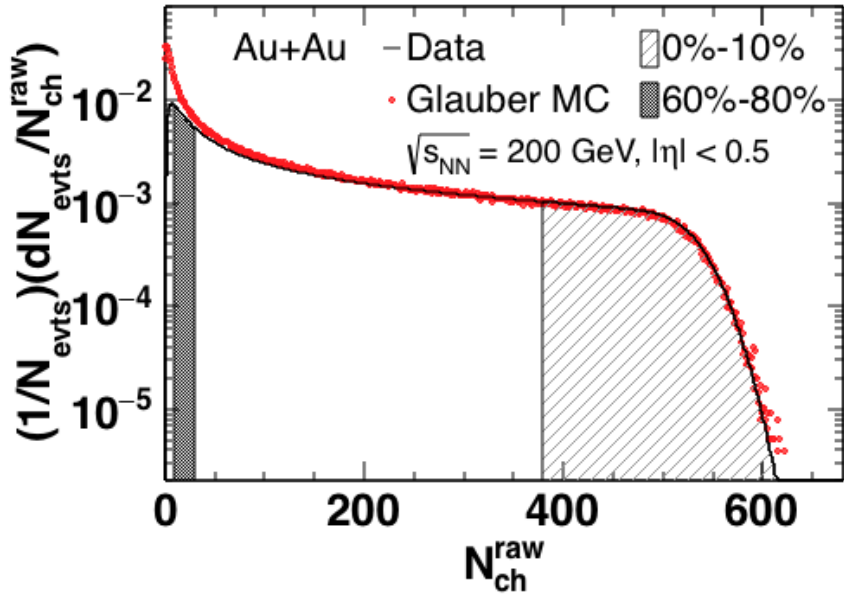


Figure 6.1: Distribution of charged track multiplicity in Au+Au collisions at $\sqrt{s_{\text{NN}}} = 200$ GeV in mid-rapidity region ($|\eta| < 0.5$) recorded by STAR (black histogram) and corresponding Glauber model calculation (red points) [55]. Central and peripheral centrality class regions are shown as filled areas. Figure adopted from [103].

- $|\mu_{\text{run}} - \mu_{\text{day}}| > 3 \cdot \sigma_{\text{day}},$

where μ_{run} is the mean value of refMult or z over a run, μ_{day} is the mean value over a day, and μ_{year} is the mean value over the whole year. σ_{day} is the standard deviation of the μ_{run} values over a day and σ_{year} is the standard deviation of the μ_{run} values over the whole year.

Fig. 6.2 shows the mean values of $\langle \text{refMult} \rangle$ and $\langle z_{\text{vertex}} \rangle$ as a function of run number. Available runs are in blue, while red points correspond to accepted runs. List of all runs which have been removed from the analysis can be found in Appendix B.

Total integrated luminosity of the dataset after all event cuts is $\sim 6\mu\text{b}^{-1}$.

Track selection

In our analysis we use primary (see Sec. 4.2.1 for the definition of primary and global tracks) charged tracks recorded with the STAR TPC. Spatial distribution of these tracks in Run11 is plotted on Fig. 6.3. Fig. 6.4 then shows distributions of the DCA of global tracks and distribution of number of fit points for each track. The tracks with large DCA come from secondary decays and are therefore excluded from the analysis. Also the tracks with a low number of fit points are not suitable candidates for the analysis since these are usually fragments of tracks artificially split by the reconstruction software.

For the jet analysis the following track quality cuts are imposed:

- number of fit points: > 14
- number of fit points/maximum number of possible fit points: > 0.52
- distance of closest approach (DCA) to primary vertex: $< 1 \text{ cm}$
- $0.2 < p_{\text{T}} < 30 \text{ GeV}/c$

The momentum cut on the tracks comes from the fact that the particles with lower momentum will not produce enough reconstruction points in the TPC, while particles with momentum greater than $30 \text{ GeV}/c$ are bent by the magnetic field only minimally, resulting in a significant uncertainty of the momentum calculation.

6.1.1 Tracking efficiency

Not every charged particle track is successfully reconstructed within the STAR TPC. The reconstruction efficiency represents a major detector effect which needs to be taken into account in the analysis of jets. The efficiency depends significantly both on the track momentum and the track multiplicity, increasing with the first, and dropping with the second.

Figure 6.5 shows the estimated single hadron reconstruction efficiency in Au+Au collisions separately for central (0–10%) and peripheral (60–80%) collisions. The momentum dependency of the tracking efficiency was parametrized by a function of the following form

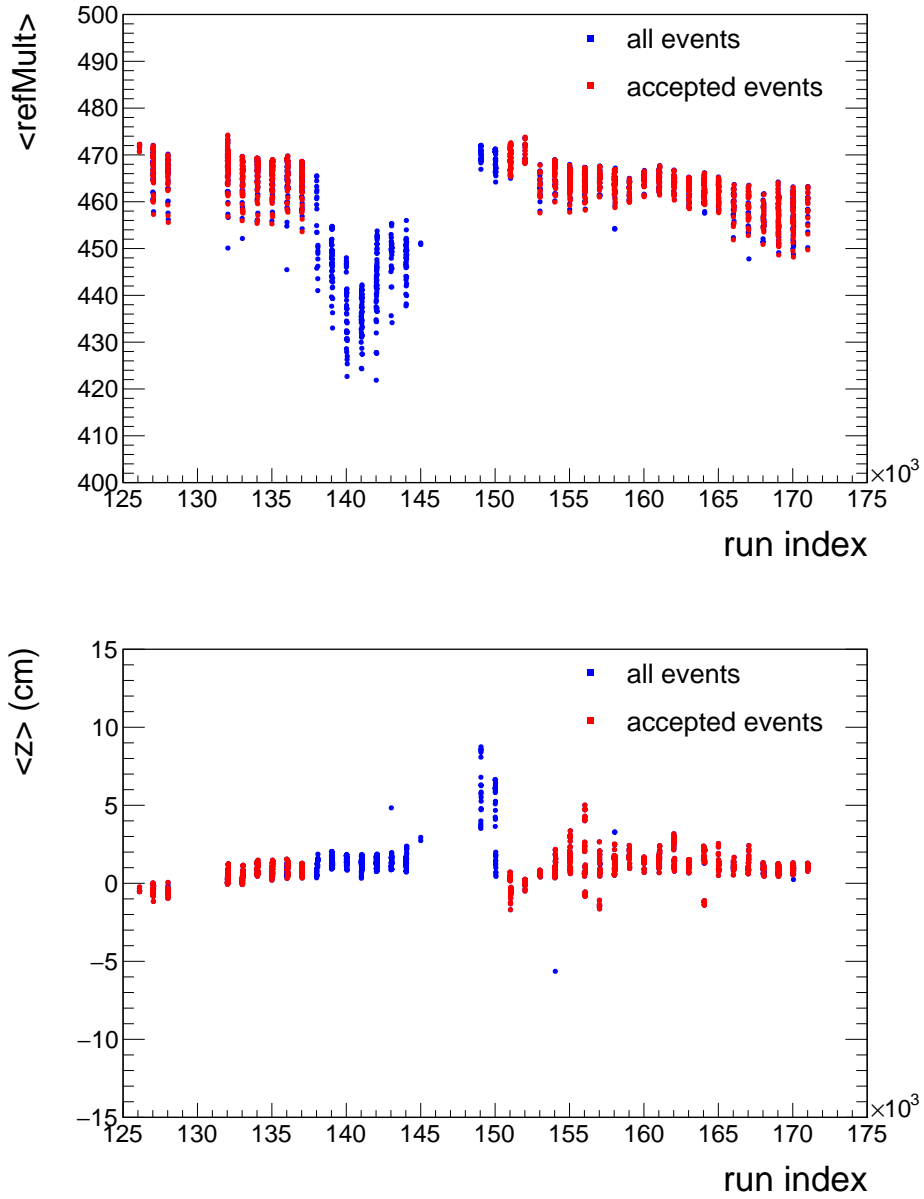


Figure 6.2: Mean value of the reference multiplicity (top) and mean value of the primary vertex z -position (bottom). Blue points mark available runs, red points denote accepted runs.

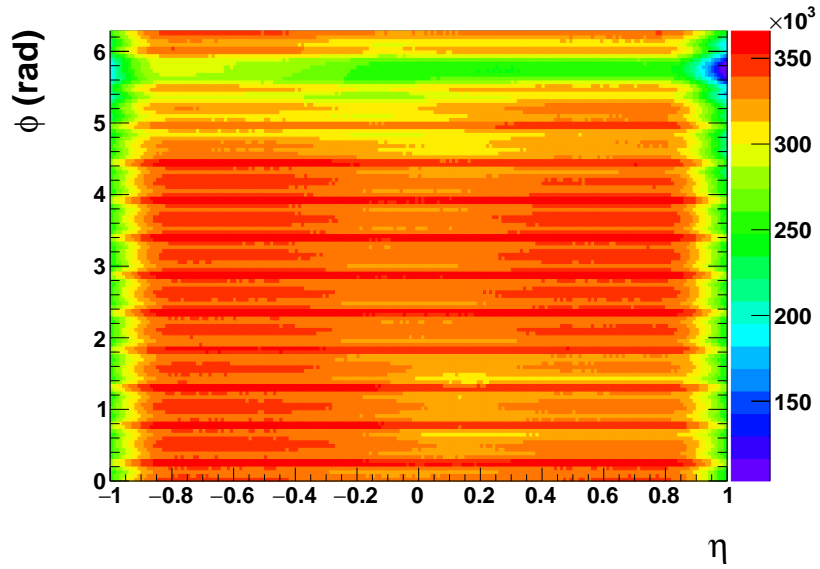


Figure 6.3: $\phi - \eta$ distribution of charged particle primary tracks in the TPC in Run11.

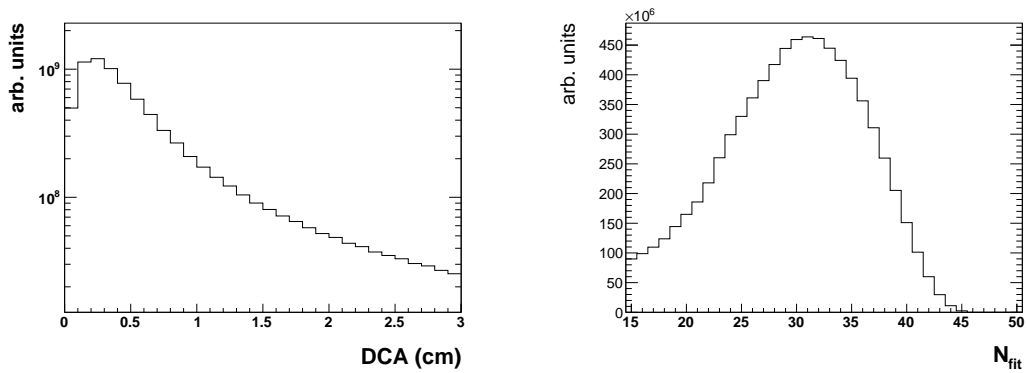


Figure 6.4: Distribution of the global tracks' DCA (left) and distribution of the number of fit points in the TPC (right).

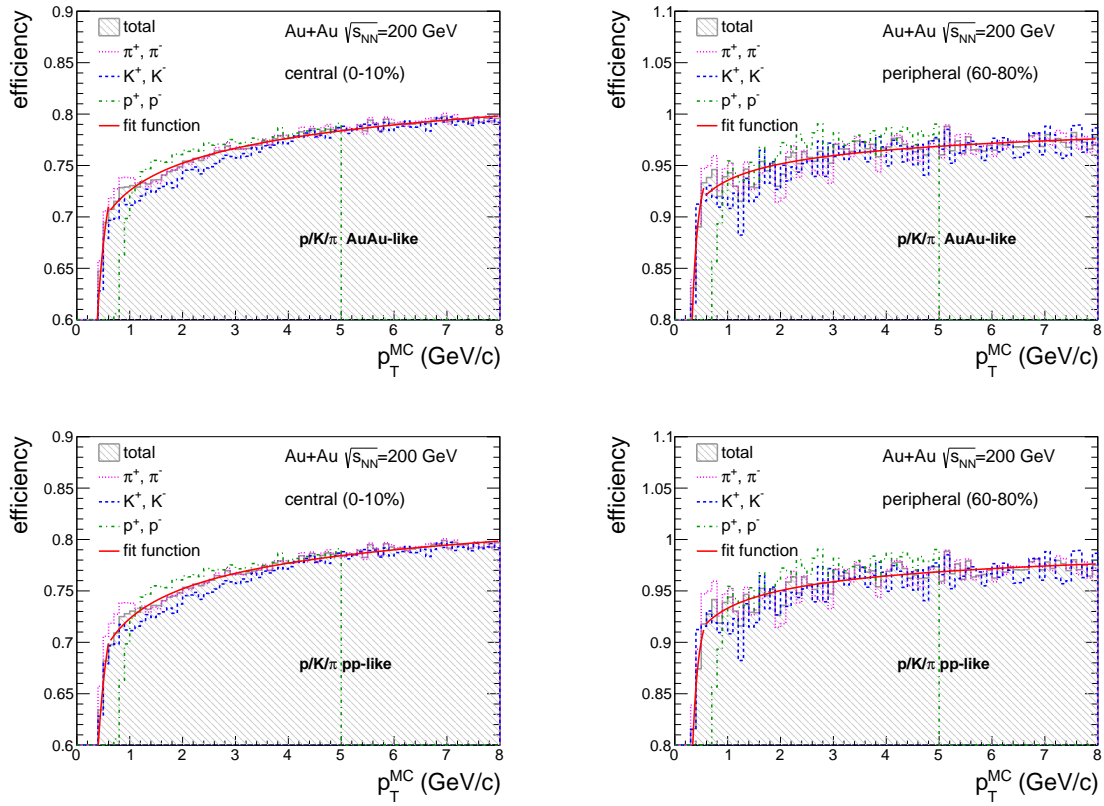


Figure 6.5: Single hadron tracking efficiency for central (left) and peripheral (right) Au+Au collisions. Two different assumptions about proton/kaon/pion ratios were made: Au+Au-like (top) and p+p-like (bottom).

$$\varepsilon(p_T) = A \cdot e^{-\left(\frac{B}{p_T}\right)^C}, \quad (6.1)$$

with free parameters A, B, C .

The efficiency was estimated by embedding simulated tracks of charged pions, kaons and protons (which are by far the most abundant charged hadrons produced in heavy ion collisions) into real events and processing them by the standard reconstruction algorithms. Further on we will refer to this procedure simply as to “embedding”. At STAR the embedding is done centrally by the embedding group and after passing the QA tests the data are made available to the collaboration.

Since the exact hadron content of a jet is unknown, two different assumptions were made about the ratio of the most abundant hadrons: pions, protons and kaons. The first scenario uses ratios of these particles measured in Au+Au collisions [118, 119, 120], while the other uses ratios obtained from measurements in p+p collisions [119, 121]. These ratios are shown on Fig. 6.6. The Au+Au-like ratio is used in the primary analysis, the p+p-like ratio is used for the systematic uncertainty calculation. The resulting difference between the two scenarios is not negligible but it is less than 10%.

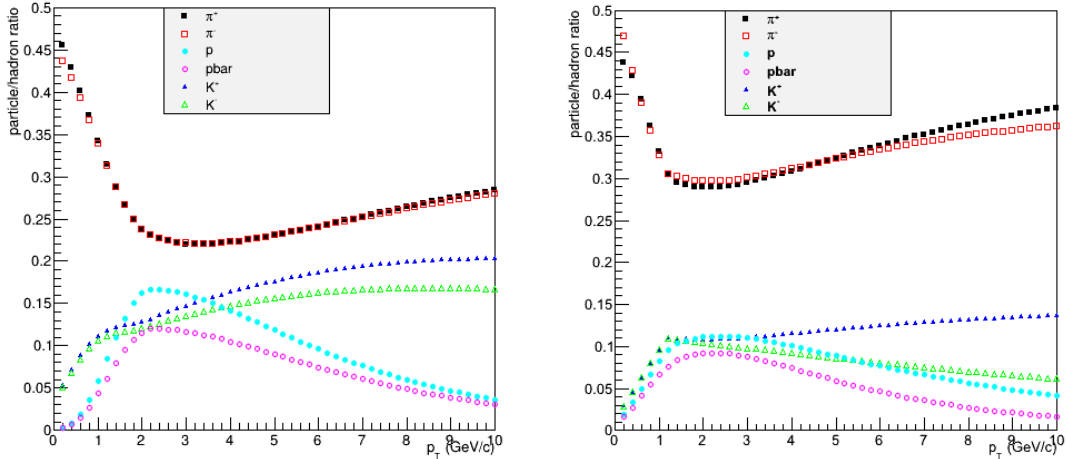


Figure 6.6: Fraction of different hadron species in Au+Au (left) and p+p (right) collisions.

6.1.2 Momentum resolution

The TPC track momentum resolution is not ideal. The measured value of the momentum is (approximately) normally distributed around the true value with a standard deviation σ . The resolution is inversely proportional to the momentum of the detected particle, since the curvature of the track in the magnetic field decreases with the increasing momentum. In the mid-rapidity region the relative resolution can be approximated by a second order

polynomial

$$\sigma \simeq a + b \cdot p_T^{\text{true}} + c \cdot (p_T^{\text{true}})^2, \quad (6.2)$$

where p_T^{true} is the true value of the transverse momentum of the track.

The value of the resolution parameters a, b, c can be obtained, like the tracking efficiency, from the embedding. Momentum resolution for the global tracks is shown on Fig. 6.7 (left). The distributions for each simulated p_T^{MC} are fitted with the Gaussian distribution. By plotting the values of σ as a function of p_T^{MC} and fitting by a polynomial one can obtain the values of a, b, c . If we require for simplicity $a = b = 0$, we get $\sigma \simeq 0.012 \cdot (p_T^{\text{true}})^2$ as we see on Fig. 6.7 (right).

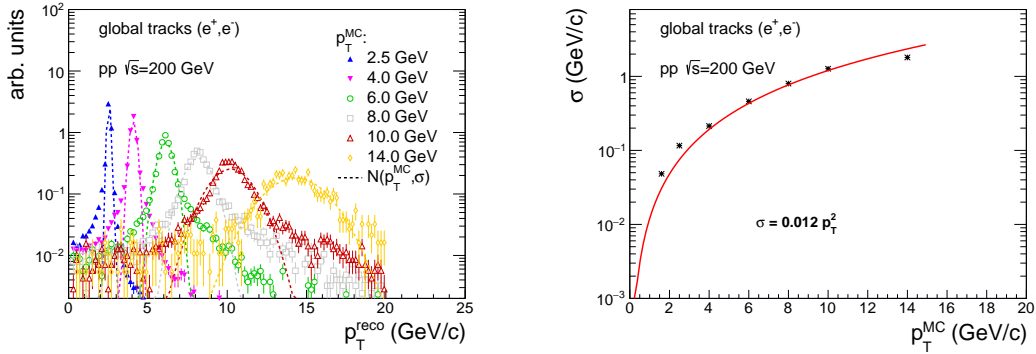


Figure 6.7: Left: Transverse momentum resolution of the embedded global tracks in p+p collisions for several different values of the embedded track momentum p_T^{MC} . Dashed curve is the Gaussian fit with $\mu = p_T^{\text{MC}}$ and σ as a free parameter. See text for details on the embedding procedure. Right: Standard deviation of the momentum resolution of the embedded global tracks in p+p collisions as a function of the embedded track momentum p_T^{MC} . The red line is a 2nd order polynomial fit with $a = b = 0$.

However in case of the primary tracks the resolution is much better, since one additional (very precise) point - the primary vertex - is included in the fit. Corresponding resolution distributions for primary tracks of charged hadrons are shown on Fig. 6.8 (left) and the polynomial fit of the σ p_T^{MC} dependence on Fig. 6.8 (right). These distributions were obtained from Run 12 p+p jet embedding, because the Au+Au hadron embedding has a limited kinematic reach. For the primary tracks the value of σ at a given p_T^{MC} is approximately half the value for global tracks. The obtained polynomial dependence of the standard deviation on transverse momentum

$$\sigma \simeq -0.026 + 0.020 \cdot p_T^{\text{true}} + 0.003 \cdot (p_T^{\text{true}})^2, \quad (6.3)$$

is used as the main momentum resolution parametrization in our analysis.

In order to find out how significant role plays the collision system one can compare the polynomial fit with the accessible values of the momentum resolution obtained from the Au+Au hadron embedding. Such a comparison is made on Fig. 6.9. The blue line

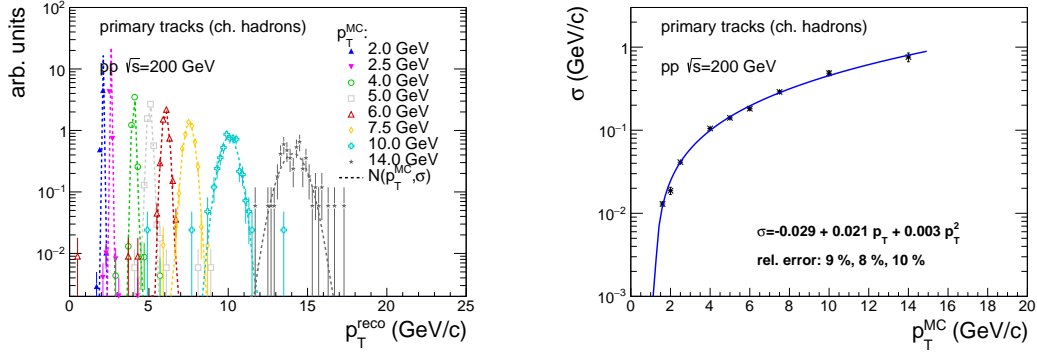


Figure 6.8: Left: Transverse momentum resolution of the embedded primary tracks of charged hadrons in p+p collisions for several different values of the embedded track momentum p_T^{MC} . The dashed curve is the Gaussian fit with $\mu = p_T^{\text{MC}}$ and σ as a free parameter. See text for details on the embedding procedure. Right: Standard deviation of the momentum resolution of the embedded primary tracks in p+p collisions as a function of the embedded track momentum p_T^{MC} . The blue line is a 2nd order polynomial fit.

represents the polynomial fit obtained from p+p embedding, the red line is a fit to the data from Au+Au embedding and the gray line represents $\sigma = 0.003 \cdot p_T^{\text{true}2}$ function used for systematic uncertainty calculation. Clearly most of the standard deviations obtained from Au+Au data lie between these two curves (blue and gray) and this effect is therefore safely covered by the systematic uncertainty.

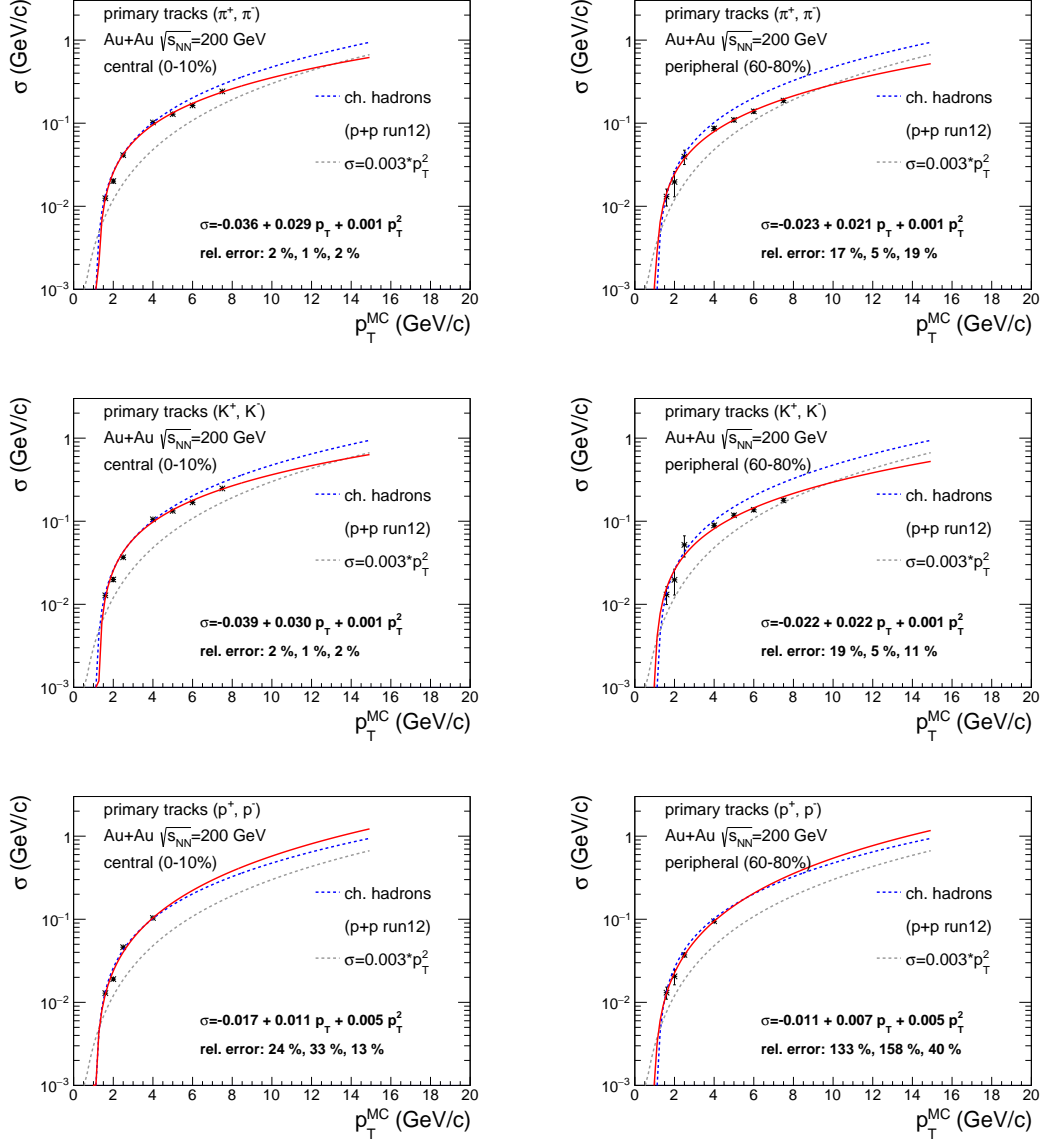


Figure 6.9: Standard deviation of the momentum resolution of the embedded primary tracks in Au+Au collisions as a function of the embedded track momentum p_T^{MC} . The red line is a 2nd order polynomial fit, the blue line represents the polynomial fit obtained from the p+p embedding (which is used as the main parametrization in the analysis), the gray line represents $\sigma = 0.003 \cdot p_T^{\text{true}2}$ function used for the systematic uncertainty study. Several hadron species are examined: pions (top), kaons (middle), (anti)protons (bottom). Left: central Au+Au collisions, right: peripheral Au+Au collisions.

6.2 Jet Reconstruction

Jets were reconstructed from charged tracks with transverse momentum $p_T > 0.2$ GeV/ c recorded with the STAR TPC. Tracks were clustered together using the anti- k_T algorithm incorporated in the FastJet software package, already described in Chapter 3.3. At the end of the process there are several jet candidates in each event constructed. However these are purely artificial objects, which may or may not correspond to the real QCD jets. Such combinatorial jets are suppressed by imposing a cut on the jet area and on the momentum of jet's leading hadron. These techniques are described in a more detail in Sec. 6.3.

6.3 Correction for Underlying Event Background

Since it is not possible to distinguish between “jet particles” and “Underlying Event (UE) particles” on jet-by-jet basis, the reconstructed jets contain additional energy contribution from the UE. This contribution is proportional to the jet size.

There are several ways how to correct for this pedestal energy. We utilize the following event-by-event correction, recommended by FastJet authors [77]. From the reconstructed jet transverse momentum $p_{T,\text{jet}}$ we subtract median jet energy density ρ multiplied by the jet area A

$$p_{T,\text{jet}}^{\text{reco,ch}} = p_{T,\text{jet}}^{\text{raw,ch}} - A \times \rho \quad (6.4)$$

The jet area A is calculated using “ghost” jets - many extremely soft “ghost” jets are added randomly to the analyzed event. Due to the IR safety of the algorithm these jets will not change the outcome of the jet reconstruction. At the end, the number of ghost jets which were included in the i -th jet is proportional to the i -th jet area A_i . This is the method of passive area calculation. Eventually, only one random ghost jet is generated several times and the jet area is then proportional to the number of how many times the ghost jet ended in the i -th jet. That is the method of active area calculation. We implement active area calculation in our analysis.

The median jet energy density ρ is calculated event-wise as

$$\rho = \text{med}\left\{\frac{p_{T,\text{jet}}^i}{A_i}\right\}, \quad (6.5)$$

where index i goes over all jets in a given event. k_T rather than anti- k_T jets are used for the ρ calculation due to a better sensitivity of the k_T jets to the soft particles. For central collisions the two most energetic jets in the event are dropped from the calculation, since these can often be true hard jets, not the background. In peripheral collisions only the most energetic jet is removed from the calculation, since the number of jets in each event is lower than in central collisions.

There is a non-negligible dependence of the shape and the central value of the ρ distribution on R (see Fig. 6.10). In the presented analysis a value of $R = 0.3$ is used for

the background energy density calculation. Other choice would lead to a different reconstructed momentum spectrum, however the effect should be canceled out via the different shapes of the δp_T functions (see Section 6.3.2), making the fully corrected spectrum almost independent on the choice of R . The small difference in the corrected results for different R values used for the ρ calculation is included in the systematic uncertainty.

The presented way of ρ calculation is purely arbitrary and several alternative choices can be made. Therefore not only the radius R of k_T jets but also the number of dropped most energetic jets was varied for the study of systematic uncertainties.

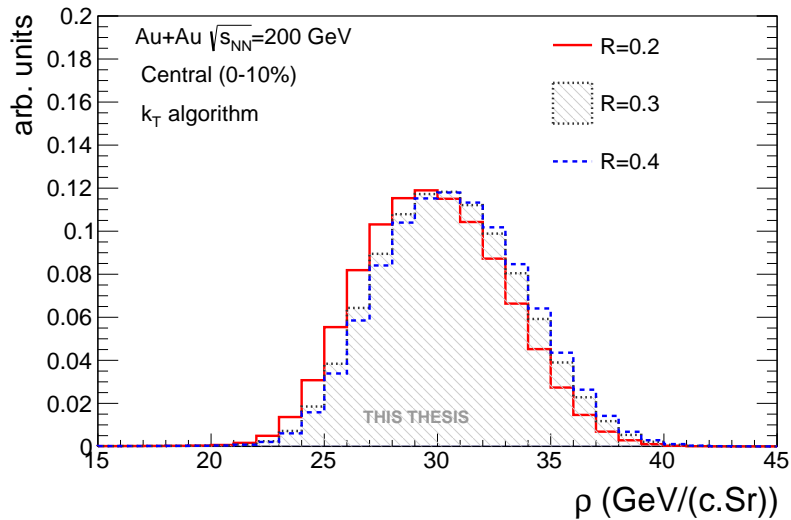


Figure 6.10: Background energy density in 0-10% most central Au+Au events at $\sqrt{s_{NN}} = 200$ GeV calculated using k_T jet reconstruction algorithm and three different jet reconstruction parameters R . A slight dependence on R is apparent.

By looking at the distribution of the corrected jet transverse momentum $p_{T,jet}^{reco,ch}$ one can see that half of the jet population would have negative values, as we can see in Fig. 6.11. This comes from the fact that ρ is the median of the jet energy density. In many jet analyses, this negative part of the jet population was said to be unphysical and discarded. However, this part of the jet population can still contain valuable information about the signal and therefore we will not discard it in this analysis.

For a given value of R the jet size and hence the jet area varies only slightly. Therefore a reasonable cut on the jet area can reduce the combinatorial background significantly. The left panels of Fig. 6.12 show the distribution of the jet area and its dependence on the reconstructed jet momentum. The dashed line represents the cut, which we impose on the jet area in our analysis, namely:

$$R = 0.2: A > 0.07 \text{ Sr}$$

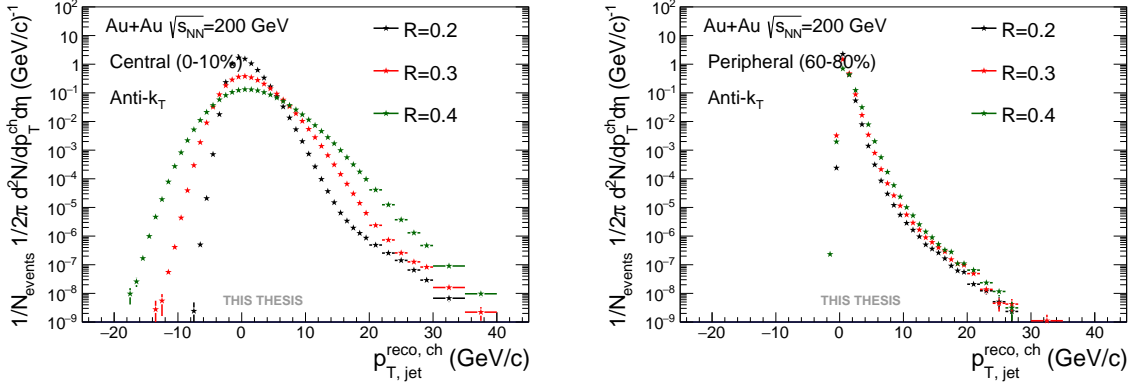


Figure 6.11: Distribution of median background energy-subtracted jet $p_{T,jet}^{reco,ch}$ in most central (left) and peripheral (right) Au+Au collisions at $\sqrt{s_{NN}} = 200$ GeV for various values of the resolution parameter R .

$$R = 0.3: A > 0.2 \text{ Sr}$$

$$R = 0.4: A > 0.4 \text{ Sr}$$

The values of the cuts were determined from the embedding of a simulated (single particle) jet into real events and calculating its area. The right panels of Figure 6.12 show both the area distribution of inclusive jets and that of embedded jets. The embedded jets have normally distributed jet area while the inclusive jet poses a large tail and a secondary peak on the left hand side (LHS), coming from the combinatorial jets.

6.3.1 p_T^{lead} cut

As discussed earlier in Sec. 6.2, the purely combinatorial jets present in the $p_{T,jet}^{reco,ch}$ distribution need to be suppressed. The above mentioned cut on the jet area is a good step, however not a sufficient one. A severe cut on the momentum of jet constituents would be efficient, on the other hand this would impose a serious bias on the jet fragmentation and make the jet quenching studies extremely complicated. A good compromise is to impose a cut on the p_T of jet's leading hadron (p_T^{lead}). This cut reduces significantly the number of soft (combinatorial) jets on one side while, on the other side, still keeps large number of jets containing mainly soft hadrons in the jet population, which are important for jet quenching studies. The trade off is that the reconstruction algorithm is no more 100% collinear safe.

The size of the effect of the p_T^{lead} cut on final results has to be carefully studied. On Fig. 6.13 one can see the effect on the uncorrected spectra. Clearly, the LHS which is dominated by the background is suppressed much strongly than the right hand side (RHS), which is dominated by the signal. However one has to compare the fully corrected spectra with different p_T^{lead} cut values in order to draw any physics conclusions.

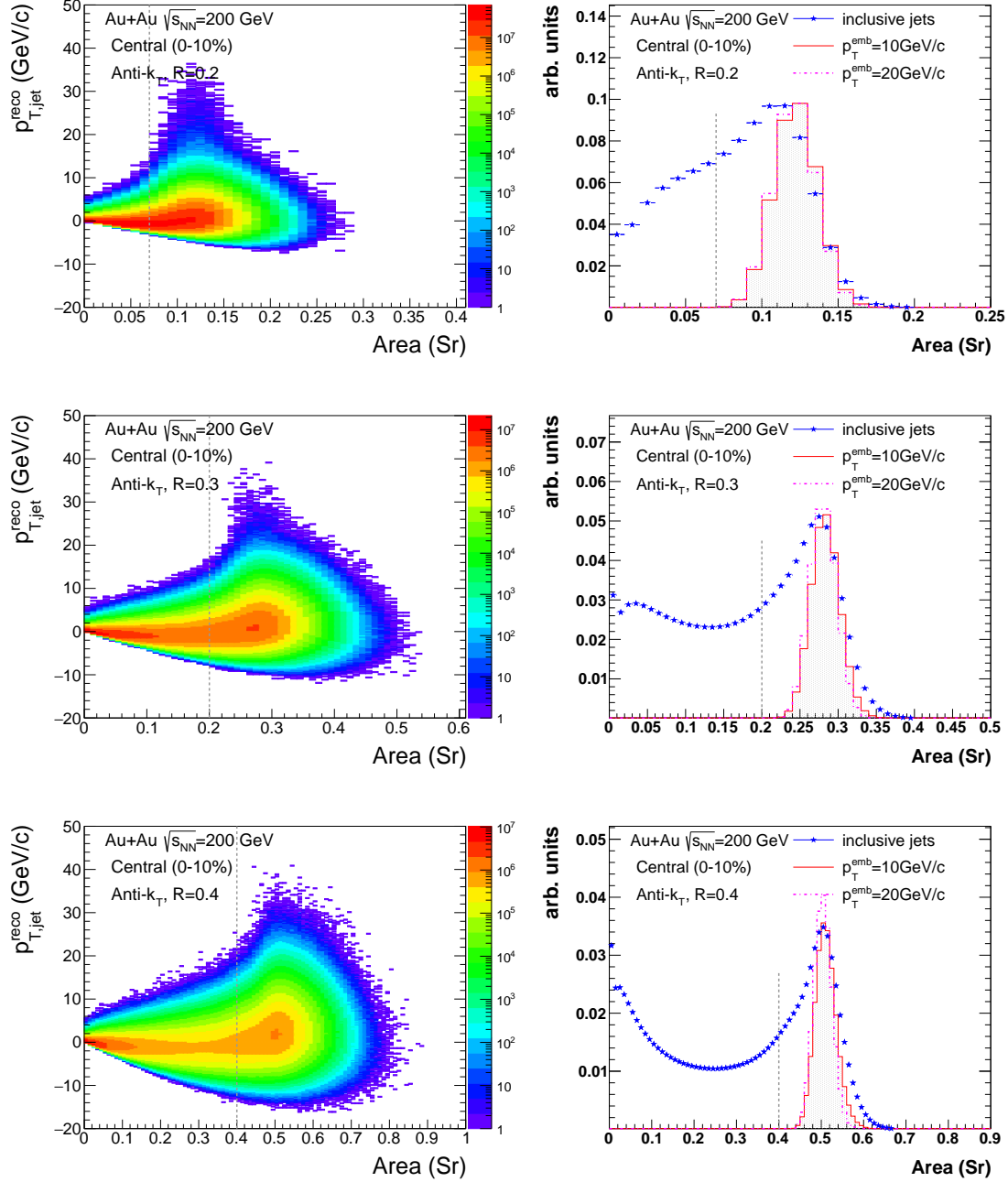


Figure 6.12: Left: Dependence of the jet area on the jet reconstructed momentum. Right: Jet area of inclusive jets (blue stars) and of embedded single particle jets (red and magenta lines). Three different resolution parameters are presented: $R=0.2$ (top), 0.3 (center), 0.4 (bottom). Dashed line marks the value of the cut used to reduce the background.

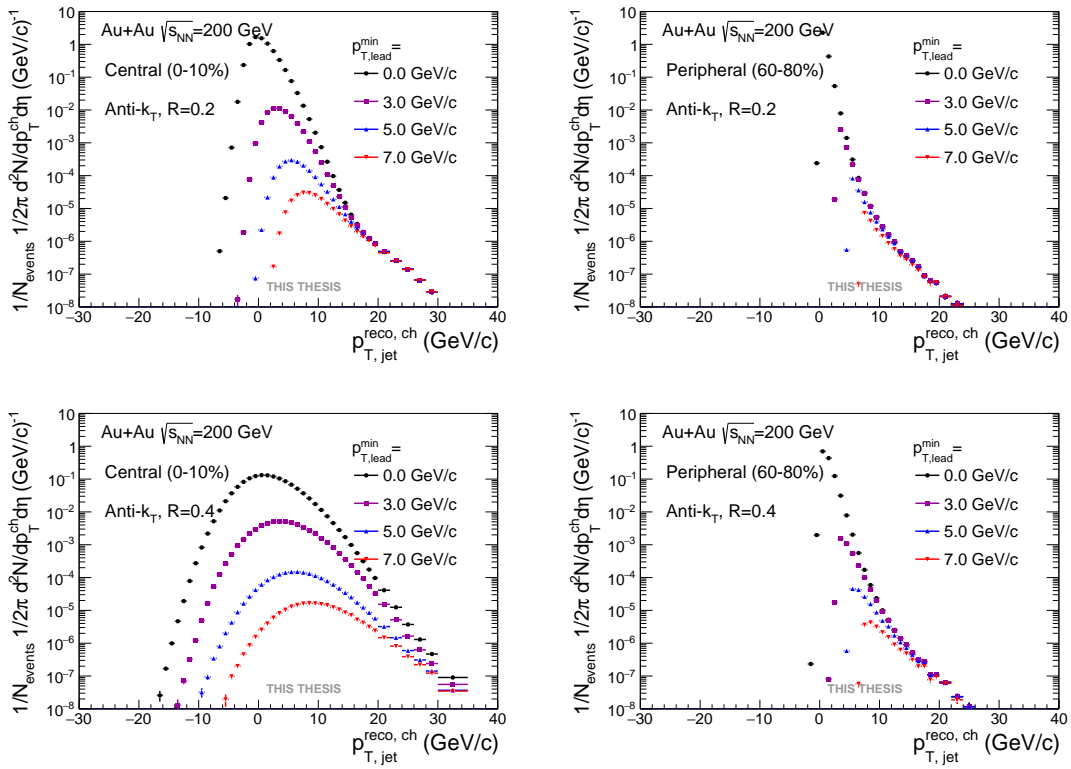


Figure 6.13: p_T spectrum of charged jets (corrected for median background energy density) in central (left) and peripheral (right) Au+Au collisions for several values of p_T^{lead} cut (0-7 GeV/c). Top: $R = 0.2$, bottom: $R = 0.4$.

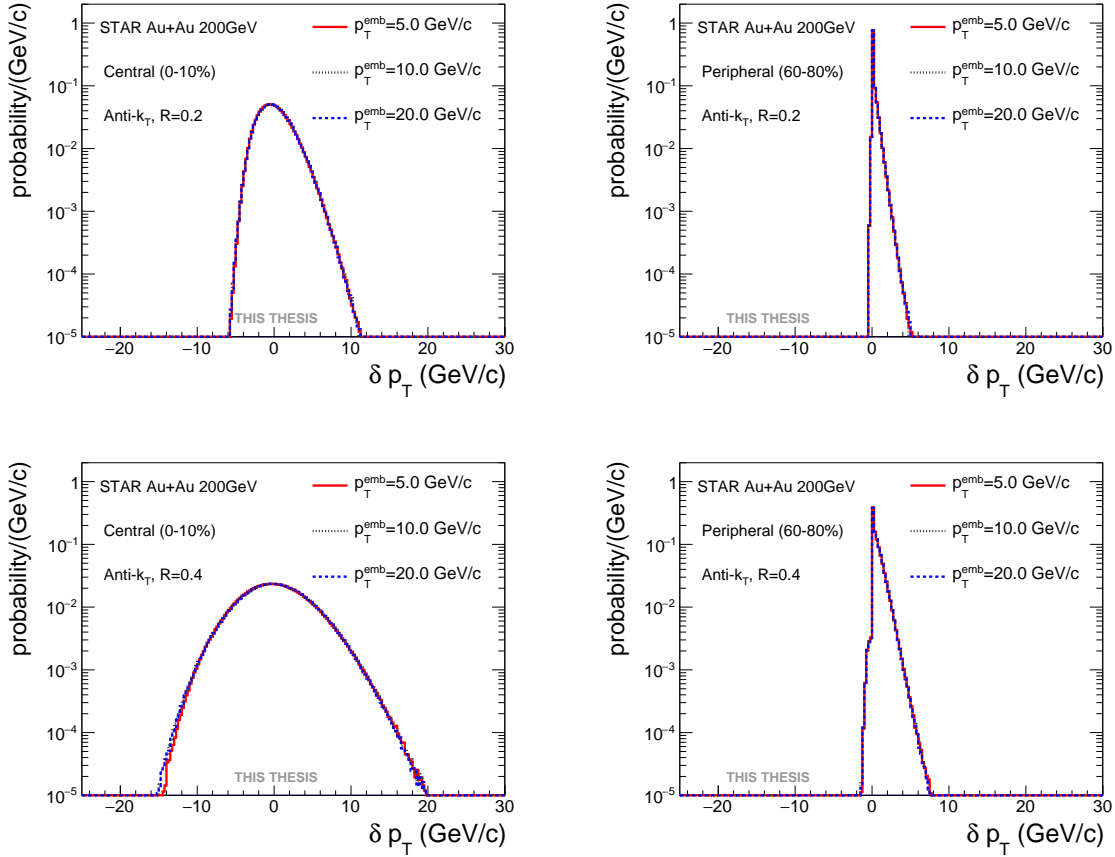


Figure 6.14: δp_T distributions for several values of p_T of the embedded probe (see legend) for jet reconstruction parameter $R = 0.2$ (top) and $R = 0.4$ (bottom) in central (left) and peripheral (right) Au+Au collisions.

6.3.2 δp_T

Subtracting the median jet energy is not a sufficient correction which would fully address the issue of the jet momentum smearing in the presence of the soft background. To find out what is the response of the high multiplicity environment of heavy-ion collision to the presence of a (hard) jet, we embedded a simulated jet into a real event and run the reconstruction algorithm. After the simulated (embedded) jet is matched with the reconstructed one the quantity δp_T which is the difference between the corrected transverse momentum of the reconstructed jet and transverse momentum of the embedded jet is calculated:

$$\delta p_T = p_{T,\text{jet}}^{\text{reco,ch}} - p_{T,\text{jet}}^{\text{emb,ch}} = p_{T,\text{jet}}^{\text{ch}} - A \cdot \rho - p_{T,\text{jet}}^{\text{emb,ch}}. \quad (6.6)$$

The shape of the δp_T distribution is almost independent of the momentum of the embedded probes for $p_{T,\text{jet}}^{\text{emb,ch}} > 5 \text{ GeV}/c$. This is demonstrated on Fig. 6.14 both for

central and peripheral Au+Au collisions.

Observables based on reconstructed jets measure energy flow associated with a high- Q^2 process, independent of the specific distribution of hadrons arising from jet fragmentation. The background response matrix should not therefore depend on the inner structure of the embedded object. In order to check this assumption, both single particle as well as PYTHIA jets are embedded and used for the δp_T calculation. By looking at Fig. 6.15 one can see that the difference between resulting δp_T distributions is small.

High- p_T hadrons can be correlated in azimuth with the Event Plane (EP) orientation. The strength of this correlation is characterized by v_2 , the second-order coefficient of the Fourier expansion of the azimuthal distribution of hadrons relative to the EP [122]. If v_2 is non-zero for $p_T = p_T^{\text{lead}}$, selection of a leading hadron will bias the EP orientation in the accepted event population and correspondingly bias the level of uncorrelated background. This bias can be taken into account in the calculation of the δp_T probability distribution by weighting the event with a weight w related to the relative orientation of the leading hadron and EP orientation $\Delta\phi$ according to

$$w = 1 + v_2 \cdot \cos(2\Delta\phi). \quad (6.7)$$

The v_2 corrected δp_T distribution is also shown on Fig. 6.15 and the resulting bias is small.

In summary, since the effect of the jet shape as well as the bias from the hadron v_2 is small, the uncorrected single particle δp_T distribution is used for the primary analysis, while the other two are used the systematic uncertainty calculation.

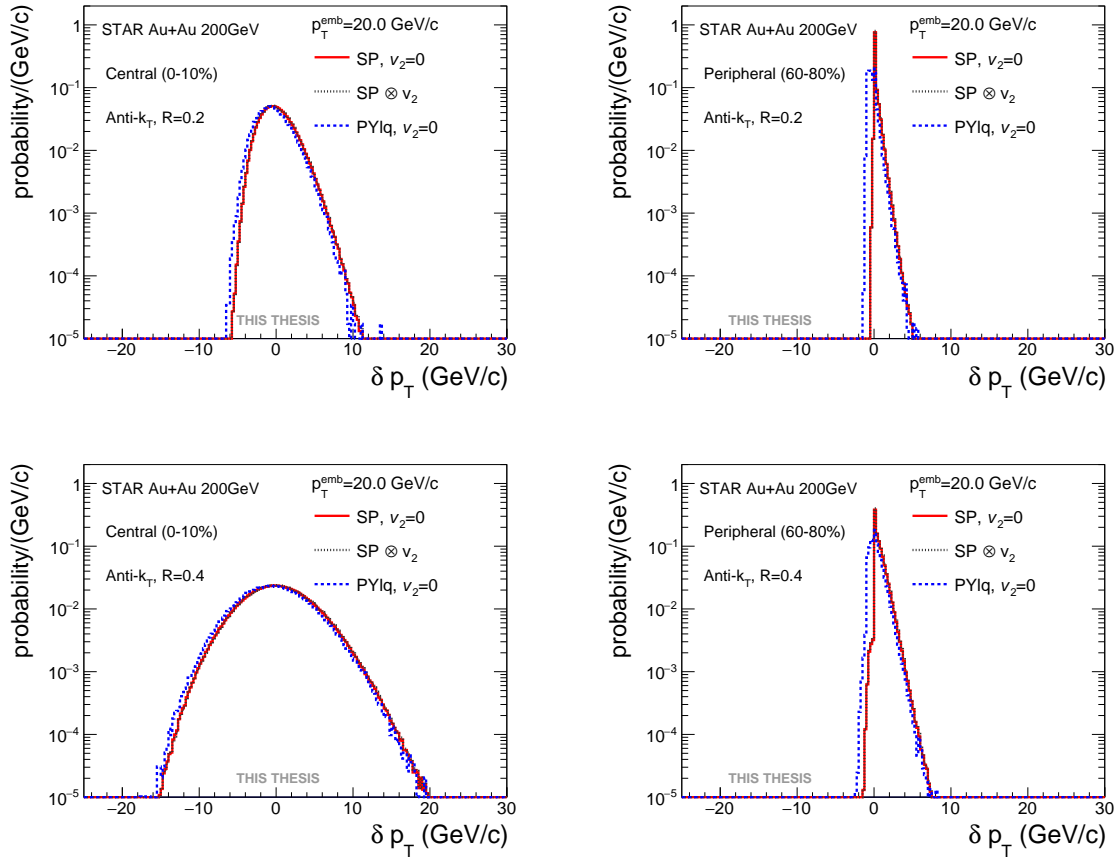


Figure 6.15: Comparison of δp_T distributions measured in central (left) and peripheral (right) Au+Au collisions for different probes: single particle (red), PYTHIA jet (blue) and single particle with v_2 modulation of background density (gray) - see text for details. All probes have the same transverse momentum $p_{T,\text{jet}}^{\text{emb, ch}} = 20$ GeV/c. Jets were reconstructed with $R = 0.2$ (top) and $R = 0.4$ (bottom).

6.4 Correction for Instrumental Effects

Generally, instrumental response, R_{instr} , can be measured utilizing the PYTHIA event generator and GEANT simulations of particle transport and real-time detector conditions. Unfortunately, in our case the full GEANT simulation of the entire detector was not available, therefore we made a parametrization of the key detector performance variables, namely TPC tracking efficiency and TPC momentum resolution. These effects were already studied in detail and described in Sec. 6.1.1 and 6.1.2.

The effect of the imperfect tracking efficiency was simulated in PYTHIA 6 by applying the efficiency cut on every jet constituent - random number $x \in (0, 1)$ is generated and if $x > \epsilon_h$, the track is discarded.

The effect of the finite TPC resolution was simulated in PYTHIA by randomly smearing p_T of each charged track as

$$p_T^{\text{smearred}} = N(\mu, \sigma) = N(p_T, \sigma(p_T)) \quad (6.8)$$

6.4.1 Instrumental Response

Instrumental response matrix $R_{\text{instr}} = \mathbf{R} [p_{T,\text{jet}}^{\text{part}} \rightarrow p_{T,\text{jet}}^{\text{dete}}]$ is obtained by comparing simulated particle-level and detector-level jets. We proceeded in several steps:

- A parton is generated with a uniform p_T from 0 to 100 GeV/ c .
- The parton is fragmented using PYTHIA6 u-quark fragmentation, or gluon fragmentation for systematic uncertainty study.
- 1 million events containing exactly one jet have been generated.
- Particle-level jet population is obtained by running the jet reconstruction algorithm on the charged tracks of the generated PYTHIA jets. The following criteria are then applied: the fiducial cut $|\eta_{\text{jet}}| < 1 - R$, condition on the leading hadron momentum $p_T^{\text{lead}} > p_{T,\text{lead}}^{\text{min}}$.
- Generated events are also propagated through parametrized detector response - simulating the effects of finite TPC reconstruction efficiency and the TPC momentum resolution (Eq. 6.3).
- Detector-level jets are reconstructed by running jet reconstruction algorithm on the propagated PYTHIA jets.
- **Jet Matching:** Corresponding particle- and detector-level jets are then matched together. Matching is done on the geometrical basis: For a given particle-level jet (PLJ1) a detector-level partner is found (DLJ1) which is closest in η - ϕ space. The distance between the two jets is required to satisfy $\sqrt{(\Delta\eta)^2 - (\Delta\phi)^2} < R$. For this

detector-level jet the closest particle-level jet (PLJ2) is found. If this jet corresponds to the original particle-level jet (PLJ1=PLJ2), both jets (PLJ1, DLJ1) are then matched together.

- Detector-level jet population is required to satisfy the same criteria as for real data analysis: $|\eta_{jet}| < 1 - R$, $p_T^{\text{lead}} > p_{T,\text{lead}}^{\text{min}}$, $A > A_{\text{min}}$.
- Particle-level jet population is required to satisfy:
 $|\eta_{jet}| < 1 - R$, $p_T^{\text{lead}} > p_{T,\text{lead}}^{\text{min}}$.
- For each matched jet pair a bin in the instrumental response matrix $R_{\text{instr}} [p_{T,\text{jet}}^{\text{dete}}, p_{T,\text{jet}}^{\text{part}}]$ corresponding to $p_{T,\text{jet}}^{\text{part}}$ and $p_{T,\text{jet}}^{\text{dete}}$ is incremented.
- Each bin of the response matrix is then scaled by $1/n_i^{\text{gen}}$, where n_i^{gen} is the total number of generated particle level jets with momentum falling into the i^{th} bin on y-axis.

6.4.2 Jet Reconstruction Efficiency

When calculating the jet reconstruction efficiency, one should not compare directly detector-level and particle-level distributions bin-by-bin. Due to the detector effects, a jet having $p_{T,\text{jet}}^{\text{part}}$ will be typically detected with $p_{T,\text{jet}}^{\text{dete}} \neq p_{T,\text{jet}}^{\text{part}}$ and thus potentially migrate from i -th p_T bin to j -th. Comparing i -th bin of particle-level spectrum with i -th bin of detector level spectrum is therefore not a good strategy and one has to take into account the fore-mentioned bin migration.

Jet reconstruction efficiency is thus defined with respect to particle-level jets as

$$\epsilon_{\text{jet}}(p_{T,\text{jet}}^{\text{part}}) = \frac{\frac{dN_{\text{jet}}}{dp_{T,\text{jet}}^{\text{dete}}} \otimes \widetilde{\mathbf{R}}^{-1} [p_{T,\text{jet}}^{\text{part}} \rightarrow p_{T,\text{jet}}^{\text{dete}}]}{\frac{dN_{\text{jet}}}{dp_{T,\text{jet}}^{\text{part}}}}, \quad (6.9)$$

where $\frac{dN_{\text{jet}}}{dp_{T,\text{jet}}^{\text{dete}}}$ and $\frac{dN_{\text{jet}}}{dp_{T,\text{jet}}^{\text{part}}}$ are the detector-level and particle-level jet spectra. The expression in the numerator of the Eq. 6.9 is to be understood as unfolded and regularized detector-level spectrum. The jet reconstruction efficiency does not depend on R significantly. The fragmentation model and the tracking efficiency uncertainty ($\pm 5\%$ absolute) change the jet reconstruction efficiency within approx. 5% as can be seen on Fig. 6.16.

6.4.3 Jet Energy Resolution

The jet energy resolution (JER) is the degree of uncertainty to which we can measure the jet momentum due to the detector effects. It is dominated by the TPC tracking efficiency and it exhibits quite significant p_T -dependence. The jet energy resolution is obtained in the same way as the detector response matrix - the same set of matched PYTHIA 6 particle level jets and detector level jets is used for this measurement.

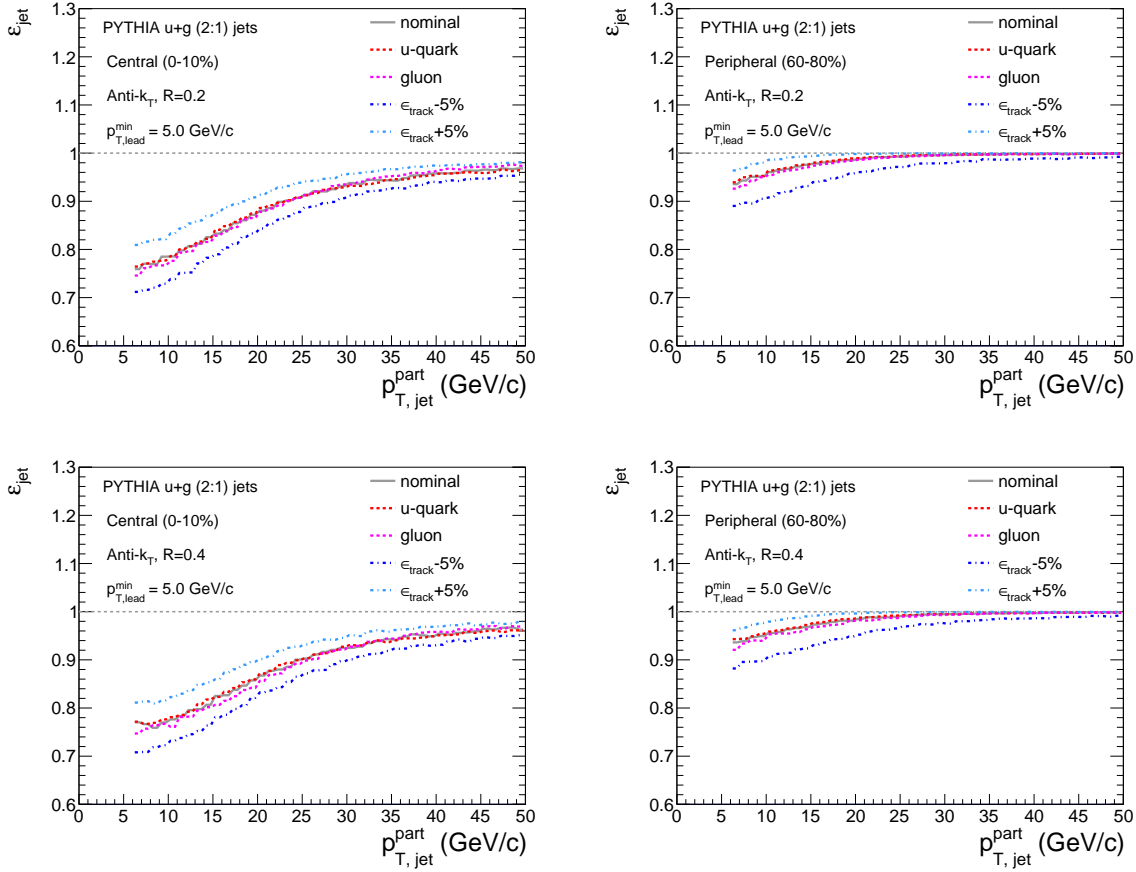


Figure 6.16: Jet reconstruction efficiency as a function of particle level jet momentum $p_{T, \text{jet}}^{\text{part}}$ in the central (left) and peripheral (right) Au+Au collisions for $R = 0.2$ (top) and 0.4 (bottom) calculated from Eq. 6.9 using PYTHIA jets (mixture of u-quark and gluon jets, 2:1). The blue dashed lines correspond to the change in the tracking efficiency $\pm 5\%$ absolute. The red dashed lines correspond to the pure u-quark jets and pure gluon jets, respectively.

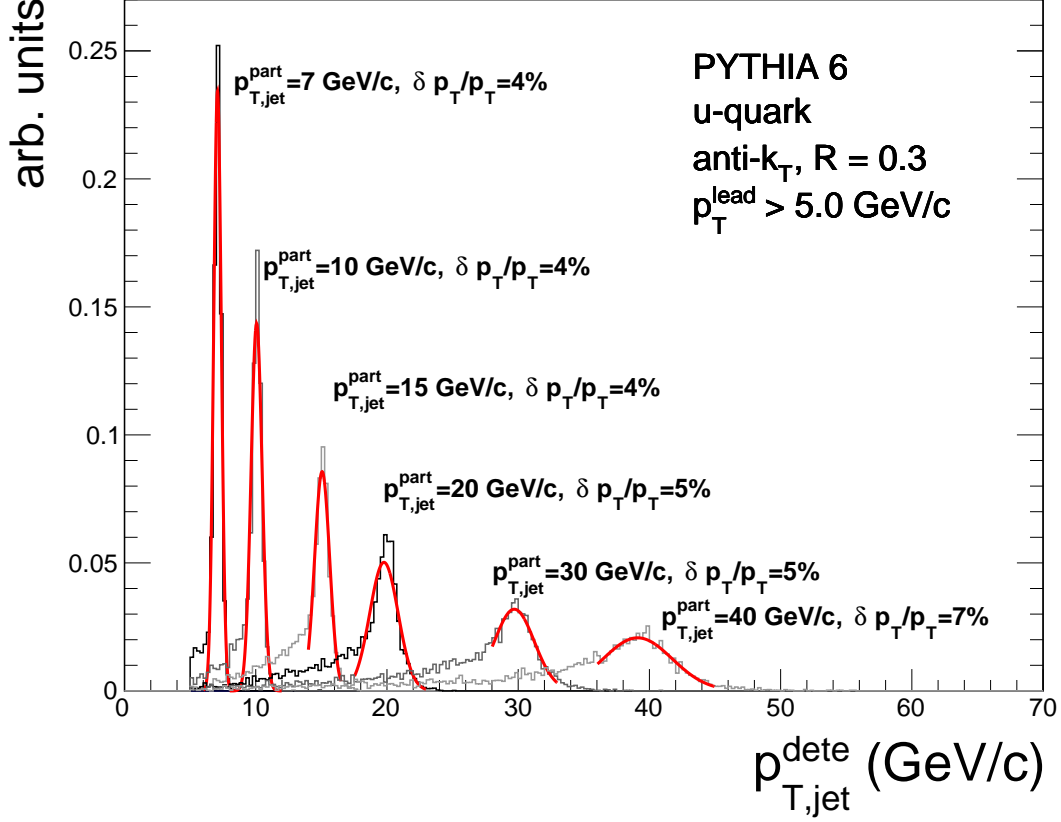


Figure 6.17: Jet energy resolution as a function of particle level jet momentum $p_{T,jet}^{part}$. For u-quark fragmentation model.

JER can be expressed as the width of the $p_{T,jet}^{dete}$ distribution corresponding to a fixed value of $p_{T,jet}^{part}$. Both the $p_{T,jet}^{dete}$ distributions and corresponding Gaussian fits are plotted on Fig. 6.17 for u-quark jets and Fig. 6.18 for gluon jets. The detector conditions used in the simulation correspond to the environment of central Au+Au collisions. The reported JER values are calculated as the ratio of the standard deviation of the Gaussian fit and the $p_{T,jet}^{part}$ value. For jets with $p_{T,jet}^{part}$ up to 30 GeV/c the JER is maximally 5%. It should be noted however that the $p_{T,jet}^{dete}$ distribution is very skewed with a large tail on the LHS.

The presented plots were obtained with the resolution parameter $R=0.3$. The $p_{T,jet}^{dete}$ distributions for different values of R are not presented since the dependence on R is negligible.

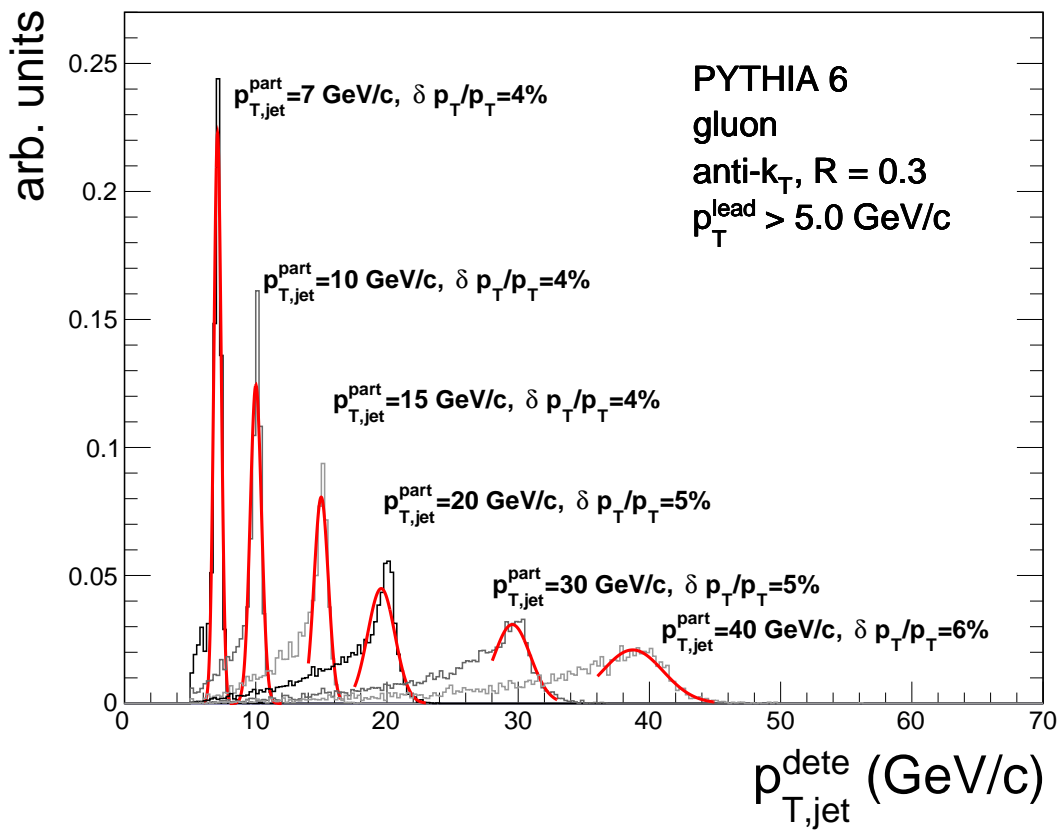


Figure 6.18: Jet energy resolution as a function of particle level jet momentum $p_{T,\text{jet}}^{\text{part}}$. For gluon fragmentation model.

6.5 Unfolding

Every act of a measurement inevitably affects the obtained values of the measured quantities. Detector inefficiency, finite resolution, nonlinear response to a linear change, varying external conditions during the measurements, background noise. These and other effects alter the true value of the studied quantity x^{true} into a measured value x^{meas} .

When conducting a measurement, a smooth distribution such as a jet transverse momentum distribution $p_{\text{T}}^{\text{true}}$ is usually divided into several bins over the measured range and one then measures the counts in each bin. The minimal bin width is given by the detector resolution. If the detector would be an ideal one, the i -th bin $p_{\text{T},i}^{\text{true}}$ would contain e.g. k entries. However, due to the efficiency lower than one and bin-to-bin migration, the i -th bin of the measured histogram $p_{\text{T},i}^{\text{meas}}$ would contain $l+m-n+b$ entries. Here l are correctly measured counts, m are counts which migrated from other bins $p_{\text{T},m1}^{\text{true}}, p_{\text{T},m2}^{\text{true}}, \dots$ into the bin $p_{\text{T},i}^{\text{meas}}$ and n are counts from the bin $p_{\text{T},i}^{\text{true}}$ which ended in bins $p_{\text{T},n1}^{\text{meas}}, p_{\text{T},n2}^{\text{meas}}, \dots$, where $m1, m2, \dots, n1, n2, \dots \neq i$. Due to the inefficiency there is an inequality $l+n < k$. Finally, b are misidentified counts coming from the background noise.

Using the vector notation, we can describe the mentioned process as

$$\mathbf{R} [p_{\text{T}}^{\text{true}}, p_{\text{T}}^{\text{meas}}] \cdot \vec{t} = \vec{m}, \quad (6.10)$$

where \vec{t} represents the true (or simulated) $p_{\text{T}}^{\text{true}}$ distribution and \vec{m} then the measured jet transverse momentum distribution $p_{\text{T}}^{\text{meas}}$. We have introduced the response matrix $\mathbf{R}[p_{\text{T}}^{\text{true}}, p_{\text{T}}^{\text{meas}}]$ which gives the probability to measure the value of $p_{\text{T}}^{\text{meas}}$ for a given “true” transverse momentum $p_{\text{T}}^{\text{true}}$ of a jet. Once the mechanism by which the detector affects the measured quantity is well understood, the response matrix can be easily calculated, e.g. using a Monte Carlo simulation.

Equation 6.10 gives a recipe how to get from the true distribution to the measured one. However it is the opposite problem one needs to solve in the experiment: how to get from measured distribution to the true one. A straightforward way would be to calculate exact inverse of the response matrix \mathbf{R}^{-1} . Unfortunately, the response matrix is often singular, therefore no inverse matrix exists. And if the matrix is not singular, statistical fluctuations would propagate to the inverse matrix, completely destroying the obtained “true” distribution.

Much more convenient way is to utilize some of the well developed unfolding techniques. Many of such techniques have been developed over last few years and can be divided into 3 categories:

- Iterative Bayesian unfolding - a method which uses Bayes’s theorem to calculate the reverse probability $P(p_{\text{T}}^{\text{true}}|p_{\text{T}}^{\text{meas}})$ from the known probability $P(p_{\text{T}}^{\text{meas}}|p_{\text{T}}^{\text{true}})$. The output solution is used as a prior distribution in the next iteration [123].
- Regularized unfolding - a regularization condition (e.g. smoothness of the distribution [124], maximum entropy of the distribution [125]) is applied in order to suppress unphysical oscillating solutions which would otherwise occur due to the large variances of the inverted response matrix coefficients.

- Bin-by-bin correction - in the most simple cases, simple bin-by-bin correction can be applied.

In this analysis the iterative Bayesian unfolding [123] and a regularized unfolding based on the Singular Value Decomposition (SVD) of the response matrix [124] are used and they will be therefore discussed in more detail.

6.5.1 Bayesian Unfolding

The Bayes theorem is used to calculate the probability of a given measurement to be caused by a given event when we know what is the probability (e.g. from simulation) of the given event to cause the given measurement.

Let us denote t_i the i -th bin of the true distribution \vec{t} and m_i the i -th bin of the measured distribution \vec{m} . Let $P(m_i|t_j)$ be the conditional probability of measuring a value in m_i given the true value is in t_j and $P(t_j|m_i)$ probability of measured value m_i being “caused” by t_j . Then the Bayes’s theorem stays

$$P(t_j|m_i) = \frac{P(m_i|t_j) \cdot P_0(t_j)}{\sum_{l=1}^{n_t} P(m_i|t_l) \cdot P_0(t_l)}, \quad (6.11)$$

where $P_0(t_j)$ is a prior probability of the j -th bin of the true distribution \vec{t} having a value of t_j . The denominator plays a role of the normalization constant. Let $n(t_j)$ and $n(m_i)$ be the contents of the bin t_j and m_i respectively. Then the best estimate $\hat{n}(t_j)$ is given by

$$\hat{n}(t_j) = n(m_i) \cdot \frac{P(m_i|t_j) \cdot P_0(t_j)}{\sum_{l=1}^{n_t} P(m_i|t_l) \cdot P_0(t_l)} \quad (6.12)$$

If we denote

$$P(t_j) \equiv \frac{\hat{n}(t_j)}{\hat{N}_{true}} \quad (6.13)$$

with \hat{N}_{true} being the estimate of the total number of entries of the true distribution, it can be shown that $P(t_j)$ lies between $P_0(t_j)$ and the true one. Therefore it seems convenient to proceed iteratively, using $P(t_j)$ instead of $P_0(t_j)$ in each but first iteration. However the number of iterations should be kept as low as possible, otherwise statistical fluctuations can be increased significantly making the unfolded solution wildly oscillating around the true value. There is no general rule what number of iterations to use and in each analysis an appropriate study should be performed.

The probability $P(m_i|t_j)$ is given by the response matrix $\mathbf{R}[p_T^{\text{true}}(j), p_T^{\text{meas}}(i)] \equiv R_{ij}$ which we have already calculated, it only remains to choose an appropriate prior distribution $P_0(t_j)$. It should reflect our initial knowledge about the true distribution. If we lack any information, a flat distribution can be used. In our analysis several steeply falling spectra are used as the prior distributions.

6.5.2 Singular Value Decomposition (SVD) Unfolding

The SVD theorem states that the (generally $m \times n$ dimensional) response matrix \mathbf{R} can be factorized as

$$\mathbf{R} = USV^T, \quad (6.14)$$

where U is a $m \times m$ orthogonal matrix, V is $n \times n$ matrix and S is $m \times n$ diagonal matrix with nonzero diagonal elements:

$$S_{ii} \equiv s_i \geq 0, \quad S_{ij} = 0 \text{ for } i \neq j. \quad (6.15)$$

Now for the measured distribution \vec{m} one wants to solve the system of equations

$$R_{ij}t_j = m_i. \quad (6.16)$$

Using the SVD, we can write

$$USV^T\vec{t} = \vec{m} \quad (6.17)$$

and by multiplying with U^T from right one gets

$$SV^T\vec{t} = U^T\vec{m}. \quad (6.18)$$

Let us denote $z \equiv V^T\vec{t}$ and $d \equiv U^T\vec{m}$. Then

$$s_i \cdot z_i = d_i \quad (6.19)$$

and finally

$$z_i = \frac{d_i}{s_i}. \quad (6.20)$$

Problems arise in cases where s_i values are close to zero (thus enhancing errors on d_i) or in cases where d_i are insignificant, having large error bars. In a procedure, which is described in detail in the original paper by Hoecker and Kartvelishvili [124], a regularization condition which effectively suppresses the insignificant s_i is therefore implemented. To find out an optimal value of the regularization parameter is however not a simple task.

See Sec. 6.5.4 for the discussion on the problem of choosing an optimal regularization parameter value (SVD unfolding) and the number of iterations (Bayesian unfolding).

6.5.3 Prior Distribution

Both the SVD and Bayesian unfolding require a starting jet momentum distribution as close to the real jet momentum distribution as possible however it should be defined prior the knowledge of the data.

Since the real jet momentum distribution (similarly to particle momentum distribution) is steeply falling, several such distributions are used as possible priors for the unfolding. They are shown on Fig. 6.19. They include power-law distributions ($p_T^{-4.5}$, p_T^{-5} , $p_T^{-5.5}$),

Table 6.1: Values of parameters for prior distributions of the form of Tsallis function.

| T [GeV/c] | 0.6 | 0.6 | 0.6 | 0.9 | 0.9 | 0.9 | 1.2 | 1.2 | 1.2 |
|-------------|-----|-----|-----|-----|-----|-----|-----|-----|-----|
| n | 4 | 8 | 12 | 8 | 12 | 16 | 12 | 16 | 20 |

biased PYTHIA distribution (p_T distribution of jets in PYTHIA p+p events with p_T^{lead} cut applied), and 9 different parametrizations of the Tsallis function

$$f(p_T) = p_T \cdot \left(1 + \frac{p_T}{n \cdot T}\right)^{-n}, \quad (6.21)$$

where the free parameters are T and n . All 9 combinations of these parameters which were used are listed in Tab. 6.1.

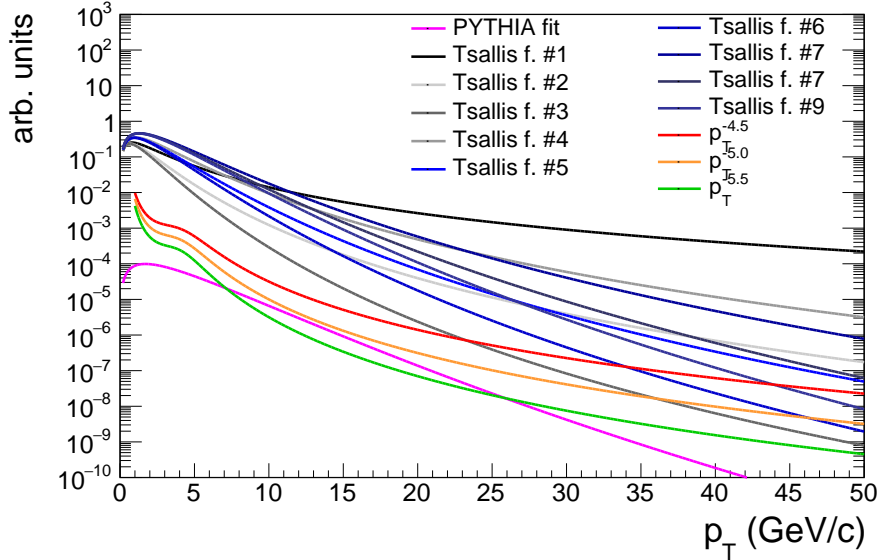


Figure 6.19: Prior distributions used for the unfolding.

6.5.4 Optimal Value of Regularization Parameter

In case of the Bayesian unfolding the optimal iteration is determined from comparison of two successive iterations and by comparison of backfolded (=unfolded distribution smeared by the response matrix) and measured distribution. In an ideal case the measured and backfolded distributions should be identical and also the two successive iterations should be close enough, once the iterative procedure converges.

For the regularization parameter k of the SVD unfolding we also compare the backfolded and measured spectrum. However, instead of comparing two spectra obtained for two successive values of k which could be largely different, we select solutions that are sufficiently “smooth“. This is measured via the curvature as defined in Eq. 6.25.

The similarity of two histograms was calculated using one of the following statistical tests:

1. χ^2 statistics:

$$\chi^2/\text{NDF} = \frac{1}{n} \sum_{i=1}^n \frac{(a_i - b_i)^2}{a_i + b_i}, \quad (6.22)$$

with n being the total number of bins, a_i content of the i -th bin of the first histogram and b_i content of the i -th bin of the second histogram.

2. Average relative distance R :

$$R = \frac{1}{n} \sum_{i=1}^n \frac{|a_i - b_i|}{\min(a_i, b_i)}. \quad (6.23)$$

3. Kolmogorov-Smirnov test:

$$\Delta_{\text{KS}} = \max_j \left| \sum_{i=1}^j \left(\frac{a_i}{I_a} - \frac{b_i}{I_b} \right) \right|, \quad j \in \langle 1, n \rangle, \quad (6.24)$$

where I_a and I_b are the total counts of the first and second histogram.

The curvature C is calculated as

$$C = \frac{1}{n} \sum_{i=2}^{n-1} \frac{((w_{i+1} - w_i) - (w_i - w_{i-1}))^2}{w_i^2}, \quad (6.25)$$

where w_i is the bin content of the i -th bin divided by the width of the i -th bin and n is the total number of bins.

In order to test the effectivity of the statistical tests, we used the Parametrized Model MC (see Chap. 7) and generated 2 samples:

- 1) a hard jet spectrum without detector effects (dataset 1),
- 2) a hard jet spectrum with simulated detector effects and soft background (dataset 2),

The jetfinder is run on both sets and the second set is then corrected via unfolding. As a next step, the distance between the unfolded solution (dataset 2) and the "true" hard spectrum (dataset 1) (True-Reconstructed-Distance, TRD) measured via the fore-mentioned tests is calculated and plotted with respect to the distance between backfolded and measured spectrum (Backfolded-Measured-Distance, BMD) or between successive iterations (Successive-Iterations-Distance, SID), measured via the tests as well. If there is a linear trend, the data points are fitted with a line and a critical value of BMD or SID is found by requiring the corresponding TRD to be lesser than the size of the systematic uncertainties.

As an example, the y-axis of Fig. 6.20 shows the TRD as a function of the BMD, both calculated with the Relative Distance test. Different columns represent different jet R size, different lines correspond to different values of the p_T^{lead} cut. There is a clear linear dependence and the red lines show the linear fit results. The quoted optimal cut values are the values of the BMD corresponding to the TRD = 0.25 ($R = 0.2, 0.3$) and 0.5 ($R = 0.4$).

On the other hand, as can be seen from Fig. 6.23 and Fig. 6.24, the χ^2 and Kolmogorov-Smirnov tests do not represent a good criterion for selecting optimal results since the y value is not a linear function of the x value. Therefore we have decided to use only the relative distance as a metric for measuring the distances between the histograms.

6.5.5 Response Matrix Construction

The response matrix relates the measured jet momentum $p_{T,\text{jet}}^{\text{measured}}$ (at x-axis) with the true (or generated) momentum $p_{T,\text{jet}}^{\text{generated}}$ (at y-axis). The response matrix R_{full} is formed from two separate parts: the background fluctuations response matrix $R_{\delta p_T}$ and the detector effects response matrix R_{instr} which are multiplied.

The $R_{\delta p_T}$ response matrix is constructed from δp_T distributions, which are first normalized to unity and representing thus probability distributions. For any $p_{T,\text{jet}}^{\text{generated}}$ for which we do not have the corresponding δp_T distribution, $R_{\delta p_T}$ is interpolated from the two closest δp_T distributions. The δp_T distributions are placed to the response matrix so their centers ($\delta p_T=0$) lay at the diagonal of the response matrix.

Construction of the R_{instr} response matrix was described in the Section 6.4.1.

Assuming independence of the instrumental effects and background fluctuations, the two matrices are multiplied, leading to the full response matrix:

$$R_{\text{full}} = R_{\delta p_T} \times R_{\text{instr}} \quad (6.26)$$

Examples of all 3 types of the response matrix are presented on Fig. 6.25.

The binning of the response matrix is $\sim 10\times$ finer than the jet energy resolution and the matrix is therefore rebinned to coarser bins. This also improves the performance of the SVD unfolding.

In order to rebin the R_{full} matrix to wider bins correctly and to make it compatible with the ROOUnfold software, the response matrix has to be reweighted:

1. A random value $p_{T,\text{jet}}^{\text{generated}}$ is generated (using a uniform distribution).
2. Corresponding measured value $p_{T,\text{jet}}^{\text{measured}}$ is calculated (using original R_{full} matrix).
3. A weight w is calculated as a probability of obtaining $p_{T,\text{jet}}^{\text{generated}}$ from a prior distribution (e.g. p_T^{-5}), which is used for the unfolding.
4. The response matrix 2D histogram is filled by $(p_{T,\text{jet}}^{\text{measured}}, p_{T,\text{jet}}^{\text{generated}}, w)$ N times, where N is the desired statistics (e.g. 10^9).

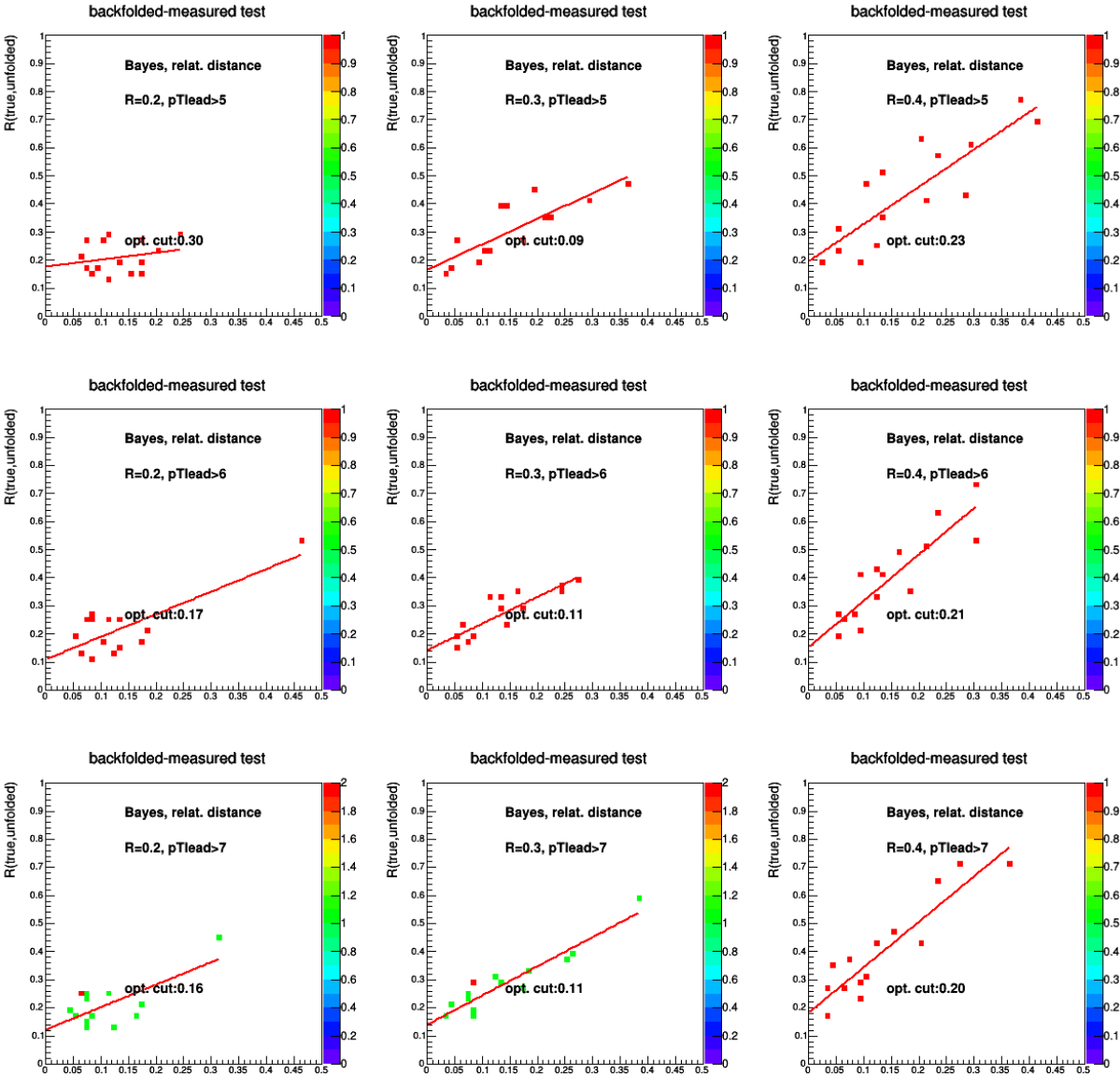


Figure 6.20: Distance between generated and unfolded jet p_T spectrum as a function of the distance between backfolded and measured distribution. Unfolded spectrum was obtained by the Bayesian unfolding. The distance is measured using relative distance metric (see text for details).

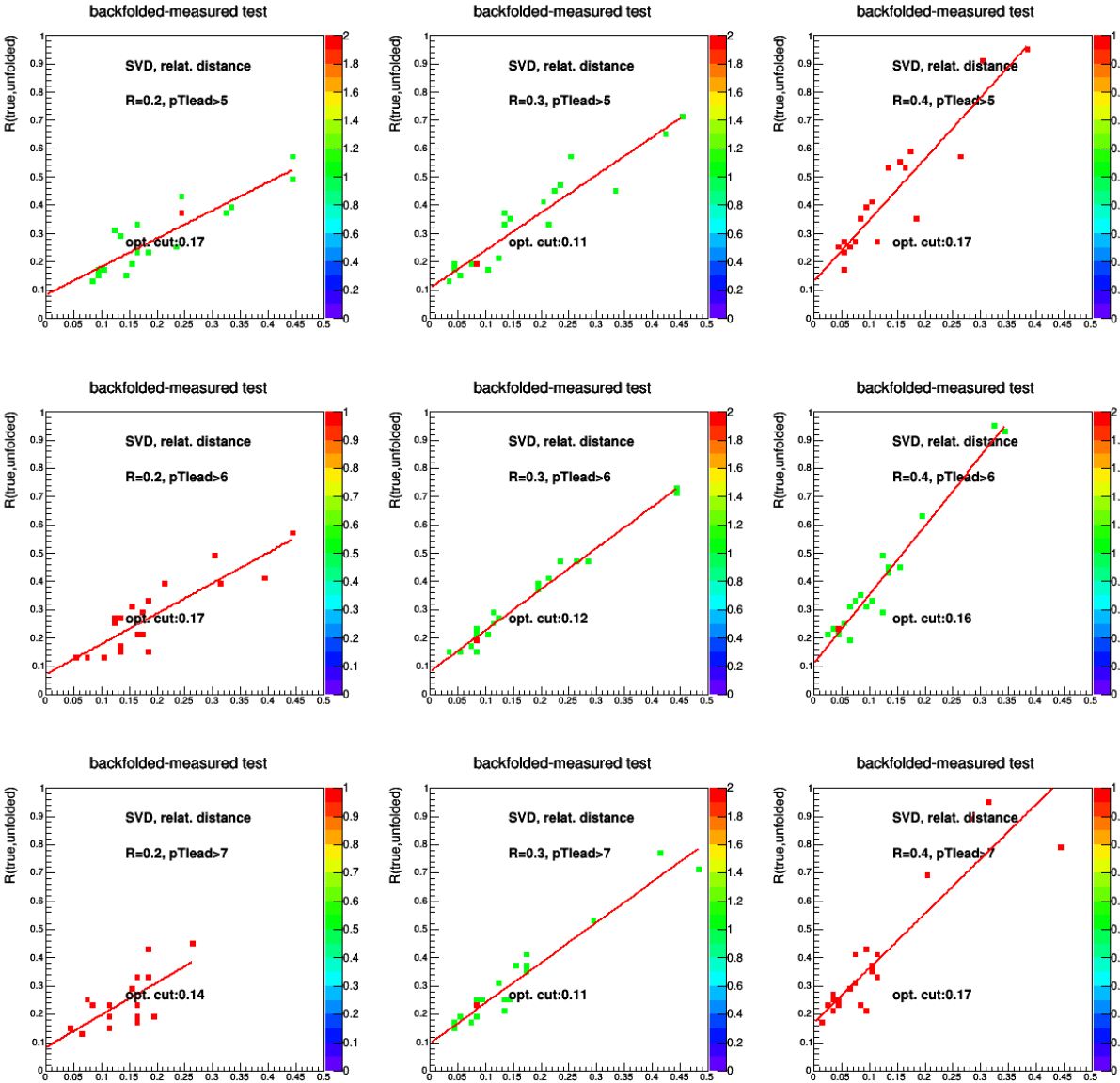


Figure 6.21: Distance between generated and unfolded jet p_T spectrum as a function of the distance between backfolded and measured distribution. Unfolded spectrum was obtained by the SVD unfolding. The distance is measured using relative distance metric (see text for details).

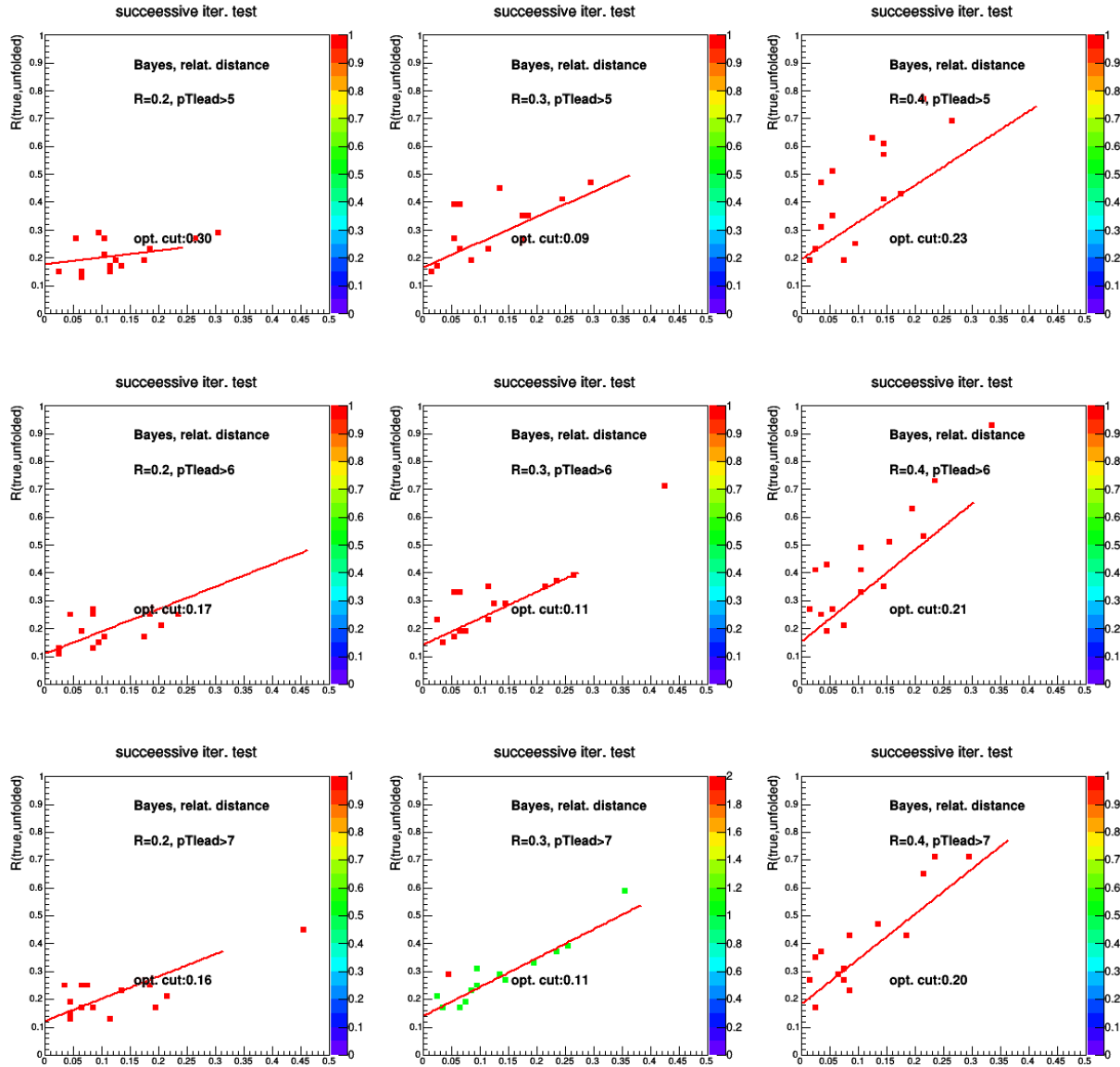


Figure 6.22: Distance between generated and unfolded jet p_T spectrum as a function of the distance between two successive iterations. Unfolded spectrum was obtained by the Bayesian unfolding. The distance is measured using relative distance metric (see text for details).

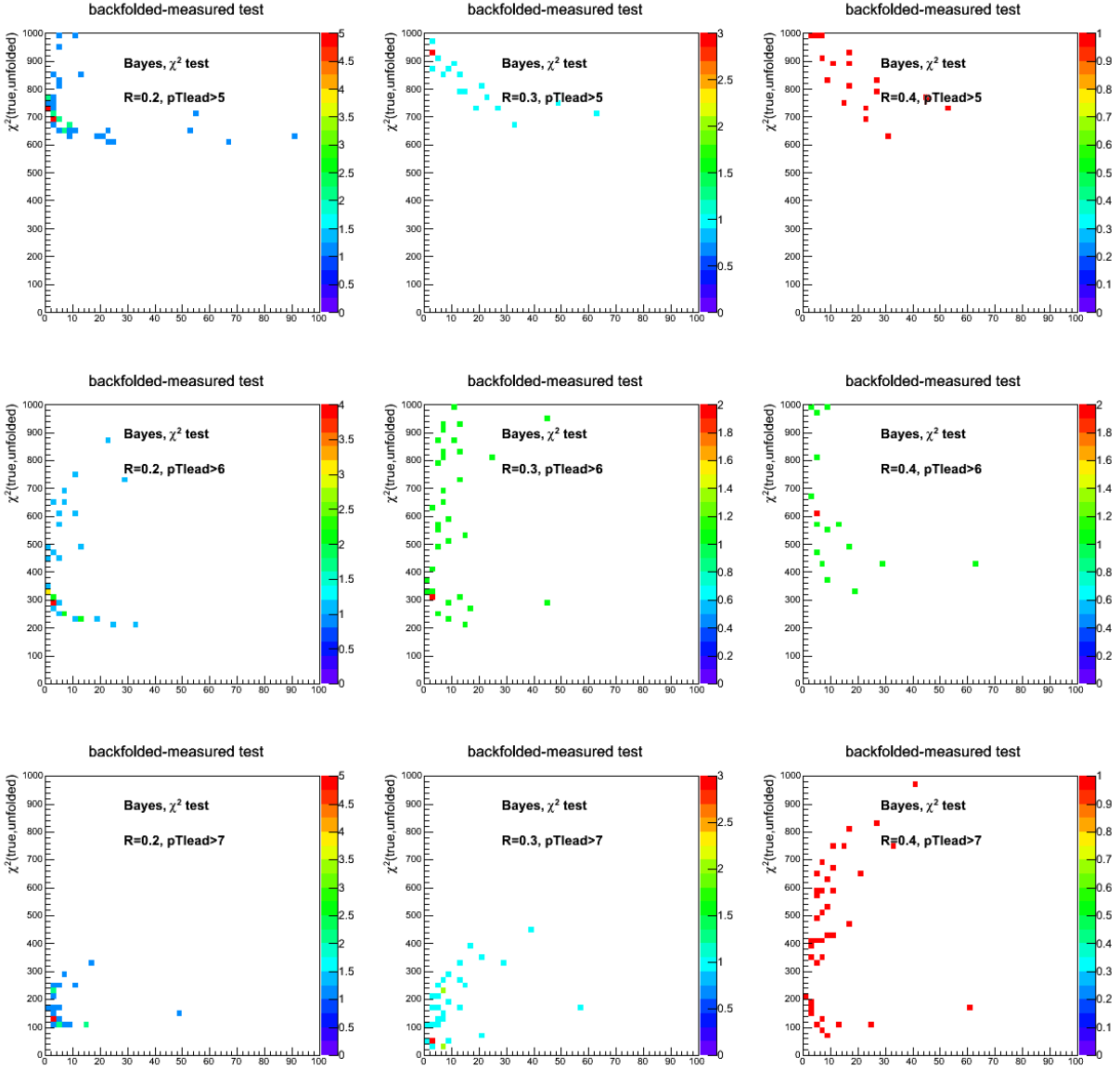


Figure 6.23: Distance between generated and unfolded jet p_T spectrum as a function of the distance between backfolded and measured distribution. Unfolded spectrum was obtained by the Bayesian unfolding. The distance is measured using χ^2 test (see text for details).

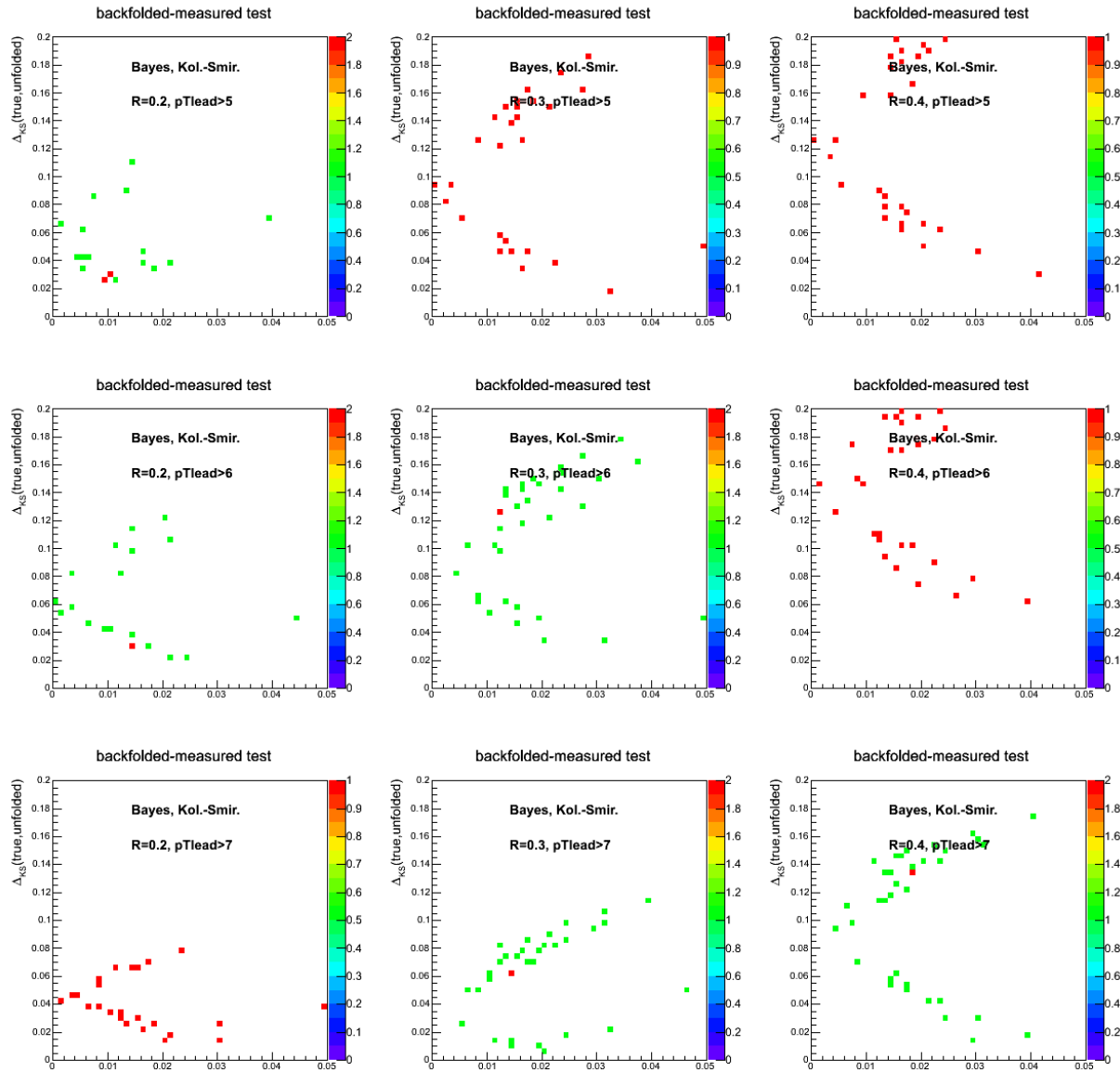


Figure 6.24: Distance between generated and unfolded spectrum as a function of the distance between backfolded and measured distribution. Unfolded spectrum was obtained by Bayesian unfolding. The distance is measured using Kolmogorov-Smirnov test (see text for details).

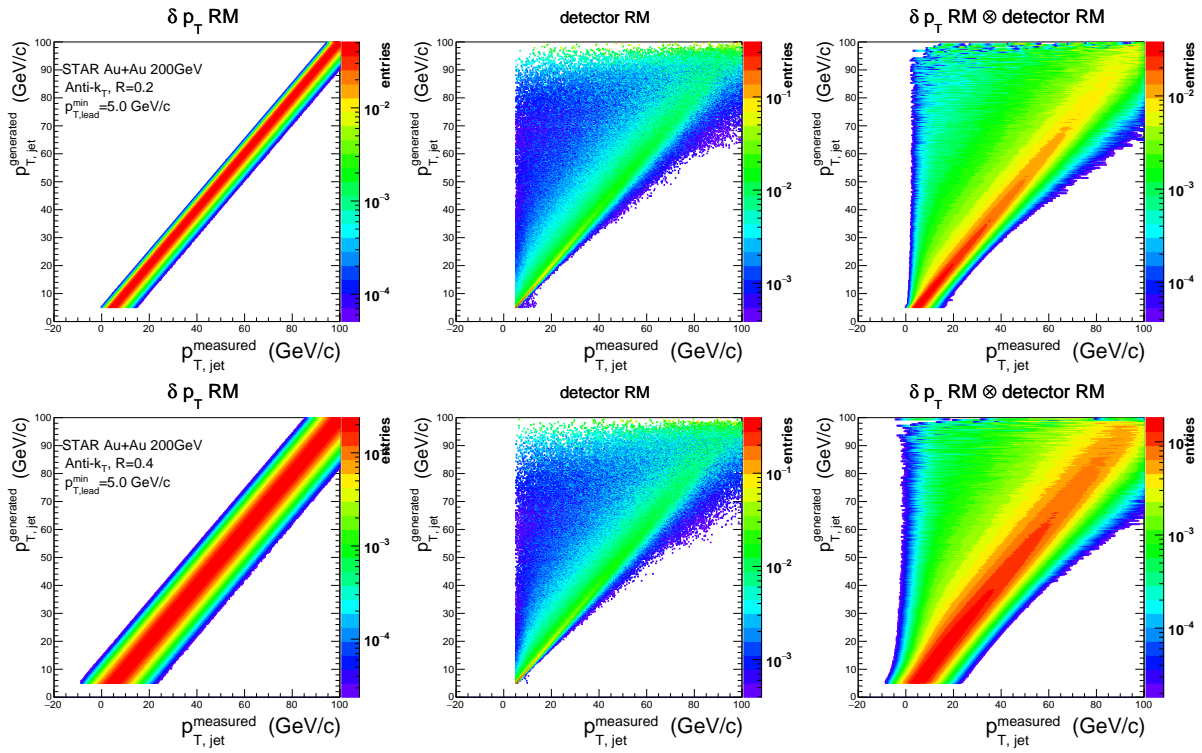


Figure 6.25: Response matrix for charged jets with $p_T^{\text{lead}} > 5 \text{ GeV}/c$. Left: background fluctuations matrix $R_{\delta p_T}$, center: detector response matrix R_{instr} , right: $R_{\text{full}} = R_{\delta p_T} \times R_{\text{instr}}$. Top: $R = 0.2$, bottom $R = 0.4$.

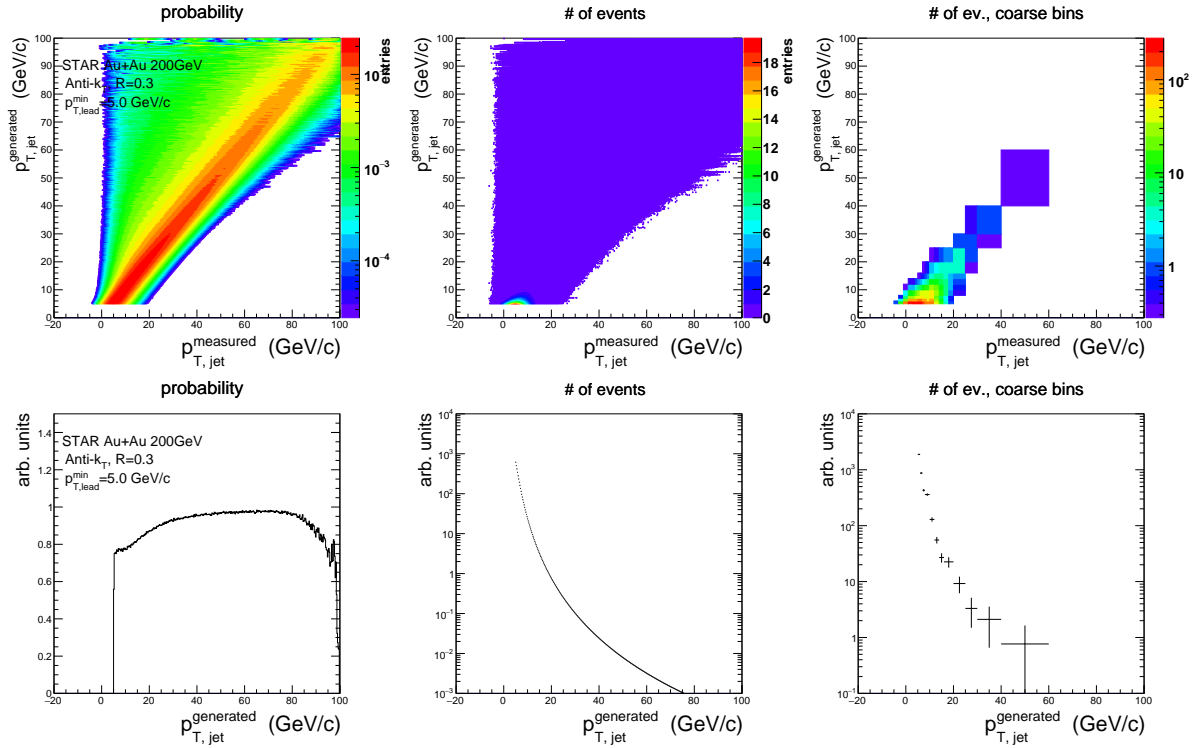


Figure 6.26: Top: Different normalizations of response matrix. Left: $p_{T,\text{jet}}^{\text{generated}}$ distribution corresponds to reconstruction efficiency, center: $p_{T,\text{jet}}^{\text{generated}}$ distribution corresponds to prior distribution, right: $p_{T,\text{jet}}^{\text{generated}}$ distribution corresponds to prior distribution, coarser binning. Bottom: Projection of the response matrix on the y-axis (for charged jets with $p_{T}^{\text{lead}} > 5$ GeV/c).

The reweighted and rebinned response matrix is the final response matrix R_{unf} used for the unfolding. Fig. 6.26 presents the response matrix prior reweighting (left), reweighted matrix (center), and also the reweighted and rebinned matrix (right). The bottom panel then shows the projections onto the Y-axis in order to better illustrate the normalization of the $p_{T,\text{jet}}^{\text{generated}}$ spectrum.

6.6 Systematic Uncertainties

We distinguish two categories of the systematic uncertainties - correlated uncertainties which do not change the shape of the spectrum and correlated (shape) uncertainties, which can change the shape of the spectrum. Both sources of the systematic uncertainties will be reported separately. However for the jet energy scale calculation we use an overall systematic uncertainty which is obtained by summing up both types of uncertainties in quadrature.

6.6.1 Shape Uncertainties

The results of the unfolding process can vary with the change of the input settings. However the physical result should not depend on our arbitrary choice of the unfolding method, the prior distribution, or the regularization parameter value. These uncertainties may be highly anti-correlated over the bins, resulting in the overall uncertainty on the shape of the spectrum.

Two unfolding methods are used in this thesis - the Bayesian and the SVD unfolding (see Section 6.5 for the description of these methods).

As discussed in Sec. 6.5.3, the prior distributions include 13 different steeply falling functions. Using each of them may lead to a slightly different result. This difference has to be included in the systematic uncertainty.

The regularization parameter is represented by the number of iterations i in case of the Bayesian unfolding. For the SVD unfolding, the regularization parameter k is an integer which determines what terms of the SVD decomposition will be dropped.

A set of results was obtained for different combinations of unfolding method, prior choice, regularization parameter (optimal value, optimal value +1). This gives us a set of 2x2x13 possible results, but only those solutions which satisfy quality criteria on difference between backfolded and measured distribution and on difference between successive iterations (Bayes method) are used. These quality criteria cuts are the same as the ones used to determine the optimal regularization parameter value (see Section 6.5.4 for details).

The baseline measurement is obtained as the average value from all accepted solutions. However, all the results should be equally valid. The uncertainty was therefore calculated by subtracting the results from the average and by summing the differences in quadrature and dividing by the square root of their count.

Table 6.2: Comparison of different sources of systematic uncertainties in central (0-10%) and peripheral (60-80%) Au+Au collisions. The uncertainties are relative, reported in percentiles. The uncertainties are reported for two values of the jet resolution parameter R and for two different p_T bins and for the selection $p_T^{\text{lead}} > 5.0$ GeV/ c . For asymmetric uncertainties only the maximal value is reported.

| 0-10% centrality class | | | | |
|-----------------------------------|-----------|-----------|-----------|-----------|
| Resolution parameter | $R = 0.2$ | | $R = 0.4$ | |
| $p_{T,\text{jet}}$ [GeV/ c] | 14 – 16 | 20 – 25 | 14 – 16 | 20 – 25 |
| tracking [%] | 15 | 28 | 16 | 19 |
| δp_T shape [%] | 13 | 15 | 5 | 21 |
| inner jet structure [%] | 9 | 7 | 5 | 10 |
| ρ calculation [%] | 4 | 4 | 6 | 4 |
| total correlated error [%] | 18 | 32 | 22 | 24 |
| unfolding [%] | 9 | 15 | 34 | 32 |
| total shape error [%] | 9 | 15 | 34 | 32 |
| 60-80% centrality class | | | | |
| Resolution parameter | $R = 0.2$ | | $R = 0.4$ | |
| $p_{T,\text{jet}}$ [GeV/ c] | 14 – 16 | 20 – 25 | 14 – 16 | 20 – 25 |
| tracking [%] | 10 | 19 | 11 | 20 |
| δp_T shape [%] | 10 | 13 | 7 | 10 |
| inner jet structure [%] | 5 | 9 | 3 | 10 |
| ρ calculation [%] | 7 | 13 | 6 | 9 |
| total correlated error [%] | 17 | 36 | 15 | 30 |
| unfolding [%] | 5 | 11 | 3 | 5 |
| total shape error [%] | 5 | 11 | 3 | 5 |

6.6.2 Correlated Uncertainties

Separately from the shape uncertainties we investigate another class of uncertainties - those which are correlated between the p_T bins and therefore do not change the shape of the spectra. Uncertainties belonging to this class come from several sources:

1. The main source of the correlated systematic uncertainty is the TPC tracking efficiency uncertainty. In order to evaluate its effect, we have varied the tracking efficiency $\pm 5\%$ (absolute). We have then repeated the whole analysis chain with these modified values of the tracking efficiency. The results were compared with the original result and the systematic uncertainty was then calculated as the difference between those results.
2. Track selection cuts may significantly affect the population of tracks taken as the input for the jet reconstruction. This effect should be however partially canceled out by the corresponding change of the tracking efficiency. For the purpose of the

systematic uncertainty calculation the number of required fitted points in the TPC was varied from 15 to 20.

3. Another source of uncertainty comes from the jet fragmentation model used for the instrumental response matrix calculation. Three different fragmentation models were therefore used for the calculation:

- (a) PYTHIA u-quark fragmentation and gluon fragmentation in 2:1 ratio,
- (b) PYTHIA u-quark fragmentation,
- (c) PYTHIA gluon fragmentation .

The result obtained for the sample containing the mixture of u-quark and gluon jets was used as a baseline, while the results using the pure u-quark jets or pure gluon jets were used to determine the systematic uncertainty.

4. For the hadron efficiency calculation we assumed the ratio of kaons, protons and pions within a jet to be the same as in Au+Au collisions. As an alternative we assumed the ratio to be the same as in p+p collisions. The resulting difference between the final results was added to the systematic uncertainty.

5. δp_T distribution could be biased by the position of the event plane due to the presence of elliptical flow. As a crosscheck a v_2 -corrected δp_T distribution is therefore used for the background fluctuations response matrix calculation, whereas the uncorrected δp_T distribution is used in the main analysis. The difference represents the systematic uncertainty.

6. The primary analysis utilizes single particle “fragmentation” to calculate δp_T . For systematic variation, the δp_T distributions were calculated utilizing PYTHIA-generated fragmentation for light-quark jets.

Obtained variations were assumed to be independent and were therefore added in quadrature in order to obtain the overall correlated uncertainty.

Example values of contributions from different sources to the overall values of correlated and shape uncertainties are presented in Tab. 6.2 for central and peripheral Au+Au collisions, two resolution parameters ($R = 0.2$ and 0.4) and in two different p_T bins. For better clarity the uncertainties from sources 1. and 2. are reported together as “tracking uncertainty”, uncertainties from sources 3. and 4. are reported under the label “jet inner structure” and uncertainties from class 5. and 6. are reported together as “ δp_T uncertainty”.

For the R_{AA} and R_{CP} measurements one additional systematic uncertainty needs to be taken into account. The p+p charged jet cross-section from PYTHIA for the R_{AA} calculation is scaled by the nuclear overlap function T_{AA} and the peripheral yield is scaled by the ratio of mean number of binary collisions in central and peripheral collisions. The related uncertainty on T_{AA} or $\langle N_{bin} \rangle$ has therefore to be taken into account. Both the T_{AA}

and the $\langle N_{\text{bin}} \rangle$ are calculate from the Glauber model Monte Carlo [55]. The values of the T_{AA} and $\langle N_{\text{bin}} \rangle$ were varied within their respective errors and the obtained results were compared to the original result. The difference was reported as a systematic uncertainty and visualized as a red box on the $y = 1$ line on Figures 9.5 - 9.8.

6.6.3 Jet Energy Scale Uncertainty

Since the shape of the jet momentum distribution is approximately exponential, a vertical shift of the distribution up and down within the uncertainties is equivalent to a horizontal shift right or left, respectively. Such uncertainty on the jet momentum is called the jet energy scale (JES) uncertainty and is dominated by the uncertainty of the tracking efficiency and by the unfolding uncertainty.

The JES uncertainty was calculated by shifting the resulting jet spectra within the systematic errors and for a given $p_{T,0}$ (x-axis) the yield y_0 was obtained (y-axis) in the unshifted spectrum. For this yield the corresponding $p_{T,\text{left}}$ and $p_{T,\text{right}}$ in both shifted spectra (left and right) were obtained by a linear interpolation. The relative JES uncertainty ρ_{JES} is then calculated as

$$\rho_{\text{JES}}(p_{T,0}) = \frac{\max(p_{T,0} - p_{T,\text{left}}, p_{T,\text{right}} - p_{T,0})}{p_{T,0}} \quad (6.27)$$

In the p_T region (5,25) GeV/ c the ρ_{JES} is approximately constant with the value of about 5% for central Au+Au collisions for both $R = 0.2$ and $R = 0.3$ and 7% for $R = 0.4$. For peripheral Au+Au collisions the ρ_{JES} is 3% for all R values studied.

6.7 Bin-shift Correction

If one would fit the jet transverse momentum spectrum with a reasonable function, the integral of the function would be higher than the corresponding bin content due to the steepness of the jet spectrum. There are two ways of correcting this effect. One can either move the bin center markers to the left or one can move them down. In both cases the integral of the fit function (going through these new centers) will be reduced. For better clarity, we decided to move the bin centers to the left using an iterative procedure:

1. The spectrum is fitted by an suitable function - in our case we use the Tsallis function

$$f(p_T) = p_T \cdot \left(1 + \frac{p_T}{n \cdot T}\right)^{-n} \quad (6.28)$$

with two parameters n and T . Alternatively instead of the smooth function a linear interpolation can be used.

2. The bin centers are shifted to the left to a new position $x_{\text{new}} = w/(1 + k)$, where w is the original position and k is a factor related to the ratio of the integral of the function in the given bin over the bin content.

3. Steps 1. - 2. are then repeated until the whole process converges. As a criterion for the convergence the change in the bin center position is required to be much smaller than ρ_{JES}).

The uncertainty on the bin center marker position is given by the uncertainty of the fit and by the difference between the fit and the linear interpolation. With values smaller than 1% it is significantly smaller than the JES uncertainty and is therefore neglected.

Chapter 7

Parametrized Model

In order to study the systematic effects of jet reconstruction in heavy-ion collisions, we use a Parametrized Model MC event generator. Despite its simplicity, it captures main aspects of the heavy-ion collision events. We tuned the parameters of the model to match the measurements and pQCD calculations. However precision is not our main aim, rather than that we want get the insight into the most important systematic sensitivity of the analysis methods.

The Parametrized Model events consist of two parts: a hard jet spectrum and soft thermal background. These components can be generated alone or both together.

The thermal background is produced following the Boltzman equation

$$B(p_T) = b^2 \cdot p_T \cdot e^{-bp_T}, \quad (7.1)$$

where the constant b is determined from the mean p_T as $b = \frac{2}{\langle p_T \rangle}$. In order to simulate the RHIC Au+Au environment, the value of $\langle p_T \rangle = 0.6$ GeV/ c is used.

For the hard jet distribution, one can use e.g. a power-law p_T distribution, fit to proton-proton jet spectrum or some other reasonable distribution. We use a fit to the PYTHIA (full) jet spectrum, with the fit function of the following form:

$$J(p_T) = A \cdot p_T \cdot \left(1 + \frac{p_T}{n \cdot T}\right)^{-n}, \quad (7.2)$$

with 3 parameters A , T , n . The hard jet function is then scaled by the nuclear overlap function $T_{AA} = 22.5$ mb $^{-1}$ corresponding to 0-10% most central Au+Au collisions and by a nuclear modification factor R_{AA} value. In order to match the Parametrized Model momentum spectrum with the STAR data as close as possible, a p_T dependent R_{AA} assumption was made. $R_{AA} = 0.2$ for $p_T < 5$ GeV/ c , then it rises linearly reaching a value of $R_{AA} = 0.5$ for $p_T > 15$ GeV/ c .

Hard jets are generated with probability distribution given by the shape of the $J(p_T)$ function and the total number of jets generated per N_{evt} events is equal to

$$n_{jets} = N_{evt} \cdot \int_{p_T^{MIN}}^{100} J(p_T) dp_T, \quad (7.3)$$

where $p_T^{MIN} = 4 \text{ GeV}/c$ is the starting value of the hard distribution.

The jet is generated using the PYTHIA 6 fragmentation (u-quark or gluon fragmentation models are used). Only the charged hadrons are saved for further reconstruction. Background soft particles are then generated following the $B(p_T)$ function with a generated multiplicity N_{gen} given as

$$N_{gen} = N_{req} - N_{jetcons}, \quad (7.4)$$

where N_{req} is the required multiplicity ($N_{req} = 650$ for central Au+Au collisions at RHIC) and $N_{jetcons}$ is the total number of jet constituents (charged hadrons) of the generated jets in the given event.

7.1 Comparison to STAR Data

Fig. 7.1 compares jet $p_{T,jet}^{corr,ch}$ spectra from Parametrized Model and STAR data. A good qualitative agreement between the Parametrized Model and the STAR data is apparent. Also the jet area dependency on δ_{pT} as shown on Fig. 7.2 exhibits similar qualitative features for the Parametrized Model as for the STAR data.

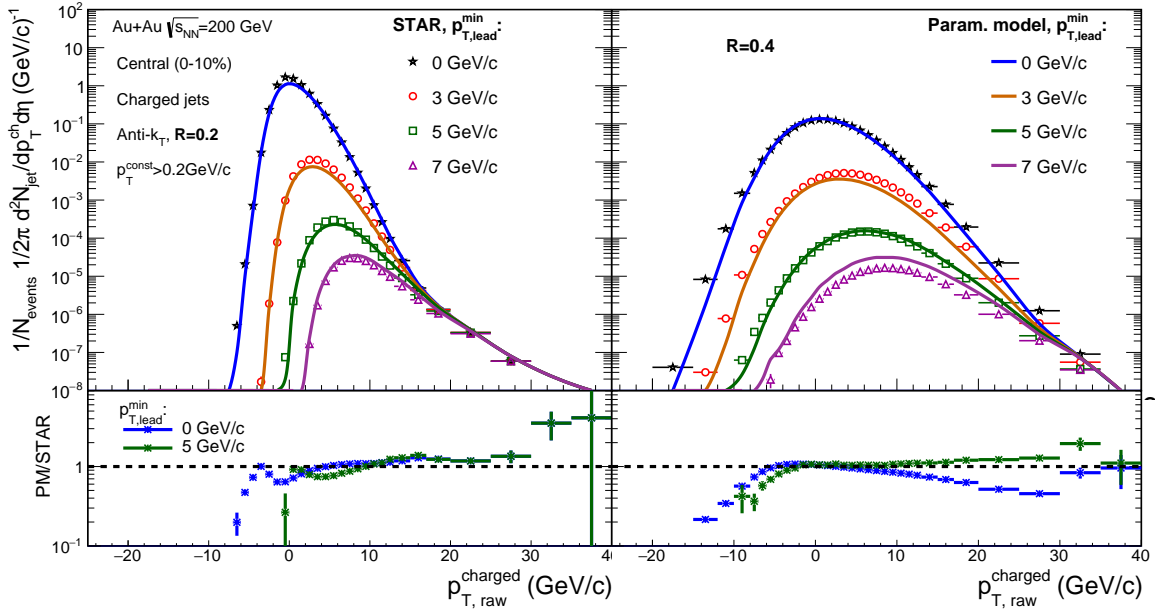


Figure 7.1: Comparison of p_T spectrum of charged jets (with subtracted background energy pedestal) for Parametrized Model simulation and STAR central Au+Au collisions at $\sqrt{s_{NN}} = 200$ GeV. Left: jet reconstruction parameter $R = 0.2$, right: $R = 0.4$. Bottom panels show the ratio of the Parametrized Model over the STAR data.

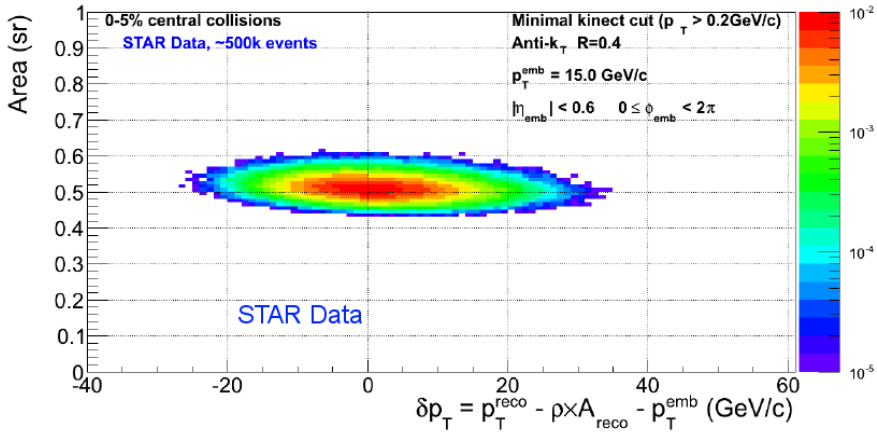
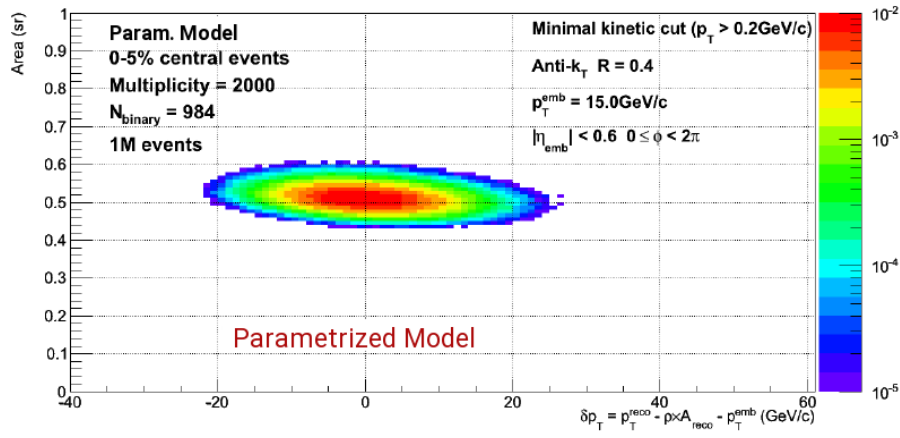


Figure 7.2: Jet area with respect to δ_{p_T} . Top: Parametrized Model simulation. Bottom: STAR central Au+Au collisions.

7.2 Parametrized Model Closure Test

The Parametrized Model can be also used to validate the whole unfolding procedure. We have generated a pure hard jet spectrum without any underlying background and run the jet reconstruction on it. We refer to this sample as a “true spectrum”. A second sample consisted of the hard jet spectrum with soft thermal background and also detector effects were simulated - momentum smearing and tracking inefficiency. After running the jet reconstruction an unfolding procedure was used to correct for the background and detector effects. The unfolding was performed exactly in the same way as in the case of the real data analysis. When we compare the unfolded results with the “true spectrum”, we can see that the difference between the two spectra is smaller than 10%, as shown on Fig. 7.3. Such a difference is well within the systematic error band. The only exception is the first bin, which is always overestimated. However we are interested in the higher p_T bins, where the p_T leading bias is small. And as we can see, the agreement in the high p_T bins is very good.

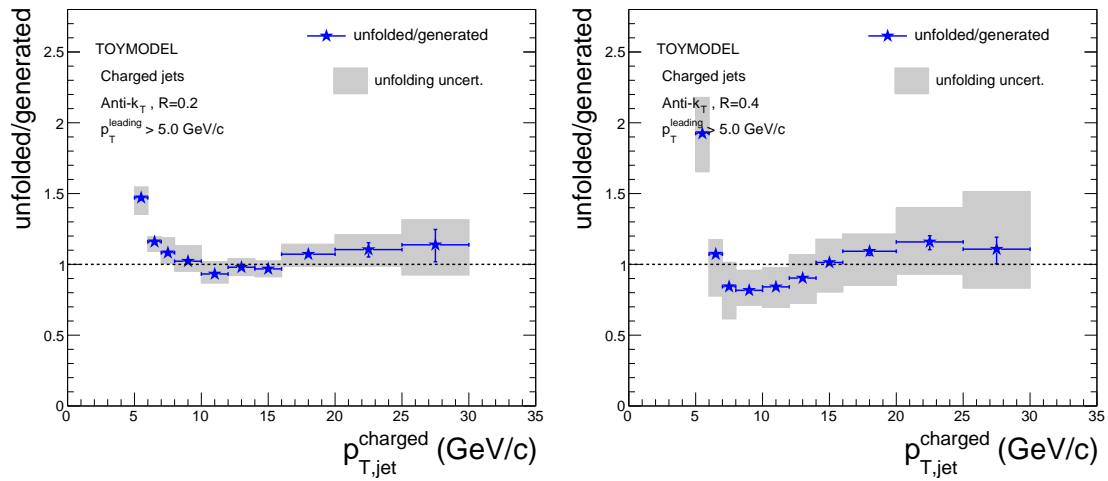


Figure 7.3: Parametrized Model closure test - comparison of unfolded and generated jet spectrum for $p_T^{lead} > 5$ GeV/c and for two jet sizes of $R=0.2$ (left) and $R=0.4$ (right). Systematic uncertainty comes from the unfolding.

Chapter 8

p+p Reference for R_{AA}

In order to obtain the nuclear modification factor R_{AA} a reference inclusive charged jet spectrum in p+p collisions is needed. So far the STAR Collaboration has measured inclusive jet cross section in pp collisions only for full jets, not for charged jets, and only for large jet radii ($R = 0.4$ and $R = 0.6$) [79, 126].

For the purpose of this thesis we have therefore performed an analysis of p+p inclusive charged jets, however with some rough approximations since a full-scale analysis would be beyond the scope of this work. Because of the large systematic uncertainties of these results and because of the limited statistical precision at high momenta we rather resort to theory and models to obtain the p+p reference, namely PYTHIA Monte Carlo event generator is used. The p+p analysis is therefore only used to validate the PYTHIA reference.

8.1 Inclusive Jet Spectrum from PYTHIA

Simulated p+p events were generated using PYTHIA 6.4.26 MC with a standard tune Perugia 0. Jets were reconstructed similarly to real data, using the Fastjet 3 software package [76] and anti- k_T reconstruction algorithm. Jet area cuts and track momentum cuts were identical to those in the Au+Au data analysis.

Both charged and full jets were reconstructed in the PYTHIA events in order to compare the PYTHIA results with the STAR published p+p full jet measurements. This comparison is shown on Fig. 8.1. In both cases the PYTHIA distribution agrees with the data within the systematic uncertainties.

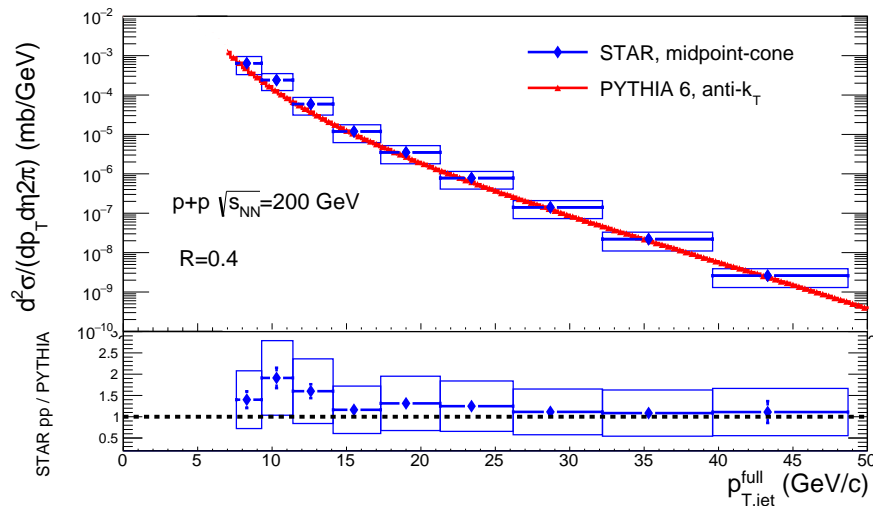


Figure 8.1: Full jet differential cross section measured by the STAR Collaboration and its comparison to PYTHIA 6.426. The STAR results are based on data from years 2003+2004 [79] and jets are reconstructed using midpoint cone algorithm with $R = 0.4$. PYTHIA jets are reconstructed with the anti- k_T algorithm, $R = 0.4$. Bottom: Ratios of the STAR measurement to a fit to PYTHIA simulated data.

8.2 Run12 p+p Analysis

In order to further validate the PYTHIA reference a simplified analysis of the STAR Run12 pp data was performed. This dataset consists of ~ 190 M events recorded with the Minimum Bias (MB) trigger and 4 M events recorded with the High Tower (HT) trigger. No event QA has been done so far and therefore no bad ran exclusion was done. The MB and HT datasets were combined together. Since the cross section of the HT trigger (or its ratio with respect to the MB trigger) is not known with a sufficient precision, the scaling of the HT events was performed by normalizing the jet distribution in a small region around 14 GeV/c to the integral of the MB distribution in the same region. This is illustrated on Fig. 8.2. For higher jet momentum values ($p_{T,\text{jet}} > 14$ GeV/c) the scaled HT distribution was used rather than the MB one, since the MB distribution lacks the statistics at high momenta.

Event and track quality cuts

The event cuts used on the p+p data sample are similar to those on the Au+Au analysis. Additionally, in order to reduce the pile up, distance between the z-position of the primary vertex measured by the TPC (z_{TPC}) and measured by the VPD (z_{VPD}) was required to be $|z_{\text{VPD}} - z_{\text{TPC}}| < 4$ cm. The basic track quality cuts are also the same as in the case of the Au+Au analysis. Furthermore for each track a corresponding hit in a fast detector (either BEMC or TOF) was required in order to remove the pile up tracks as discussed later.

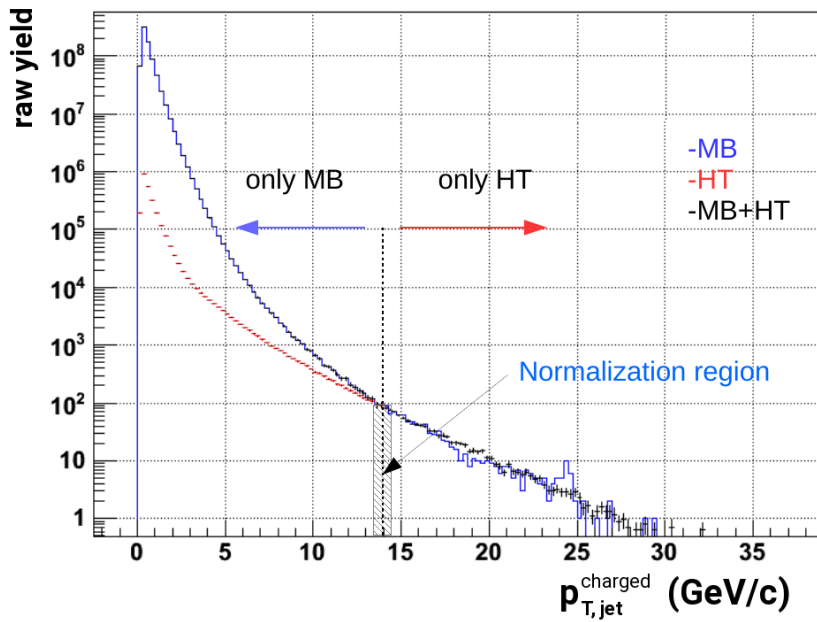


Figure 8.2: Uncorrected charged jet spectra in Run12 p+p collisions from minimum bias (MB) (blue) and high tower (HT) triggered datasets (red). The HT spectrum was scaled such that the integral of the normalization region is the same as for the MB spectrum. The final spectrum used for the analysis (black) was obtained by taking the MB distribution for $p_{T,jet} < 14$ GeV/ c and taking the scaled HT distribution for $p_{T,jet} > 14$ GeV/ c .

Pile up removal

It was already mentioned in Sec. 4.2.1 that during the TPC readout time of 40 μs multiple collisions can occur. Such Pile Up (PU) of events represents an issue especially in p+p collisions where the RHIC collider is capable of delivering much higher luminosities than in the case of Au+Au collisions. For the same reason the trigger-based PU protection used in heavy-ion collisions cannot be used in p+p collisions and another way of PU reduction has to be sought out.

In order to determine whether the selected set of events suffers from pile up one can study the TPC track multiplicity as a function of luminosity. In case of no PU the multiplicity should be independent of the luminosity. Vice-versa, the growth of the multiplicity with the luminosity is a clear sign of the pile up.

In this study we use the coincidence rate of the BBC scintillators as a measure of the luminosity. Fig. 8.3(a) shows the TPC multiplicity as a function of the BBC coincidence rate. Clearly, there is a significant linear growth of the multiplicity with the increasing luminosity (BBC rate).

On the event selection stage one should pick-up only events where the primary vertex reconstructed from the TPC tracks lays close to the position of the PV determined by the fast VPD detector, otherwise one would be looking at the PV from a piled up event. The VPD's time resolution of ~ 80 ps corresponds to a distance of ~ 2.4 cm traveled by a particle moving at the speed of light. Therefore a cut on the PV z position of $|z_{\text{VPD}} - z_{\text{TPC}}| < 4$ cm is applied which corresponds to $1\frac{2}{3}\sigma$ of the VPD resolution. In order to select only tracks which come from the selected vertex and not from other (pile up) vertices a cut on DCA < 1 cm is applied. As can be seen on Fig. 8.3(b), these two measures reduce the effect of the pile up significantly, however there is still non negligible increase of the multiplicity with the luminosity.

An ultimate solution is to require for each track a corresponding hit in a fast detector - either the BEMC or TOF. Fig. 8.3(c) shows that this step indeed removes the pile up events/tracks entirely. Unfortunately the track reconstruction efficiency is reduced by another 30-40% by this condition as can be clearly seen on Fig. 8.4. This additional inefficiency has to be corrected for by the unfolding.

Background and detector effects

The combinatorial background in p+p collisions is much less of a concern than in Au+Au collisions. By applying the same cut on $p_{\text{T}}^{\text{lead}}$ as in the Au+Au analysis the background is extinguished. The detector effects on the other hand influence the p+p data in the same way as the heavy-ion data. We therefore apply a correction on the tracking efficiency and momentum resolution. The momentum resolution is almost independent of the collision system and track multiplicity. Hence we apply the same momentum parametrization as in the case of the Au+Au analysis. The tracking efficiency depends on the tracking multiplicity. Instead of estimating the tracking efficiency in p+p collisions we rather use the tracking efficiency for peripheral Au+Au collisions which possesses similarly low multiplicities.

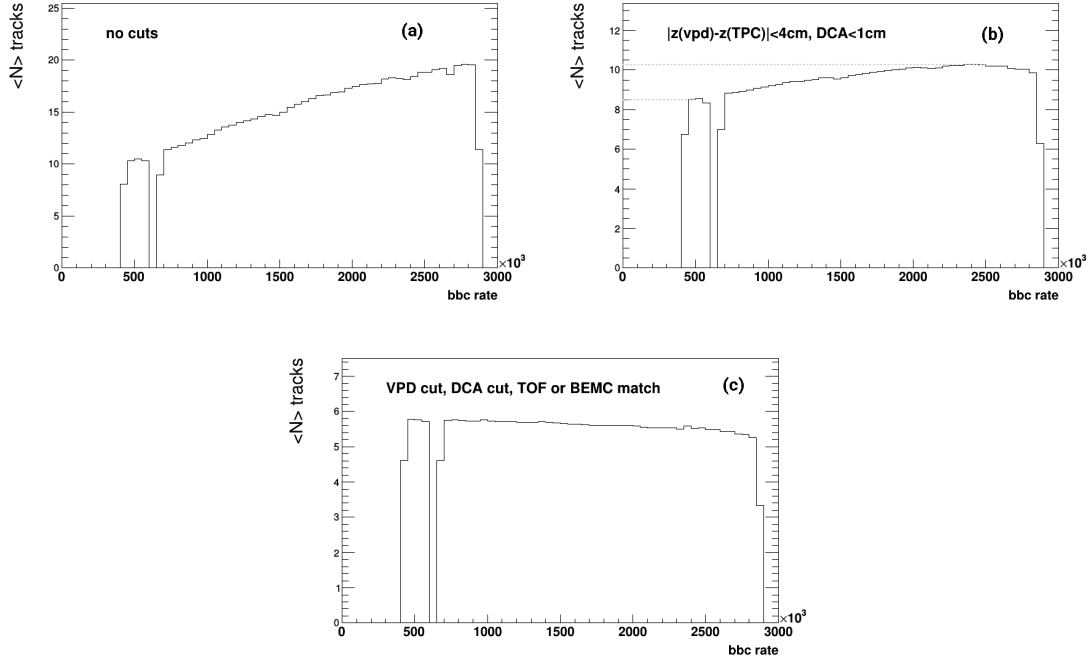


Figure 8.3: TPC charged track multiplicity as a function of BBC coincidence rate. (a) No pile up reduction. (b) Additional event selection condition: $|z_{\text{VPD}} - z_{\text{TPC}}| < 4$ cm and only tracks with $\text{DCA} < 1$ cm accepted. (c) Same as (b) plus for each track a corresponding hit either in the BEMC or TOF is required.

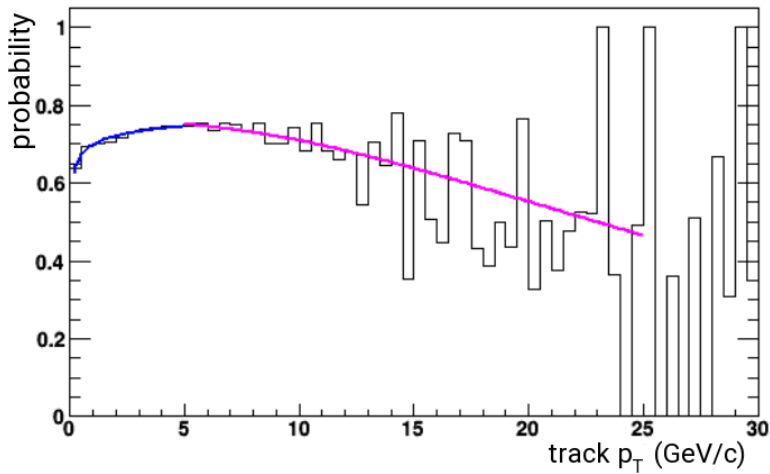


Figure 8.4: Probability of a matched hit in the BEMC or TOF detector for a TPC track in p+p collisions at $\sqrt{s} = 200$ GeV as a function of the track p_T . Blue and magenta lines represent a fit to the data in low p_T and high p_T region, respectively.

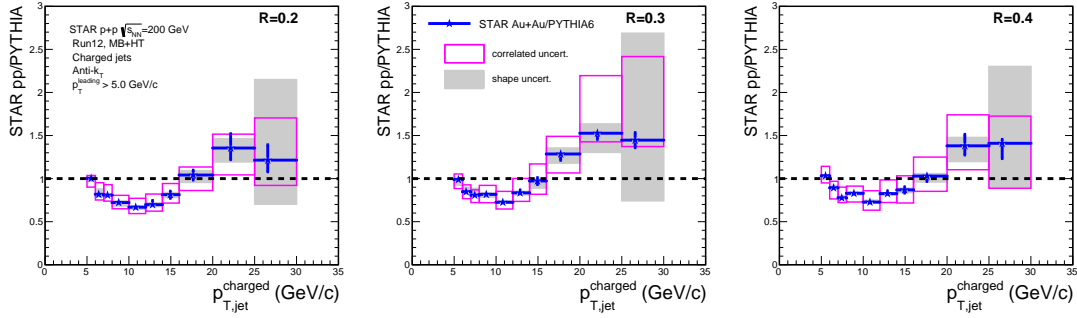


Figure 8.5: Ratio of inclusive charged jet spectra in p+p collisions measured by STAR at $\sqrt{s} = 200$ GeV over PYTHIA 6.426 Perugia 0. A cut of $p_T^{\text{lead}} > 5.0$ GeV/c is applied on both the numerator and denominator. Caution: The jet spectra used for the numerator were reconstructed with several approximations and one should not draw any physics conclusions from them. See text for the details on this simplified analysis.

The reconstructed jet spectra are corrected for the detector effects via unfolding in a similar way as in the case of Au+Au analysis. The correlated systematic uncertainty is quite large and is driven by the tracking efficiency uncertainty.

The ratio of the unfolded spectra and PYTHIA 6.426 Perugia 0 spectrum is plotted on Fig. 8.5. A cut on $p_T^{\text{lead}} > 5$ GeV/c was applied both in the numerator and the denominator. The p+p spectrum is in a decent agreement with the PYTHIA spectrum, taking into account the systematic errors. Thus the PYTHIA spectrum is validated as a reasonable baseline for the R_{AA} measurement discussed in the following section.

Chapter 9

Results and Discussion

9.1 Corrected Charged Jet Spectra

Figure 9.1 shows the charged jet yield in peripheral and central Au+Au collisions at $\sqrt{s_{\text{NN}}} = 200$ GeV corrected for the background fluctuations and the TPC tracking efficiency. The results are reported for 3 different R parameter values, 0.2, 0.3 and 0.4, and 3 $p_{\text{T,lead}}^{\text{min}}$ values, 5, 6 and 7 GeV/ c . Note that the low p_{T} values (approx. up to $2p_{\text{T,lead}}^{\text{min}}$) are strongly biased due to the cut on the leading hadron momentum.

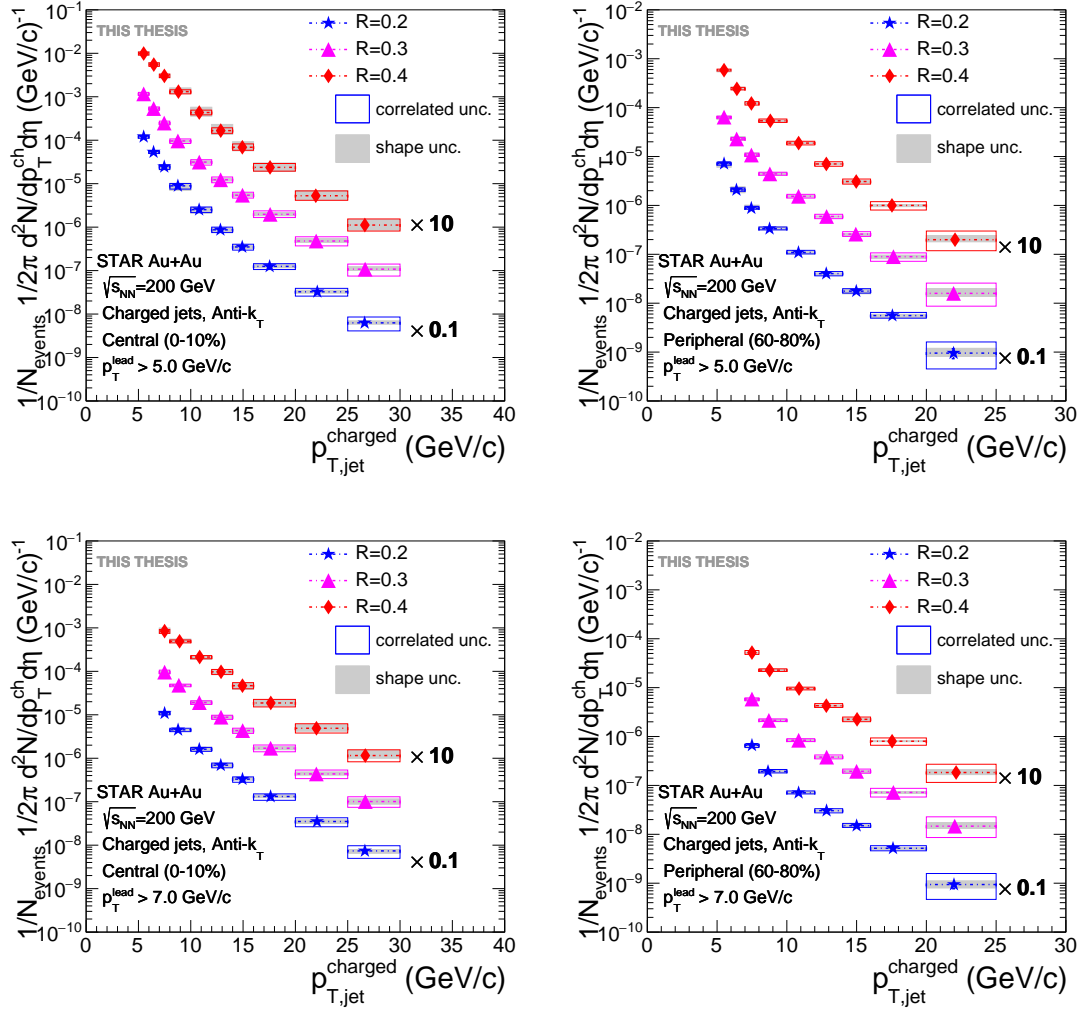


Figure 9.1: Unfolded charged jet spectra with $p_T^{\text{lead}} > 5$ (top) and $p_T^{\text{lead}} > 7$ GeV/c (bottom) for $R = 0.2 - 0.4$ in the central (left) and peripheral (right) Au+Au collisions at $\sqrt{s_{\text{NN}}} = 200$ GeV.

9.2 Spectra Ratios - different p_T^{lead} cuts

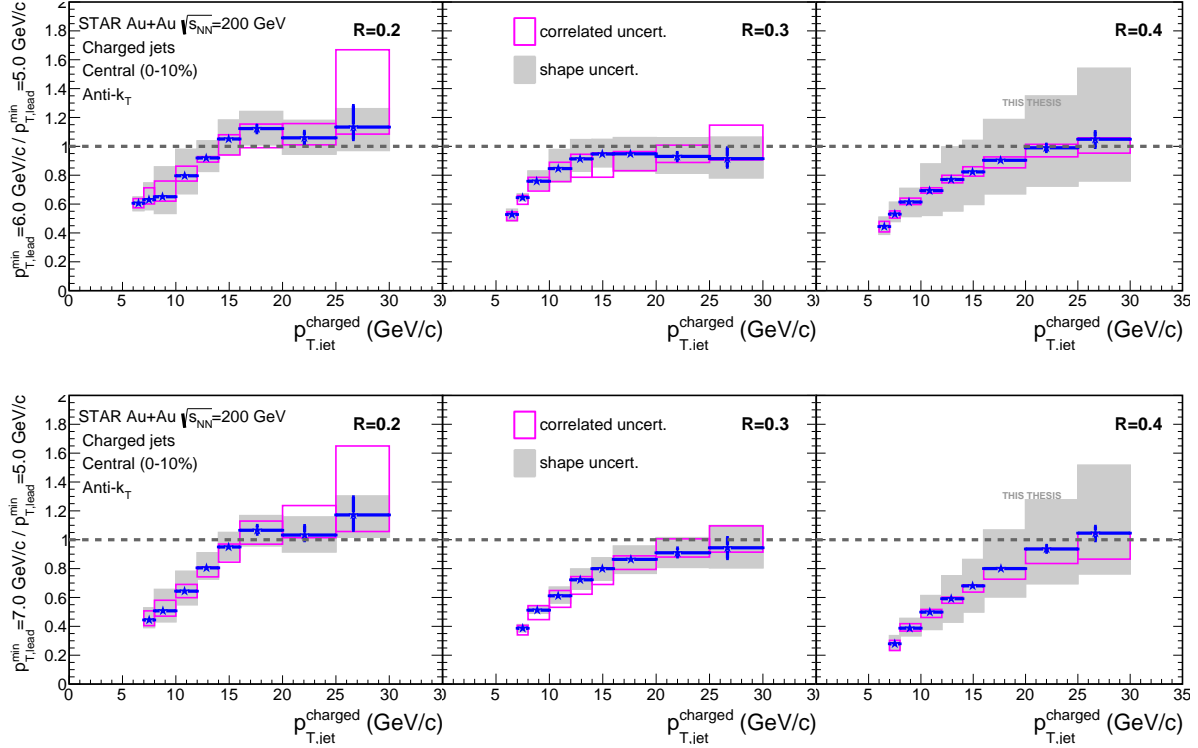


Figure 9.2: Ratios of charged jet spectra with $p_T^{\text{lead}} > 6 \text{ GeV}/c$ over $p_T^{\text{lead}} > 5 \text{ GeV}/c$ (top) and $p_T^{\text{lead}} > 7 \text{ GeV}/c$ over $p_T^{\text{lead}} > 5 \text{ GeV}/c$ (bottom) in the central Au+Au collisions. From the left to the right the R value rises from 0.2 to 0.4.

The momentum cut imposed on the jet leading hadron strongly biases the jet spectrum. The uncorrected spectra presented in Sec. 6.3.1 revealed that the hard jet spectrum is affected minimally by the cut. The question is, where this “safe part” of the spectrum starts. In order to find it out, one would need to compare the fully corrected spectra with and without the p_T^{lead} cut. This is unfortunately impossible in our case and we therefore compare the spectra obtained with different values of the p_T^{lead} cut. Such a comparison is shown on Fig. 9.2. Since we do not compare the spectra to an unbiased spectrum, we can only state what is the minimal value of $p_{T,\text{jet}}$ which is still affected by the p_T^{lead} cut. If we denote this value $p_{T,\text{bias}}^{\text{min}}$ we can write down an approximate relation

$$p_{T,\text{bias}}^{\text{min}} \simeq 5 \cdot (0.2 + R) \cdot p_{T,\text{lead}}^{\text{min}} \quad (9.1)$$

based on the results of Fig. 9.2.

For the jet momenta above the $p_{T,\text{bias}}^{\text{min}}$ value the ratio of the distributions is consistent with unity. This means that the jet distributions with $p_{T,\text{lead}}^{\text{min}} = 7.0 \text{ GeV}/c$ or $p_{T,\text{lead}}^{\text{min}} = 6.0 \text{ GeV}/c$ represent a subset of the jet distribution with $p_{T,\text{lead}}^{\text{min}} = 5.0 \text{ GeV}/c$.

9.3 Spectra Ratios - different R

By looking at the ratios of the jet spectra for different jet resolution parameters R , one can study the jet's inner structure. Figure 9.3 shows three spectra ratios: $R=0.2/R=0.3$, $R=0.2/R=0.4$ and $R=0.3/R=0.4$ in peripheral Au+Au collisions with $p_{T,\text{lead}}^{\text{min}} = 5.0$ GeV/ c and 7.0 GeV/ c . Fig. 9.4 shows the same quantity in central Au+Au collisions. As can be seen, the ratios are very similar in both collision centralities and rise with the increasing value of $p_{T,\text{lead}}^{\text{min}}$. This would imply that the $p_{T,\text{lead}}^{\text{min}}$ cut biases the jet structure towards the jets which carry their energy inside a narrow cone. The ratio $R=0.2/R=0.3$ is significantly lower than $R=0.3/R=0.4$ and the ratio $R=0.3/R=0.4$ is not far from unity. The inner structure of the $R = 0.3$ jets seems to be therefore very similar to that of the $R = 0.4$ jets while the small jets with $R = 0.2$ are basically dominated by the leading particle.

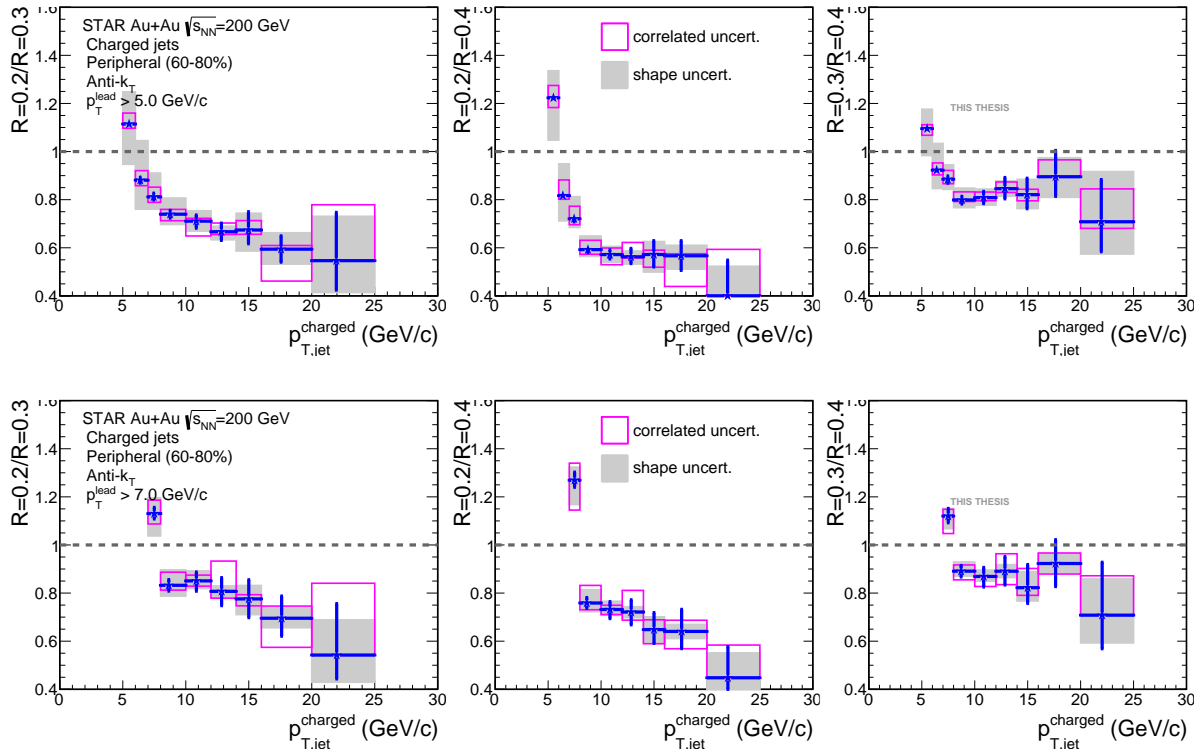


Figure 9.3: Charged jet spectra ratios of different R with $p_{T,\text{lead}}^{\text{min}} > 5$ (top) and $p_{T,\text{lead}}^{\text{min}} > 7$ GeV/ c (bottom) in peripheral Au+Au collisions.

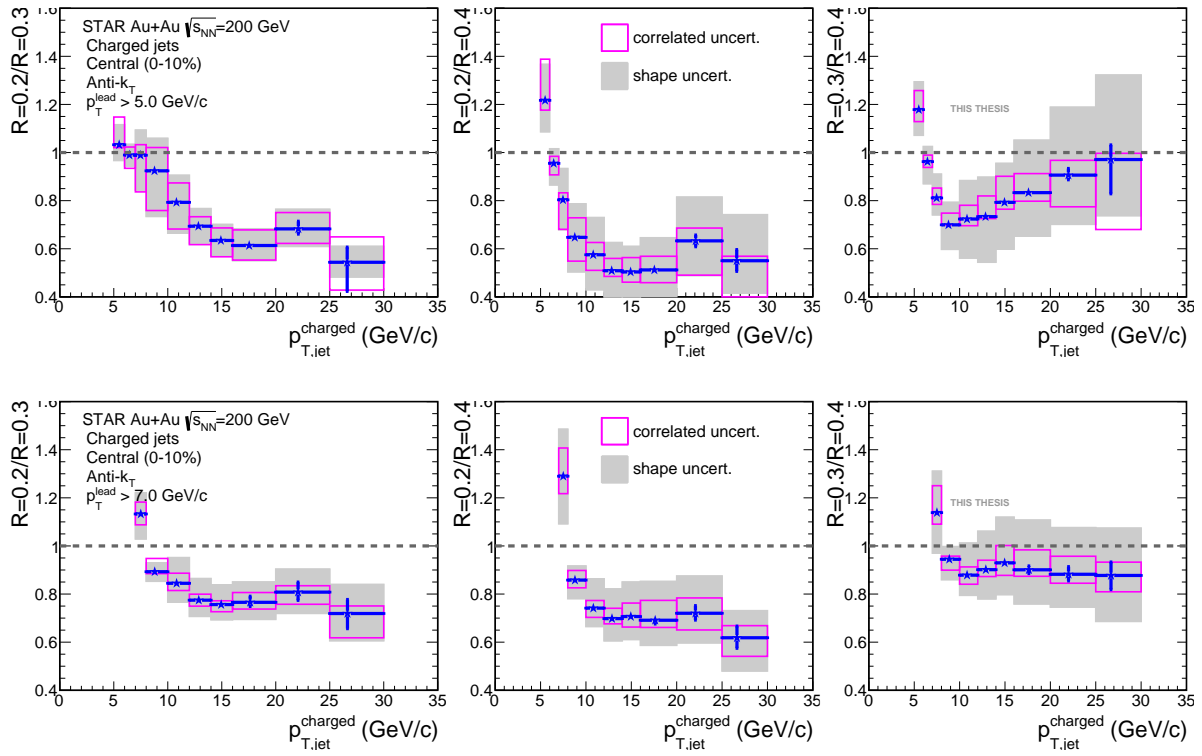


Figure 9.4: Charged jet spectra ratios of different R with $p_T^{\text{lead}} > 5$ (top) and $p_T^{\text{lead}} > 7$ GeV/c (bottom) in central Au+Au collisions.

9.4 R_{CP}

Fig. 9.5 shows R_{CP} - the ratio of the inclusive jet yields in central to peripheral Au+Au collisions normalized by the corresponding mean number of binary collisions:

$$R_{CP} = \frac{\frac{1}{N_{\text{events}}^{\text{cent}}} \cdot \frac{d^2 N_{\text{cent}}}{dp_{T,\text{jet}} d\eta}}{\frac{1}{N_{\text{events}}^{\text{peri}}} \cdot \frac{d^2 N_{\text{peri}}}{dp_{T,\text{jet}} d\eta}} \cdot \frac{\langle N_{\text{bin}}^{\text{peri}} \rangle}{\langle N_{\text{bin}}^{\text{cent}} \rangle}. \quad (9.2)$$

A strong suppression of the charged jet production is observed in central with respect to peripheral collisions. The measured R_{CP} value is 0.4 – 0.5 and the dependence of the R_{CP} on both $p_{T,\text{jet}}$ and R seems to be very weak within the studied range.

The systematic uncertainty of the R_{CP} takes into account the correlated uncertainties of numerator and denominator and some of the major systematic uncertainties (e.g. the tracking efficiency uncertainty) largely cancel out in the ratio.

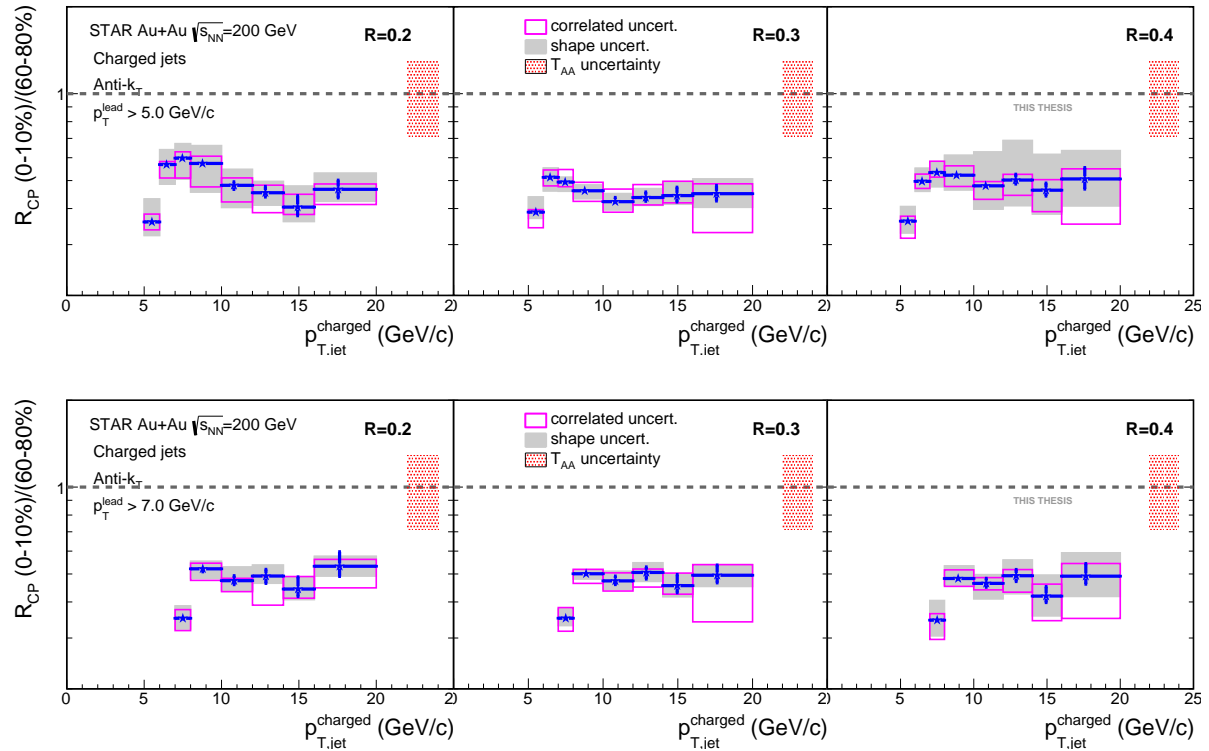


Figure 9.5: Charged jet R_{CP} with $p_T^{\text{lead}} > 5$ (top) and $p_T^{\text{lead}} > 7$ GeV/c (bottom) for $R = 0.2 - 0.4$.

Since the shape of the jet momentum distribution is approximately exponential, for a range of jet p_T in which the R_{CP} is constant, suppression of R_{CP} can be expressed equivalently as a shift between the peripheral and central distributions. The value of the shift is ~ 2 GeV/c and no dependency on R up to $R = 0.4$ is observed. The exact values of

the shift are listed later in Tab. 9.2. The p_T shift was calculated as a x-distance between the two linearly interpolated spectra - jet yield in peripheral collisions normalized by the mean number of binary collisions and jet yield in central collisions normalized by the mean number of binary collisions. The uncertainty of the shift was estimated by shifting the distributions within their total uncertainties.

9.5 R_{AA}

Nuclear modification factor R_{AA} quantifies the change of spectra due to hot nuclear effects by comparing Au+Au spectra with appropriately scaled p+p spectra. It is defined as

$$R_{AA} = \frac{1}{N_{\text{events}}} \cdot \frac{d^2 N_{Au+Au}}{dp_{T,\text{jet}}^{\text{ch}} d\eta}}{T_{AA} \cdot \frac{d^2 \sigma_{p+p}}{dp_{T,\text{jet}}^{\text{ch}} d\eta}}, \quad (9.3)$$

where the numerator is the differential jet yield in central A+A collisions per event and the denominator is the differential jet cross section in p+p collisions scaled by T_{AA} . The nuclear overlap function T_{AA} is defined as the mean number of binary collisions (in A+A collisions) divided by the p+p inelastic cross section:

$$T_{AA} = \frac{\langle N_{\text{bin}} \rangle}{\sigma_{\text{inelastic}}^{p+p}} \simeq 22.2 \pm 1.0. \quad (9.4)$$

T_{AA} (or equivalently N_{bin}) is determined from the Glauber Monte Carlo model [55].

The p+p reference was provided by PYTHIA 6.4.26 (tune Perugia 0) Monte Carlo event generator. We denote the measured nuclear modification factor as R_{AA}^{Pythia} in order to emphasize the fact that the denominator is provided by the PYTHIA event generator. See Chapter 8 for further details on the p+p reference spectrum.

Fig. 9.6 shows R_{AA}^{Pythia} of the charged jets in peripheral Au+Au collisions and Fig. 9.7 shows the same quantity in central Au+Au collisions corrected for the background fluctuations and the TPC tracking efficiency. The results are reported for 3 different jet radii R and 2 $p_{T,\text{lead}}^{\text{min}}$ values. Note that the low p_T values (approx. up to $2 \times p_{T,\text{lead}}^{\text{min}}$) are again strongly biased due to the cut on the leading hadron momentum, as shown on Fig. 9.2 and discussed in previous section.

Clearly, with the increasing value of R , R_{AA}^{Pythia} does not change. This suggests that the parton's energy is recovered only within a very large jet radius $R > 0.4$. Also, R_{AA}^{Pythia} does not seem to change with the increasing $p_{T,\text{lead}}^{\text{min}}$ value, except low p_T bins, which are strongly biased by this cut.

Alternatively, one could impose a cut on the leading hadron momentum also in the case of the (PYTHIA) p+p baseline. In such a case the two biases could cancel out. However, as already discussed in Sec. 3.2.5, the size of the bias is expected to be different in the p+p collisions than in the Au+Au collisions. Therefore we call such a ratio “double biased” R_{AA}^{Pythia} rather than “unbiased”. Nevertheless the biases will cancel out at least partially, therefore we consider it useful to present this quantity as well. The “double biased” R_{AA}^{Pythia} is shown on Fig. 9.8. Apparently in this case the momentum dependency is very weak.

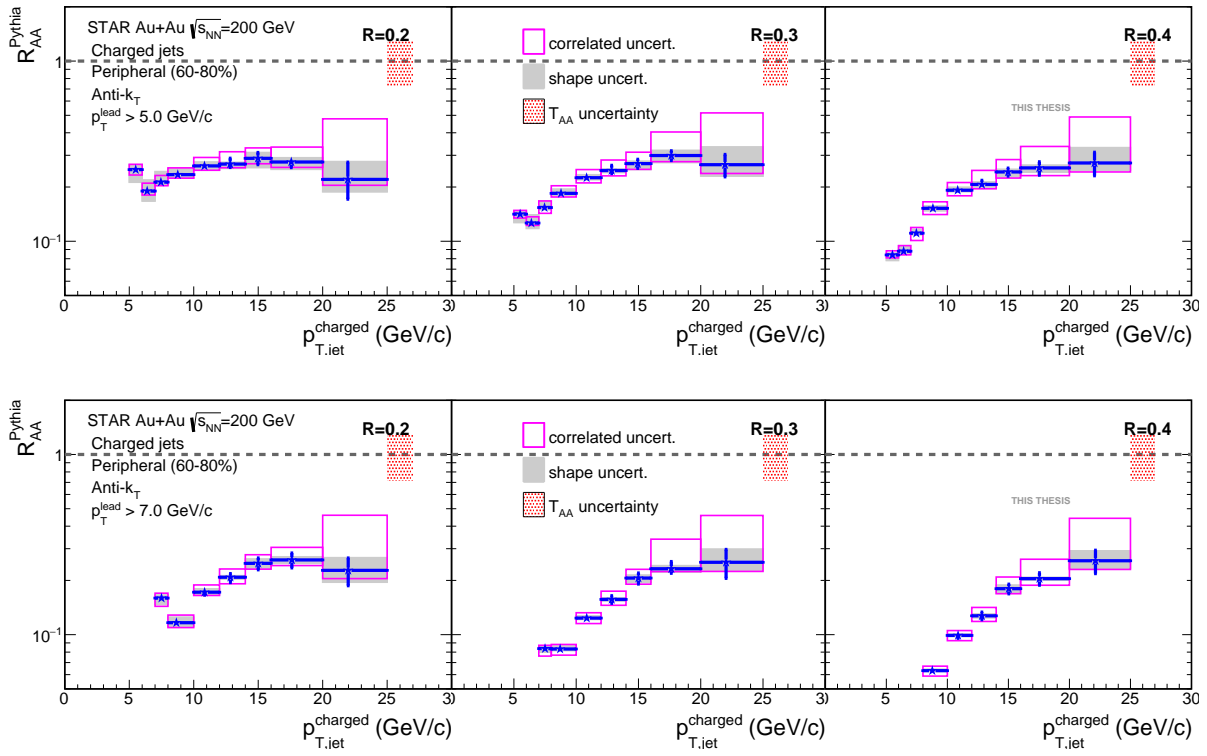


Figure 9.6: Charged jet “biased” R_{AA}^{Pythia} (p_T^{lead} -biased Au+Au spectrum over unbiased PYTHIA baseline) with $p_T^{\text{lead}} > 5$ (top) and $p_T^{\text{lead}} > 7$ GeV/c (bottom) for $R = 0.2 - 0.4$ in peripheral Au+Au collisions.

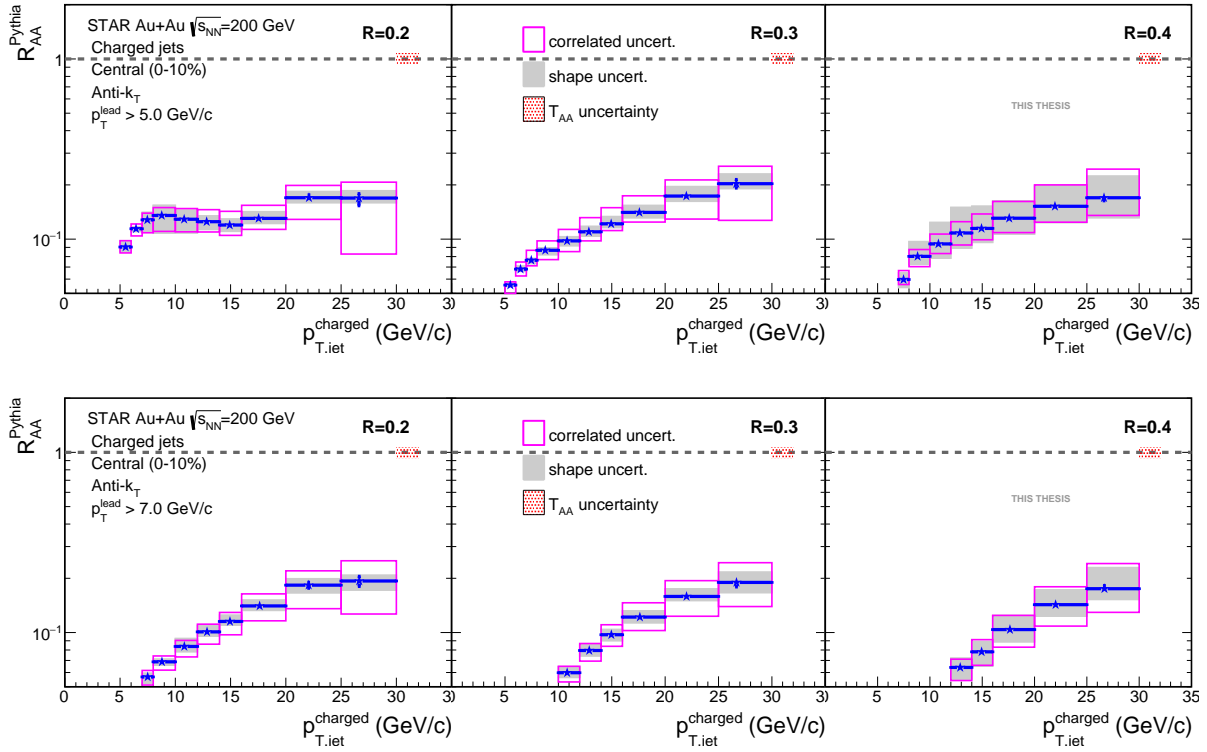


Figure 9.7: Charged jet “biased” R_{AA}^{Pythia} (p_T^{lead} -biased Au+Au spectrum over unbiased PYTHIA baseline) with $p_T^{\text{lead}} > 5$ (top) and $p_T^{\text{lead}} > 7$ GeV/c (bottom) for $R = 0.2 - 0.4$ in central Au+Au collisions.

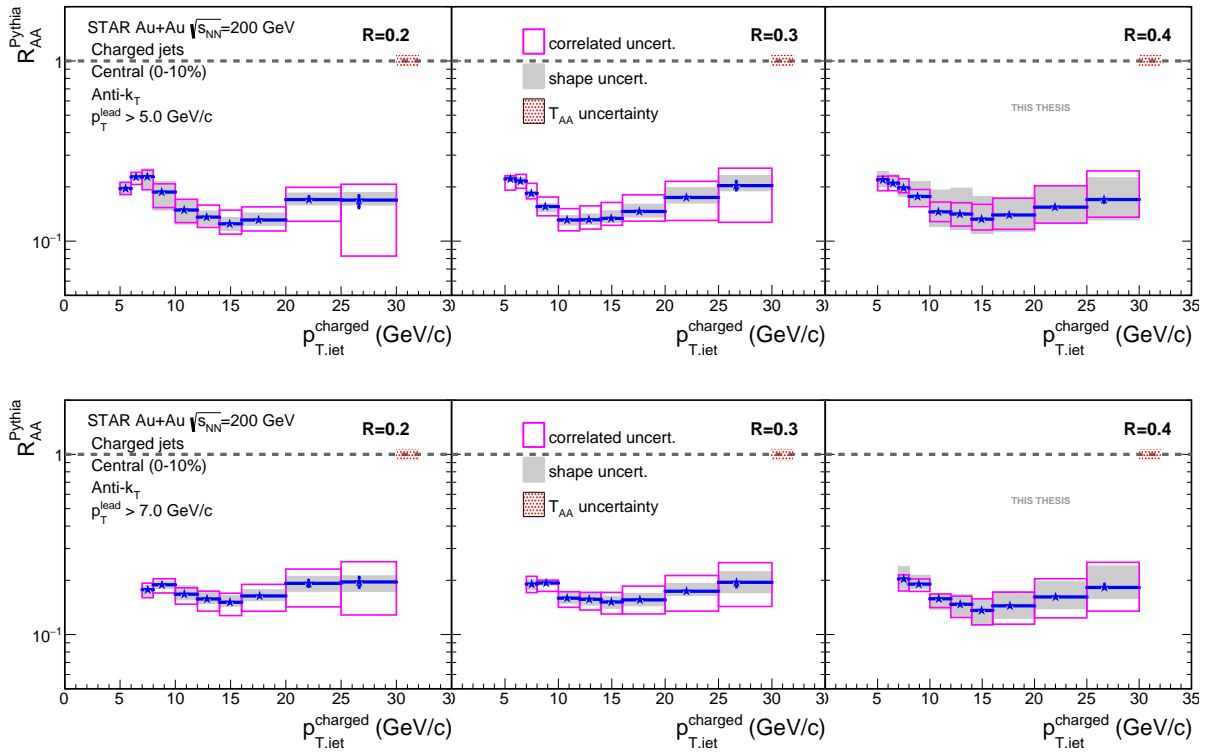


Figure 9.8: Charged jet “double biased” R_{AA}^{Pythia} (p_T^{lead} -biased Au+Au spectrum over p_T^{lead} -biased PYTHIA baseline) with $p_T^{\text{lead}} > 5$ (top) and $p_T^{\text{lead}} > 7$ GeV/c (bottom) for $R = 0.2 - 0.4$ in central Au+Au collisions.

9.6 Comparison to Theoretical Models and Other Experiments

The ratio of the charged jet spectra $R=0.2/R=0.4$ was compared with several theoretical models as can be seen on Fig. 9.9. The theoretical models used for the comparison are listed in Tab. 9.1.

The first model, labeled as “Vitev1”, is a relatively simple model based on the NLO pQCD calculation of the jet production cross section and incorporating the collisional parton energy loss to account for the medium effects [127].

The second model, “Vitev2”, is a more complex one. The DGLAP equations are used to control the evolution of parton distribution and fragmentation functions. The resummation of large logarithms that arise from ratios of energy and momentum scales in elementary collisions is done within the soft-collinear effective theory (SCET) which is extended for the propagation in matter, via Glauber gluon exchange (SCET_G). The initial state CNM effects which are considered by the model include dynamical nuclear shadowing [128], Cronin effect [129] and initial state parton energy loss [130].

The third model combines different calculational frameworks for the two different energy scales of the jet evolution - the weakly coupled formation and (in vacuum) evolution of the jet, which can be described by the pQCD, and nonperturbative, strongly coupled interaction of the jet with the medium [131]. We will refer to it as to “Hybrid Model”. The weakly coupled part of the jet evolution is calculated using the DGLAP equations. The soft interactions between the jet and the medium are modeled using qualitative insights inferred from holographic calculations of the energy loss of energetic light quarks and gluons in a strongly coupled plasma, obtained via gauge/gravity duality [132]. This hybrid model is then embedded into a hydrodynamic description of the space-time evolution of the medium.

There is a good agreement between all theoretical predictions and the measurement for $p_T^{\text{lead}} > 5 \text{ GeV}/c$ in central Au+Au collisions. It should be however emphasized that the theoretical models were calculated for full jets and without any requirement on the $p_{T,\text{lead}}^{\text{min}}$ value.

Also, no significant difference is observed between $R = 0.2/R = 0.4$ ratios in p+p collisions from PYTHIA and HERWIG and the measurements in central and peripheral Au+Au collisions. This would suggest that in the central heavy-ion collisions the small jets are modified by the medium in a similar way as the large jets.

Table 9.1: Description of several theoretical models used for comparison with STAR data.

| label | description | reference | jet type | $p_{T,\text{lead}}^{\text{min}}$ value |
|--------------|---|-----------|--------------|--|
| Vitev1 | NLO calculation + partonic energy loss | [127] | full jets | 0 |
| Vitev2 | soft-collinear effective theory (SCET) + CNM effects + full medium induced splitting functions | [133] | full jets | 0 |
| Hybrid Model | DGLAP evolution + hybrid strong/weak coupling approach to jet quenching | [131] | full jets | 0 |
| PYTHIA | PYTHIA MC event generator, version 6.4.26, tune Perugia 0 | [134] | charged jets | 5, 7 GeV/c |
| HERWIG | HERWIG MC event generator, version 6.521, default settings | [135] | charged jets | 5, 7 GeV/c |

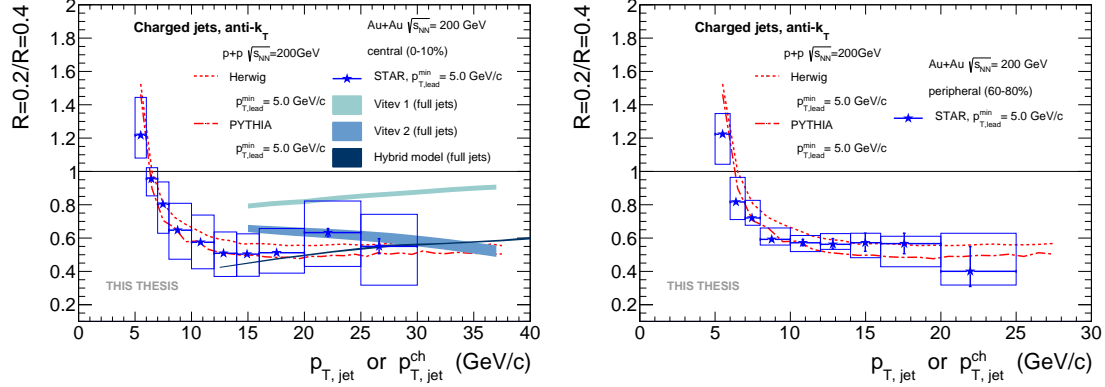


Figure 9.9: Charged jet spectra ratios of different R with $p_T^{\text{lead}} > 5$ GeV/c in central (left) and peripheral (right) Au+Au collisions and their comparison to theoretical models [127, 131, 133] and p+p event generators [134, 135].

Fig. 9.10 compares the R_{AA} result with theoretical models listed in Tab. 9.1. The STAR charged jet R_{AA} is lower than all three models. The Hybrid Model overpredicts the R_{AA} value significantly, but qualitatively catches the R -independence. On the other hand Vitev1,2 models are much closer to the STAR R_{AA} value for $R = 0.2$, but exhibit a strong R -dependency, which is not supported by the STAR results. From the available models no one therefore describes the STAR R_{AA} properly. As already mentioned, all the presented theoretical models were calculated for full jets and without any requirement on the $p_{T, \text{lead}}^{\text{min}}$ value.

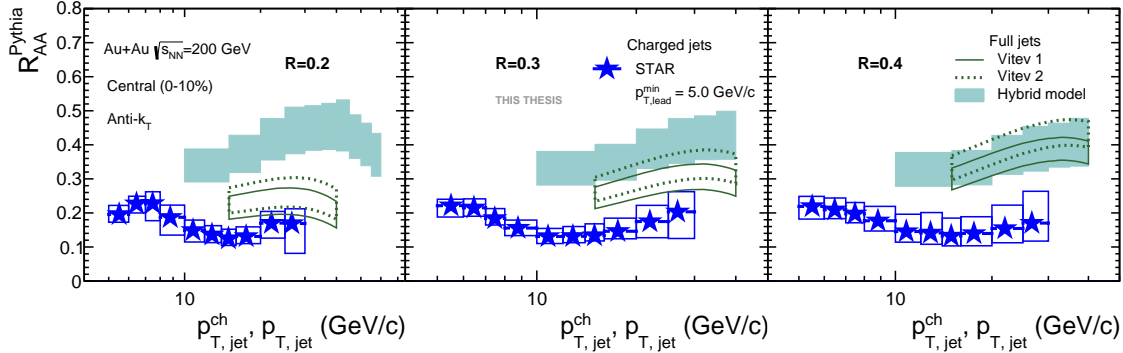


Figure 9.10: Measured charged jet R_{AA} (wrt. biased PYTHIA baseline) with $p_T^{\text{lead}} > 5$ GeV/c for $R = 0.2$, $R = 0.3$ and $R = 0.4$ in central Au+Au collisions compared to full jet R_{AA} obtained from several theoretical models [127, 131, 133]. The calculations were made for the same collision system and the same values of R as the STAR measurement, but no $p_{T, \text{lead}}^{\text{min}}$ value was required.

A direct comparison of the charged jet R_{CP} with the ALICE measurement of the charged

jet R_{CP} in Pb+Pb collisions at $\sqrt{s_{NN}} = 2.76$ TeV [136] is presented on Fig. 9.11. The ALICE measurement uses similar procedures as the STAR measurement. Jets are reconstructed using the anti- k_T algorithm, a cut on momentum of the leading hadron $p_T^{\text{lead}} > 5.0$ GeV/ c is applied, SVD unfolding is used to correct the spectra for the background and the detector effects. In spite of the different collision energies at RHIC and the LHC, both measurements yield comparable results for $R = 0.3$, as well as $R = 0.2$. More quantitative conclusions are however not possible due to the large uncertainties of the STAR data. In both measurements no significant R -dependence is apparent.

Charged jet R_{CP} results can be also compared with the charged hadron R_{CP} measurements. These are plotted as open symbols on Fig. 9.11. There is a very nice agreement between the STAR data [137] and the ATLAS measurement [138]. Interestingly, the LHC charged jet R_{CP} is lower than the hadron R_{CP} with the same momentum, but it is comparable with the hadron R_{CP} at lower momenta. At RHIC on the other hand the charged jet R_{CP} is higher than the corresponding hadron R_{CP} . But once again, it is comparable with the R_{CP} of the hadrons with lower momentum.

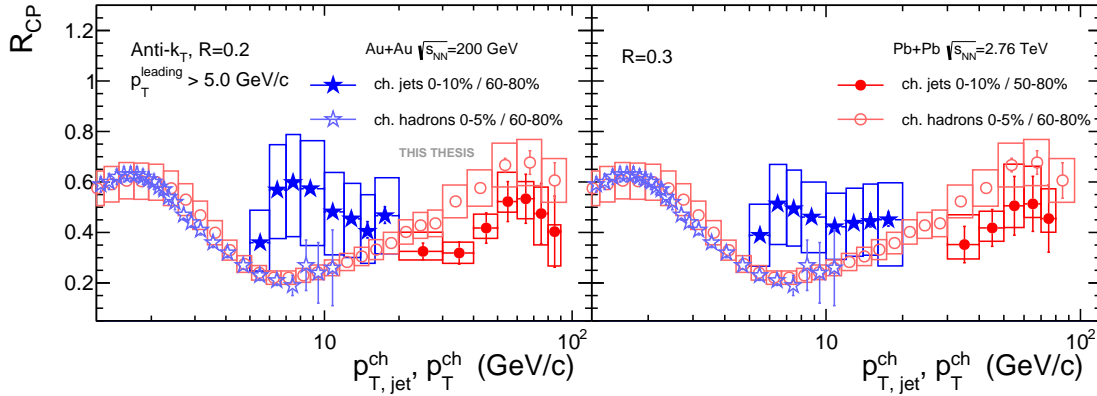


Figure 9.11: Measured charged jet R_{CP} with $p_T^{\text{lead}} > 5$ GeV/ c for $R = 0.2 - 0.4$ in central Au+Au collisions at $\sqrt{s_{NN}} = 200$ GeV (blue full symbols) and charged jet R_{CP} in central Pb+Pb collisions at $\sqrt{s_{NN}} = 2.76$ TeV measured by the ALICE collaboration (red full symbols) [136]. Open symbols represent charged hadron R_{CP} measurements from RHIC [137] and the LHC [138].

Beside the R_{CP} value the p_T -shift between the peripheral and central spectrum was calculated as well. These values can be directly compared with values obtained by the hadron+jet analysis conducted at STAR in Au+Au collisions $\sqrt{s_{NN}}=200$ GeV [103]. As can be seen in Tab. 9.2 the recoil jets exhibit approximately two times larger p_T -shift between the central and peripheral collisions than the inclusive jets. This observation could be explained e.g. by the fact that the high momentum hadron trigger biases the population of the recoiled jets towards the jets with longer path length through the medium rather than towards the tangential jets as illustrated on Fig. 3.21.

Table 9.2: p_T -shift between jet yield distribution in peripheral and central collisions normalized by the average number of binary collisions for inclusive jets (left) and semi-inclusive recoil jets (right).

| Au+Au collisions, $\sqrt{s_{NN}}=200$ GeV $10 < p_{T,jet}^{ch} < 20$ GeV/ c | | |
|--|---|-------------------------------------|
| R | p_T -shift peripheral \rightarrow central (GeV/ c) | |
| | inclusive jets | h+jet [103] |
| 0.2 | $-2.2 \pm 0.1_{stat} \pm 0.5_{sys}$ | $-4.4 \pm 0.2_{stat} \pm 1.2_{sys}$ |
| 0.3 | $-2.3 \pm 0.1_{stat} \pm 0.5_{sys}$ | $-5.0 \pm 0.5_{stat} \pm 1.2_{sys}$ |
| 0.4 | $-2.1 \pm 0.1_{stat} \pm 0.6_{sys}$ | $-5.1 \pm 0.5_{stat} \pm 1.2_{sys}$ |

Chapter 10

Summary

In this thesis the first measurement of fully reconstructed and fully corrected charged jets in Au+Au collisions at $\sqrt{s_{NN}} = 200$ GeV at STAR has been reported.

The jet reconstruction in heavy-ion collisions represents a challenging task due to the large and fluctuating background from the underlying event with fluctuations of the magnitude of the signal. In this analysis the background was suppressed by applying a minimal cut on the jet area A_{\min} and on the momentum of the jet's leading hadron $p_{T,\text{lead}}^{\min}$. The later condition reduces the background effectively, unfortunately it also breaks the collinear safety of the jet reconstruction procedure and induces a bias on the jet fragmentation. The size of this bias was studied by comparing corrected charged jet spectra reconstructed using different values of $p_{T,\text{lead}}^{\min}$. The bias is decreasing with the jet momentum and for values of $p_{T,\text{jet}} > 3p_{T,\text{lead}}^{\min}$ it starts to be negligible.

The reported charged jet observables were corrected for background fluctuations as well as for the detector effects by means of Bayesian and SVD unfolding. A new framework for setting up and evaluating the unfolding procedure was presented. No significant difference between the results of these two methods was observed.

Measurement of nuclear modification factors R_{AA} and R_{CP} clearly show that the jet production is strongly suppressed in central Au+Au collisions with respect to p+p and peripheral Au+Au collisions at STAR (scaled by the mean number of binary collisions). Since no measurement of charged jet spectra in p+p collisions has been made by the STAR Collaboration so far, a simulated p+p spectrum from PYTHIA 6 MC event generator was first crosschecked with published full jet cross section in p+p collisions and then used as a baseline for the R_{AA} calculation. The obtained value of R_{AA} was compared with several theoretical models. All tested models significantly overestimate the R_{AA} value. However all the models calculate full (not charged) jet R_{AA} and do not impose any cut on leading hadron.

The measured R_{CP} of jets with momentum in range 10 – 20 GeV/c is consistent with the R_{CP} measurement done by ALICE at higher collisional energy of $\sqrt{s_{NN}} = 2.76$ TeV and for higher momentum range of the reconstructed jets, 40 – 100 GeV/c. At STAR the jet R_{CP} is higher than the hadron R_{CP} in the same momentum range, whereas on ALICE the jet R_{CP} is lower than the hadron one. This would suggest that the jet R_{CP} is driven

by hadrons with lower momentum: $p_T < 5$ GeV/ c in case of STAR and $p_T < 30$ GeV/ c in case of ALICE.

The jet inner structure was roughly explored by measuring ratios of jet yields for different jet radii. These ratios are consistent in Au+Au central, peripheral and p+p collisions which implies that the small jets are modified by the medium in a similar way as the large jets. The theoretical models, which were unable to describe the R_{AA} , describe the spectra ratios of different radii well.

Additionally, no dependence of R_{AA} and R_{CP} on R was observed. This would suggest that jet radius $R = 0.4$ is still insufficient to recover the energy dumped into medium. This is in a good agreement with the LHC results, where very large values $R > 0.8$ were required to recover the missing energy [105]. Looking at the ratios of spectra for different radius furthermore, one can conclude that the remaining core of the jet lies within a cone of radius $0.2 < R \leq 0.3$ since the ratio $R = 0.3/R = 0.4$ is very close to unity.

The future steps in the jet analysis at STAR would be utilization of high statistics High-Tower triggered data with use of the information from barrel electromagnetic calorimeter, allowing thus full jet reconstruction (i.e. including neutral energy) and higher kinematic reach with improved statistics.

As a part of the service work for the STAR Collaboration several tasks connected to the development of the Heavy Flavor Tracker for STAR were performed. Simulations of Λ_c reconstruction with the HFT showed that using the Kalman filter procedure for the secondary vertex reconstruction would allow the reconstruction of these heavy baryons down to very low momentum. Such a measurement would allow to study the meson/baryon anomaly also for heavy quarks. This would improve our understanding of the collectivity of the heavy quarks. As another task a procedure for measuring a whole sector of the Pixel subdetector with an optical scanning machine was developed and tested. Such a measurement in combination with an interpolation technique was necessary to determine the exact position of each pixel with precision of $\sim 1\mu m$. This was a necessary condition in order to achieve the HFT's designed secondary vertex reconstruction capabilities.

The Heavy Flavor Tracker was installed in 2013 for a testing run and since 2014 it was fully operational. It was successfully working for 3 years. It was decommissioned in 2016. The valuable data recorded by this state of the art detector are nowadays being analyzed. We can now joyfully trifle with the idea of how interesting and maybe surprising results are awaiting us.

Appendices

A STAR Data Production Chain

Data collecting by the STAR experiment is done in several-minutes-long sessions called “runs”¹). The data collecting is started by the personnel operating the detector once there are optimal conditions for the start of a run (the RHIC machine delivers stable beams and the collisions take place, the required STAR detectors are operational and working correctly). The run is stopped when the RHIC operators start to prepare for a beam down or when a problem either with the RHIC machine or with the STAR detector occurs.

The raw data from the STAR subdetectors are recorded when an event satisfying the triggering conditions (e.g. high energy deposition in a calorimetric cell) occurs. These data are then processed offline once the required computational resources are available. This processing consists of several tasks, e.g. track reconstruction, vertex finding, calculation of energy deposition in calorimetric cells, etc. These processed data are saved into so called microDST files. The microDST files are however very large, one year’s production can occupy several petabytes of the disk space. Therefore for each group of similar analyses a set of smaller dedicated files is produced containing only information necessary for the given analyses. These smaller files are called picoDST and one year’s production occupies only a few tens of terabytes of the disk space.

¹The RHIC’s one-year data collecting period is also called “Run”, but with the capital R and usually followed by the year number, e.g. Run 11.

B Bad Run List

Following runs have been removed from the analysis ²⁾:

12138*, 12139*, 12140*, 12141*, 12142*, 12143*, 12144*, 12145*, 12149*, 12150*, 12113091,
12114007, 12114035, 12114078, 12114092, 12114116, 12115009, 12115014, 12115015, 12115016,
12115018, 12115019, 12115020, 12115022, 12115023, 12115062, 12115073, 12115093, 12115094,
12116012, 12116054, 12117010, 12117016, 12117020, 12117065, 12119040, 12119042, 12120017,
12120026, 12121017, 12121022, 12121034, 12121050, 12121067, 12122019, 12127003, 12127010,
12127011, 12127017, 12127018, 12127032, 12128025, 12132043, 12132061, 12133018, 12134023,
12136005, 12136006, 12136014, 12136017, 12136022, 12136023, 12136024, 12136025, 12136027,
12136028, 12136029, 12136030, 12136031, 12136034, 12136054, 12146004, 12146006, 12146007,
12146008, 12151035, 12153002, 12153004, 12153007, 12153013, 12154043, 12157038, 12157051,
12158040, 12158041, 12158054, 12158056, 12158057, 12162055, 12162056, 12162057, 12162058,
12164037, 12164078, 12164079, 12166002, 12166003, 12167015, 12167024, 12167052, 12168002,
12168009, 12168022, 12168077, 12170044, 12170045, 12170054, 12170056, 12172050, 12172051,
12172055, 12173030, 12173031, 12173032, 12173033, 12173034, 12174067, 12174085, 12175062,
12175087, 12175113, 12175114, 12175115, 12176001, 12176044, 12176054, 12176071, 12177015,
12177061, 12177092, 12177099, 12177101, 12177106, 12177107, 12177108, 12178003, 12178004,
12178005, 12178006, 12178013, 12178099, 12178120

²⁾The asterix stands for all runs in a day

C List of Acronyms

| | |
|-------|---|
| ALICE | A Large Ion Collider Experiment |
| BEMC | Barrel Electro-Magnetic Calorimeter |
| CMS | Center of Mass |
| DCA | Distance of Closest Approach |
| DGLAP | Dokshitzer–Gribov–Lipatov–Altarelli–Parisi equation |
| EP | Event Plane |
| HFT | Heavy Flavor Tracker |
| HT | High Tower (trigger) |
| IST | Intermediate Silicon Tracker |
| JER | Jet Energy Resolution |
| JES | Jet Energy Scale |
| LHC | Large Hadron Collider |
| LHS | Left Hand Side |
| LO | Leading Order (calculation) |
| MB | Minimum Bias (trigger) |
| MC | Monte Carlo (method) |
| MWPC | MultiWire Proportional Chamber |
| NLO | Next to Leading Order (calculation) |
| pQCD | perturbative Quantum Chromo-Dynamics |
| PV | Primary Vertex |

| | |
|------|---------------------------------|
| PXL | Pixel detector |
| QA | Quality Assurance |
| QCD | Quantum Chromo-Dynamics |
| QED | Quantum Electro-Dynamics |
| QGP | Quark Gluon Plasma |
| RHIC | Relativistic Heavy Ion Collider |
| RHS | Right Hand Side |
| SSD | Silicon Strip Detector |
| STAR | Solenoidal Tracker at RHIC |
| SV | Secondary Vertex |
| SVD | Singular Value Decomposition |
| TOF | Time Of Flight |
| TPC | Time Projection Chamber |
| VPD | Vertex Position Detector |

Bibliography

- [1] J. T. F.R.S., *Philosophical Magazine Series 6* **7**, 237 (1904), <http://dx.doi.org/10.1080/14786440409463107> .
- [2] H. Geiger, *Proceedings of the Royal Society of London A: Mathematical, Physical and Engineering Sciences* **81**, 174 (1908), <http://rspa.royalsocietypublishing.org/content/81/546/174.full.pdf> .
- [3] H. Geiger and E. Marsden, *Proceedings of the Royal Society of London A: Mathematical, Physical and Engineering Sciences* **82**, 495 (1909), <http://rspa.royalsocietypublishing.org/content/82/557/495.full.pdf> .
- [4] H. Geiger, *Proceedings of the Royal Society of London A: Mathematical, Physical and Engineering Sciences* **83**, 492 (1910), <http://rspa.royalsocietypublishing.org/content/83/565/492.full.pdf> .
- [5] S. E. Rutherford, *Philosophical Magazine Series 6* **27**, 488 (1914), <http://dx.doi.org/10.1080/14786440308635117> .
- [6] E. Rutherford, *Philosophical Magazine* **90**, 31 (1919), <http://dx.doi.org/10.1080/14786431003659230> .
- [7] J. Chadwick, *Nature* **129**, 312 (1932).
- [8] M. Gell-Mann, *Physics Letters* **8**, 214 (1964).
- [9] G. Zweig, in *DEVELOPMENTS IN THE QUARK THEORY OF HADRONS. VOL. 1. 1964 - 1978*, edited by D. Lichtenberg and S. P. Rosen (1964) pp. 22–101.
- [10] S. L. Glashow, J. Iliopoulos, and L. Maiani, *Phys. Rev. D* **2**, 1285 (1970).
- [11] J. J. Aubert *et al.*, *Phys. Rev. Lett.* **33**, 1404 (1974).
- [12] J. E. Augustin *et al.*, *Phys. Rev. Lett.* **33**, 1406 (1974).
- [13] J. H. Christenson, J. W. Cronin, V. L. Fitch, and R. Turlay, *Phys. Rev. Lett.* **13**, 138 (1964).
- [14] M. Kobayashi and T. Maskawa, *Progress of Theoretical Physics* **49**, 652 (1973).

- [15] S. W. Herb *et al.*, *Phys. Rev. Lett.* **39**, 252 (1977).
- [16] F. Abe *et al.* (CDF Collaboration), *Phys. Rev. Lett.* **74**, 2626 (1995).
- [17] S. Abachi *et al.* (D0 Collaboration), *Phys. Rev. Lett.* **74**, 2422 (1995).
- [18] J. Bulava, K. Jansen, and A. Nagy, *Phys. Lett.* **B723**, 95 (2013), arXiv:1301.3416 [hep-lat] .
- [19] O. Eberhardt, G. Herbert, H. Lacker, A. Lenz, A. Menzel, U. Nierste, and M. Wiebusch, *Phys. Rev. Lett.* **109**, 241802 (2012).
- [20] “Figure: Standard model of elementary particles,” https://upload.wikimedia.org/wikipedia/commons/0/00/Standard_Model_of_Elementary_Particles.svg, accessed: 2016-05-04.
- [21] T. Ma and S. Wang, *Discrete Contin. Dyn. Syst.* **A35**, 1103 (2015), arXiv:1210.0448 [physics.gen-ph] .
- [22] G. Hooft, *Nuclear Physics B* **72**, 461 (1974).
- [23] A. Migdal, *Physics Reports* **102**, 199 (1983).
- [24] E. V. Shuryak, *Physics Reports* **61**, 71 (1980).
- [25] R. Hagedorn and J. Ranft, *Nucl. Phys.* **B48**, 157 (1972).
- [26] E. Fermi, *Prog. Theor. Phys.* **5**, 570 (1950).
- [27] I. Ya. Pomeranchuk, *Dokl. Akad. Nauk Ser. Fiz.* **78**, 889 (1951).
- [28] L. D. Landau, *Izv. Akad. Nauk Ser. Fiz.* **17**, 51 (1953).
- [29] R. Fiore, R. Hagedorn, and F. d’Isep, *Nuovo Cim.* **A88**, 301 (1985).
- [30] Z. Fodor and S. D. Katz, *JHEP* **04**, 050 (2004), arXiv:hep-lat/0402006 [hep-lat] .
- [31] T. Bhattacharya *et al.* (HotQCD Collaboration), *Phys. Rev. Lett.* **113**, 082001 (2014).
- [32] F. Karsch, *Lectures on quark matter. Proceedings, 40. International Universitätswochen for theoretical physics, 40th Winter School, IUKT 40, Lect. Notes Phys.* **583**, 209 (2002), arXiv:hep-lat/0106019 [hep-lat] .
- [33] G. Odyniec, *Journal of Physics: Conference Series* **455**, 012037 (2013).
- [34] G. Odyniec, *Proceedings, 3rd International Conference on New Frontiers in Physics (ICNFP 2014): Kolymbari, Crete, Greece, July 28-August 6, 2014, EPJ Web Conf.* **95**, 03027 (2015).

- [35] B. Svetitsky and A. Uziel, *Phys. Rev. D* **55**, 2616 (1997).
- [36] J. Kapusta, P. Lichard, and D. Seibert, *Phys. Rev. D* **44**, 2774 (1991).
- [37] X. Zhu, M. Bleicher, S. Huang, K. Schweda, H. Stöcker, N. Xu, and P. Zhuang, *Physics Letters B* **647**, 366 (2007).
- [38] A. Ali and G. Kramer, *The European Physical Journal H* **36**, 245 (2011).
- [39] J. D. Bjorken, (1982).
- [40] J. C. Collins, D. E. Soper, and G. F. Sterman, *Adv. Ser. Direct. High Energy Phys.* **5**, 1 (1989), [arXiv:hep-ph/0409313](https://arxiv.org/abs/hep-ph/0409313) [hep-ph] .
- [41] F. D. Aaron *et al.* (ZEUS, H1), *JHEP* **01**, 109 (2010), [arXiv:0911.0884](https://arxiv.org/abs/0911.0884) [hep-ex] .
- [42] H. Abramowicz *et al.* (ZEUS, H1), *Eur. Phys. J.* **C75**, 580 (2015), [arXiv:1506.06042](https://arxiv.org/abs/1506.06042) [hep-ex] .
- [43] V. N. Gribov and L. N. Lipatov, *Sov. J. Nucl. Phys.* **15**, 438 (1972), [*Yad. Fiz.*15,781(1972)].
- [44] Y. L. Dokshitzer, *Sov. Phys. JETP* **46**, 641 (1977), [*Zh. Eksp. Teor. Fiz.*73,1216(1977)].
- [45] G. Altarelli and G. Parisi, *Nuclear Physics B* **126**, 298 (1977).
- [46] “Lhapdf,” <https://lhapdf.hepforge.org>, accessed: 2016-08-31.
- [47] D. de Florian and W. Vogelsang, *Phys. Rev. D* **76**, 074031 (2007).
- [48] F. W. K. Firk, (2010), [arXiv:1011.1943](https://arxiv.org/abs/1011.1943) [nucl-ex] .
- [49] A. Ali and G. Kramer, *Eur. Phys. J.* **H36**, 245 (2011), [arXiv:1012.2288](https://arxiv.org/abs/1012.2288) [hep-ph] .
- [50] G. Altarelli and G. Parisi, *Nucl. Phys.* **B126**, 298 (1977).
- [51] K. Olive and P. D. Group, *Chinese Physics C* **38**, 090001 (2014).
- [52] L. Kluberg, P. A. Piroue, R. L. Sumner, D. Antreasyan, J. W. Cronin, H. J. Frisch, and M. J. Shochet, *Phys. Rev. Lett.* **38**, 670 (1977).
- [53] F. E. Close, J. Qiu, and R. G. Roberts, *Phys. Rev. D* **40**, 2820 (1989).
- [54] P. Shukla, (2001), [arXiv:nucl-th/0112039](https://arxiv.org/abs/nucl-th/0112039) [nucl-th] .
- [55] M. L. Miller, K. Reygers, S. J. Sanders, and P. Steinberg, *Ann. Rev. Nucl. Part. Sci.* **57**, 205 (2007), [arXiv:nucl-ex/0701025](https://arxiv.org/abs/nucl-ex/0701025) [nucl-ex] .
- [56] M. H. Thoma, *Phys. Lett.* **B273**, 128 (1991).

- [57] B. G. Zakharov, *JETP Letters* **86**, 444 (2007).
- [58] X.-N. Wang, M. Gyulassy, and M. Plumer, *Phys. Rev.* **D51**, 3436 (1995), arXiv:hep-ph/9408344 [hep-ph] .
- [59] R. Baier, Y. L. Dokshitzer, A. H. Mueller, S. Peigne, and D. Schiff, *Nucl. Phys.* **B483**, 291 (1997), arXiv:hep-ph/9607355 [hep-ph] .
- [60] B. G. Zakharov, *JETP Lett.* **65**, 615 (1997), arXiv:hep-ph/9704255 [hep-ph] .
- [61] R. Baier, D. Schiff, and B. G. Zakharov, *Ann. Rev. Nucl. Part. Sci.* **50**, 37 (2000), arXiv:hep-ph/0002198 [hep-ph] .
- [62] R. Baier, Y. L. Dokshitzer, A. H. Mueller, S. Peigne, and D. Schiff, *Nucl. Phys.* **B484**, 265 (1997), arXiv:hep-ph/9608322 [hep-ph] .
- [63] M. Gyulassy and M. Plumer, *Particles and nuclei. Proceedings, 12th International Conference, PANIC XII, Cambridge, USA, June 25-29, 1990*, *Nucl. Phys.* **A527**, 641 (1991).
- [64] D. A. Appel, *Phys. Rev.* **D33**, 717 (1986).
- [65] J. P. Blaizot and L. D. McLerran, *Phys. Rev.* **D34**, 2739 (1986).
- [66] C. A. Salgado and U. A. Wiedemann, *Phys. Rev. Lett.* **93**, 042301 (2004), arXiv:hep-ph/0310079 [hep-ph] .
- [67] R. Perez Ramos, *Eur. Phys. J.* **C62**, 541 (2009), arXiv:0811.2418 [hep-ph] .
- [68] R. Perez Ramos, *J. Phys.* **G36**, 105006 (2009), arXiv:0811.2934 [hep-ph] .
- [69] R. P. Feynman, R. D. Field, and G. C. Fox, *Nucl. Phys.* **B128**, 1 (1977).
- [70] R. Baier, *Nucl.Phys.* **A715**, 209 (2003), arXiv:hep-ph/0209038 [hep-ph] .
- [71] I. Vitev (2002) arXiv:hep-ph/0212109 [hep-ph] .
- [72] X.-N. Wang, *Statistical QCD. Proceedings, International Symposium, Bielefeld, Germany, August 26-30, 2001*, *Nucl. Phys.* **A702**, 238 (2002), arXiv:hep-ph/0208094 [hep-ph] .
- [73] G. P. Salam and G. Soyez, *JHEP* **05**, 086 (2007), arXiv:0704.0292 [hep-ph] .
- [74] S. D. Ellis and D. E. Soper, *Phys. Rev.* **D48**, 3160 (1993), arXiv:hep-ph/9305266 [hep-ph] .
- [75] M. Cacciari, G. P. Salam, and G. Soyez, *JHEP* **04**, 063 (2008), arXiv:0802.1189 [hep-ph] .

- [76] M. Cacciari, G. P. Salam, and G. Soyez, *Eur. Phys. J.* **C72**, 1896 (2012), [arXiv:1111.6097 \[hep-ph\]](#) .
- [77] M. Cacciari, G. P. Salam, and G. Soyez, *JHEP* **04**, 005 (2008), [arXiv:0802.1188 \[hep-ph\]](#) .
- [78] G. Voronoi, *Journal für die reine und angewandte Mathematik* **134**, 198 (1908).
- [79] B. I. Abelev *et al.* (STAR), *Phys. Rev. Lett.* **97**, 252001 (2006), [arXiv:hep-ex/0608030 \[hep-ex\]](#) .
- [80] B. Jäger, M. Stratmann, and W. Vogelsang, *Phys. Rev. D* **70**, 034010 (2004).
- [81] A. Adare *et al.* (PHENIX), *Phys. Rev. Lett.* **116**, 122301 (2016), [arXiv:1509.04657 \[nucl-ex\]](#) .
- [82] R. D. Ball, L. D. Debbio, S. Forte, A. Guffanti, J. I. Latorre, J. Rojo, and M. Ubiali, *Nuclear Physics B* **838**, 136 (2010).
- [83] B. Abelev *et al.*, *Physics Letters B* **722**, 262 (2013).
- [84] G. Soyez, *Physics Letters B* **698**, 59 (2011).
- [85] G. Aad *et al.* (ATLAS), *Eur. Phys. J.* **C71**, 1512 (2011), [arXiv:1009.5908 \[hep-ex\]](#) .
- [86] B. B. Abelev *et al.* (ALICE), *Phys. Rev.* **D91**, 112012 (2015), [arXiv:1411.4969 \[nucl-ex\]](#) .
- [87] G. Aad *et al.* (ATLAS), *JHEP* **02**, 153 (2015), [Erratum: *JHEP*09,141(2015)], [arXiv:1410.8857 \[hep-ex\]](#) .
- [88] Z. Nagy, *Phys. Rev.* **D68**, 094002 (2003), [arXiv:hep-ph/0307268 \[hep-ph\]](#) .
- [89] J. Adam *et al.* (ALICE), *Phys. Lett.* **B749**, 68 (2015), [arXiv:1503.00681 \[nucl-ex\]](#) .
- [90] G. Aad *et al.* (ATLAS), *Phys. Lett.* **B748**, 392 (2015), [arXiv:1412.4092 \[hep-ex\]](#) .
- [91] J. Adam *et al.* (ALICE), *Eur. Phys. J.* **C76**, 271 (2016), [arXiv:1603.03402 \[nucl-ex\]](#) .
- [92] N. Armesto, D. C. Gülhan, and J. G. Milhano, *Physics Letters B* **747**, 441 (2015).
- [93] A. Bzdak, V. Skokov, and S. Bathe, *Phys. Rev.* **C93**, 044901 (2016), [arXiv:1408.3156 \[hep-ph\]](#) .
- [94] M. Alvioli, B. A. Cole, L. Frankfurt, D. V. Perepelitsa, and M. Strikman, *Phys. Rev. C* **93**, 011902 (2016).
- [95] T. Renk, *Phys. Rev.* **C88**, 014905 (2013), [arXiv:1302.3710 \[hep-ph\]](#) .

- [96] K. C. Zapp, F. Krauss, and U. A. Wiedemann, *JHEP* **03**, 080 (2013), [arXiv:1212.1599 \[hep-ph\]](#) .
- [97] J. Adam *et al.* (ALICE), *Phys. Lett.* **B746**, 1 (2015), [arXiv:1502.01689 \[nucl-ex\]](#) .
- [98] T. Renk, *Phys. Rev. C* **78**, 034908 (2008).
- [99] G. Aad *et al.* (ATLAS), *Phys. Rev. Lett.* **114**, 072302 (2015), [arXiv:1411.2357 \[hep-ex\]](#) .
- [100] Y. He, I. Vitev, and B.-W. Zhang, *Phys. Lett.* **B713**, 224 (2012), [arXiv:1105.2566 \[hep-ph\]](#) .
- [101] C. Collaboration (CMS), (2012).
- [102] J. Adam *et al.* (ALICE), *JHEP* **09**, 170 (2015), [arXiv:1506.03984 \[nucl-ex\]](#) .
- [103] L. Adamczyk *et al.* (STAR), (2017), [arXiv:1702.01108 \[nucl-ex\]](#) .
- [104] G. Aad *et al.* (ATLAS), *Phys. Rev. Lett.* **105**, 252303 (2010), [arXiv:1011.6182 \[hep-ex\]](#) .
- [105] S. Chatrchyan *et al.* (CMS Collaboration), (2011), [arXiv:1102.1957 \[nucl-ex\]](#) .
- [106] L. Adamczyk *et al.* (STAR), (2016), [arXiv:1609.03878 \[nucl-ex\]](#) .
- [107] S. Campbell (sPHENIX), *Proceedings, Hot Quarks 2016: Workshop for Young Scientists on the Physics of Ultrarelativistic Nucleus-Nucleus Collisions (HQ2016): South Padre Island, Texas, September 12-17, 2016*, *J. Phys. Conf. Ser.* **832**, 012012 (2017), [arXiv:1611.03003 \[physics.ins-det\]](#) .
- [108] P. Thieberger, M. McKeown, and H. E. Wegner, *Proceedings of the 1983 Particle Accelerator Conference (PAC 83): Accelerator Engineering and Technology, Santa Fe, New Mexico March 21-23, 1983*, *IEEE Trans. Nucl. Sci.* **30**, 2746 (1983).
- [109] H. Hahn *et al.*, *Nucl. Instrum. Meth.* **A499**, 245 (2003).
- [110] A. Zelensky *et al.*, *Polarized sources and targets. Proceedings, 9th International Workshop, PST 2001, Nashville, USA, September 30-October 4, 2001*, *Rev. Sci. Instrum.* **73**, 888 (2002), [,194(2002)].
- [111] “Nuclear science and technology,” <http://nsw.org/projects/bnl/star/sub-systems.php>, accessed: 2016-09-23.
- [112] D. Beavis *et al.*, “The STAR Heavy Flavor Tracker Technical Design Report,” <https://drupal.star.bnl.gov/STAR/starnotes/public/sn0600> (2011).
- [113] B. I. Abelev (STAR Collaboration), *Phys. Rev. Lett.* **97**, 152301 (2006).

- [114] S. Voloshin, [Nuclear Physics A **715**, 379c \(2003\)](#), quark Matter 2002 Proceedings of the 16th International Conference on Ultra-Relativistic Nucleus-Nucleus Collisions.
- [115] S. Gorbunov and I. Kisel, CBM-SOFT-note-2007-003 (2007).
- [116] J. Kapitan (STAR), *Proceedings, Workshop for Young Scientists on the Physics of Ultrarelativistic Nucleus-Nucleus Collisions (Hot Quarks 2008): Estes Park, USA, August 18-23, 2008*, [Eur. Phys. J. **C62**, 217 \(2009\)](#), [arXiv:0811.2311 \[nucl-ex\]](#) .
- [117] J. Kapitan, Private communication. (2011).
- [118] B. I. Abelev *et al.* (STAR), [Phys. Rev. Lett. **97**, 152301 \(2006\)](#), [arXiv:nucl-ex/0606003 \[nucl-ex\]](#) .
- [119] G. Agakishiev *et al.* (STAR), [Phys. Rev. Lett. **108**, 072302 \(2012\)](#), [arXiv:1110.0579 \[nucl-ex\]](#) .
- [120] G. Agakishiev *et al.* (STAR), [Phys. Rev. Lett. **108**, 072301 \(2012\)](#), [arXiv:1107.2955 \[nucl-ex\]](#) .
- [121] J. Adams *et al.* (STAR), [Phys. Lett. **B616**, 8 \(2005\)](#), [arXiv:nucl-ex/0309012 \[nucl-ex\]](#) .
- [122] A. Adare *et al.* (PHENIX), [Phys. Rev. **C92**, 034913 \(2015\)](#), [arXiv:1412.1043 \[nucl-ex\]](#) .
- [123] G. D'Agostini, ArXiv e-prints (2010), [arXiv:1010.0632 \[physics.data-an\]](#) .
- [124] A. Hocker and V. Kartvelishvili, [Nucl.Instrum.Meth. **A372**, 469 \(1996\)](#), [arXiv:hep-ph/9509307 \[hep-ph\]](#) .
- [125] R. Narayan and R. Nityananda, [Annual Review of Astronomy and Astrophysics **24**, 127 \(1986\)](#), <https://doi.org/10.1146/annurev.aa.24.090186.001015> .
- [126] X. Li, *Proceedings, 23rd International Workshop on Deep-Inelastic Scattering and Related Subjects (DIS 2015): Dallas, Texas, USA, April 27-May 01, 2015*, [PoS **DIS2015**, 203 \(2015\)](#), [arXiv:1506.06314 \[hep-ex\]](#) .
- [127] I. Vitev and B.-W. Zhang, [Phys. Rev. Lett. **104**, 132001 \(2010\)](#), [arXiv:0910.1090 \[hep-ph\]](#) .
- [128] J.-W. Qiu and I. Vitev, [Phys. Lett. **B587**, 52 \(2004\)](#), [arXiv:hep-ph/0401062 \[hep-ph\]](#) .
- [129] A. Accardi, (2002), [arXiv:hep-ph/0212148 \[hep-ph\]](#) .
- [130] H. Xing, Y. Guo, E. Wang, and X.-N. Wang, [Nucl. Phys. **A879**, 77 \(2012\)](#), [arXiv:1110.1903 \[hep-ph\]](#) .

- [131] J. Casalderrey-Solana, D. C. Gulhan, J. G. Milhano, D. Pablos, and K. Rajagopal, *JHEP* **10**, 019 (2014), [Erratum: *JHEP*09,175(2015)], [arXiv:1405.3864 \[hep-ph\]](#) .
- [132] J. Casalderrey-Solana, H. Liu, D. Mateos, K. Rajagopal, and U. A. Wiedemann, (2011), [10.1017/CBO9781139136747](#), [arXiv:1101.0618 \[hep-th\]](#) .
- [133] Y.-T. Chien, A. Emerman, Z.-B. Kang, G. Ovanesyan, and I. Vitev, *Phys. Rev.* **D93**, 074030 (2016), [arXiv:1509.02936 \[hep-ph\]](#) .
- [134] T. Sjöstrand, S. Mrenna, and P. Skands, *Journal of High Energy Physics* **2006**, 026 (2006).
- [135] M. Bahr *et al.*, *Eur. Phys. J.* **C58**, 639 (2008), [arXiv:0803.0883 \[hep-ph\]](#) .
- [136] B. Abelev *et al.* (ALICE Collaboration), (2013), [arXiv:1311.0633 \[nucl-ex\]](#) .
- [137] J. Adams *et al.* (STAR), *Phys.Rev.Lett.* **91**, 172302 (2003), [arXiv:nucl-ex/0305015 \[nucl-ex\]](#) .
- [138] G. Aad *et al.* (ATLAS), *JHEP* **09**, 050 (2015), [arXiv:1504.04337 \[hep-ex\]](#) .

Published Papers

Inclusive spectrum of charged jets in central Au+Au collisions at $\sqrt{s_{NN}} = 200$ GeV by STAR

Jan Rusnak^{*†}

Nuclear Physics Institute, Academy of Sciences of Czech Republic, Na Truhlárce 39/64, 180 86 Prague, Czech Republic

E-mail: rusn@email.cz

Jets are collimated sprays of particles arising from the fragmentation of hard-scattered partons in high-energy collisions. In collisions of heavy nuclei, jets serve as probes of the hot and dense nuclear matter created, and the study of the modification of their structure due to interaction with the surrounding medium (known as "jet quenching") is an important tool for understanding the medium properties.

Jet quenching can be studied via single particle and few-particle correlations, however, only full jet reconstruction can lead to a comprehensive understanding of jet quenching and corresponding medium properties. Due to the large and fluctuating background, full jet reconstruction in heavy-ion collisions is an extremely challenging task.

In this proceedings a new measurement of the inclusive spectrum of charged jets in central Au+Au collisions at center of mass energy $\sqrt{s_{NN}}=200$ GeV, by the STAR collaboration at RHIC is presented. An experimental technique is utilized, in which the jet reconstruction is stable against emission of an additional soft hadron ("infrared safety"), even in the high-multiplicity environment. The large combinatorial background is suppressed by a threshold cut on the leading hadron of each jet candidate. The influence of the background density fluctuations on the inclusive jet spectrum is then corrected by an iterative unfolding technique based on Bayes's Theorem.

*The European Physical Society Conference on High Energy Physics -EPS-HEP2013
18-24 July 2013
Stockholm, Sweden*

^{*}Speaker.

[†]for the STAR Collaboration

1. Motivation

At high energy density (about $1 \text{ GeV}/\text{fm}^3$) Quantum Chromodynamics (QCD) predicts a transition between confined, hadronic matter and a new, deconfined state of matter - the Quark-Gluon Plasma (QGP) [1] where quarks and gluons rather than hadrons are expected to be the dominant degrees of freedom over length scales larger than that of nucleon. Experiments studying the collision of heavy nuclei at high energy at both the Relativistic Heavy Ion Collider (RHIC) [2], and recently at the Large Hadron Collider (LHC) [3, 4], have made several key observations that point to the formation of a hot, dense and strongly coupled system - possibly the Quark Gluon Plasma.

A QCD jet is a correlated spray of hadrons arising from the fragmentation and hadronization of a virtual quark or gluon which is generated in a hard momentum transfer between partons in the nucleus-nucleus collisions. However, the definition of a jet is not unique, and various jet reconstruction algorithms have been developed that satisfy certain criteria (collinear and infrared safety, numerical robustness, speed) that allow them to be applied to both experimental data and perturbative QCD calculations in a systematically well-controlled and comparable way. Jet production rate is calculable using perturbative QCD. It can be compared to the measurements in elementary proton-proton collisions, with a good agreement found over a broad kinematic range of next-to-leading-order (NLO) perturbative QCD calculations and the measurements [5].

Jets, as large momentum transfer probes, are well calibrated tools to study the properties of the matter created in heavy-ion collisions. The scattered partons generated in a hard momentum exchange are created in the initial stages of the collision. They propagate through the medium, where their form observed jets of hadrons. However, their fragmentation is expected to be modified relative to the vacuum case by interactions with the dense, colored medium (jet quenching) [6]. This modification of parton fragmentation provides sensitive observables to study properties of the created matter.

Jet reconstruction in the environment of a high energy nuclear collision is a challenging task, due to the large and complex underlying background, whose magnitude is comparable to the highest jet energies accessible at RHIC, and whose local fluctuations within an event can easily disturb measured jet distributions.

Jet quenching was therefore initially accessed using inclusive production of hadrons with high transverse momentum (p_T) and semi-inclusive correlations. They were observed to be strongly suppressed in central A-A collisions when compared to p-p collisions at both RHIC and LHC [7, 8].

Since jet quenching results in softening of the distribution of hadronic fragments within a jet, selection of jets containing high p_T hadrons biases the observed population against jets that have undergone significant energy loss in the medium. High p_T hadron probes provide therefore only indirect and biased information on the parton evolution in the medium. The aim of full jet reconstruction is to measure jet modifications due to energy loss without imposing any strong bias.

Our main goal is to perform jet measurements at the STAR experiment at RHIC using the same techniques and algorithms as at the ALICE experiment at the LHC so the results can be directly compared.

2. Jet Reconstruction and Analysis

Data from 0-10% most central Au+Au collisions at $\sqrt{s_{NN}} = 200$ GeV measured by the STAR experiment at RHIC during Run 2011 are used in this analysis.

Charged tracks from the Time Projection Chamber (TPC) are used as an input for the jet reconstruction. All tracks are required to have $p_T > 200 \text{ MeV}/c$. FASTJET software and its implementation of k_T and anti- k_T algorithms [9] are used for the jet reconstruction. Anti- k_T algorithm is then used to reconstruct signal jets whereas k_T algorithm is used for the calculation of background energy density. Jet resolution parameter R (which roughly corresponds to the radius of jet cone $R \sim \sqrt{(\Delta\eta)^2 + (\Delta\phi)^2}$) is chosen to be $R = 0.4$ and $R = 0.2$. The fiducial jet acceptance is then $|\eta| < 1 - R$ in pseudorapidity and full azimuth. Jet is defined as the output of anti- k_T algorithm in order to overcome the difficulties arising from complex relations between hard jet component and underlying fluctuating background. The separation of hard jets from background is left to a later step.

In the next step, reconstructed jet transverse momentum p_T^{rec} is corrected for the background energy density

$$p_T^{corr} = p_T^{rec} - \rho \cdot A \quad (2.1)$$

where $\rho = \text{med}\left\{\frac{p_{T,i}^{rec}}{A_i}\right\}$ is the event-wise median background energy density calculated using the k_T algorithm, i runs through all reconstructed jets in the event and A is the jet area calculated using the FASTJET method [10].

In order to determine the response of the jet to the presence of the highly fluctuating and complex background we embed a simulated jet (single particle, Pythia jet) with known transverse momentum (p_T^{emb}) into a real event and calculate δp_T given by

$$\delta p_T = p_T^{rec} - \rho \cdot A - p_T^{emb} = p_T^{corr} - p_T^{emb} \quad (2.2)$$

It was shown, that the δp_T distribution is practically independent on the choice of the fragmentation model of the embedded jet [11]. With the knowledge of the δp_T and with use of a Monte Carlo (MC) generator, a response matrix of the system can be calculated which maps the true p_T distribution to the measured one.

In the final step, the measured p_T^{corr} distribution is ‘‘unfolded’’ using an iterative unfolding technique based on Bayes’ theorem [12]. However to make the unfolding process converge, one has to reduce the background prior the unfolding [13]. To do so, a cut on jet area [10] $A > 0.4$ in case of $R = 0.4$ and $A > 0.09$ for $R = 0.2$ is applied. Moreover a cut on the transverse momentum of the leading hadron ($p_T^{leading}$) of the jet is imposed. Such a cut still allows the jet to have a large part of its energy carried by the soft hadrons, which is essential for the unbiased jet quenching studies.

3. Results

Since an iterative unfolding technique is used, one has to choose an optimal number of iterations. Using the MC simulations, 4 to 5 iterations were determined as a sufficient number. Unfolded results should be comparable for two successive iterations if the process converges. Such

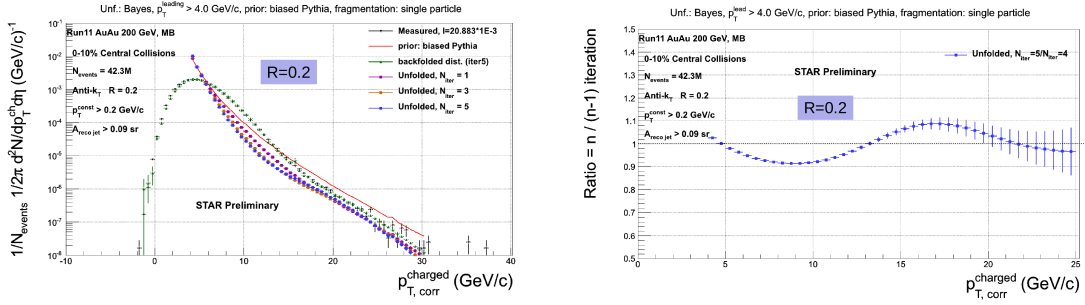


Figure 1: Left: The unfolded p_T spectrum of charged jets in central Au+Au collisions for several iterations. Right: Ratio of unfolded spectra for 4th and 5th iteration. The jets were reconstructed with anti- k_T algorithm with $R=0.2$ and $p_T^{\text{leading}} > 4\text{GeV}/c$.

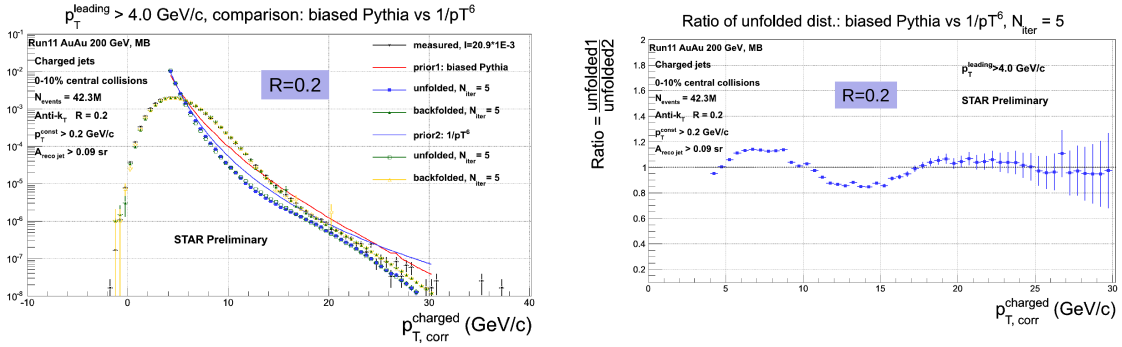


Figure 2: Left: The unfolded p_T spectrum of charged jets in central Au+Au collisions for two choices of prior: p_T^{-6} and “biased Pythia”. Right: Ratio of unfolded spectra. The jets were reconstructed with anti- k_T algorithm with $R=0.2$, $p_T^{\text{leading}} > 4\text{GeV}/c$.

a comparison is shown in Fig. 1. A less than 10% difference between the 4th and 5th iteration has been achieved.

As a starting point for the iterative unfolding technique, one has to choose prior p_T distribution. Ideally, the unfolded result should be independent on the choice of the prior. In practice, however, this holds only until the prior is chosen reasonably close to the expected result. In our study we compare results obtained from two physically reasonable priors: p_T^{-6} spectrum and spectrum of Pythia jets with imposed p_T^{leading} cut (“biased Pythia”). Fig. 2 compares unfolded spectra for these two choices of priors. A difference of less than 20% has been achieved.

4. Conclusion and Outlook

We have showed that the Bayesian iterative unfolding of p_T spectrum of inclusive charged jets converges and is not significantly dependent on the choice of prior distribution. Jets were reconstructed with $R = 0.2$ in this analysis and $p_T^{\text{leading}} > 4\text{GeV}/c$ showed up as a sufficient value to make the unfolding converge.

As a next step a different unfolding technique - Singular Value Decomposition (SVD) [14] will be used as a crosscheck in order to verify the results of Bayesian unfolding. Final step will

be the full jet reconstruction using the information from the Barrel ElectroMagnetic Calorimeter (BEMC).

References

- [1] F. Karsch and E. Laermann. Thermodynamics and in-medium hadron properties from lattice QCD. In Rudolph C. Hwa, editor, *Quark-Gluon Plasma 3*, pages 1-59. World Scientific, 2003.
- [2] J. Adams et al. Experimental and theoretical challenges in the search for the quark gluon plasma: The STAR collaboration's critical assessment of the evidence from RHIC collisions. *Nucl. Phys.*, A757:102-183, 2005.
- [3] K. Aamodt et al. Charged-particle multiplicity density at mid-rapidity in central Pb-Pb collisions at $\sqrt{s_{NN}} = 2.76$ TeV. *Phys. Rev. Lett.*, 105(25):252301, December 2010.
- [4] K. Aamodt et al. Elliptic flow of charged particles in Pb-Pb collisions at 2.76 TeV. *Phys. Rev. Lett.*, 105(25):252302, December 2010.
- [5] B. Abelev et al. Longitudinal Double-Spin Asymmetry and Cross Section for Inclusive Jet Production in Polarized Proton Collisions at $\sqrt{s} = 200$ GeV. *Phys. Rev. Lett.*, 97:252001, 2006.
- [6] Miklos Gyulassy and Michael Plumer. Jet quenching in dense matter. *Phys. Lett.*, B243:432-438, 1990.
- [7] K. Adcox et al. Suppression of Hadrons with Large Transverse Momentum in Central Au+Au Collisions at $\sqrt{s_{NN}} = 130$ GeV. *Phys. Rev. Lett.*, 88:022301, 2002.
- [8] K. Aamodt et al. Suppression of Charged Particle Production at Large Transverse Momentum in Central Pb-Pb Collisions at $\sqrt{s_{NN}} = 2.76$ TeV. *Phys. Lett.*, B696:30-39, 2011.
- [9] M. Cacciari, G. P. Salam, G. Soyez. FastJet user manual. *arXiv:1111.6097*, 2011.
- [10] M. Cacciari, G. P. Salam and G. Soyez, *JHEP*, 0804:005, 2008.
- [11] P. Jacobs. Background Fluctuations in Heavy Ion Jet Reconstruction. *arXiv:1012.2406*, 2010.
- [12] G. D'Agostini. Improved iterative Bayesian unfolding. *arXiv:1010.0632*, 2010.
- [13] G. O. V. de Barros, B. Fenton-Olsen, P. Jacobs, M. Ploskon. Data-driven analysis methods for the measurement of reconstructed jets in heavy ion collisions at RHIC and LHC.
- [14] A. Hoecker, V. Kartvelishvili. SVD Approach to Data Unfolding. *Nucl.Instrum.Meth.*, A372:469-481, 1996. *arXiv:1208.1518*, 2012.

Charged jet reconstruction in Au+Au collisions at $\sqrt{s_{NN}} = 200$ GeV at RHIC

Jan Rusnak¹

¹*rusn@email.cz, Nuclear Physics Institute ASCR, Na Truhlarce 39/64, 180 86 Praha 8, Czech Republic*

Abstract. Jets represent an important tool to explore the properties of the hot and dense nuclear matter created in heavy-ion collisions. However, full jet reconstruction in such events is a challenging task due to extremely large and fluctuating background, which generates a large population of combinatorial jets that overwhelm the true hard jet population. In order to carry out accurate, data-driven jet measurements over a broad kinematic range in the conditions of small signal to background ratio, we use several novel approaches in order to measure inclusive charged jet distributions and semi-inclusive charged jet distributions recoiling from a high p_T hadron trigger in central Au+Au collisions at $\sqrt{s_{NN}} = 200$ GeV. A very low infrared cutoff on jet constituents of 200 MeV/ c is applied in all measurements. These jet measurements allow a direct comparison of jet quenching at RHIC and the LHC.

1 Motivation

Jets - collimated sprays of hadrons - are well calibrated tools to study the properties of the matter created in heavy-ion collisions [1]. They are created by fragmentation and hadronization of scattered partons generated in hard momentum exchange in the initial stages of the collision. While traversing the medium, they interact with the surrounding hot and dense matter resulting in modification of their fragmentation with respect to the vacuum case (jet quenching)[2]. This modification of parton fragmentation provides sensitive observables to study properties of the created matter.

Jet reconstruction in the environment of a high energy nuclear collision is a challenging task, due to the large and complex underlying background and its fluctuations within an event which can easily disturb measured jet distributions. In order to overcome the obstacles of jet reconstruction in heavy-ion collisions, we utilize two different methods. The first method filters out the fake “combinatorial” jets by imposing a cut on the transverse momentum of the leading hadron of each jet. This procedure however imposes a bias on the jet fragmentation. The second method chooses the hard event by requiring a high momentum hadron trigger. A jet back-to-back to the trigger is then reconstructed. No cut is imposed on the jet constituents (except a low- p_T cut of 200MeV/ c) and the jet fragmentation is therefore nearly unbiased.

2 Analysis

We have analyzed data from 0-10% central Au+Au collisions at $\sqrt{s_{NN}} = 200$ GeV measured by the STAR experiment at RHIC during the run 2011.

Jets are reconstructed using only charged tracks recorded by the STAR Time Projection Chamber (TPC). All tracks are required to have $p_T \geq 200$ MeV/ c . Implementation of the anti- k_T algorithm in the FASTJET software [3] is used for jet reconstruction.

The jet resolution parameter R is chosen to be $R = 0.3$. The fiducial jet acceptance is then $|\eta| < 1 - R$ in pseudorapidity and full azimuth.

In the next step, reconstructed jet transverse momentum p_T^{rec} is corrected for the average background energy density

$$p_T^{corr} = p_T^{rec} - \rho \cdot A \quad (1)$$

where $\rho = \text{med}\left\{\frac{p_{T,i}^{rec}}{A_i}\right\}$ is the event-wise median background energy density and A is the jet area calculated with the k_T algorithm using the method [4].

2.1 Inclusive Jet Analysis

In order to determine the response of the jet to the presence of the highly fluctuating and complex background we embed a simulated jet with known transverse momentum (p_T^{emb}) into a real event and calculate δp_T as

$$\delta p_T = p_T^{rec} - \rho \cdot A - p_T^{emb} = p_T^{corr} - p_T^{emb} \quad (2)$$

It was shown, that the δp_T distribution is not significantly dependent on the choice of the fragmentation model of the embedded jet [5]. With the knowledge of the δp_T and with use of a Monte Carlo (MC) generator, a response matrix of the system can be calculated which maps the true p_T distribution to the measured one.

A jet momentum distribution is smeared not only by background fluctuations, but also by detector effects. An MC simulation using a parametrization of the TPC tracking efficiency is used to calculate an approximate detector response matrix.

In order to reduce the combinatorial background, a cut on the transverse momentum of the leading hadron ($p_T^{leading}$) of the jet is imposed. Also a cut on the jet area [4] $A > 0.2$ in case of $R = 0.3$ and $A > 0.09$ for $R = 0.2$ is applied.

In the final step, the measured p_T^{corr} distribution is corrected for the background and detector effects

using an iterative unfolding technique based on Bayes' theorem [6].

Results

Figure 1 shows the p_T spectrum of inclusive charged jets in central Au+Au collisions at $\sqrt{s_{NN}} = 200$ GeV for $R=0.3$ corrected for background and detector effects.

2.2 Trigger Recoil Jet Analysis

A trigger hadron is required to have momentum $9 \leq p_T \leq 19$ GeV/c. A jet is then reconstructed in azimuth ϕ satisfying

$$|\phi - \pi| < \frac{\pi}{4} \quad (3)$$

where the position $\phi = 0$ is defined by the trigger position.

In order to estimate the effect of the presence of the fluctuating background a set of Mixed Events (ME) is created. A mixed event is composed of N tracks randomly picked up from N different, randomly chosen events (however all the N events come from the same centrality bin, z -vertex bin and event plane direction Ψ_{EP} bin). All high- p_T tracks are discarded. Such a mixed event does not exhibit any physical correlations between the tracks; on the other hand it describes the key features of the background (detector acceptance inhomogeneities, total track multiplicity, etc.). The mixed event distribution is then subtracted from the (unmixed) Same Event (SE) distribution.

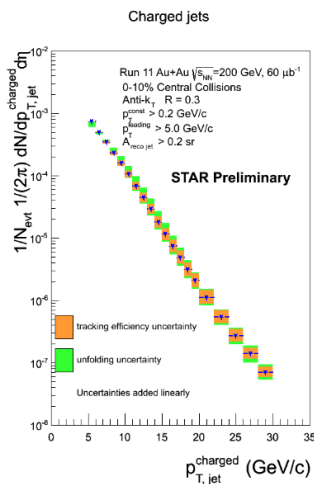


Figure 1. The corrected p_T spectrum of inclusive charged jets in central Au+Au collisions at $\sqrt{s_{NN}} = 200$ GeV for $R=0.3$.

Instead of correcting the results for background and detector effects by means of unfolding, a simulated PYTHIA p+p spectrum is smeared by these effects. This smeared p+p reference is then compared with the measured Au+Au data.

Results

Figure 2 shows a comparison of the measured recoil jet spectrum (SE-ME) in central Au+Au collisions and smeared PYTHIA p+p spectrum for $R=0.3$. A suppression of the measured spectrum is apparent with respect to PYTHIA.

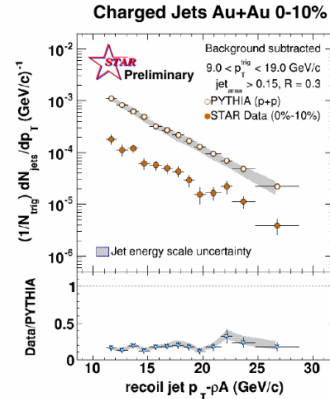


Figure 2. The recoil jet spectrum in central Au+Au collisions and smeared PYTHIA p+p spectrum at $\sqrt{s_{NN}} = 200$ GeV for $R=0.3$.

3 Conclusion

We have presented preliminary results of ongoing jet measurements at the STAR experiment. These measurements utilize low-bias methods of jet reconstruction allowing direct comparison with theory.

We have used a new technique of the mixed events for jet background estimation in heavy-ion collisions.

Further detector corrections and other effects are yet to be included.

4 Acknowledgment

The work has been supported by the MEYS grant CZ.1.07/2.3.00/20.0207 of the European Social Fund (ESF) in the Czech Republic: “Education for Competitiveness Operational Programme” (ECOP).

References

- [1] B. I. Abelev *et al.*, Phys. Rev. Lett. **97** 252001 (2006).
- [2] Miklos Gyulassy and Michael Plumer, Phys. Lett. B **243** 432-438 (1990).
- [3] M. Cacciari, G. P. Salam, G. Soyez. FastJet user manual. *arXiv:1111.6097* (2011).
- [4] M. Cacciari, G. P. Salam and G. Soyez, JHEP **0804** 005 (2008).
- [5] P. Jacobs, Background Fluctuations in Heavy Ion Jet Reconstruction. *arXiv:1012.2406* (2010).
- [6] G. D’Agostini, Improved iterative Bayesian unfolding. *arXiv:1010.0632* (2010).

Semi-Inclusive Jet measurements in Au+Au collisions at $\sqrt{s_{NN}} = 200$ GeV at STAR

Jan Rusnak^{*†}

*Nuclear Physics Institute, Czech Academy of Sciences,
Na Truhlarce 39/64, 180 86 Prague, Czech Republic
E-mail: rusn@email.cz*

Jets represent an important tool to explore the properties of the hot and dense nuclear matter created in heavy-ion collisions. However, their reconstruction presents a challenging task due to the extremely large and fluctuating background that overwhelms the true hard jet population. We present recent measurements of charged jets in Au+Au collisions, by the STAR collaboration at RHIC, where the background is suppressed via a new technique based on event mixing. The measured observable is the semi-inclusive yield of recoil jets from a high p_T hadron trigger. This jet measurement allows a comparison of jet quenching at RHIC and the LHC and provides new constraints on theoretical calculations of jet quenching.

*The European Physical Society Conference on High Energy Physics
22–29 July 2015
Vienna, Austria*

^{*}Speaker.

[†]for the STAR collaboration

1. Introduction

Jet reconstruction in the environment of heavy-ion collisions has to correct for the large and highly fluctuating background. A way to avoid the bias on the jet fragmentation caused by imposing a momentum cut on the jet constituents is to bias the event selection instead. This can be done by selecting a high momentum hadron trigger. Jets reconstructed on the away side in azimuth will be completely unbiased with respect to their fragmentation (there is no need to impose a cut on the constituents' momenta). On the other hand such a jet population will be biased towards larger path-length in the medium. We measure an observable of this process which is calculable by means of pQCD, the semi-inclusive recoil jet yield per trigger.

2. Experimental Setup

The data were recorded by the STAR experiment at the Relativistic Heavy Ion Collider (RHIC) in Brookhaven National Laboratory, USA. The STAR detector has full azimuthal coverage and possesses a tracking ability via a large Time Projection Chamber (TPC) which tracks and identifies charged particles down to a transverse momentum of 100 MeV/c. The TPC is surrounded by a Barrel Electromagnetic Calorimeter (BEMC), Time Of Flight (TOF), a Muon Telescope Detector (MTD) and a solenoidal magnet with field strength of 0.5 T. Further information about the STAR experiment and the TPC can be found in [1, 2].

The data were recorded with a Minimum Bias (MB) trigger during the 2011 RHIC run, for Au+Au collisions at $\sqrt{s_{NN}}=200$ GeV. Two collision centrality classes were selected, corresponding to the 0-10% (central) and 60-80% (peripheral) percentile intervals of the distribution of raw TPC multiplicity. Events are required to have the z position of the primary vertex within 30 cm of the center of the TPC.

3. Jet Reconstruction

Charged jets are reconstructed from TPC charged tracks. The TPC tracks were required to have transverse momenta $p_T > 0.2$ GeV/c, pseudo-rapidity $|\eta| < 1$ and at least 15 TPC space-points. The tracks were clustered into jets using the anti- k_T algorithm implemented in the FastJet software package [3, 4]. The jet area A was then calculated using the population of soft "ghost particles" [5]. Each reconstructed jet p_T is adjusted for background energy on an event-by-event basis according to

$$p_{T,\text{jet}}^{\text{reco}} = p_{T,\text{jet}} - \rho \times A \quad (3.1)$$

where ρ is the background energy density calculated for each event as the median jet energy density $\frac{p_{T,\text{jet}}^i}{A_i}$ from all reconstructed jets in the event, excluding 2 (peripheral) or 3 (central events) hardest jets in the event. The background jets are reconstructed using the k_T algorithm.

The size of the reconstructed jet is determined by the jet resolution parameter R , with $R = 0.3$ for the results reported here. All jets are required to lie within the fiducial rapidity acceptance $|\eta| < 1 - R$. Jets accepted for the recoil distribution have their centroid within 45 degrees of the trigger axes, opposite in azimuth to the trigger hadron,

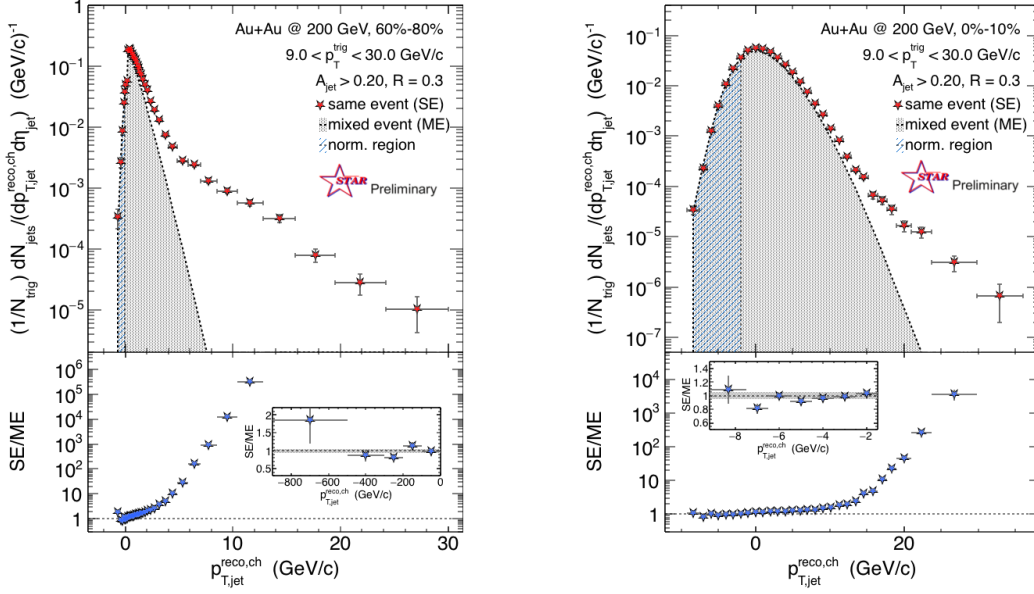


Figure 1: Raw recoil jet spectrum and mixed event (top panel) and their ratio (bottom panel) in Au+Au collisions at $\sqrt{s_{NN}} = 200$ GeV. Left: peripheral (60-80%) collisions, right: central (0-10%) collisions.

$$|\phi_{Jet} - (\phi_{Trig} + \pi)| \leq \pi/4. \quad (3.2)$$

Trigger hadrons lie in the interval $9 < p_T^{\text{trig}} < 20$ GeV/c. Event selection is based solely on the presence of a trigger hadron. All jets falling into the recoil acceptance are counted in the recoil spectrum, which is normalized per trigger and is constructed to be semi-inclusive.

4. Background Subtraction

In order to subtract the uncorrelated combinatorial background that is unavoidably present in a heavy-ion collision high multiplicity environment, a unique mixed event method was developed. The mixed event is generated by randomly selecting tracks from real events in the same centrality bin, event plane direction bin and primary vertex z position bin. Tracks with $p_T > 3$ GeV/c are discarded. A fully uncorrelated sample of tracks is thus created, which preserves essential features of the real events, such as the detector acceptance inefficiencies.

The jet analysis is then carried out on the mixed event (ME) population in the same way as for the real events (SE), but with the trigger hadron now chosen in a random direction. The resulting ME recoil jet spectrum is absolutely normalized, with a small adjustment in normalization to match the LHS of the real event spectrum. The normalization region was systematically varied and the resulting variance was included in the systematic uncertainties.

Fig. 1 shows both the same event and mixed event recoil charged jet spectra in peripheral and central Au+Au collisions, normalized per trigger yield. As one would expect, the background is much less severe in the peripheral collisions than in the most central ones. The bottom panels show the ratio SE/ME. There is excellent agreement of the ME background distribution with the

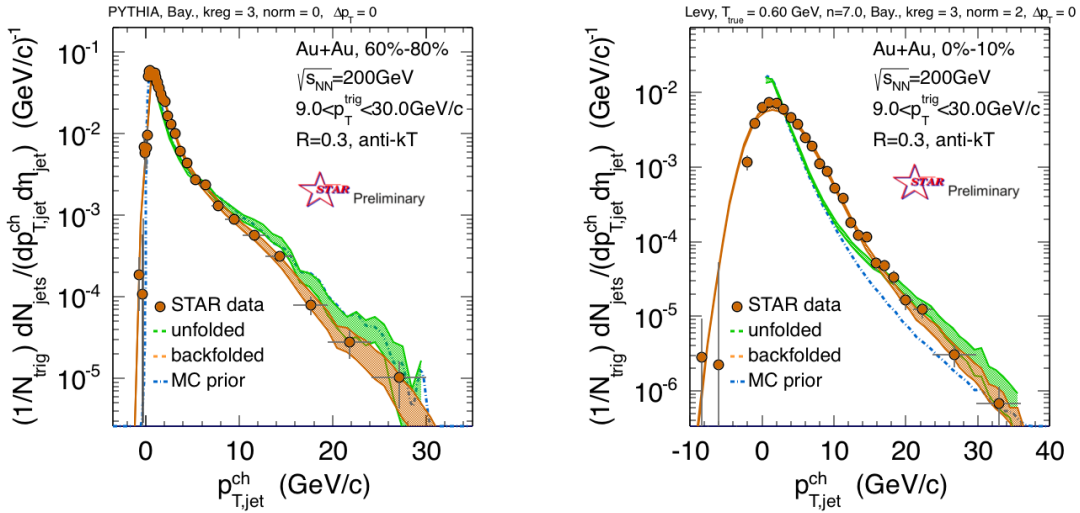


Figure 2: Example of unfolded recoil jet spectra for one particular prior distribution and regularization parameter value. Left: peripheral (60-80%) collisions, right: central (0-10%) collisions.

LHS of the SE; the ME distribution describes accurately the uncorrelated background in the SE distribution. In central collisions, the low momentum spectrum is dominated by the background. The correlated recoil jet signal is then extracted by subtracting the mixed event spectrum from the same event.

5. Results

The most significant effect which needs to be taken into account in this analysis is the large, fluctuating background. The jet response to such fluctuations is measured on an ensemble basis by embedding simulated jets into real events. By comparing the momenta of the embedded jet and the geometrically matched reconstructed jet one can evaluate the response in terms of the δp_T distribution

$$\delta p_T = p_{T,\text{jet}}^{\text{reco}} - p_{T,\text{jet}}^{\text{emb}} = p_{T,\text{jet}} - \rho \times A - p_{T,\text{jet}}^{\text{emb}}. \quad (5.1)$$

Knowing the δp_T distribution and describing the detector response by parametrization of the TPC tracking efficiency and momentum resolution, the fully corrected spectrum was obtained by the method of unfolding. Two different methods of unfolding have been used: Bayesian and Singular Value Decomposition (SVD) unfolding [6, 7]. The systematic uncertainty of the unfolded solution includes variation in the choice of prior and regularization parameter.

Fully corrected recoil jet spectra were obtained for a large number of different prior distributions and regularization parameter values. Fig. 2 shows two examples of unfolded results for two particular choices of unfolding method, prior distribution and regularization parameter. Spectra both in peripheral and central collisions are shown.

The ratio of recoil yield in central and peripheral collisions (I_{CP}) measures jet modification due to the medium. Fig. 3 shows the fully corrected spectra both in peripheral and central collisions

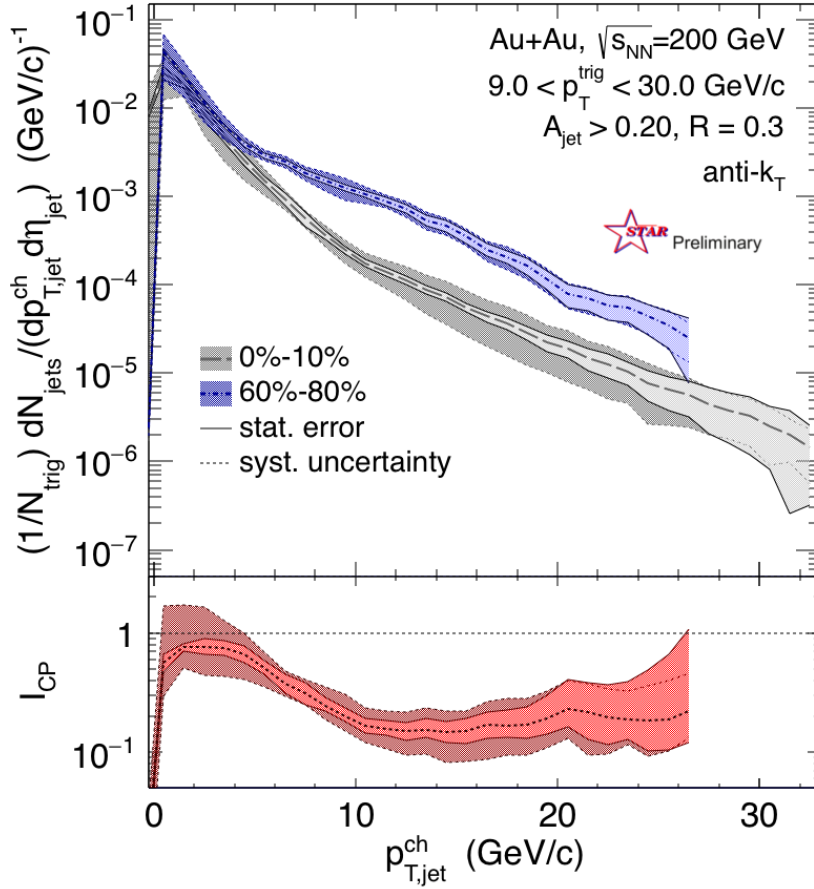


Figure 3: Upper panel: Fully corrected recoil-jet yield per trigger for central and peripheral Au+Au collisions at $\sqrt{s_{NN}} = 200$ GeV. Bottom panel: I_{CP} , ratio of fully corrected recoil jet spectra in central (0-10%) and peripheral (60-80%) Au+Au collisions at $\sqrt{s_{NN}} = 200$ GeV.

(top panel) and their ratio I_{CP} (bottom panel). The systematic error includes unfolding uncertainty (prior choice, regularization parameter value) and uncertainty on the tracking efficiency. For low jet momenta $p_T < 5$ GeV/c, I_{CP} is close to unity. For higher jet momenta $p_T > 10$ GeV/c I_{CP} drops to ~ 0.2 , which indicates significant jet suppression in central Au+Au collisions compared with peripheral collisions. This is a stronger suppression than observed in a similar measurement by the ALICE collaboration in Pb+Pb collisions at $\sqrt{s_{NN}} = 2.76$ TeV. ALICE measured $I_{CP} \approx 0.6$ for $20 < p_{T,jet} < 100$ GeV/c with $R = 0.4$ [8]. However the jet p_T shift, the horizontal shift needed for the peripheral spectra to match the central spectra, is similar in both experiments. Therefore, the larger suppression observed at RHIC may be due to similar out-of-cone energy transport combined with a steeper falling spectrum at RHIC energies than LHC energies. The observed suppression could be also influenced by the different surface bias from different trigger particle p_T and collision

energies at STAR and ALICE.

6. Summary and Outlook

Fully corrected semi-inclusive recoil jet spectra measured by the STAR experiment in 0-10% and 60-80% Au+Au collisions at $\sqrt{s_{NN}} = 200$ GeV have been presented. A stronger jet suppression is observed at RHIC energies than LHC energies, which however corresponds to a similar horizontal p_T shift in the jet spectrum.

The measurement will be extended by utilizing the high statistics 2014 data with more than one billion Au+Au events at $\sqrt{s_{NN}}=200$ GeV, together with incorporation of signals from the BEMC detector.

Acknowledgment

The work has been supported by the grant 13-20841S of the Czech Science Foundation (GACR).

References

- [1] STAR Collaboration, M. E. Beddo *et al.*, BNL-PUB-5347 (1992).
- [2] STAR Collaboration, M. Anderson *et al.*, Nucl. Instrum. Meth. A **499**, 659 (2003).
- [3] M. Cacciari, G. P. Salam, and G. Soyez, JHEP **04**, 063 (2008), 0802.1189.
- [4] <http://www.lpthe.jussieu.fr/salam/fastjet/>.
- [5] M. Cacciari, G. P. Salam, and G. Soyez, JHEP **04**, 005 (2008), 0802.1188.
- [6] G. D'Agostini, ArXiv e-prints (2010), 1010.0632.
- [7] A. Hocker and V. Kartvelishvili, Nucl.Instrum.Meth. **A372**, 469 (1996), hep-ph/9509307.
- [8] ALICE, J. Adam *et al.*, JHEP **09**, 170 (2015), 1506.03984.

Jet Measurements at STAR

Jan Rusnak^{*†}

*Nuclear Physics Institute, Czech Academy of Sciences,
Na Truhlarce 39/64, 180 86 Prague, Czech Republic*

E-mail: rusn@email.cz

Jets are an important tool to explore the properties of the hot and dense nuclear matter created in heavy-ion collisions. However, full jet reconstruction in such events is a challenging task due to the extremely large and fluctuating background, which generates a large population of combinatorial jets that overwhelm the true hard jet population.

In order to carry out accurate, data-driven jet measurements over a broad kinematic range in these conditions of small signal to background, we use modern approaches in order to measure inclusive charged jet distributions and semi-inclusive charged jet distributions recoiling from a high momentum trigger in central Au+Au collisions. In addition we present the measurement of the di-jet transverse momentum asymmetry, A_J . These jet measurements allow a direct comparison of jet quenching at RHIC and the LHC.

*7th International Conference on Physics and Astrophysics of Quark Gluon Plasma
1-5 February, 2015
Kolkata, India*

^{*}Speaker.

[†]For the STAR collaboration.

1. Motivation

Hard scattering processes produce partons with high transverse momentum p_T . These recoiled partons fragment and then hadronize into a collimated stream of mesons and baryons. These final state hadrons are clustered into a jet, which should reflect the kinematics of the hard scattered parton. Due to the fact that jets originate from hard processes, perturbative QCD is applicable for calculation of their cross-section. The pQCD calculations describe measurements of jet production in elementary collisions (pp, e+e) with high accuracy [1].

In heavy-ion collisions, jets are produced in an early stage of the collision, allowing them to interact with the surrounding medium (quark gluon plasma, QGP). A parton traverses through the hot, dense, strongly interacting medium, losing energy via radiative and collisional processes, which will soften and broaden the final state jet [2]. By comparing properties of jets in heavy-ion collisions with theoretically well described jets in elementary collisions, one can indirectly study properties of the QGP. Jets are therefore a good probe of the QCD matter.

2. Experimental Setup and Data-sets

Analyses presented in this proceeding are based on data recorded by the Solenoidal Tracker At RHIC (STAR), which is a complex detector consisting of several sub-detectors and full azimuthal coverage. Its main sub-detector is a large Time Projection Chamber (TPC) capable of tracking and identification of charged particles down to a transverse momentum of 100 MeV/c. The TPC is surrounded by a Barrel Electromagnetic Calorimeter (BEMC) and other detectors such as Time Of Flight (TOF) and Muon Telescope Detector (MTD) and a massive solenoidal 0.5 T magnet. Full description of the STAR experiment and its main sub-detectors can be found in [3, 4, 5].

Inclusive and semi-inclusive jet analyses use minimum bias (MB) data from Au+Au collisions at an energy per nucleon pair of $\sqrt{s_{NN}}=200$ GeV recorded by the STAR experiment at RHIC in 2011. Events with TPC multiplicities corresponding to 0-10% and 60-80% most central Au+Au collisions and having the z position of the primary vertex within 30 cm from the center of the TPC are further used in these data analyses.

The $|A_J|$ analysis uses High-Tower (HT) triggered events (events with energy deposit in a BEMC tower above a certain threshold) recorded by the STAR experiment in Au+Au collisions at $\sqrt{s_{NN}}=200$ GeV in 2007 with the TPC multiplicity corresponding to the 0-20% most central Au+Au collisions.

3. Jet Reconstruction

Inclusive and semi-inclusive jet analyses presented below use the TPC tracks to reconstruct charged jets. The TPC tracks were required to have transverse momenta $p_T > 0.2$ GeV/c, pseudo-rapidity $|\eta| < 1$ and at least 20 TPC space-points.

The di-jet asymmetry $|A_J|$ measurement is based on full jets, utilizing also energy deposited in the BEMC towers. 100% hadronic correction was applied to the BEMC towers (the entire p_T of a track matched to a calorimeter tower is subtracted from that tower's energy).

The TPC tracks (and calorimetric towers) were collected into jets using the anti- k_T algorithm provided by the FastJet package [6, 7]. The jet area A was then calculated using the population of soft “ghost particles” [8]. The background energy was subtracted jet-by-jet from the reconstructed jet transverse momentum by

$$p_{T,\text{jet}}^{\text{reco}} = p_{T,\text{jet}} - \rho \times A \quad (3.1)$$

where ρ is the background median energy density calculated for each event as

$$\rho = \text{med}\left\{\frac{p_{T,\text{jet}}^i}{A_i}\right\} \quad (3.2)$$

where the index i goes through all reconstructed jets in the event (with exclusion of the 2-3 hardest jets in the event). The background jets are reconstructed using the k_T algorithm.

The jet resolution parameter R , which determines the size of the reconstructed jet, was chosen to be 0.2, 0.3 and 0.4. All jets are required to lie within the fiducial rapidity acceptance $|\eta| < 1 - R$.

4. Inclusive Charged Jet Measurements

The inclusive jet cross-section in p+p collisions represents an important observable that is calculable in pQCD. In heavy-ion collisions jet fragmentation will be affected by the presence of the hot and dense medium created in these collisions. Therefore it is of a high importance to compare the p+p measurements with those in the nucleus-nucleus collisions.

Jet reconstruction in the environment of the heavy-ion collisions has to correct for the large and highly fluctuating background. In order to reduce the combinatorial jet background in the Au+Au collisions a cut on the transverse momentum of the leading hadron in the jet (hadron with the highest transverse momentum) is applied. In our case we impose a cut of $p_T^{\text{leading}} > 5 \text{ GeV}/c$. Such a cut induces a fragmentation bias, which needs to be systematically studied (see Fig. 1). However, as there are no requirements on the rest of the jet constituents, the effect of the bias is negligible for high-momentum jets.

The most significant effect which needs to be taken into account in this analysis is the large background fluctuation. The jet response to such fluctuations is measured on ensemble basis by embedding simulated jets into real events. By comparing the momenta of the embedded jet and the geometrically matched reconstructed jet one can evaluate the response in terms of the δp_T distribution

$$\delta p_T = p_{T,\text{jet}}^{\text{reco}} - p_{T,\text{jet}}^{\text{emb}} = p_{T,\text{jet}} - \rho \times A - p_{T,\text{jet}}^{\text{emb}} \quad (4.1)$$

It has been shown [9] that the shape of the δp_T distribution is almost independent of the fragmentation model of the embedded jet. Also the dependency of the δp_T distribution on the momentum of the embedded probe is very weak as can be seen in Fig. 2.

The δp_T distribution is sampled in order to produce the corresponding response matrix $\mathbf{R}_{\delta p_T} \left[p_{T,\text{jet}}^{\text{reco}}, p_{T,\text{jet}}^{\text{emb}} \right] = \mathbf{R}_{\delta p_T} \left[p_{T,\text{jet}}^{\text{emb}} + \delta p_T, p_{T,\text{jet}}^{\text{emb}} \right]$. The detector response is approximated by the parametrization of the TPC tracking efficiency which was estimated by the embedding of simulated tracks into real events and running the TPC track reconstruction algorithm on such events.

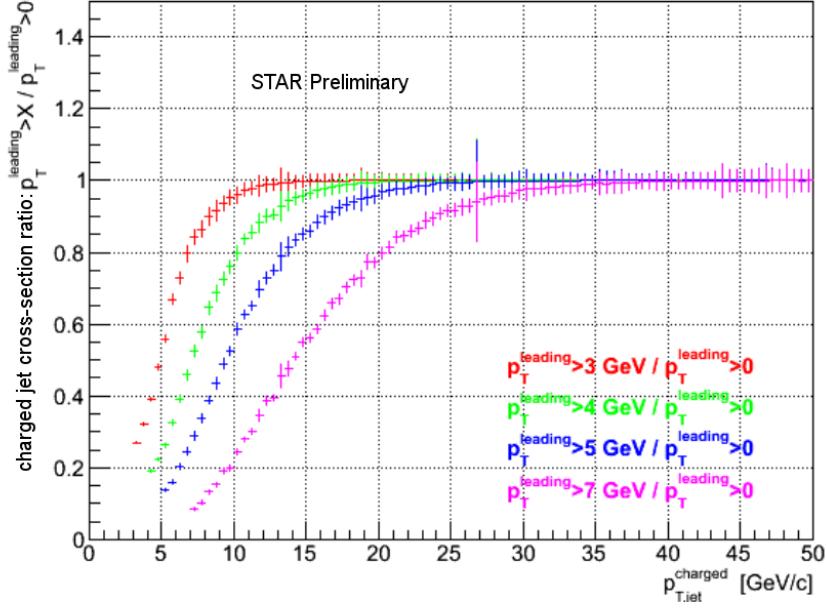


Figure 1: Effect of the p_T^{leading} cut on PYTHIA charged jet spectra at $\sqrt{s_{NN}}=200$ GeV and within STAR acceptance.

The tracking efficiency for hadrons is 68% at $p_T=0.5$ GeV/c and 72% for $p_T > 1$ GeV/c in central collisions.

Using jets generated by PYTHIA, a detector response matrix $\mathbf{R}_{instr} [p_T^{\text{det}}, p_T^{\text{part}}]$ was calculated, where p_T^{part} is the transverse momentum of the generated (and reconstructed) PYTHIA jet and p_T^{det} is the momentum of the same (geometrically matched) jet after the tracking efficiency was applied to its constituents.

The full correction response matrix \mathbf{R}_{full} is obtained by multiplying the two response matrices

$$\mathbf{R}_{full} = \mathbf{R}_{\delta p_T} \times \mathbf{R}_{instr} \quad (4.2)$$

Using this response matrix and a power-law prior distribution, the jet transverse momentum spectrum is corrected for the background fluctuations and the TPC tracking efficiency via an iterative Bayesian unfolding [10]. No p_T cut-off is applied on the jet spectrum prior unfolding.

The systematic uncertainty arising from the unfolding was estimated by varying the power of the initial power-law prior distribution (from -3 to -6) and by varying the number of iterations. Another component of the systematic uncertainty comes from the uncertainty on the tracking efficiency. It was estimated by varying the tracking efficiency $\pm 5\%$ (absolute).

After the unfolding procedure the jet spectrum is further corrected for the jet reconstruction efficiency by multiplying a given momentum bin with the inverse value of the corresponding efficiency. When calculating the jet reconstruction efficiency, one should not compare directly detector-level and particle-level distributions bin-by-bin. Due to the detector effects, a jet having $p_{T,jet}^{\text{part}}$ will be typically detected with $p_{T,jet}^{\text{det}} \neq p_{T,jet}^{\text{part}}$ and thus potentially migrate from i -th p_T bin to j -th. Comparing i -th bin of particle-level spectrum with i -th bin of detector level spectrum is

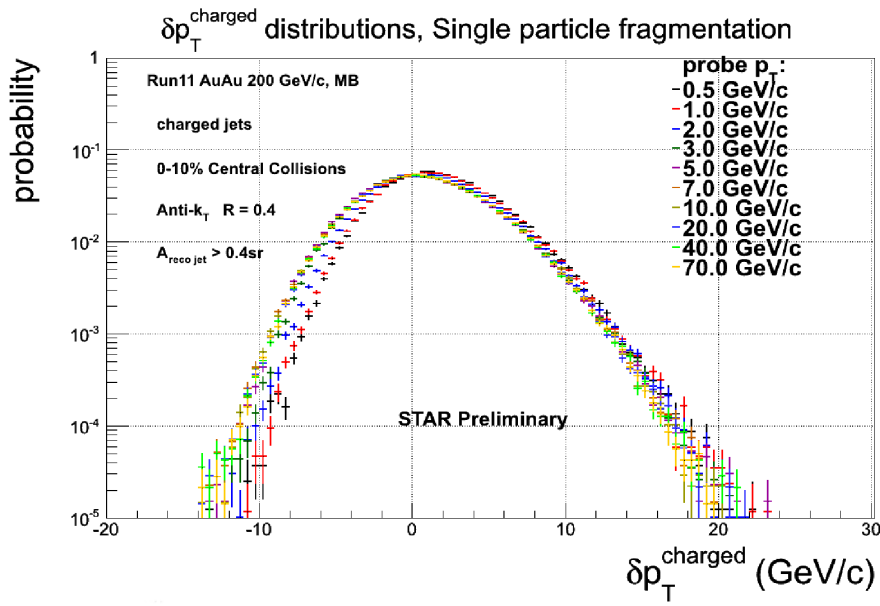


Figure 2: δp_T distribution for central Au+Au collisions at $\sqrt{s_{NN}}=200$ GeV for several momenta of embedded probes.

therefore not a good strategy and one has to take into account the above mentioned bin migration. Jet reconstruction efficiency was thus defined with respect to the particle-level jets as

$$\varepsilon(p_{T,\text{jet}}^{\text{part}}) = \frac{\frac{dN_{\text{jet}}}{dp_{T,\text{jet}}^{\text{det}}} \otimes \widetilde{\mathbf{R}}_{\text{instr}}^{-1} \left[p_{T,\text{jet}}^{\text{part}} \rightarrow p_{T,\text{jet}}^{\text{det}} \right]}{\frac{dN_{\text{jet}}}{dp_{T,\text{jet}}^{\text{part}}}} \quad (4.3)$$

where $\frac{dN_{\text{jet}}}{dp_{T,\text{jet}}^{\text{det}}}$ and $\frac{dN_{\text{jet}}}{dp_{T,\text{jet}}^{\text{part}}}$ are the detector-level and particle-level jet spectra. The expression in the numerator of Equation (4.3) is to be understood as unfolded and regularized detector-level spectrum. Unfolding of the detector-level spectrum was done using only the instrumental response matrix $\mathbf{R}_{\text{instr}}$.

Fig. 3 shows the inclusive charged jet spectra for jet resolution parameters $R = 0.2$ and 0.3 , corrected for the background fluctuations, TPC tracking efficiency and jet reconstruction efficiency. Systematic uncertainties from unfolding and tracking efficiencies are added linearly.

The low momentum part of the spectra is biased by the cut on the momentum of the leading hadron $p_T^{\text{leading}} > 5$ GeV/c. PYTHIA simulations shown on Fig. 1 reveal that the effect of this bias is significant up to momenta $p_{T,\text{jet}} \simeq 4 \cdot p_T^{\text{leading}} = 20$ GeV/c.

In order to calculate the charged jet nuclear modification factor R_{AA} a valid pp baseline is needed.

5. Semi-Inclusive Recoil Charged Jet Measurements

A way to avoid the bias on the jet fragmentation caused by imposing a momentum cut on the jet constituents is to bias the event selection instead. This can be done by selecting a high momentum

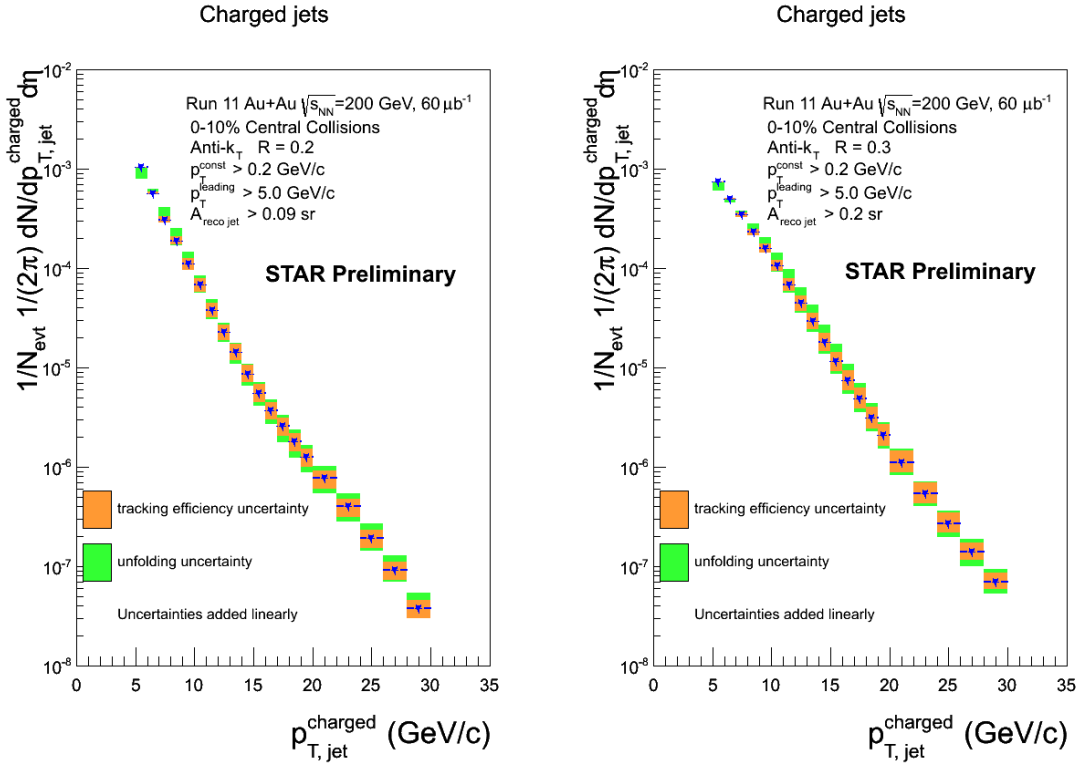


Figure 3: The unfolded p_T spectrum of charged jets in central Au+Au collisions at $\sqrt{s_{NN}}=200$ GeV for $R = 0.2$ (left) and $R = 0.3$ (right).

hadron trigger. Jets reconstructed on the away side in azimuth will be completely unbiased with respect to their fragmentation (there is no need to impose a cut on the constituents' momenta). Furthermore such a jet population will be biased towards larger path-length in the medium making it a viable probe of the medium. An observable which is easily calculable by means of pQCD is the recoil jet yield per trigger. Jets are reconstructed with anti- k_T algorithm with resolution parameter $R = 0.3$. The azimuthal acceptance of the recoil jets is chosen to be within 45 degrees from the recoil direction opposite to the trigger hadron,

$$|\phi_{Jet} - (\phi_{Trig} + \pi)| \leq \pi/4. \quad (5.1)$$

The hadron trigger momentum range is chosen to be 9-19 GeV/c.

A unique mixed event method was developed which should describe the background as closely as possible. The mixed event is created by replacing all tracks in a real event by randomly selected tracks from randomly chosen events (one track from one event) from the same centrality bin, event plane direction bin and primary vertex z position bin. All high momentum tracks ($p_T > 3$ GeV/c) which could possibly come from a hard jet are discarded. This creates a perfectly uncorrelated sample of tracks which preserve some important features of the real events, e.g. the detector acceptance inefficiencies.

The jet reconstruction algorithm is then run on the mixed event (ME) sample with the same settings as on the real events (“same event”, SE). The obtained ME jet spectrum is normalized by

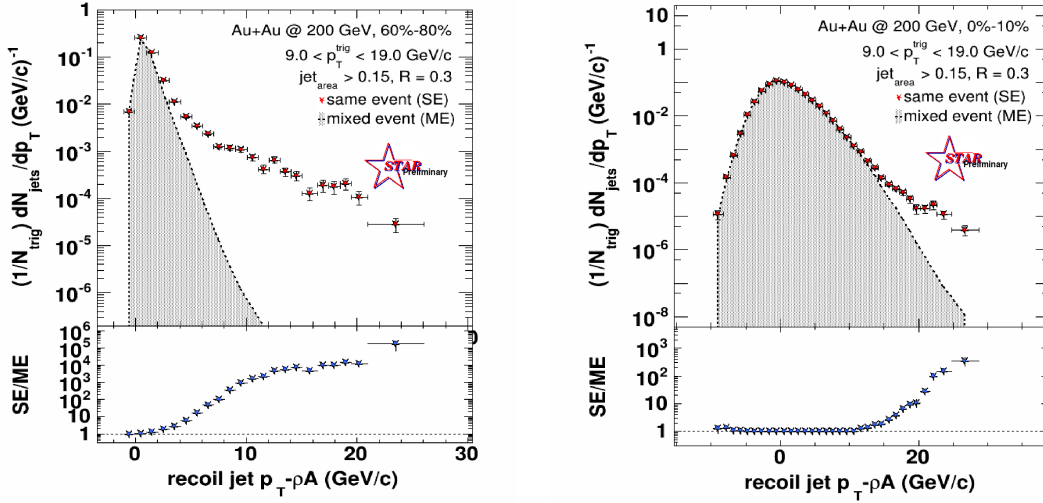


Figure 4: Uncorrected recoil charged jet spectrum in comparison with mixed event spectrum in peripheral (left) and central (right) Au+Au collisions at $\sqrt{s_{NN}}=200$ GeV.

matching the integral of the left hand side (LHS) of the spectrum with the LHS of the SE spectrum. The size of this normalization region was systematically varied and the resulting variance was included in the systematic uncertainties.

Fig. 4 shows both the same event and mixed event recoil charged jet spectra in peripheral and central Au+Au collisions normalized per trigger yield. As one would expect, the background is much less severe in the peripheral collisions than in the most central ones. The bottom panels show the ratio SE/ME. In central collisions, the low momentum spectrum is dominated by the background. Since the ratio SE/ME is consistent with unity up to 10 GeV/c in the central collisions (right bottom panel), this means the background is perfectly described by the mixed event. The recoil jet signal is then extracted by subtracting the mixed event spectrum from the same event.

The recoil jet spectrum shown in Fig. 5 is not corrected for the background fluctuations and detector effects yet. However, as a first approximation, it can be compared with PYTHIA 8 p+p spectrum smeared with δp_T distribution, hence simulating the effect of the presence of heavy-ion collision background, and with tracking efficiency applied to the PYTHIA jets constituents.

Such “detector level” recoil jet spectra normalized per trigger yield are shown on Fig. 5 both for the peripheral and central Au+Au collisions. In peripheral collisions there is no sign of a suppression of the Au+Au spectra with respect to PYTHIA, as can be seen from the ratio plot in the bottom. However in central Au+Au collisions a strong suppression is evident.

6. $|A_J|$ Measurements

The di-jet imbalance A_J is defined as

$$A_J = \frac{p_{T,1} - p_{T,2}}{p_{T,1} + p_{T,2}} \quad (6.1)$$

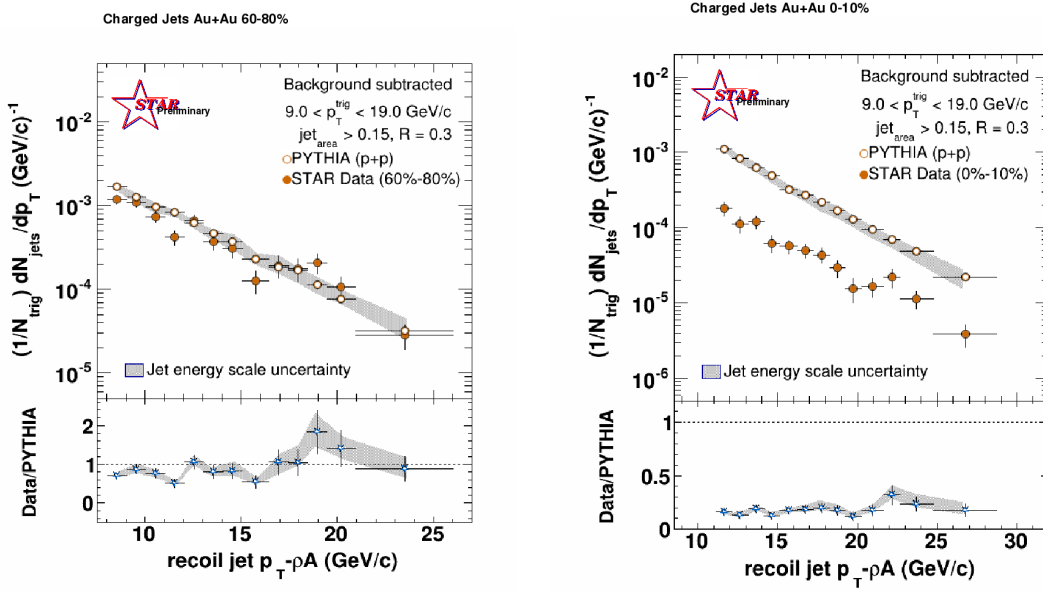


Figure 5: Charged recoil jet spectrum after background subtracted in peripheral (left) and central (right) Au+Au collisions at $\sqrt{s_{NN}}=200$ GeV compared with PYTHIA charged recoil jet spectrum smeared with background fluctuations and simulated detector effects.

with $p_{T,1}$ and $p_{T,2}$ being the transverse momentum of the leading (most energetic) and sub-leading (second most energetic) jet. In the absence of a medium in the elementary collisions, produced pairs of jets have the same p_T and are back-to-back with an azimuthal angle difference $\Delta\phi = \pi$ (at leading order pQCD). In heavy-ion collisions on the other hand it is expected that the presence of the hot, dense and strongly interacting medium would lead to the observation of highly unbalanced di-jets.

In order to study the effect of the fragmentation bias, two jet samples were compared. A highly biased jet sample was obtained by requiring the jet constituents' momentum to satisfy $p_{T,const} > 2$ GeV/c. The jet imbalance A_J^{biased} was then calculated for leading jets with momentum $p_{T,jet}^{Lead} > 20$ GeV/c (16 GeV/c for $R=0.2$) and sub-leading jets with $p_{T,jet}^{SubLead} > 10$ GeV/c (8 GeV/c for $R=0.2$). A second jet sample was created by imposing only minimal cut on jet constituents $p_{T,const} > 0.2$ GeV/c. Leading and sub-leading jets were geometrically matched with jets from the first sample. Using this unbiased jet sample the jet imbalance $A_J^{unbiased}$ was calculated.

As a baseline HT pp events from 2006 embedded into Au+Au MB events from 2007 were also used. These events were created to test whether the jet imbalance is merely due to the fluctuating background under the jets, and not any QGP effect.

Fig. 6 shows calculated values of di-jet imbalance A_J^{biased} (circles) and $A_J^{unbiased}$ (squares) in triggered central Au+Au collisions (full symbols) and pp events embedded into minimum bias Au+Au events (open symbols). Jets with $R = 0.2$ (left) possess significant difference between Au+Au and pp collisions, both for the biased and unbiased jet sample. However a good agreement between Au+Au and pp events in case of $R = 0.4$ for unbiased jets (containing soft particles) is observed. Such an energy restoration within the cone of $R = 0.4$ has not been observed at the LHC

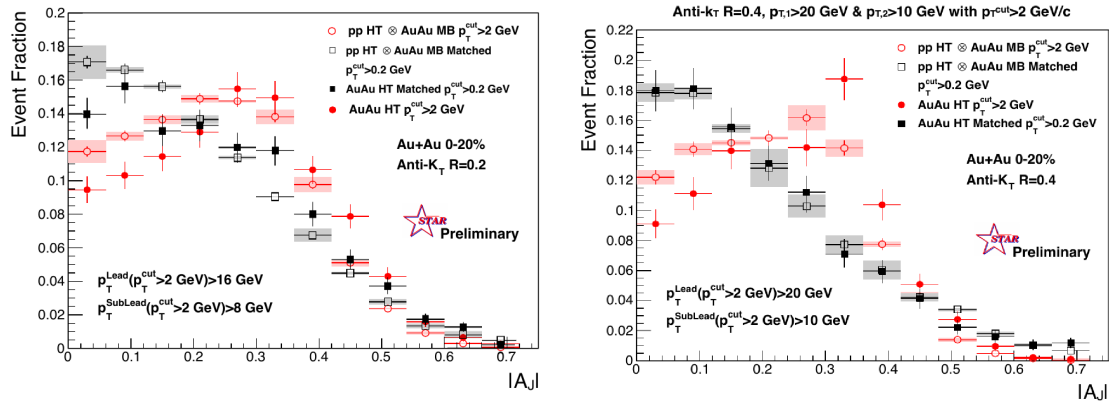


Figure 6: $|A_J|$ of full jets with resolution parameter $R = 0.2$ (left) and $R = 0.4$ (right) in Au+Au collisions (full symbols) and pp collisions with embedded Au+Au background (open symbols) at $\sqrt{s_{NN}}=200$ GeV.

[11, 12].

7. Conclusions and Outlook

We have presented recent measurements of inclusive charged jet spectra in central Au+Au collisions corrected for the background fluctuations and detector effects. The low momentum part of the presented spectra exhibits a bias due to the cut on the leading hadron momentum. However a valid pp baseline is necessary in order to calculate the charged jet nuclear modification factor R_{AA} .

In central Au+Au collisions, the semi-inclusive recoil charged-jet spectrum normalized per trigger shows a strong suppression relative to the "detector level" PYTHIA pp spectrum. There is no evidence of suppression in peripheral Au+Au collisions.

The measurement of the di-jet momentum imbalance $|A_J|$ reveals energy recovery in the most central Au+Au collisions for larger jets with $R = 0.4$ when low momentum particles are included in the jet. The observation that for $R = 0.4$ the energy lost is recovered within the cone of the jet is different than what has been seen at the LHC.

However the A_J measurement and the recoil-jet measurement are significantly different analyses due to a strong selection bias of the A_J measurement (and also some bias due to the hadron trigger in the recoil-jet analysis) and hence their observations should not be directly compared.

All the presented analyses will be further improved by utilizing the high statistics 2014 data with more than one billion Au+Au events at $\sqrt{s_{NN}}=200$ GeV. As a next step, inclusive and semi-inclusive jet analyses will also use the information from the BEMC thus extending their kinematic reach.

Acknowledgment

The work has been supported by the grant 13-20841S of the Czech Science Foundation (GACR).

References

- [1] A. Ali and G. Kramer, The European Physical Journal H **36**, 245 (2011).

- [2] M. Gyulassy and M. Plumer, Phys. Lett. **B243**, 432 (1990).
- [3] STAR Collaboration, M. E. Beddo *et al.*, BNL-PUB-5347 (1992).
- [4] STAR Collaboration, M. Anderson *et al.*, Nucl. Instrum. Meth. A **499**, 659 (2003).
- [5] STAR Collaboration, M. Beddo *et al.*, Nucl. Instrum. Meth. A **499**, 725 (2003).
- [6] M. Cacciari, G. P. Salam, and G. Soyez, JHEP **04**, 063 (2008), 0802.1189.
- [7] <http://www.lpthe.jussieu.fr/salam/fastjet/>.
- [8] M. Cacciari, G. P. Salam, and G. Soyez, JHEP **04**, 005 (2008), 0802.1188.
- [9] STAR Collaboration, P. Jacobs, (2010), 1012.2406.
- [10] G. D'Agostini, ArXiv e-prints (2010), 1010.0632.
- [11] ATLAS, G. Aad *et al.*, Phys. Rev. Lett. **105**, 252303 (2010), 1011.6182.
- [12] CMS, D. Krofcheck, PoS **ICHEP2012**, 418 (2013).